Structural Integrity of Active Pharmaceutical Ingredients in Formulations by Electron Microscopy Techniques

Mark S'ari

School of Chemical and Process Engineering

University of Leeds

A thesis submitted for the degree of

Doctor of Philosophy

28th September 2018

The candidate confirms that the work submitted is their own, except where work which has formed part of jointly authored publications has been included. The contribution of the candidate and the other authors to this work has been explicitly indicated below. The candidate confirms that appropriate credit has been given within the thesis where reference has been made to the work of others.

The work in Chapter 4 of the thesis has appeared in *Molecular Pharmaceutics* as follows: Mark Sari, Helen Blade, Rik Brydson, Stephen D. Cosgrove, Nicole Hondow, Leslie P. Hughes, and Andy Brown. (2018). Toward Developing a Predictive Approach To Assess Electron Beam Instability during Transmission Electron Microscopy of Drug Molecules. *Molecular Pharmaceuticals*, DOI: 10.1021/acs.molpharmaceut.8b00693.

The candidate was responsible for carrying out the experiment work, data analysis and writing. The other authors contributed to writing the manuscript.

Acknowledgements

Firstly, I would like to thank all my academic supervisors, Dr Andy Brown, Professor Rik Brydson and Dr Nicole Hondow for giving me the opportunity to pursue this PhD and for all their help and scientific guidance over the last four years. Many thanks to Dr Helen Blade, Dr Les Hughes and Dr Steve Cosgrove at AstraZeneca for their useful feedback and discussions during our meetings in Leeds and at Macclesfield. I would also like to thank AstraZeneca and the EPSRC for funding.

Besides my supervisors, I would like to thank all the LEMAS staff for training I received and their help while using the electron microscope when things went wrong. I would also like to thank all the technicians that have helped me carry out various experiments.

Dr Alex Eggeman at the University of Manchester is acknowledged for collecting the scanning electron diffraction results and I thank him for helping me with the data analysis. Stuart Micklethwaite at LEMAS is acknowledged for collecting the focused ion beam results.

Special thanks to all my friends that have provided me with many entertaining times and our multiple dug-ups throughout the past four years. Finally, I want to thank my girlfriend Alex and all of my family, especially my Mum, Dad and sister for all their kind and loving support not only over the past four years but throughout my life and I am very grateful for all that you have done for me.

Abstract

It has been estimated that up to 75% of drugs in development exhibit low water solubility. This can be problematic due to low solubility and slow dissolution rates, resulting in limited bioavailability of the drug. Amorphous solid dispersions (ASDs) have been developed to increase solubility by dispersing the drug within an amorphous polymer matrix. The amorphous drug must remain dispersed in the correct physical form throughout the shelf-life of the product but due to thermodynamic instability of the amorphous drug phase, phase separation and recrystallisation tend to occur. Therefore characterisation techniques that can detect phase separation and crystallisation at the earliest possible stage are desirable. This thesis outlines the use of transmission electron microscopy (TEM) to address these problems within ASDs, however, the use of TEM presents its own challenge in examining organic crystals due to electron beam damage.

TEM was used to determine electron fluence limits for a range of poorly water-soluble compounds and from this predict the stability of other compounds. The electron fluence limits were determined by measuring the fading of electron diffraction patterns (typically giving critical electron fluence values of 0.1 - 15 $e^{-}/Å^{2}$). This information can be used to reduce electron beam induced effects such as crystal damage when trying to detect low levels of crystallinity in ASD.

ASDs of felodipine and copovidone, prepared by hot-melt extrusion and spray-drying at two drug loadings of 15 and 30% felodipine were examined by powder X-ray diffraction (pXRD), differential scanning calorimetry (DSC) and Fourier transform infrared spectroscopy (FTIR)

and TEM. pXRD, DSC and FTIR identified the ASDs to be amorphous and TEM was found to be the most sensitive method in detecting crystal particles at 4% by number of areas examined and also identified the presence of multiple polymorphs of felodipine (mainly forms I and II). A similar sample was then stored at 75% and 85% relative humidity to accelerate ageing to determine the amount, size and type of nucleation and growth of crystals from the ASD. It was found that the addition of water to the system caused crystallisation to occur at the edges of ASD particles in size ranges of 10 - 1000 nm and into metastable forms (II, III and IV) of felodipine.

Several preliminary experiments using different electron microscopy techniques were tested to determine the viability of TEM for providing further details on the recrystallisation of ASDs. FIB-SEM, scanning moiré fringe imaging and scanning electron diffraction (SED) imaging were tested. The scanning techniques provide the most promise and are shown to be capable of imaging atomic lattice of crystalline felodipine by the moiré technique and identify size and form of crystals in ASDs by SED.

Overall the results show TEM to be a useful addition to the range of tools used to characterise ASDs, providing detail on the size, phase and location of the early stages of crystallisation in ASD. Further work is required to fully quantify amounts of crystalline material present and defect levels of crystals within new and aged ASDs by TEM.

Abbreviations

ADF	Angular dark field
AIC	Akaike information criterion
API	Active pharmaceutical ingredient
ASD	Amorphous solid dispersion
ATR	Attenuated total reflection
BCS	Biopharmaceutical classification system
BF	Bright field
BIC	Bayesian information criterion
BSE	Back scattered electron
CB	Conduction band
CCD	Charged coupled device
C_F	Critical fluence
DF	Dark field
DLR	Dose limited resolution
DQE	Detector quantum efficiency
DSC	Differential scanning calorimetry
EDX	Energy dispersive X-ray
EELS	Electron energy loss spectrum
EM	Electron microscopy
FEG	Field emission gun
FFT	Fast Fourier transform
FIB	Focused ion beam
FTIR	Fourier transform infra-red
HAADF	High angle angular dark field
HME	Hot melt extrusion
IR	Infra-red
J	Electron flux
MLR	Multiple linear regression
NCE	New chemical entity
NMF	Non-negative matrix factorisation
PC	Principal component

PCA	Principal component analysis
pXRD	Powder X-ray diffraction
RH	Relative humidity
SAED	Selected area electron diffraction
SD	Spray drying
SDD	Silicon drift detector
SED	Scanning electron diffraction
SEM	Scanning electron microscopy
σ	Standard deviation
SMF	Scanning moiré fringes
SNR	Signal to noise
STEM	Scanning transmission electron microscopy
TEM	Transmission electron microscopy
T_g	Glass transition temperature
UHV	Ultra high vacuum
VB	Valence band
WAXS	Wide angle X-ray scattering
Z	Atomic number

Contents

List of Figures

Chapter 1

Introduction

Approximately 75% of drugs in development exhibit low water solubility which can be problematic as low solubility and slow dissolution rates and can result in limited bioavailability of a drug. Amorphous solid dispersion (ASD) is one technique that has been developed to increase solubility, and hence bioavailibity, by dispersing a drug within an amorphous polymer matrix. The amorphous drug must remain dispersed in the correct physical form throughout the shelf-life of the drug product. However, due to thermodynamic instability of the amorphous drug phase, phase separation and recrystallisation tend to occur. It is therefore important to apply characterisation techniques that are able to detect phase separation and crystallisation at the earliest possible stage. This thesis outlines the use of high spatial resolution, transmission electron microscopy (TEM) to address these problems within ASDs. However, TEM presents its own challenge in examining organic crystals due to electron beam damage.

The following chapter briefly introduces the problems associated with poorly water-soluble drugs, methods used to improve solubility and to characterise their structure and finally problems associated with electron beam damage of organic samples within TEM. The overall aims and objectives of the thesis are described at the end of the second chapter and the key findings regarding the possibilities and limits of TEM analysis for characterising drug products are presented in the final chapter and abstract.

1.1 Problems of Poorly Water-Soluble Drugs

The preferred administration route for the majority of medicines is by oral drug delivery which includes the use of tablets and capsules. These methods of formulation are generally stable, easy to produce and can be accurately dosed in addition to being the most convenient method for the majority of patients to administer. For these methods to be effective and reproducible in all patients, the drug needs to be readily released from the formulation and dissolve in an aqueous solution. The dissolved drug is then required to permeate across epithelial cells, typically in the small intestine before being absorbed into the bloodstream and transported around the body to the required target.

Developments in the field of combinatorial chemistry and high throughput screening have allowed for a large number of new chemical entities (NCE) to be generated (Hann and Oprea, 2004). A drive towards increasing the potency of drugs by synthesising drug candidates that form stronger interactions between the drug and a target receptor has resulted in an increase in lipophilic drugs (Lipinski, 2000). Therefore the absorption of the NCE and their potential drugs are limited by low solubility in water. It has been estimated that up to 75% of drugs in drug development exhibit low water solubility and that approximately 40% of drugs marketed as medicines are classed as poorly water-soluble (Di et al., 2012; Takagi et al., 2006).

The Biopharmaceutics Classification System (BCS) is a framework used to categorise active pharmaceutical ingredients (APIs) and solid dosage forms according to their permeability, aqueous solubility and dissolution which governs the rate and extent of drug absorption by humans and the oral bioavailability (Amidon et al., 1995). Drugs with high water solubility and membrane permeability (defined below) are classified as Class I; those with low solubility and high permeability are Class II; those with high solubility and low permeability are Class III and drugs with low solubility and low permeability are BCS IV. The criteria for determining if a drug has low solubility, permeability and dissolution are as follows:

- Low solubility is classified when the highest dose strength is insoluble in 250 ml or less of aqueous media across physiological pH ranges (1 - 7.5)

(Chavda et al., 2010).

- Low permeability is classified when the extent of absorption in humans is less than 90% of the administered dose or in comparison to an intravenous dose.
- Slow dissolution is classified if $< 85\%$ of the immediate release dose dissolves within 30 minutes in an aqueous medium containing 0.1 N HCl or simulated gastric fluid or pH 4.5 buffer and pH 6.8 buffer or simulated intestinal fluid; carried out using standardised dissolution apparatus.

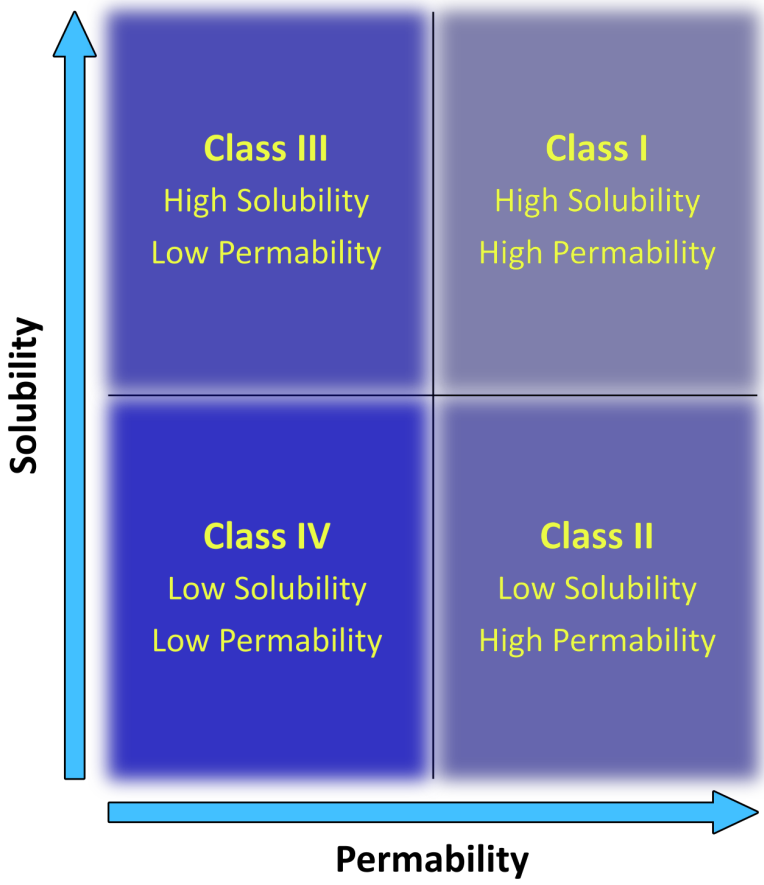

Figure 1.1: Biopharmaceutical classification system (BCS)

Solubility and dissolution are the rate-determining steps for drug absorption for BSC II and IV drugs, as the API must first be dissolved in solution before permeating through epithelial cells. Therefore, to improve the oral bioavailability, strategies to improve aqueous solubility are often considered in an attempt to move compounds from BCS classes II and IV into BCS classes I and III, respectively.

1.2 Methods to Improve Aqueous Solubility

A variety of methods that physically or chemically modify an API can be implemented in order to increase solubility and therefore enhance bioavailability (Rodriguez-Aller et al., 2015). Examples include the use of salt formation, particle size reduction, pH adjustments, lipidic formulations, micro/nanoemulsions and solid dispersions (Khadka et al., 2014; Sareen et al., 2012). However, practical limitations exist for some of these strategies, for example, salt formations are not feasible for neutral, weakly acidic or weakly bases compounds and particle size reduction is limited in how much the size can be decreased, difficulties in controlling the final characteristics of the API and wettability/handling.

Solid dispersions are one such method that can overcome many of these practical limitations and increase solubility and rate of dissolution for poorly water-soluble drugs (Janssens and Van den Mooter, 2009a). The solid dispersions can be described as a mixture of two or more components in the solid state. Typically an amorphous drug and polymer matrix. This solid dispersion can be formed using fusion also known as melt base techniques or solvent-based techniques. It is known that the higher energy state of the metastable (generally amorphous) phase has an increased solubility compared to more thermodynamically stable phases (Huang and Tong, 2004; Pudipeddi and Serajuddin, 2005). For the amorphous phase, there is a lack of long-range crystalline order and therefore there is no energy barrier to overcome from the crystal lattice energy before dissolving into solution. In amorphous solid dispersions (ASDs), ideally, the amorphous drug interacts strongly with a suitable water soluble polymer to form hydrogen bonds to create a single phase that is molecularly mixed (Janssens and Van den

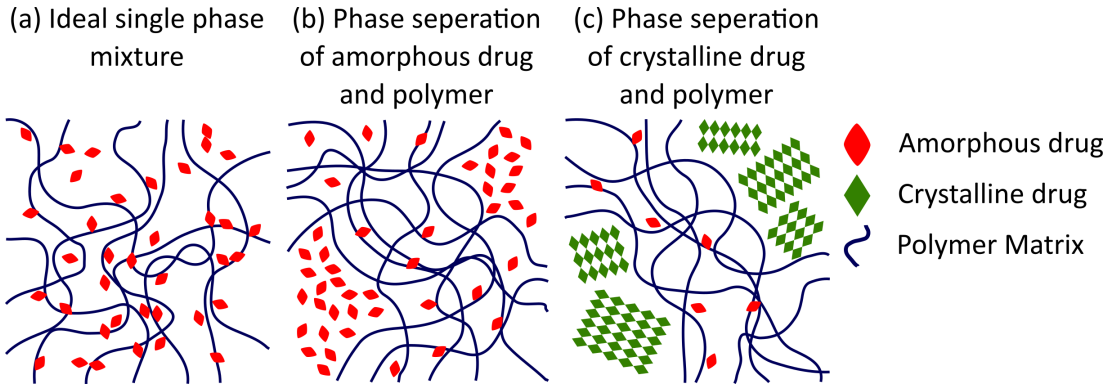

Figure 1.2: (a) Schematic of amorphous solid dispersion of a molecularly mixed drug and polymer, (b) amorphous-amorphous phase separation (c) and drug crystallisation.

Mooter, 2009a). The polymer kinetically stabilises and improves the physical stability and prevents or reduces the rate of amorphous-amorphous phase separation or crystallisation. Polymers that are used must be biologically inert and water soluble. Examples of commonly used polymers are hydroxypropyl methylcellulose (HPMC), hydroxypropyl cellulose (HPC), polyvinylpyrrolidone (PVP) and polyvinylpyrrolidone-vinyl acetate (PVP/VA).

Despite kinetically stabilising the amorphous phase, thermodynamic drivers will always exist that can cause the metastable amorphous form to recrystallise to a more thermodynamically stable form over time or when influenced by an external stimulus, for example, moisture or heat during the formulation process or storage (Baird and Taylor, 2012). If recrystallisation occurs, even in small amounts in an ASD, the solubility and dissolution rate of the drug can decrease leading to lower bioavailability and further recrystallisation of the API. Standard methods for the analysis of crystallinity in an ASD include powder X-ray diffraction (pXRD), Fourier transform infrared spectroscopy (FTIR) and differential scanning calorimetry (DSC). In order to assess different formulation options available during drug development, used to produce ASDs, an early indication of recrystallisation is required and hence the growing need for improved limits of detection (currently 2 - 10% by volume) (Eddleston et al., 2010; Leuner and Dressman, 2000). This presents the opportunity to use less conventional but more

sensitive techniques such as transmission electron microscopy (TEM) to identify and understand the early stages of phase separation and crystallisation.

1.3 Electron Beam Damage

TEM is an analytical technique that has very high spatial resolution and can measure crystallite size, orientation and morphological form at a single particle level and even when only trace amounts of a material are present (Eddleston et al., 2010). This is achieved through bright field (BF), dark field (DF) imaging and selected area electron diffraction (SAED). In addition energy dispersive X-ray (EDX) spectroscopy and electron energy loss spectroscopy (EELS) can provide information on elemental composition and chemical configuration. All of these techniques are well established for the characterization of metals and other inorganic materials but have been less widely applied to organic crystals, due to the ease with which the latter are damaged by the electron beam.

Upon irradiation of an organic crystal by TEM, secondary electrons are produced which generate free radicals and ions. These are highly reactive species that can cause bond breakage, known as radiolysis, and this is understood to be the main mechanism for damage in organic crystals leading to changes in structure and, in some cases, composition and chemistry (Egerton, 2013; Egerton et al., 2004; Stenn and Bahr, 1970). This damage leads to a loss of order in crystals which can be observed through the fading of diffraction spots to amorphous rings (Henderson and Glaeser, 1985; Jones and Thomas, 1979). A loss of molecular structure can be observed in EELS spectra and possibly changes in chemical composition by EELS and EDX (Egerton et al., 2004). Mass loss of lighter atoms due to bond breakage and sputtering may be seen as a change in mass-thickness contrast where areas that atoms have been removed from appear less intense in the BF image (Egerton et al., 2004; Jones and Thomas, 1979). The propensity for damage to be caused to the sample by the electron beam can be quantified by measuring the characteristic/critical electron fluence (C_F) in units of $e^-/Å^2$.

The terms electron dose and electron fluence tend to be used interchangeably, by the electron microscopy community although, strictly, dose is the energy absorbed by the sample per unit mass (in units of Grays). Critical electron fluence

is the total number of electrons per unit area irradiating the sample at which the intensity of a feature, such as a diffraction spot, drops to e^{-1} of the initial maximum intensity (Henderson and Glaeser, 1985). The value of the critical fluence depends on the material and a variety of experimental parameters; in general, for irradiation energies of 80 - 300 kV, biological materials have C_F in the range of 1 - 15 $e^-/Å^2$ organic crystals 0.2 - 120 $e^-/Å^2$, zeolites 100 - 600 $e^-/Å^2$, and transition metal oxides $> 10^7$ $e^-/Å^2$ (Glaeser, 1971; Kumar and Adams, 1990; Pan and Crozier, 1993; Pan et al., 2010; Revol and Manley, 1986). Organic compounds generally show a large range of C_F, making it difficult to know the electron beam sensitivity without determining it experimentally. Although it is generally believed that crystals comprised of aromatic molecules are more beam stable compared to aliphatic molecules (Alexander and Charlesby, 1954; Fryer, 1987; Fryer et al., 1992). Little work, however, has been carried out in a single study on either a range of organic compounds with different structural motifs or on determining how other factors relating to molecular structure may influence C_F.

In summary the following chapter will carry out a review on the scientific literature regarding the use of amorphous solid dispersions in the pharmaceutical industry and the effects of electron beam damage during TEM analysis, with particular emphasis on organic crystals. The aims and objectives of this thesis will then be laid out to directly detail how TEM has been used in this study to investigate the electron beam stability of APIs in ASDs. These points will then be experimentally analysed and discussed in the following results chapters (4 - 7) and the main conclusions and future work be reported in the final chapter.

Chapter 2

Literature Review

This chapter will explore previous and current scientific literature regarding amorphous solid dispersions (ASDs) and electron beam damage in TEM, with particular focus on organic crystals. The types of solid dispersions in terms of physical structure, preparation methods, physical stability and solid state characterisation will be discussed. This includes challenges associated with stabilising ASDs and methods that have been used to address and characterise these issues; one of which being electron microscopy techniques. Then the literature surrounding the effects of electron irradiation in TEM will be examined, investigating the types of damage that occur, how they affect different materials, how the damage can be quantified and then methods that have been used to reduce beam-induced effects. Following the review of the literature, the motivation for the work carried out in this thesis will be discussed, and the aims and objectives of the experimental work detailed in subsequent chapters will be outlined.

2.1 Review of Solid Dispersions

There are a number of advantages that formulating APIs as a solid dispersion provides, making this approach particularly attractive to the pharmaceutical industry as a strategy for improving oral bioavailability. Despite existing since the early 1960s relatively few marketed drugs have taken advantage of formulating drugs using ASDs. According to a review paper by Jermain et al. (2018) only 8 marketed ASD products were released before 2010. However, within 8 years at

least 16 new products have been released; demonstrating the increasing interest in using ASDs as a formulation strategy to increase solubility.

2.1.1 Classifications of Solid Dispersions

Solid dispersions can be described as a mixture of two or more components in the solid state, typically an API and carrier matrix, and is an umbrella term for various different solid state structures. The various solid state structures can be used to classify different types of solid dispersions available with each having differences in the physical stability, dissolution rate and solubility and in some cases compressibility.

In a review by Meng et al. (2015) solid dispersions were classified into six distinct categories these being: crystalline API dispersed in crystalline carrier (C*-C); crystalline API dispersed in amorphous carrier (C*-A); amorphous API dispersed in crystalline carrier (A*-C); amorphous API dispersed in amorphous carrier (A*-A); API molecularly dispersed in crystalline carrier (M*-C) and API molecularly dispersed in amorphous carrier (M*-A). Schematics of all these solid dispersions are shown in Figure 2.1

The first solid dispersion to be prepared for dissolution enhancement was class C*-C and was formed by Sekiguchi and Obi (1961) who demonstrated the use of a eutectic mixture of sulfathiazole and urea in improving the solubility. This was achieved by producing a microcrystalline suspension during dissolution with increased surface area resulting in faster dissolution rate (Goldberg et al., 1966). A eutectic mixture exhibits a single solid-to-liquid phase transition and is considered to be an intimate mixture of microcrystals of two crystalline components. Typically, sugars and crystalline polymers, such as polyethylene glycol (PEG), are used as crystalline carriers. Chiou and Riegelman (1969) reported an increase in the dissolution rate of an A*-C solid dispersions of griseofulvin when formulated using crystalline PEG as a carrier. Both class C*-C and C*-A are generally undesirable due to the limited solubility of many crystalline APIs, requiring more energy to dissolve due to the crystal lattice energy of the API (Vo et al., 2013). Active pharmaceutical ingredients that have a high tendency to crystallise generally possess high melting points, low miscibility between the API and carrier,

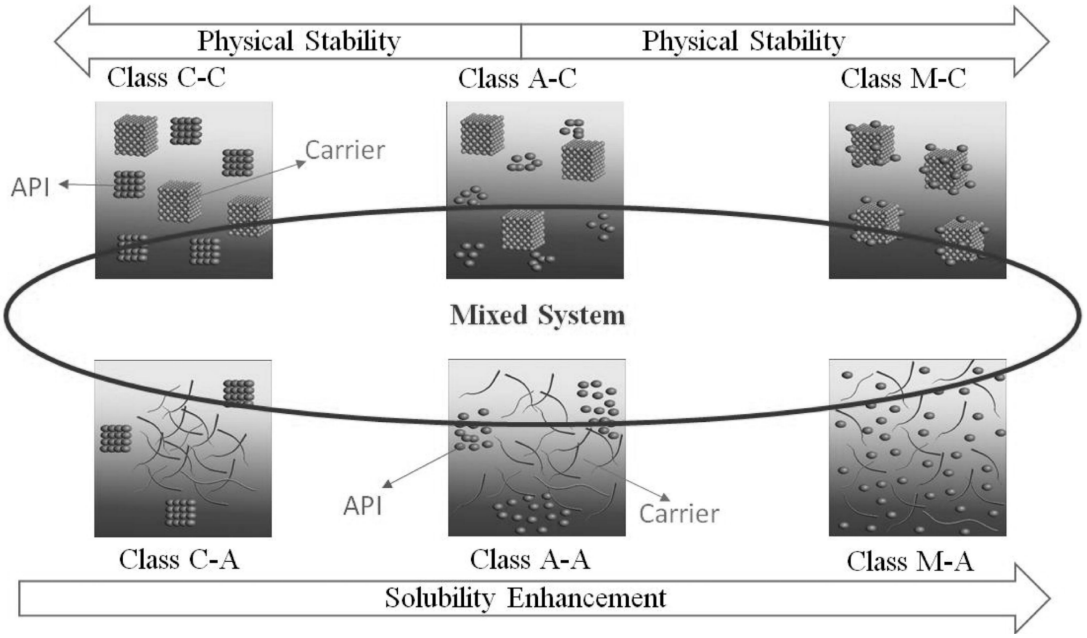

Figure 2.1: Classification of binary solid dispersions based on their physical structure (C: crystalline, A: amorphous, M: molecularly dispersed). Rank order of physical stability and solubility enhancement between systems are shown. Usually, solid dispersions are mixed systems, which contain two or more classes. Taken from Meng et al. (2015).

formulated in low carrier concentrations and by inefficient preparation methods (Baird and Taylor, 2012; van Drooge et al., 2006; Vo et al., 2013). C*-C and C*-A solid dispersions may be used in some cases as they are more stable and are effective when small improvements in solubility are required without compromising the chemical and physical stability.

Class A*-C and class A*-A solid dispersions have been extensively researched as methods to enhance the dissolution of poorly water-soluble drugs (Adibkia et al., 2013; Chauhan et al., 2013; Eloy and Marchetti, 2014; Guo et al., 2013; Okonogi et al., 1997). A study by Okonogi et al. (1997) observed a solubility enhancement for a class A*-C solid dispersion containing ofloxacin and urea, attributing the increase due to the presence of the amorphous phase of ofloxacin. However, the solid dispersion was unstable and over time crystallised which limited the miscibility. In class A*-A solid dispersions the API exists as amorphous

clusters within the amorphous carrier matrix forming an API-rich phase and polymer-rich phase. Despite not being molecularly mixed together intermolecular bonds can be formed between the API and polymer, which play a significant role in stabilising the API in the amorphous phase (to a certain degree) (Baird and Taylor, 2012; Chauhan et al., 2013).

Solid dispersion of the class M*-C and M*-A are highly desirable due to stability compared to A*-A and enhanced dissolution behaviour due to the size of the API being as small as possible (a single molecule), increasing the surface area for dissolution (Leuner and Dressman, 2000). Extremely high miscibility and strong molecular interactions are required to form molecular dispersions (Baird and Taylor, 2012). In the case of M*-C solid dispersions, co-crystals are formed by crystallising the API and carrier together and generally form non-covalent bonds (Aakeröy, 1997; Vishweshwar et al., 2006). Previous studies have shown good dissolution and physical stability for these co-crystals (Basavoju et al., 2008; Hickey et al., 2007). In class M*-A solid dispersions a single phase is formed through the homogeneous mixing between the API and amorphous matrix. Polymeric carriers are often used in formulating M*-A and A*-A solid dispersions, as they tend to form amorphous polymer chain networks. Amorphous solid dispersions can refer to either M*-A or A*-A. It is crucial to find a suitable polymer that is miscible and forms strong bonds with the API to properly form a single phase mixture and prevent phase separation and crystallisation. The preparation method also affects the formation of M*-A solid dispersion.

It is also important to characterise which type of solid dispersion is present since it influences the stability and dissolution properties. Combinations of different classes of solid dispersions can often be found due to very high or low drug loadings, during manufacturing/storage and when administering the drug. In most cases a mixture of class A*-A and C*-A are observed, indicating some crystallisation of the amorphous phase (Guo et al., 2013; Marsac et al., 2008b). In addition to the six classes discussed other solid dispersion systems exist were additional components such as another polymer or surfactant are added to the mixture (Janssens et al., 2008). These solid dispersions can be used to alter the release and dissolution profile of the API (Huang et al., 2006).

2.1.2 Preparation Techniques

There are two main preparation methods used to manufacture amorphous solid dispersions these being; fusion-based methods, such as hot-melt extrusion (HME), and solvent evaporation-based methods, for example, spray-drying. In addition, other techniques have been reported in the literature, such as compression moulding, co-grinding/milling, solvent wetting and microwave irradiation (Broman et al., 2001; Kim et al., 2006; Moneghini et al., 2008; Vogt et al., 2008). However, here HME and spray drying are discussed in more detail, regarding the method, potential problems and scalability for manufacturing.

Hot-melt extrusion

Hot-melt extrusion involves the use of high shear mixing of molten material to produce a homogeneous dispersion, resulting in an increased number of or stronger drug-polymer interactions.

To carry out HME the material (API and amorphous polymer) are fed into an extruder from a hopper. In general, a basic extruder is divided into three sections: a feed zone where the mixture enters, the compression zone where the material is melted and homogenised and a metering zone where the flow of the extrudate is stabilised to ensure a uniform thickness of the resulting product. One or two rotating screws are located inside a cylindrical barrel that moves the molten material along and mixes the API and polymer together through a high shear force. The geometry and configuration of the screws, rotation direction, speed and temperature can vary for each section of the extruder. Interchangeable screws are used to allow for different conditions and configurations to be tested. At the end of the metering zone, the molten material passes through a die that determines the shape of the extrudate. Further down-stream processing such as milling of the extrudate can then be carried out (Agrawal et al., 2016; Chokshi and Zia, 2010; Patil et al., 2016).

An advantage of HME is the scalability of the technique and that it can be used during small-scale production or testing and during manufacturing since it is a continuous manufacturing process. Hot-melt extrusion does not require

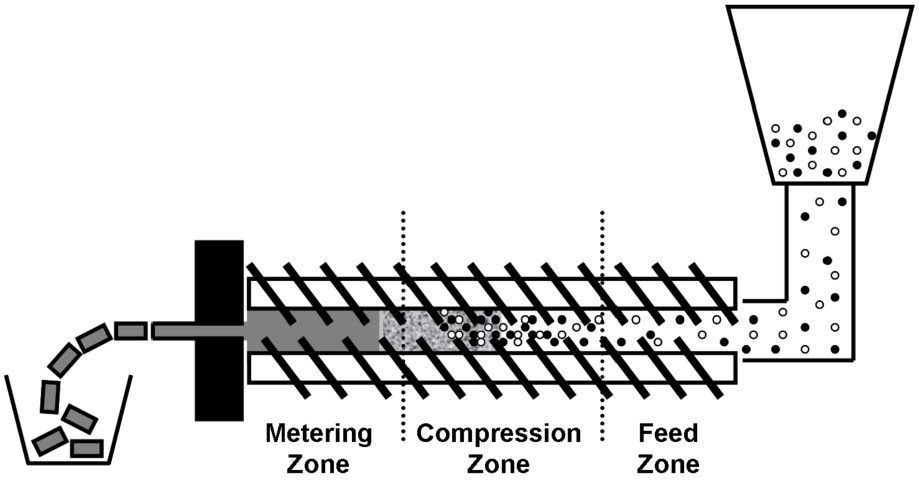

Figure 2.2: Schematic of hot-melt extrusion process, showing the flow of powder from the hopper and the different zones within the barrel of the extruder.

any solvent which is desirable for ASDs as they can affect the stability (Serajuddin, 2000). Despite these advantages, hot-melt extrusion is not always a suitable method for production of amorphous solid dispersions. The main limiting factor is the use of high temperatures to melt the API and polymer, which can lead to thermal degradation of APIs and polymers with low degradation temperatures. Additionally, the number of conditions that can be varied during the melt extrusion process, such as the feed rate, screw speed/size and extrusion temperature require extensive experimentation and analysis to fully optimisation manufacturing using this technique. Furthermore, thermal expansion of the polymer when leaving the extruder can result in non-homogeneous mixing (Qi et al., 2011).

Solvent evaporation

Solvent evaporation techniques generally involve a two-step process; the API and polymer carrier must be completely dissolved at the desired ratio in the same organic solvent. The resulting solution is subsequently evaporated to leave the ASD particles (Serajuddin, 2000). On a small scale, thin films can be produced by spin-coating the solution or by depositing onto a substrate. Although, slow

solvent evaporation can lead to crystallisation of the API (Konno and Taylor, 2006; Lin et al., 1995; Rumondor et al., 2009a).

Other solvent techniques include rotary evaporation, freeze drying and spray-drying (Crowley and Zografi, 2002; Rumondor et al., 2009c; Vasanthavada et al., 2005). Spray-drying is a particularly attractive option for the pharmaceutical industry due to low thermal stress, rapid evaporation preventing crystallisation and scalability (Miller et al., 2016). During the spray drying process, the stock solution of the dissolved API and polymer is passed through a spray nozzle to atomises it into a hot gas. The small droplet size, allows the solvent to rapidly evaporate resulting in precipitation of solid particles. These are then passed through a cyclone to a collection chamber.

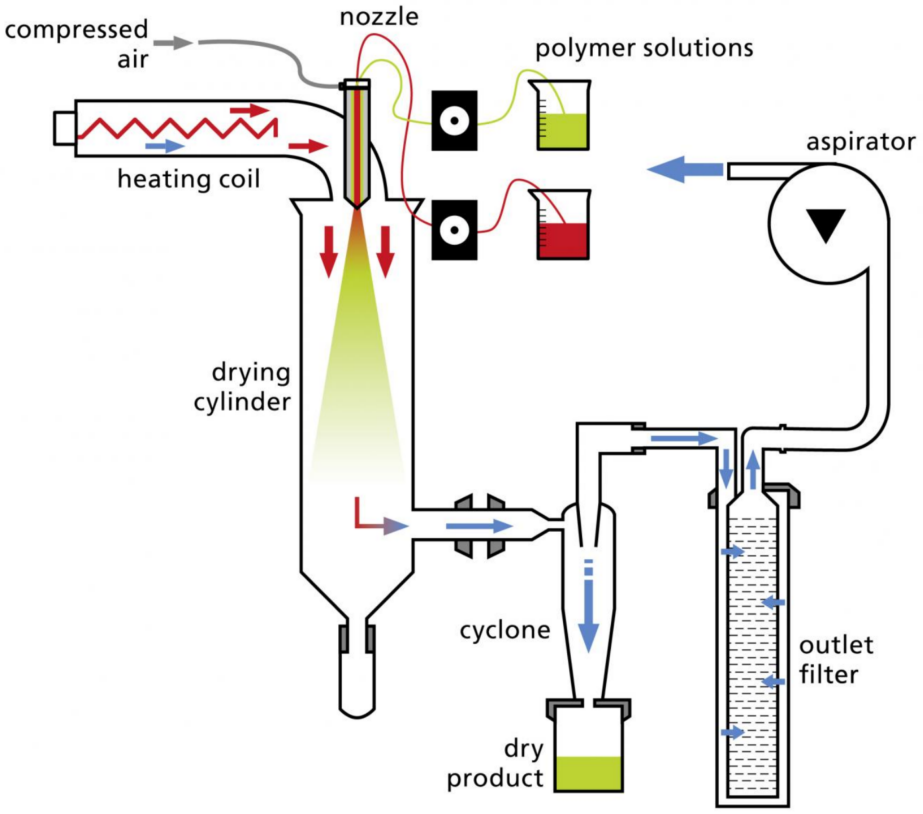

Figure 2.3: Schematic of spray-drying process, showing the flow of powder from the stock solution into the drying cylinder after passing through the spray nozzle that atomises the solution into a hot gas.

Spray-drying offers several advantages, for example, production of material with a consistent particle size distribution, produce amorphous solid dispersions of thermally-sensitive APIs and the ability to be scaled up for large-scale manufacturing. However, due static charge build up on the powder, it can be difficult to handle and collect particles from the spray drier. Recrystallisation can be problematic if the API and polymer are not completely dissolved in the solvent and if the presence of residual solvent alters the physical properties of the ASD (e.g. by acting as a plasticiser).

2.1.3 Physical Stability

The advantages of using ASDs (A*-A and M*-A) are apparent in the increase in solubility and dissolution properties of the amorphous API compared to the crystalline form. However, the amorphous form of an API is metastable, and not the most thermodynamically stable configuration. As the amorphous phase is not stable there is a high risk of amorphous-amorphous phase separation in M*-A and subsequent crystallisation of the API, both resulting in a loss of solubility enhancement. Hence, it is important to stabilise ASDs over the lifetime of a drug product and to understand physical stability. The main factors known to influence physical stability of ASDs are the glass transition temperature (T_g), miscibility, molecular interactions and crystallisation tendency (Baird and Taylor, 2012; Guo et al., 2013).

Crystallisation tendency

Crystallisation is generally thought of as a two-step process whereby clusters of a material nucleate to a size sufficient to be thermodynamically stable and then subsequently grow by interface or diffusion limited process. Nucleation can occur spontaneously from a supersaturated solution (homogeneous nucleation) or in the presence of a foreign particle or surface (heterogeneous nucleation). The supersaturation of the material is the thermodynamic driving force required for homogeneous nucleation and is defined as the difference in chemical potential between molecules in solution and that in the bulk crystal phase.

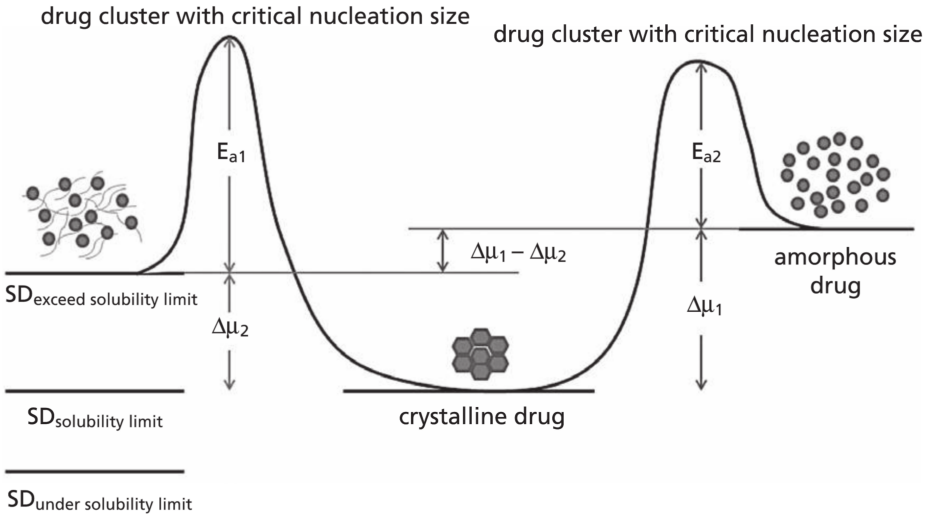

Figure 2.4: Schematic of energy barrier showing the amorphous and crystalline forms of drug, and single phase ASDs. SD represents solid dispersion. $\Delta\mu_1$ represents the chemical potential difference between amorphous drug and crystalline drug. $\Delta\mu_2$ represents the chemical potential difference between amorphous drug in solid dispersion and crystalline drug. E_{a1} and E_{a2} represent the nucleation energy barriers of amorphous drug recrystallised from solid dispersion and its pure amorphous form, respectively. Taken from Li et al. (2013).

The tendency for an amorphous API to recrystallise is thought to be correlated to the recrystallisation of the same API when formulated as a solid dispersions (Eerdenbrugh et al., 2010; Marsac et al., 2006). One example was reported by Marsac et al. (2006) where the recrystallisation of amorphous felodipine and amorphous nifedipine in solid dispersions of polyvinyl pyrrolidone (PVP) and of the pure APIs was examined. Felodipine and nifedipine are structurally analogous and have similar physical properties. Using DSC to determine the enthalpy, entropy and free energy of crystallisation, felodipine was reported to be more stable due to the higher activation energy for nucleation and lower thermodynamic driving force for crystallisation The addition of a polymer carrier can help form a stable ASD even when APIs have a high tendency to crystallise as the API-polymer interaction can increase the thermodynamic barrier to nucleation. Schematically shown in Figure 2.4 (Li et al., 2013). Polymer carriers also reduce the kinetic factors for crystal growth by reducing the rate of attachment of

material at the growing interface or reducing the rate of diffusion through the amorphous matrix).

Miscibility

The API and polymer may be miscible, partially miscible or immiscible within a solid dispersion and it is important to determine how these effect the physical stability and the molecular interactions. Strong interactions between API and polymers will favour the formation of miscible solid dispersions. Thermodynamically this can be shown as the free energy of mixing (ΔG_{mix}) being < 0 for miscible systems and ΔG_{mix} being equal to 0 or greater for immiscible systems (Rumondor et al., 2009a; Van Eerdenbrugh and Taylor, 2012). ΔG_{mix} depends on the the entropy of mixing ΔS_{mix}, which is always positive, and the enthalpy of mixing ΔH_{mix}, shown in Equation 2.1

$$\Delta G_{mix} = \Delta H_{mix} - T\Delta S_{mix} \tag{2.1}$$

ΔH_{mix} is therefore the determining factor for miscibility, meaning that strong molecular interactions reduce ΔG_{mix}.

Flory-Huggins theory can be applied to solid dispersion systems to describe the thermodynamics of mixing that occurs between a binary system, shown in Equation 2.2 (Flory, 1942). The Flory-Huggins/interaction parameter (χ) characterises the strength of the energetic interaction between two molecules relative to their self-interactions (cohesive forces) and is an important parameter to quantify the degree of miscibility.

$$\frac{\Delta G_{mix}}{RT} = n_d ln\Phi_d + n_p ln\Phi_p + n_d\Phi_p\chi \tag{2.2}$$

where n is the number of moles, Φ is the volume fractions of the drug and polymer (denoted by d and p), R is the universal gas constant, T is the absolute temperature and χ, as mentioned above, is the interaction parameter between the drug and polymer. The first two terms on the right-hand side of the Equation 2.2 represent ΔS_{mix}. From Equation 2.2 it can be deduced that a negative or small positive value of χ will reduce the third term that represents ΔH_{mix} thereby reducing ΔG_{mix} and increasing the miscibility. A moderate or large positive

value of χ suggests the molecules tend to interact with like-molecules, leading to immiscibility and phase separation (Janssens and Van den Mooter, 2009a; Marsac et al., 2006; Rumondor et al., 2009a). Stronger interaction between unlike components of a mixture (negative or small χ) increase the stability of an ASD. The value of χ is determined by the total effects of adhesive forces (drug-polymer) and cohesive forces.

Tian et al. (2013a) demonstrated that stronger molecular interactions between two materials do favour higher miscibility by applying Flory-Huggins theory to construct phase diagrams of felodipine solid dispersions prepared using two different polymers (Soluplus and HPMAC). The area in the phase diagram where felodipine and the polymer were miscible was larger in Soluplus than HPMC. Stronger intermolecular interactions were found between felodipine and Soluplus by calculating χ values, which are estimated by measuring the melting point depression by DSC, and were always found to be smaller for felodipine-Soluplus than felodipine-HPMC.

Molecular mobility

Molecular mobility has been associated with amorphous-amorphous phase separation in class M*-A dispersions and the tendency for crystallisation of M*-A and A*-A dispersions. The temperature relative to T_g of an amorphous material is associated with global molecular mobility, also termed α-relaxation (Bhattacharya and Suryanarayanan, 2009). At temperatures below T_g the global mobility decreases, preventing crystallisation and stabilising the amorphous phase through kinetic barriers (Vyazovkin and Dranca, 2005). Temperature and humidity can affect molecular mobility within an ASD as can, manufacturing (poor mixing), storage condition (temperature and humidity) and physical properties of the system (hygroscopicity and T_g). However, crystallisation has been reported to still occur at temperatures below T_g, even when the molecular mobility can be considered to be negligible (Guo et al., 2013).

Johari and Goldstein (1970) suggested that this might be due to the local molecular mobility of polymer chains in a single molecule, also termed as β-relaxation. A greater energy barrier exists for α-relaxation due to it requiring

cooperative motion between multiple molecules, compared to β-relaxation which has a much lower energy barrier and can be important at low temperatures (Vyazovkin and Dranca, 2005).

2.1.4 Solid State Characterisation

Earlier the different types of solid dispersions were discussed as were the different properties concerning API dissolution, the solid state stability and the existence of solid dispersion combinations, for example, A*-A and C*-A. In many cases, it remains difficult to determine the exact state of all of the API within the carrier, especially if multiple combinations exist in low concentrations. Traditional methods used to study the solid state characteristics of solid dispersions include powder X-ray diffraction (pXRD), differential scanning calorimetry (DSC), Fourier transform infrared spectroscopy (FTIR) and hot-stage optical microscopy.

pXRD can easily determine if a sample is crystalline or amorphous, in addition, pXRD has been used by Rumondor and Taylor (2010b) to determine the % crystallinity of ASD overtime when exposed to increased relative humidity. Characteristic Bragg peaks relate to the crystal structure of either the API or carrier (depending on the type of solid dispersion) and can be compared to the pure API and carrier to determine which has crystallised. The detection limits of this technique are generally between 2 - 10% by volume making it difficult to determine low concentrations of crystallinity (Eddleston et al., 2010; Ricarte et al., 2015). For microcrystalline or nanocrystalline particles peak broadening can cause the diffraction pattern to appear amorphous. Kanaze et al. (2006) demonstrated the use of pXRD in identifying microcrystalline API when forming a solid dispersion with amorphous PVP or crystalline PEG. pXRD provides no information regarding bonding or if a solid dispersion is molecularly mixed.

DSC can be used to detect if each component of a solid dispersion is crystalline, amorphous or a mixture of both. This is achieved through the identification of melting temperatures (T_m) and glass transition temperatures (T_g) for each of the components. If a molecularly mixed solid dispersion is examined a single T_g that is at an intermediate value between the T_gs of the separate components would

be expected (Gordon and Taylor, 1952). Similarly if API rich and polymer rich regions are present then two separate T_gs would be observed.

Complimentary information to pXRD and DSC can be acquired using hot-stage optical microscopy and polarised light microscopy regarding the melting or crystallisation of solid dispersions. However, with light microscopy it is not possible to resolve very high-resolution details ($<$ 100 nm) and it cannot identify the degree of mixing between the two components.

Transmission electron microscopy (TEM) is a high-resolution technique that can provide information on the nanoscale. Bhardwaj et al. (2018); Karavas et al. (2007); Marsac et al. (2010) have all used TEM to examine phase separation in ASDs by the use of bright field imaging via contrast differences between heavier atoms such as S and Cl that are present within the API. Similarly, Ricarte et al. (2015) has used TEM to study ASDs, in this case, TEM was used to identify crystals within a solid dispersion of the API, griseofulvin, and polymer, hydroxypropyl methylcellulose acetate succinate (HMPCAS), prepared via spray-drying.

Information relating to the adhesive (drug-carier) and cohesive interactions (drug-drug and carrier-carrier) can be identified through spectroscopic methods such as Fourier-transform infrared spectroscopy (FTIR) and Raman spectroscopic mapping. Knowing the bonding environment of functional groups within the solid dispersions can be useful in determining the class of solid dispersion present.

The majority of studies use a combination of techniques to characterise solid dispersion samples for example, in a study by Lin et al. (1995) the change in intermolecular bonding with varying temperature was shown in a theophylline-Eudragit L system through a combination of DSC, pXRD and FTIR data. Another study by Song et al. (2013) used pXRD, FTIR, NMR and DSC to confirm the formation of homogeneous molecular dispersions of felodipine in copovidone prepared by HME. A final example where more novel techniques were used was from a study by Qi et al. (2011), where pulse-force mode atomic force microscopy and localised thermal analysis were used to characterise specific sites of an extruded systems and identified two different crystal forms of felodipine from separate areas. Thus, it is apparent that multiple techniques are required to be used in combination to provide the best information and interpretation regarding solid state characterisation of solid dispersions.

2.2 Electron Beam Damage in TEM

Although electrons can be used to provide useful information in SEM and TEM/STEM the use of high energy electrons can result in alterations to surface or bulk structure of the sample. The type of damage that occurs can be categorised into either elastic scattering, inelastic scattering or a combination of both. Figure 2.5 shows how different beam damage effects are categorised.

Over extended periods of time almost all samples will exhibit some form of visible damage to the sample due to the strong interactions between electrons and matter. Certain types of materials are more prone to these interactions causing them to damage at a much faster rate, notably organic crystals, biological samples, zeolites, metal organic frameworks and polymers.

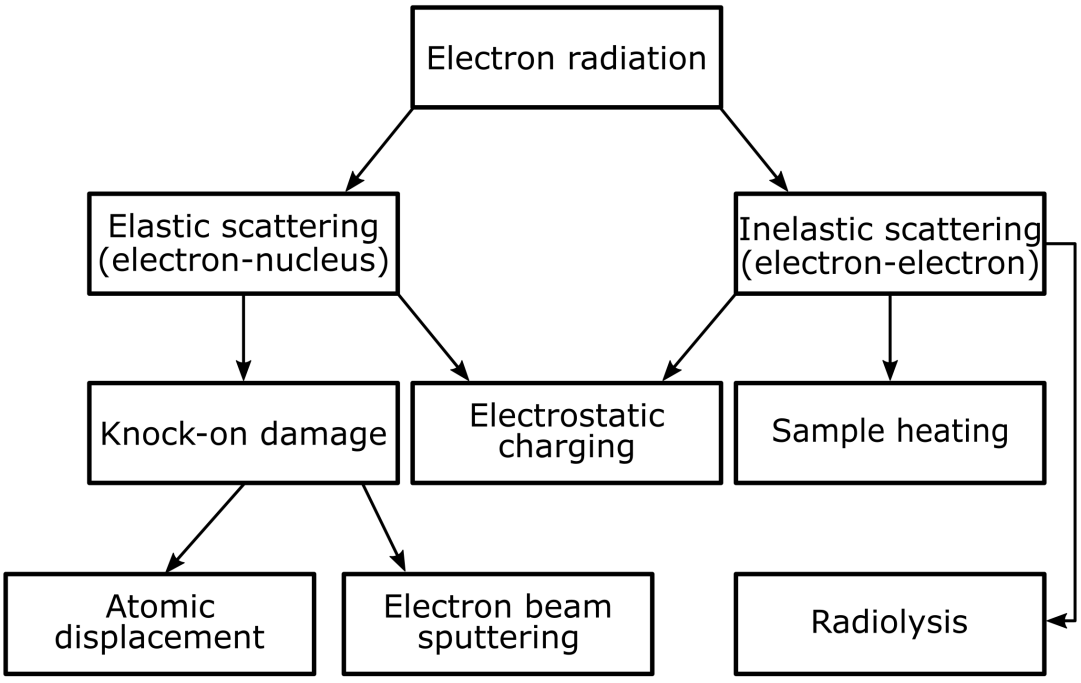

Figure 2.5: Classification of electron radiation damage according to the type of electron scattering and effects produced. Adapted from Egerton et al. (2004).

2.2.1 Elastic Scattering

Elastic scattering occurs between incident electrons from the electron beam and the electrostatic field of an atomic nucleus. When the incident electron interacts with the atom nucleus the total amount of kinetic energy within the system is preserved and no energy is lost through vibrations/heating. The elastically scattered electrons gives rise to electron diffraction patterns and phase contrast in TEM images (Williams and Carter, 2009).

Elastic scattering causes knock-on damage which can be further categorised into atomic displacement and electron beam sputtering, which results in structural changes and mass loss. Electrostatic charging of the sample is also a partly due to elastic scattering.

Knock-on displacement/sputtering

Atomic displacement occurs when the energy transferred from the primary incident electron to the nucleus exceeds the displacement energy (E_d) of the material. E_d is a property of the material relating to the bond strength, crystal lattice and atomic weight of the constituent atoms. The amount of energy transferred depends on the angle of deflection (θ) of the incident electron, Equation 2.3.

$$E = E_{max} \sin^2\left(\frac{\theta}{2}\right) = \left(\frac{E_{max}}{2}\right)(1 - \cos\theta) \tag{2.3}$$

where E_{max} is the maximum energy exchange when the primary electron is deflected by an angle of $\theta = 180°$ and is given by Equation 2.4 (Egerton, 2012; Egerton et al., 2004).

$$E_{max}(eV) = E_0\left(\frac{1.1}{A}\right)\left(2 + \frac{E_0}{m_0c^2}\right) \tag{2.4}$$

where A is the atomic weight of the scattering atom, m_0c^2 is the electron rest energy equal to 511 keV. For very small angles of scattering the energy transferred will be negligible ($<<$ 1eV) and electrons do not cause displacement. As the angle increases the energy transferred to the nucleus increases. When $\theta >$ 90° the electrons back scatter and the resulting energy transferred may be several eV. In Equation 2.3, $E = E_{max}$ when $\theta = 180°$ if E exceeds E_d then the atomic

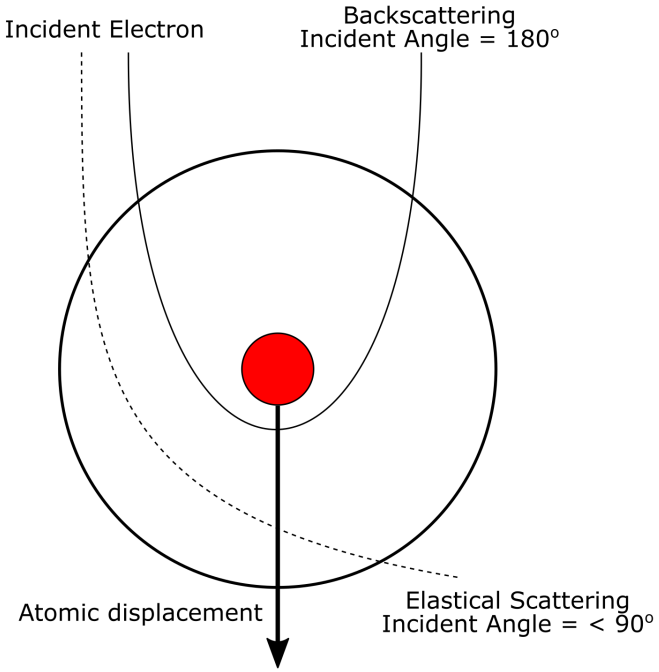

Figure 2.6: Elastic scattering of electrons from an atomic nucleus, shown schematically using a particle model for a collision angles $< 90°$ and for head-on collisions at 180°. Adapted from Egerton et al. (2010).

nuclei can be displaced into nearby interstitial sites. Figure 2.6 demonstrates how the incident electron interact with the atomic nucleus (Egerton et al., 2010).

Atomic displacement can become problematic when high incident electron energies are used on samples that consist of atoms of low or medium atomic numbers. In some organic materials, hydrogen atoms that are involved in hydrogen bonding can have a displacement threshold energy < 2 keV. This means that hydrogen atoms can be easily displaced and may contribute to the damage observed in organic crystals (Egerton, 2012). Due to the mass of the hydrogen atoms, the kinetic energy of a displaced atom is relatively low compared to other atoms and it is unclear if they cause any secondary damage and even how much primary damage the loss causes.

To control displacement damage the incident electron energies can be reduced to avoid exceeding the E_d of the material. Temperature has no effect on displacement due to the momentum being transferred remaining the same, therefore,

cryogenic conditions would have no effect (discussed later in methods to control electron beam damage). An example of using a lower accelerating voltage to prevent displacement damage can be seen when imaging graphene sheets and the use of an accelerating voltage of less than 80 kV has been shown to prevent displacement of individual carbon atoms (Girit et al., 2009).

Similar to atomic displacement, electron beam sputtering only occurs when the incident energy of the electron exceeds a certain threshold value. Equations 2.3 and 2.4 remain valid for sputtering. However, atoms at the surface are ejected into the vacuum rather than interstitial sites and these have a smaller threshold energy compared to displacememt of atoms within the material. A schematic diagram of electron beam sputtering is shown in Figure 2.7 (Egerton et al., 2010).

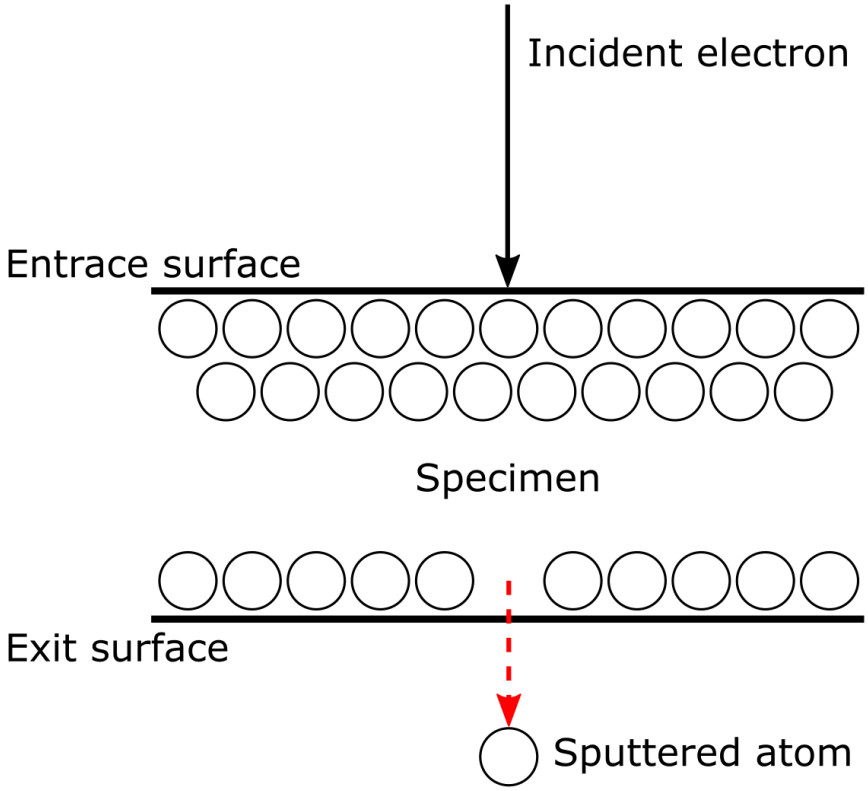

Figure 2.7: Elastic scattering of electrons from a material, shown schematically using a particle model for sputtering of a surface atom. Adapted from Egerton et al. (2010).

E_d is often taken as the sublimation energy per atom (E_{sub}), although values between 1 - 2 E_{sub} have been proposed (Bradley and Zaluzec, 1989). Sputtering mainly involves atoms with low atomic numbers as the threshold energy for sputtering these atoms is lower compared to atoms with a high atomic number (Cherns et al., 1977, 1976). By having a high atomic number material as a coating on the exit surface of the specimen the rate of sputtering can be decreased for light atoms in the specimen, although, the best way to avoid sputtering damage altogether is to limit the incident electron energy (Egerton, 2013).

2.2.2 Inelastic Scattering

Inelastic scattering occurs between incident electrons from the electron beam and atomic electrons that surround each atomic nucleus in the sample. When these collisions occur kinetic energy is transferred and some of the energy is converted into vibrational energy, causing breakage of chemical bonds and heating, which leads to changes to the internal states of the particles (Egerton et al., 2004). Secondary electrons are produced after primary collision events and cause radiolysis which can result in a change in structure and a loss of mass of the specimen (Stenn and Bahr, 1970).

Radiolysis

Radiolysis occurs when the sample is exposed to some form of radiation i.e. electrons, resulting in the cleavage of chemicals bonds and dissociation of molecules. Different materials have different sensitivities to radiolytic damage as well as different mechanisms in which it can propagate. In a primary collision event the energy loss from a primary electron is transferred to a single atomic electron. The excited electron then undergoes a single-electron transition (electron moves to a higher energy state), or a plasmon is formed (oscillations of free electrons). Plasmon oscillations may predominate over single-electron transitions but are rapidly dampened and still result in one or more single-electron transitions (Egerton, 2013; Egerton et al., 2004).

Radiolysis of metals and conductors

In metallic samples or materials with good conductivity single electron transitions occur between the conduction band (CB) and empty states above the Fermi level E_f (unoccupied electron energy levels). This transition leaves a hole in the valence band (VB), although, due to the high density of conduction electrons the hole is filled rapidly on the order of <1 fs, shown in Figure 2.8a.

By the time it takes an atomic vibrations to occur (approximately 1000 fs) the hole is filled and the atom has no time for bonds to break or diffuse away (Hobbs, 1979). The energy that is released during de-excitation creates several phonons with energies of < 0.1 eV generating thermal energy. Overall, there is no lasting displacement of atoms and the amount of radiolytic damage that occurs is little or non-existent in metals and conductors (Egerton, 2013).

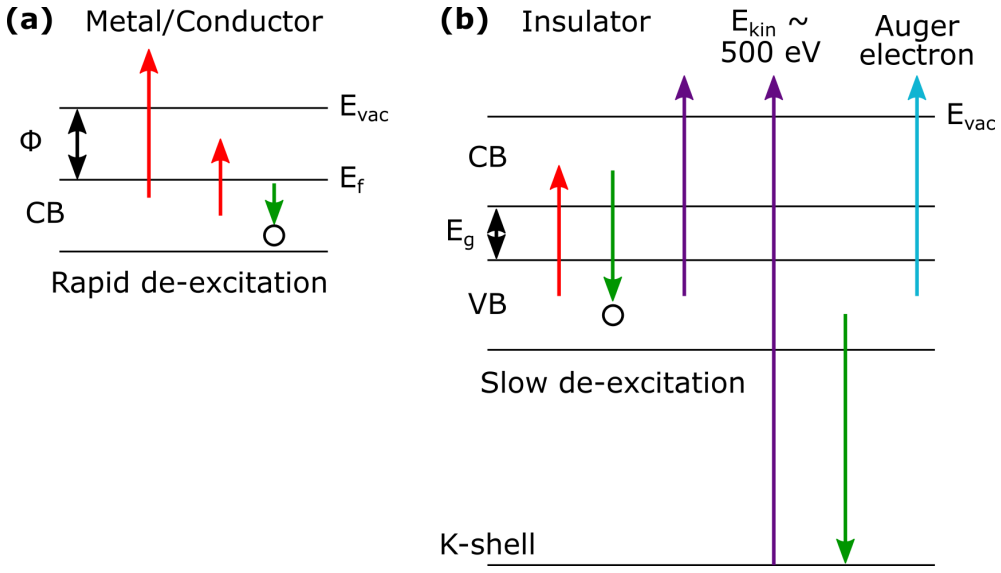

Figure 2.8: Energy-band diagram of a (a) metal /conductor sample and (b) insulating sample. ϕ represents the work function, E_{vac}, E_f, E_g, CB and VB are the vacuum energy, Fermi energy, band gap energy, conduction band and valence band respectively. Upward arrows represent single-electron excitations, while downward arrows are de-excitation processes. Adapted from Egerton (2013).

Radiolysis of insulating materials

In insulating materials such as most organics and some inorganic materials, single-electron transitions (generated directly or through plasmons) occur between the VB and the CB, generating electron-hole pairs. Since the average energy of these electrons are several times the band gap energy, E_g, the electron-hole pairs have excess energy (primary electrons). As the primary electrons travel through the sample more electron-hole pairs are produced (internal secondary electrons) (Shockley, 1961). The electron-hole pairs lose the excess energy within about 1 ps and due to the low concentration of electrons in the CB of an insulating material a long time relative to the frequency of atomic vibrations elapses before the hole in the VB is filled (Arumainayagam et al., 2010). This is demonstrated in the energy diagram shown in Figure 2.8b. During the elapsed time between the primary collision and recombination the interatomic bonding may have changed as a result of interactions with secondary electrons and atomic vibrations. Resulting in the creation of free radicals, ions and molecular fragments. Figure 2.9 shows the different pathways that can occur after a primary inelastic scattering event for a simple diatomic molecule, illustrating the complex reactions that can occur (Arumainayagam et al., 2010).

It is believed that most of the damage occurring in organics is a result of secondary electrons rather than primary inelastic scattering events. The average energy loss of a valence electron is typically 20 - 30 eV and the energy required to break chemical bonds are of the order of a few eV. Resulting in the majority of the excess energy going toward formation of secondary electrons (Egerton, 2014). Therefore most of the electron beam damage for poorly insulating materials is due to secondary electron damage generated by excitation of valence electrons by the electron beam rather than primary inelastic scattering events. A study by Wu and Neureuther (2001) on poly(methylmethacrylate) (PMMA) estimated that 80% of the inelastic damage was a result of secondary electron production and was carried out by modelling the interaction and energy of primary and secondary electrons.

Inelastic scattering of a primary electron can excite an inner-shell electron, although the probability of this happening is lower than that for excitation of

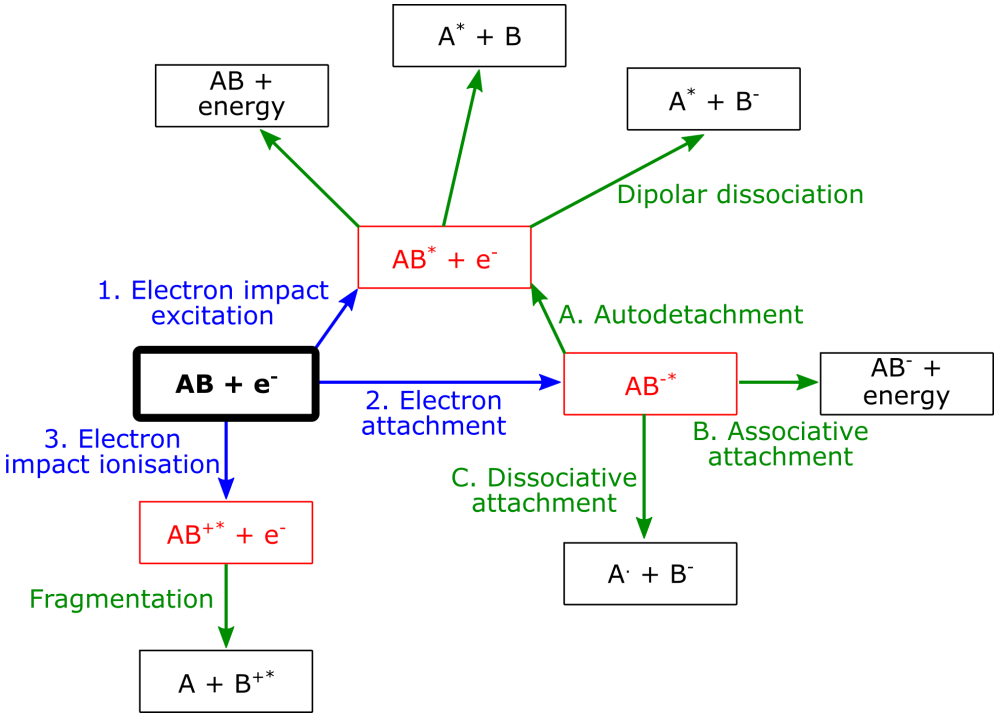

Figure 2.9: Fragmentation pathways induced by an incident electron for a simple diatomic molecule AB. Adapted from Arumainayagam et al. (2010).

a valence electron. For example electrons in the carbon K-shell are around 100 times less likely to be excited (Egerton, 2013). However, as much as 30% of the energy exchanged in organic compounds could be the result of K-shell excitation, due to the mean energy loss between a primary electron and inner shell electron being much higher than for valence electrons (Egerton et al., 2012). Electrons excited from the K-shell have hundreds of eV of kinetic energy and will produce more secondary electrons that will cause further damage by undergoing more inelastic collisions.

Furthermore, when the hole left in the K-shell is filled by an electron in the VB, an Auger electron is released which has a kinetic energy of 270 eV producing further damage. Aromatic compounds are thought to be damaged mostly through the excitation of the K-shell electrons, due to conduction from delocalised electrons in the conjugated rings (Egerton et al., 2012).

The disruption or breaking of chemical bonds results in mass loss (mainly

light elements such as hydrogen, nitrogen and oxygen), resulting in changes in molecular shape and movement in a crystal. This causes a loss in crystallinity, which can be observed in the fading of diffraction spots in the electron diffraction pattern (Henderson and Glaeser, 1985).

Hydrocarbon Contamination

During sample preparation, the sample can be exposed to hydrocarbons from multiple sources, such as the air or solvents. These hydrocarbon molecules on the surface of the sample can become polymerised when irradiated by electrons. Once polymerised the surface mobility of the hydrocarbons decrease and they have low vapour pressures causing an areas of increased thickness as exposure to the electron beam continues. Vacuum pumps remove most hydrocarbon content which has entered the column, although the sample may act as a source of hydrocarbon contamination (Egerton et al., 2004). When hydrocarbon contamination occurs it can cause blurring of the image and loss of resolution.

The amount of hydrocarbon contamination can be reduced by plasma cleaning the sample to remove the surface layer of the sample which may be contaminated with hydrocarbons (Isabell et al., 1999). Cooling the sample also reduces the surface mobility of hydrocarbons, causing less to diffuse across the surface of the specimen (Wall, 1980).

Electrostatic Charging

Electrostatic charging mainly affects insulating materials and involves elastically scattered electrons and inelastically scattered electrons. The overall charge of the specimen added per second is dependent on the balance between the negative current entering the area of the sample and the loss of electrons from backscattering and secondary emission, shown in Equation 2.5.

$$I - I_t + \frac{V_s}{R_s} = I\eta(t) + I\delta(V_s) \tag{2.5}$$

The terms on the left hand side of the equation relates to electrons entering the sample, I being the incident current from the electron beam. I_t is the transmitted electron current due to the sample being very thin, V_s is the surface

potential in the beam and R_s represents the electrical resistance between the area of illumination and the unexposed regions surrounding this area. The terms on the right hand side are related to the loss of electrons by backscattering and secondary emission, η(t) is the reduced backscattering coefficient for thin samples and $\delta(V_s)$ is the effective secondary electron yield.

As the thickness of the specimen is reduced I_t becomes similar to I in magnitude, due to very few electrons being absorbed by the thin sample at high accelerating voltages (>120 kV). By increasing I_t, V_s becomes positive above certain incident energies, usually at around 2 - 10 keV (Reimer et al., 1992). Current balance can be achieved under positive-charging conditions when V_s is positive. When small fluctuations in V_s arise, bee-swarming (distortion of the image) occur in electron microscopy images (Curtis and Ferrier, 1969).

V_s can become very high at high current densities and if the voltage is too high it can lead to an electrical field that can cause electrical breakdown of the sample and lateral migration of the ions towards the edges of the illuminated area (Hobbs, 1990). This electrostatic charge can also produce a mechanical force that the sample may not be able to tolerate. For example, in polymer films tearing can occur due to the mechanical force generated and mechanical softening due to heating effects from the electron beam (Hobbs, 1990).

Electron beam heating

Inelastic scattering involves collisions between incident electrons and atomic electrons and a substantial amount of energy can be transferred. The majority of this energy is converted into heat, which causes a local temperature increase in the area the scattering event took place. Heating can also be caused by the production of phonons. These are collective oscillations of atoms in a solid that arise from electrons striking an atomic lattice. This causes the whole crystal to vibrate which is equivalent to sample heating. Other mechanisms of heating include interband transitions, Auger electrons and X-ray emission (Williams and Carter, 2009).

The heating on the sample depend of the electron beam current, mean free path of the sample, thickness, thermal conductivity and emissivity. Materials

with low thermal conductivity (0.2 - 2 W/(m K)) such as organics and some ceramics are vulnerable to melting or thermal degradation even at low temperatures or when there is only a small increase in temperature. It has been suggested that heating may be insignificant at fairly low electron fluence rates (less than 50 $e^-/(Å^2\ s)$) from single-particle experiments of proteins frozen and imaged at liquid nitrogen temperatures (77 K) (Karuppasamy et al., 2011).

2.2.3 Quantification of Electron Beam Damage

Electron dose vs fluence

The radiation dose, G, is measured in Grays (Gy), one Gray is defined as the absorption of one joule of ionising radiation by one kilogram of matter. The amount of radiolysis damage is assumed to by proportional to the energy deposited in the specimen, shown in Equation 2.6.

$$G = \left(\frac{F}{\rho}\right)\left(\frac{E_{av}}{\lambda_i}\right) \tag{2.6}$$

F is the fluence, measured in incident electrons per m^2, more commonly used units are C/cm^2, e^-/nm^2 or $e^-/Å^2$, ρ is the density in kg/m^3, λ_i is the inelastic mean free path of an electron (in m) and E_{av} is the average energy exchange per inelastic or absorption event (in J). At an accelerating voltage of 100 kV, λ_i = 100 nm and ρ = 1000 kg/m^3 a fluence of 0.01 C cm^{-2} is equivalent to a dose of 30 MGy (Egerton, 2013).

For thin sample most of the incident electrons pass through and the energy deposited in a sample is only a small portion of the total energy carried by the incident beam (Jiang and Spence, 2012). Therefore it is more convenient to use the number of incident electrons per unit area during an exposure (fluence, $e^-/Å^2$) to represent the degree of irradiation the sample has been exposed to.

Electron fluence is defined as the product of electron current density (electron flux, $e^-/(Å^2\ s)$) and the illumination time (s). In the majority of scientific literature regarding electron microscopy when an electron dose is given or referred to, the authors provide it in $e^-/Å^2$ or equivalent units, meaning they are actually referring to electron fluence. In the electron microscopy community both dose and

fluence tend to be used interchangeably. Here the correct term, electron fluence is used here throughout unless otherwise stated.

Methods of measuring electron beam damage

Multiple methods have been used to quantitatively measure electron beam damage in TEM. The most common method is to measure the intensity of electron diffraction spots over a period of time and plot the normalised intensities against the cumulative electron fluence (amount of electrons the sample has been exposed to overall). The critical fluence (C_F), sometimes referred to as characteristic fluence, is defined as the electron fluence at which the effect being measured (diffraction spot intensity, peak height in EELS etc.) decreases to 1/e of the maximum value and is measured in either C cm^{-2} or $e^-/Å^2$ (Henderson and Glaeser, 1985; Knapek and Dubochet, 1980; Reimer and Spruth, 1982). The total end point fluence is sometimes used as a measurement of electron beam damage, which is the electron fluence at which no diffraction spots are visible in the diffraction pattern. C_F is a measurement of the radiation resistance of a material, an alternative way to express damage is in terms of radiation sensitivity which can be expressed as a damage cross-section, σ_d, this can be calculated from C_F and e, the charge of an electron:

$$\sigma_d = \frac{e}{C_F} \tag{2.7}$$

C_F is obtainable experimentally whereas σ_d can only be calculated and is expressed as target area per atom or per molecule. The ratio of σ_d to $< \sigma_i >$ (average inelastic cross-section per molecule) is equal to η (radiolysis efficiency) (Reimer and Spruth, 1982). This can be used to estimate the amount of inelastic collisions occurring within a specimen. If $\eta < 1$ then more than one inelastic collision per atom is needed for damage to occur. If $\eta = 1$ then one excitation per molecule is responsible for the damage. If $\eta > 1$ then single inelastic collisions may destroy an entire molecule.

Electron energy loss spectroscopy (EELS) has been used as a method to determine electron beam damage by Li and Egerton (2004). This was been achieved by measuring the π excitation peak at 6 eV in the energy loss spectrum of coronene,

p-terphenyl and rubrene which are all highly conjugated aromatic compounds. The intensity of the π excitation peak is measured at different times and a similar plot to the one used for electron diffraction can be constructed to measure C_F. The C_F obtained from EELS has been reported to be 9 times higher for the same compound compared to electron diffraction, although this was only shown for coronene and may not be true for all compounds since L-Histidine showed 330 times increase (Li and Egerton, 2004). The increase of C_F by EELS is due to the EEL spectra relating to the loss of fine structure within the molecular crystal (measurement of molecular order) compared to the loss of longer range order in the electron diffraction pattern (measurement of crystalline order). This increase in C_F has also been shown in experiments on crystalline nucleic acid bases (Isaacson, 1975).

Quantification of the mass loss of a sample can also be used to determine electron beam damage. This has been achieved two ways, the first by Grubb (1974) where the reduction in scattering power of a thinning sample resulted in reduced contrast overtime and secondly by Egerton (1980), where the electron beam damage was quantified from the EELS intensity of individual elements or changes in elemental ratios, such as in carbon, nitrogen and oxygen.

2.2.4 Control of Radiation Damage

Although some samples have very low damage thresholds to electron radiation, different methods have been developed to try and minimise the overall damage, allowing the maximum amount of information to be gathered before the sample is destroyed. Ways to increase the stability of the samples include, changing the surface of the specimen with a coating to prevent sputtering and help dissipate heat for insulting materials, using different support films when preparing the specimen, cooling the specimen down or freezing to very low temperatures, using different electron fluence rates and controlling operating conditions of the microscope.

Coatings

Coatings have been used to successfully reduce the loss of crystallinity in a crystalline specimen (Fryer, 1984; Fryer and Holland, 1984; Salih and Cosslett, 1974). By coating the sample with SiO_2, carbon or a metal the amount of mass loss due to sputtering has been shown to be reduced (Egerton et al., 1987). It is believed that coatings allows the sample to return to its original molecular state due to the coating acting as a diffusion barrier and preventing lighter elements (hydrogen, oxygen and nitrogen) escaping (Fryer and Holland, 1983).

Reduction of electrostatic charging and heating for an insulating specimen may also be reduced by depositing a conductive coating as this may act as a source of electrons that can increase the rate of recombination for electron-hole pairs (Salih and Cosslett, 1974). However semi-conductors such as SiO_2 have been shown to be just as effective (Fryer, 1984).

Cooling and cryogenic conditions

The radiation sensitivity of a sample has been shown to be reduced by lowering the temperature to liquid nitrogen temperatures (77 K) or lower providing advantages for samples that damage via radiolysis such as biological and other organic samples (Henderson and Glaeser, 1985; International Experimental Study Group, 1986; Wade, 1984; Wade and Pelissier, 1982). By plunge freezing the specimen in liquid nitrogen or liquid ethane the initial structure of the specimen is preserved and is kept hydrated (Marc Adrian and McDowall, 1984).

The increase in radiation stability is thought to be the result of a reduction in atomic mobility. When the sample is frozen, the movement and degrees of freedom for the atoms and molecules are inhibited and this in turn limits the degree of structural rearrangement that can occur as a result of electron beam damage. Due to the reduced diffusion rate this caging effect can prevent or slow down the generation of damage caused by secondary electrons (Knapek and Dubochet, 1980). An irradiated cryo sample that is returned to room temperature allows the atoms that were trapped, due to the caging effect, to then diffuse out and mass loss can occur without further irradiation (Egerton, 1980; Siegel, 1972). The occurrence of a thermally activated reverse reaction or a healing effect may also

prevent a proportion of the damage. Allowing for the structure to stay intact until the cumulative damage is too great and the structure finally breaks down (Egerton, 1980; Reimer and Spruth, 1982; Siegel, 1972).

Cryo electron microscopy at liquid nitrogen temperatures has been shown to improve C_F by a factor between 1 and 10 over standard room temperature imaging for biological and organic crystals (International Experimental Study Group, 1986). Although the exact reduction factor varies between different materials with more sensitive samples generally providing a larger increase in stability when using cryo (Egerton, 2014, 2013). Further cooling to temperatures as low as 4 K has increased the C_F by a factor of two compared to liquid nitrogen temperatures in specimens containing membrane protein crystals (Fujiyoshir, 1998).

Electron flux rate

The the electron flux (J) used during irradiation can have an effect on how the sample interacts with incident electrons. In inorganic materials where J can be relatively high compared to organics there can be a threshold J at which no damage can be observed (Jiang and Spence, 2012; Salisbury et al., 1984). It is fairly common for organic materials to show no dependency on J, possibly due to such low fluence being required for damage to occur. However in aqueous environments and at low temperatures J has been shown to have an effect on organics (Egerton and Rauf, 1999).

In standard TEM, the J of the area exposed to the electron beam is constant. However, in scanning transmission electron microscopes (STEM) a highly focused probe is scanned across the sample and a large J is applied to a very small area depending on the size of the probe. In this case, only the area exposed to the scanning probe and a small area around surrounding it (due to declocalised inelastic scattering) will be damaged while in all other areas the electron fluence is equal to zero (Egerton, 2017). Egerton and Rauf (1999) demonstrate an increase in C_F when measuring the mass loss of a sample by STEM compared to TEM. It was found that an initial increase in J resulted in an increase in electron beam damage up to a point and further increases in J then lead to a decrease in damage relative to a linear dependency. Therefore, if the sample exhibits an

inverse relationship between damage and J, like in the case for some organic crystals, then STEM could be advantageous (Egerton and Rauf, 1999).

Accelerating voltage

The velocity and energy of incident electrons, which is determined by the accelerating voltage has an effect on the electron beam damage. As previously mentioned increasing the energy of incident electrons can increase the degree of knock-on displacement/sputtering that occurs, especially if the incident energy exceeds the threshold energy of an atom in the material. By reducing the accelerating voltage sufficiently elastic scattering can generally be overcome for most materials (Egerton, 2014, 2012).

However, if radiolysis is the main damage mechanism then reducing the accelerating voltage increases the damage cross-section for inelastic scattering, thereby increasing the number of inelastic scattering events that occur and the overall damage. The inelastic scattering cross-section is inversely proportional to the square of the electron speed, while the elastic cross-section is proportional to the square of the electron speed (Egerton, 2014; Isaacson, 1975). Therefore higher accelerating voltages are preferable in the case of damage by radiolysis to reduce electron beam damage, this is despite an increase in electron energy leading to $E_d > E_0$; the rate of radiolysis is much faster than the rate of displacement/sputtering and therefore dominates (Egerton, 2012, 2013). Changes to the accelerating voltage also effects the contrast and the signal to noise ratio due to differences in elastic-scattering cross-section; at higher kV for the same thin sample the contrast will decrease compared to lower kV (Egerton, 2014). This leads to the concept of a dose-limited resolution which is discussed in more detail in later chapters. Furthermore, unlike elastic scattering where there is a threshold for damage, no such threshold exists for radiolytic damage.

2.2.5 Stability of Organic Crystals

Electron beam sensitive materials have been the focus of studies for the past few decades. The stability of these materials have been measured at different conditions and by different techniques therefore it is difficult to directly compare

the C_F but in general measuring by electron diffraction, using irradiation energies of 80 - 300 kV and cryogenic conditions in some cases, biological materials such as protein crystals have C_F in the range of 1 - 15 $e^-/Å^2$ (Downing and Li, 2001; Fujiyoshir, 1998; Henderson and Glaeser, 1985; Stark et al., 1996), organic crystals vary between 0.2 - 120 $e^-/Å^2$ (Eddleston et al., 2010; Egerton, 1980; Fryer, 1984; Glaeser et al., 2011; Knapek and Dubochet, 1980; Kumar and Adams, 1990; Li and Egerton, 2004; Reimer and Spruth, 1982), zeolites 100 - 600 $e^-/Å^2$ (Greer and Zhou, 2011; Pan and Crozier, 1993), and transition metal oxides $> 10^7$ $e^-/Å^2$ (Pan et al., 2010). Extensive research has historically been carried out on organic crystals, most of the initial research was conducted between the early 1970 and late 80s by studies from Clark et al. (1980); Egerton (1980); Fryer (1987); Grubb (1974); Henderson and Glaeser (1985); Jones et al. (1975); Knapek and Dubochet (1980); Knapek et al. (1984); Reimer and Spruth (1982); Siegel (1972); Stenn and Bahr (1970); Wade (1984); Wade and Pelissier (1982). The C_F for organic crystals can vary significantly between different compounds due to different conditions and methods used to measure C_F and the differences in structure of organic materials. Although no previous study has carried out C_F on a large number of compounds using standard operating condition and measurement method.

A few different factors have been shown to effect the electron beam stability of pharmaceuticals these being thermal stability, conjugation and hydrogen/halogen atoms. In the former cause the electron radiation stability of an organic crystal or polymer has previously been compared to the thermal stability of the compounds by Kumar and Adams (1990), for melting temperatures ranging between 300 K to 1000 K. The results showed a correlation of C_F and melting temperature and it is thought that more thermally stable organics require a larger electron fluence to cause noticeable damage due to increased strength of intermolecular bonds, for example, hydrogen bonding, van der Waals, dipole-dipole and hydrophobic interactions. However many other factors are also thought to have an effect such as crystal morphology and atomic bonding (covalent, ionic and metallic bonding) (Martin et al., 2005).

Aromatic compounds have been shown to provide higher radiation resistance due to the relatively stable conjugated ring structures that contain high resonance energy and delocalised π electrons (Fryer, 1987; Fryer et al., 1992). This allows the

energy deposited by inelastic scattering to be shared by many electrons without bond breakage.

Clark et al. (1980) demonstrated that the electron beam stability of copper phthalocyanine (Cu Pc) increased when H atoms were replaced by halogen atoms in this case Cl and Br, suggesting that halogens had an effect on the C_F. One reason which might explain halogens increasing the stability is due to the larger atoms surrounding the molecules and providing a caging effect/steric hindrance that prevents the displacement and diffusion of damaged fragments.

Pharmaceutical organic crystals

Little scientific literature exists for directly applying TEM to examine pharmaceutical crystals. Some of the more recent studies that have been carried out are by Bhardwaj et al. (2018); Eddleston et al. (2010); Karavas et al. (2007); Marsac et al. (2010); Martin et al. (2005); Ricarte et al. (2015, 2016).

Eddleston et al. (2010) studied theophylline, paracetamol and aspirin via TEM and successfully identified a previously unknown form of theophylline from electron diffraction data when crystallised from nitromethane rather than methanol. Crystalline defects were also observable through disruptions in bend contours and was proposed that this information was not obtainable through the use of any other characterisation techniques currently used in the pharmaceutical industry.

Bhardwaj et al. (2018); Karavas et al. (2007); Marsac et al. (2010) have all used TEM to examine phase separation in ASDs through the use of bright field imaging via contrast differences between heavier atoms such as S and Cl that are present within the API. Similarly Ricarte et al. (2015) has used TEM to study amorphous solid dispersions, in this case TEM was used to identify crystallinity within a solid dispersion of the API, griseofulvin and HMPCAS prepared via spray-drying. The results were compared to wide-angle X-ray scattering (WAXS) and modulated differential scanning calorimetry (MDSC) and demonstrated that WAXS and MDSC were not sensitive enough to detect crystals due to the overall crystallinity being 3 vol %, which was below the practical lower limit of detection for WAXS and MDSC. Whereas crystals of griseofulvin were successfully identified by TEM.

One difficulty found when reviewing the literature on TEM of pharmaceuticals and other electron beam sensitive materials was comparing the experimental electron fluence used between different studies as the values were not always reported. As mentioned earlier organic crystals have large variations in C_F values resulting in a number of crystals being too sensitive to be analysed or lead to beam induced artefacts being observed rather than effects related to the specific sample.

2.3 Project Aim

Overall, the current lack of consistent information on pharmaceutical materials by TEM represents an opportunity for a more rigourous analysis of these materials and techniques. Therefore the aim of this project is to demonstrate the use of transmission electron microscopy in identifying and characterising crystallisation within amorphous solid dispersions.

2.4 Objectives

- To establish electron fluence limits in TEM for a range of chemically diverse active pharmaceutical ingredients and identify the properties that have the largest influence on critical electron fluence.
- To determine the possibility of identifying low levels of crystallinity or phase separation within a model amorphous solid dispersion by TEM before the sample is excessively damaged by electron beam irradiation.
- To provide information regarding recrystallisation process occurring in a model amorphous solid dispersion, subjected to accelerated ageing conditions, by TEM.
- To identify and develop the use of a variety of electron microscopy techniques to characterise pharmaceuticals without causing extensive electron beam irradiation damage.

Chapter 3

Materials and Methods

This chapter will provide an overview of the materials and characterisation techniques used throughout this thesis for the analysis of individual active pharmaceutical ingredients (API) and the amorphous solid dispersion (ASD) samples. The theory behind each characterisation techniques used will be presented, including the reasoning behind their use. Since the aim of this chapter is to give an overview on the materials and methods, the full details for each experiment and the parameters used will be addressed as they are encountered in future chapters.

3.1 Materials

3.1.1 Active Pharmaceutical Ingredients

Overall 20 different poorly water-soluble APIs were analysed by pXRD and TEM. Poorly water-soluble compounds were classified as compounds with an aqueous solubility of log $S_w < -4$ ($\log_{10}$ of solubility measured in mol/L). This selection consisted of compounds containing a variety of different functional groups and exhibiting a range of different properties such as melting temperature.

The majority of APIs that were used in this study were selected based on work by Nurzynska et al. (2015). The original study by Nurzynska et al. (2015) used a database of 1327 APIs and significantly reduced the number of APIs down to 171 by filtering compounds that had poor aqueous solubility ($logS_w < -4$), low molecular weight ($M_w < 800 g/mol$) and were neutral in the gastrointestinal

pH range (1.2 – 6.5). After filtering, principal component analysis (PCA) was used to categorise the remaining APIs into 35 different groups, each containing between 1 - 50 compounds with similar chemical structures. From these groups 25 compounds were selected to be representative of the larger population and from this 19 were selected for the current work, with the other 6 being unavailable. Indomethacin another poorly water-soluble compound, was also included to give a total of 20 different APIs to be investigated by TEM. The table in Appendix A details the names, chemical structures, crystal structure reference and molecular descriptors used in Chapter 4.

3.1.2 Amorphous Solid Dispersions

A review of solid dispersion literature is provided in Chapter 2.1, discussing the classification of solid dispersions, brief overview of common manufacturing method, the physical stability and finally characterisation methods.

A model amorphous solid dispersion system was used in this project that consisted of felodipine and copovidone. The methods used to create the ASDs included hot-melt extrusion and spray-drying which have been previously discussed in Chapter 2.1.2.

Felodipine

Felodipine is a calcium channel blocker and is prescribed to treat hypertension (high blood pressure). It is a generic drug but was originally patented by AstraZeneca under the trade name Plendil.

There are four known polymorphs of felodipine, crystallographic information for each polymorph is shown in Table 3.1. Forms I and III are the most thermodynamically stable forms under ambient conditions and form II is less thermodynamically stable than the previous two forms. Less information is available on form IV due to problems with the reproducibility of experiments used to obtain isolated single crystals (Surov et al., 2012), although more recent studies have demonstrated more reliable methods in obtaining crystals of form IV (Wang et al., 2015).

Table 3.1: Crystallographic data for felodipine polymorphic forms I-IV, from Surov et al. (2012).

	Form I	**Form II**	**Form III**	**Form IV**
Crystal system	monoclinic	monoclinic	monoclinic	monoclinic
Space Group	$P2_1/c$	$C2/c$	$P2_1/n$	$P2_1/n$
a (Å)	12.09	32.39	15.13	11.11
b (Å)	12.08	18.72	7.230	12.57
c (Å)	13.43	23.77	17.28	13.50
α (°)	90	90	90	90
β (°)	116.1	91.0	110.2	107.0
γ (°)	90	90	90	90
Volume (Å^3)	1759.3	14373	1773.5	1802.7
CCDC Reference	DONTIJ	DONTIJ01	864026	864027

When administrated orally and in solution felodipine is rapidly absorbed in the body, although it has low bioavailability due to its low solubility (Wingstrand et al., 1990). There have been numerous studies investigating the bioavailability of felodipine when formulated into an ASD, which makes it a good candidate to use as a model system (Anderberg et al., 1988; Fu et al., 2018; Jermain et al., 2018; Karavas et al., 2007, 2006; Konno et al., 2008; Konno and Taylor, 2006; Mahmah et al., 2013; Marsac et al., 2008a, 2006; Nollenberger et al., 2009; Rumondor et al., 2009c; Song et al., 2013). Felodipine is also included as one of the poorly water-soluble APIs examined in Chapter 4.

Copovidone

Copovidone is a copolymer of polyvinylpyrrolidone (PVP) and polyvinyl acetate and is analogous to povidone. Both polymers are amorphous and commonly used as excipients in the pharmaceutical industry. Particularly copovidone, which is widely used as a film forming agent providing good adhesion, elasticity, hardness and acts as a moisture barrier and a tablet binder for direct compression and wet granulation (Mellert et al., 2004).

Copovidone and PVP have regularly been used in ASDs to inhibit the crystallisation of an amorphous drug and enhance dissolution properties by controlling the release profiles of formulations (Alonzo et al., 2010; Karavas et al., 2006;

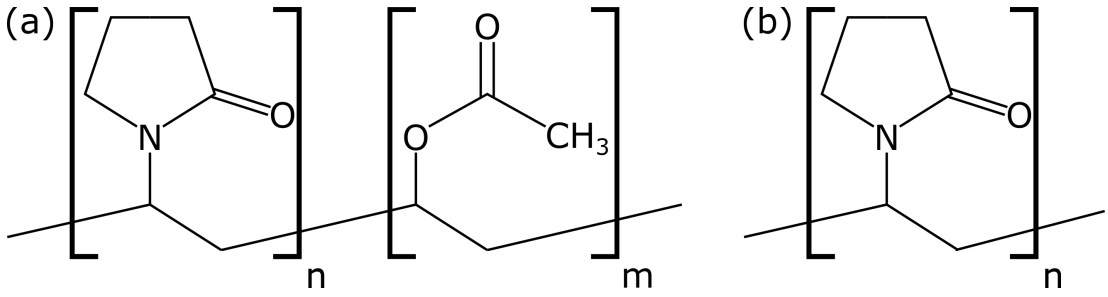

Figure 3.1: Chemical structure of (a) copovidone (b) povidone (PVP)

Konno et al., 2008; Marsac et al., 2008a, 2006; Rumondor et al., 2009c; Tres et al., 2016).

3.2 Electron Microscopy

Electron microscopy is used considerably in both material science and biological science to probe both the surface and sub-surface features of a material using SEM and the internal micro-structure using TEM at sub-micrometre resolution. TEM is a general term used to cover both conventional TEM i.e. parallel beam and STEM. A variety of imaging modes and analytical techniques can be employed to obtain high-resolution information on a material's structure and chemical composition; making electron microscopy one of the most useful structural characterisation methods available.

Conventional TEM was the main characterisation technique used throughout this thesis, in addition to this, SEM and STEM were also used. A brief analysis of how each of these techniques works, the difference between them and details on the information that can be obtained are outlined in the following sections. Many textbooks have been written on the different aspects of electron microscopy, the ones that were used when writing this section include; Brydson (2011); Egerton (2005); Goodhew et al. (2001); Williams and Carter (2009); Zhou et al. (2006).

3.2.1 The Electron

During the 1920s it was proposed by the scientist Louis de Broglie that all matter possessed a dual nature where they can behave as either waves or particles. This theory was known as wave-particle duality and the relationship between the wave-like nature and the particle-like nature of matter was given by Equation 3.1, which relates the wavelength (λ) to momentum (p) through Planck's constant ($h = 6.63 \times 10^{-34}\ m^2 kg s^{-1}$).

$$\lambda = \frac{h}{p} \tag{3.1}$$

Three years after this theory was proposed by de Broglie the wave nature of electrons was experimentally shown by both Thomson and Davisson through electron diffraction experiments. The associated wavelength of energetic electrons is much smaller than the wavelength of light when calculated using 3.1 and the prospect of using this radiation to image led to the development of magnetic coils being used as electron lenses to control the path of electrons. Ruska and Knoll used a series of these magnetic coils to develop the first TEM in 1931.

Electrons within an electron microscope are accelerated to very high velocities by an acceleration anode. The velocity of the electrons can reach between 1% of the speed of light (c) in low voltage microscopes and 95% of c in MV microscopes. As an object accelerates towards (c) its mass will increase requiring its relativistic mass and velocity to be taken into account to accurately calculate λ. Equation 3.2 corrects for the relativistic effects that occur and can be used to calculate the wavelength of an electron at a particular accelerating voltage:

$$\lambda_e = \frac{h}{\sqrt{2m_0 eV_a - (1 + \frac{eV_a}{2m_0 c^2})}} \tag{3.2}$$

Here m_0 is the rest mass of an electron (9.11×10^{-31} kg) and e is the elementary charge (1.60×10^{-19} C). V_a is the accelerating voltage and ultimately determines the velocity of the electron. A comparison of the non-relativistic λ and relativistic λ as a function of accelerating voltages are shown in Table 3.2.

Table 3.2: Electron wavelength (non-relativistic and relativistic) and relativistic mass and velocity as a function of accelerating voltage, based on a table from Williams and Carter (2009).

Accelerating Voltage (kV)	**Non-Relativistic λ (nm)**	**Relativistic λ (nm)**	**Mass $\times m_0$**	**Velocity $\times c$**
2	0.02742	0.02740	1.004	0.088
10	0.01225	0.01220	1.020	0.195
20	0.00867	0.00859	1.039	0.272
80	0.00434	0.00418	1.157	0.502
100	0.00388	0.00370	1.196	0.548
120	0.00354	0.00335	1.235	0.587
200	0.00274	0.00251	1.391	0.695
1000	0.00122	0.00087	2.957	0.941

3.2.2 Resolution Limits

The ultimate purpose of a microscope is to map points within an object to corresponding points in an image. This is achieved through the use of lenses to change the direction of the radiation from the source which is scattered by the object in order to magnify the object and form an image. Using the thin lens approximation, which ignores optical effects due to lens thickness, the formation of an image can be modelled by the lens equation:

$$\frac{1}{f} = \frac{1}{u} + \frac{1}{v} \tag{3.3}$$

The distance between the object plane and lens (u) and the distance between the image plane and lens (v) can be used to calculate the focal length (f), the distance between the centre of a lens and the point of focus, which occurs in the back focal plane (Equation 3.3 and Figure 3.2). The closer the object distance is to the focal length the greater the image is magnified. However, if an image is constantly enlarged then eventually areas will become indistinguishable due to the limits on resolution, which is the distance that two adjacent features in the object can be separated and appear as two distinct points in the image.

When a point source passes through a circular lens or aperture, rather than being focused to a single point, due to diffraction it forms an interference pattern consisting of a series of concentric rings that diminish in intensity with increasing

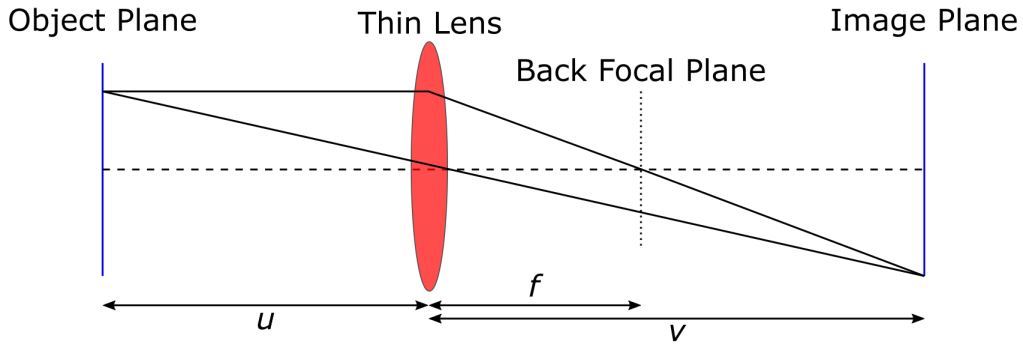

Figure 3.2: Diagram showing how an image is focused by a thin lens. Rays from an object in the object-plane at distance u from the lens pass through the lens and focus in the back focal plane then continue to be projected in the image plane.

radius. The central bright disk contains approximately 84% of the energy and intensity and is known as the Airy disk, the radius of this disk is given by Equation 3.4.

$$r_d = \frac{0.61\lambda}{n_r \sin\alpha} \tag{3.4}$$

where λ is the wavelength, n_r the refractive index of the intervening medium and α is the collection semi-angle of the lens or aperture. Assuming incoherent radiation, adjacent points in the image have individual disks associated with them and one measurement of resolution is how closely the points can be brought together, while still being viewed as separate sources in the image. The maximum overlap that can occur between two disks while still being able to resolve each one is given when the separation is equal to the radius of the Airy disk, known as Rayleigh criterion (Figure 3.3). For an electromagnetic lens in an electron microscope, n_r can be assumed to be unity since the column is held in a vacuum and $\sin\alpha \approx \alpha$ (in radians) when the semi-angle collected by the lens is less than a few degrees, which is the case for high kV electrons. This simplifies the to Equation 3.5.

$$r_d \approx \frac{0.61\lambda}{\alpha} \tag{3.5}$$

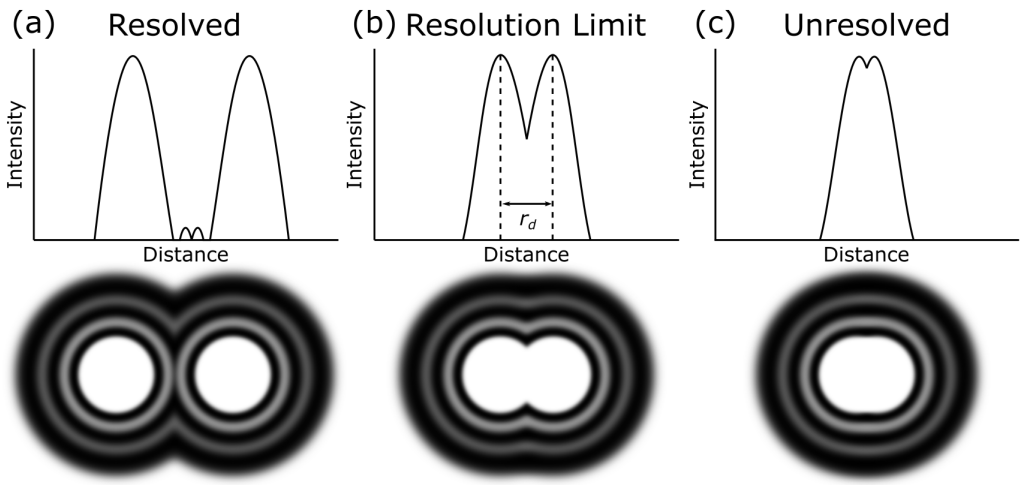

Figure 3.3: 2D profile through two Airy disks as they converge (a) Airy disks are separated meaning that point object can be resolved (b) Resolution limits defined by the Rayleigh criterion in equation 3.4 (c) Airy disk overlaps and each point cannot be resolved.

This shows that the resolution of an optical system is ultimately limited by the wavelength of the radiation. Hence, due to the smaller wavelengths of electrons (Table 3.2) compared to the wavelength of visible light ($380 - 750$ nm), the resolution of electron microscopes are much greater than light microscopes. Note the diffraction limitation on the resolution has now been overcome in light microscopy through work done by Betzig and Trautman (1992), Dickson et al. (1997) and Klar et al. (2000) using a number of different super-resolution methods including the use of fluorescent markers to improve resolution. However not withstanding optical resolution is still significantly less good than in EM. The collection semi-angle is also a limiting factor for resolution and is determined by the diameter of the lens and size of the apertures used.

3.2.3 Basics of Transmission Electron Microscopy

The two types of transmission based electron microscopes are conventional transmission electron microscopes and scanning transmission electron microscopes. Details on SEM is outlined in section 3.2.10. The overall construction and layout

of each type of microscope are similar and a schematic diagram of a modern TEM capable of operating in STEM mode is shown in Figure 3.4.

An electron beam is produced using an electron source which is subsequently focused onto a thin specimen by a series of electromagnetic lenses. The majority of electrons are transmitted through a very thin specimen (< 200 nm) without interacting with the specimen. Some electrons may interact with atomic nuclei and atomically bound electrons contained within the specimen, causing incident electrons to be scattered. Specific interactions can be detected using certain detectors (i.e. X-rays). Images are produced by projecting the scattered and un-scattered electrons through another series of lenses onto a phosphorescent screen or image recording device. The column that the electrons travel down and specimen within are kept under high vacuum ($\approx 10^{-5}$ Pa) to maximise the mean free path of electrons and prevent gas molecules in the column from scattering the electrons. A series of pumps and airlocks allows the column to be kept under high vacuum while exchanging between different samples.

The main difference between TEM and STEM is the way the electron beam illuminates the specimen. In conventional TEM a near parallel beam continuously illuminates the specimen and energy from the beam is spread across a large area. An objective lens is situated below the specimen to collect and focus transmitted electrons to form images and diffraction patterns. In STEM the electron beam is finely focused into a very small probe (typically < 0.1 nm) at the specimen surface by the condenser system and objective lens (which sits before the specimen in STEM). The probe is then rastered across the specimen collecting information at each point along the scan. One of the main advantages of STEM is the ability to spatially resolve characteristic X-ray and electron energy loss spectra. More detailed information on STEM is covered in section 3.2.9.

A major problem that is associated with all forms of electron microscopy is radiation damage caused by exposure to the high energy electron beam. Damage can be observed by an induced movement to the specimen, shrinkage and fading of certain features i.e. diffraction spots. Ultimately radiation damage causes the specimen to structurally change from the original. The effects of radiation damage depends on sample preparation, stability of the material to radiation damage and

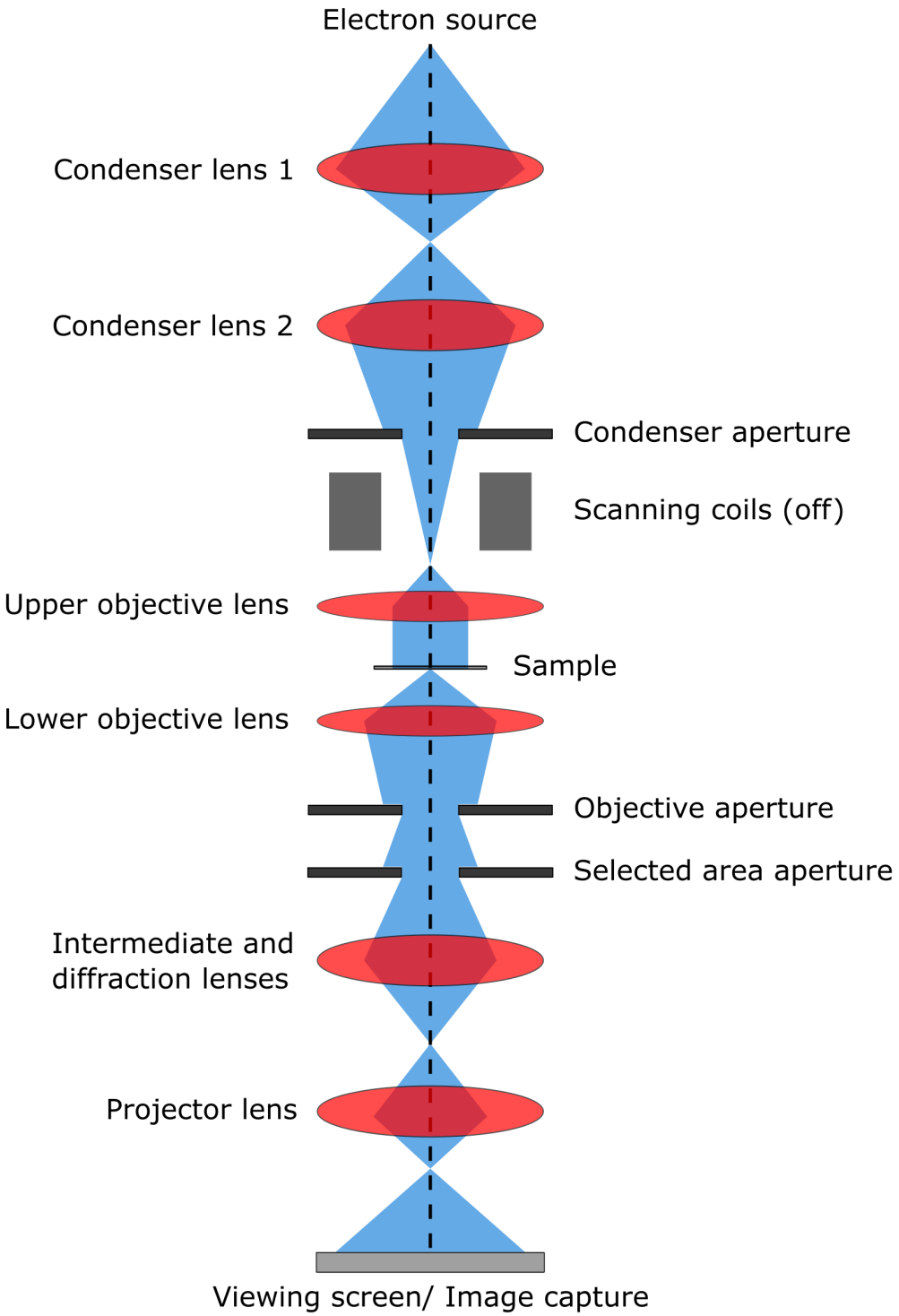

Figure 3.4: Schematic diagram of a modern TEM showing how lenses and apertures are used to illuminate the sample and produce an image. This particular example uses a condenser-objective lens to create a parallel beam.

different microscope conditions; accelerating voltage, fluence rate/total fluence and temperature. All of these have been previously discussed in Chapter 2.

The following section details important components used in electron microscopes.

3.2.4 Electron Source

An electron source, commonly called an electron gun, produces a high energy beam of electrons. The type of source used affects the brightness, beam current, energy spread and stability of the generated electron beam. There are two types of electron sources, thermionic emission and field emission. Schematic diagrams of how each type produces electrons are shown in Figure 3.5.

Thermionic sources produce electrons by heating a filament to a very high temperature, 1700 - 2700 K depending on the material. Electrons are released from the surface of a material when the energy supplied is greater than the minimum energy required to remove an electron from the surface of a material into a vacuum, known as the work function (ϕ) The number of electrons produced

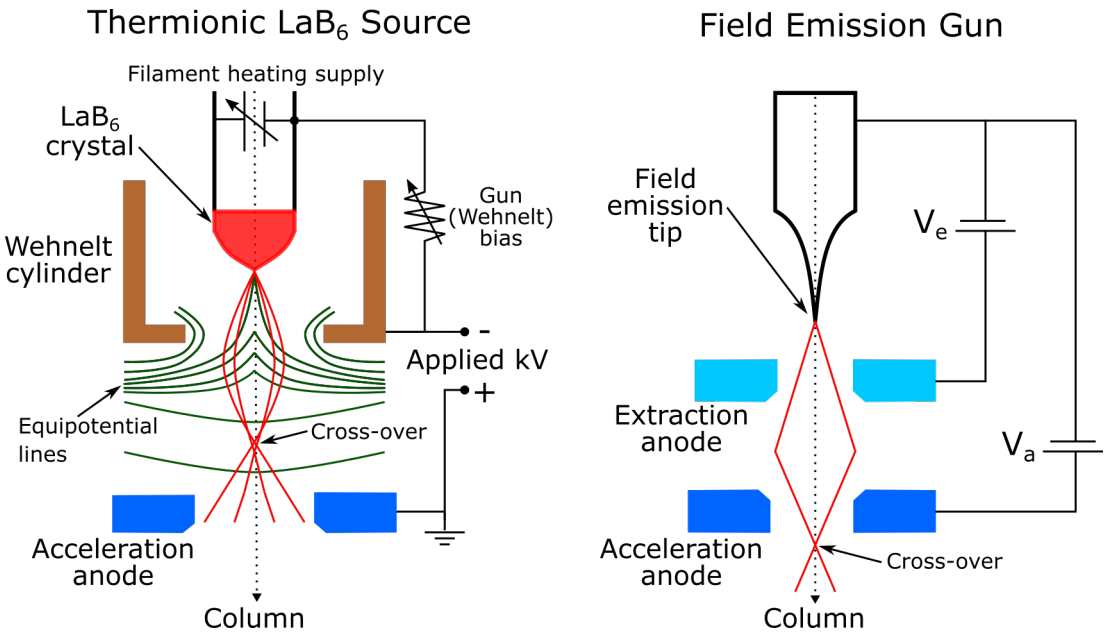

Figure 3.5: Diagram of a thermionic emission gun and a field emission gun

depend on both ϕ and the temperature of the material. Once electrons have been released from the filament, the electrons pass through a Wehnelt cylinder to focus the emitted electrons towards an anode. This anode is held at a particular voltage which accelerates the electrons into the vacuum column and towards the specimen. Traditionally tungsten filaments were used due to their stability at high temperature, but modern thermionic sources use a crystal of lanthanum hexaboride (LaB_6) due to its low ϕ.

Field emission guns (FEG) emit electrons from an atomically sharpened tip, typically made from single crystal tungsten. To produce the electron beam a potential (V_e) of $3-5$ kV is applied across an extraction anode, this generates a strong electric field which enables electrons to tunnel out of the tip. These electrons are then accelerated by a second anode to the required accelerating voltage. The fields of each anode, when combined, produces an electron crossover point which is effectively the source of illumination for the microscope. The FEG must also be held at ultra-high vacuum (UHV, $< 2 \times 10^{-6}$ Pa) to minimise surface contamination.

There are two distinct types of FEGs that are used: thermally assisted or Schottky FEGs that coat the tip with a metal oxide, typically ZrO_2, and are heated to moderately high temperatures (≈ 1600 K). This effectively allows more electrons to be extracted and provides higher beam currents. Cold FEGs operate at ambient temperatures and produce electron beams with narrower energy spread compared to Schottky FEGs. These are typically used in SEMs and ded-

Table 3.3: Characteristic properties of the different electron sources used in electron microscopes, at accelerating voltage of 100 kV, based on a table from Williams and Carter (2009)

Properties	**Tungsten**	**LaB_6**	**Schottky FEG**	**Cold FEG**
Work function, ϕ (eV)	4.5	2.4	3.0	4.5
Operating temperature (K)	2700	1700	1700	300
Current density (A/m^2)	5	10^2	10^5	10^6
Crossover size (nm)	$> 10^5$	10^4	15	3
Brightness (A/m^2sr)	10^{10}	5×10^{11}	5×10^{12}	10^{13}
Energy spread (eV)	3	1.5	0.7	0.3
Vacuum (mbar)	10^{-4}	10^{-6}	10^{-8}	10^{-11}
Lifetime (hours)	100	1000	> 5000	> 5000

icated STEMs. A comparison of electron sources and their properties are shown in Table 3.3.

3.2.5 Lenses, Apertures and Aberrations

Electromagnetic Lenses

Electromagnetic lenses are used to focus electrons emitted from the electron source and to magnify the final image in electron microscopes, similar to the use of glass lenses in optical microscopes A magnetic field is generated by the electromagnetic lenses when a current is passed through a set of copper coils surrounded by soft iron pole piece. Electrons are charged particles and are influenced by the magnetic field as they pass through the lens, which alters the direction of electrons. Magnetic lenses acting similarly to a convex lens by bringing off axis rays back onto the optic axis. The magnetic field also causes the electrons to travel in a helical trajectory. When relativistic effects are ignored and only the perpendicular component of the electron's velocity (v) is taken into account the radius of the helical path can be calculated using equation 3.6.

$$r = \frac{m_0 v \sin\theta}{eB} \tag{3.6}$$

where r is the radius of the helical path and B is the strength of the magnetic field. To change the focus of an electromagnetic lens the current is altered which varies the strength of the magnetic field produced. This changes the radial distance of the electrons from the optic axis as shown in Equation 3.6. When more current is flowed through a lens the lens is said to be strong and focuses at a point closer to the lens and if less current flows through the lens is weak and focuses further away.

The useful collection angles obtainable from electron magnetic lenses is typically $\leq 5^\circ$ due to the small scattering angles of the electrons and large aberrations within the lenses.

Apertures

Apertures are metallic masks which are used to block certain electrons at different points within the microscope as they travel down the column. Some apertures are often fixed i.e the first condenser aperture which blocks high angle electrons. While others, such as the objective aperture in the back focal plane of the objective lens can be adjusted in order to provide differing levels of contrast in the image and the selected area electron diffraction aperture situated in the image plane of one of the intermediate or projector lenses. Some apertures have different sizes available to allow varying levels of electron beam exclusion.

Condenser Lens

Within the electron microscope there are multiple lens systems and apertures. The first one that immediately follows the acceleration anode is the condenser lens system. Here one or more (normally two) lenses and an aperture are used to focus the beam on the sample. The first condenser lens creates a demagnified image of the gun crossover and controls the minimum spot size obtainable in the condenser system. The second condenser lens affects the beam convergence and the diameter of the illuminated area on the sample.

A condenser aperture is used to limit the amount of high-angle electrons allowed through to the sample, helps to control the intensity of illumination and reduce spherical aberrations from the condenser lenses. Near parallel illumination can be achieved at the sample by over focusing the lenses (using a weak lens). Similarly, by using a strong lens and the condenser aperture to control the convergence angle a convergent beam can be formed.

Objective Lens

Electrons that are transmitted and scattered by the specimen are collected by the objective lens to focus the diffraction pattern and magnify the image. An electron diffraction pattern is produced in the back focal plane by the objective lens. The positions that electrons are focused to in the diffraction pattern relates to the scattering angles and amount of scattering caused when they interact with

the specimen. These electrons subsequently recombined in the image plane to form the final image.

An objective aperture is situated within the back focal plane and can be used to select which scattering angles of the transmitted electrons are used to contribute to the final image. This is important to enhance contrast and to carry out dark field imaging.

Intermediate, Diffraction and Projector Lenses

Intermediate and diffraction lenses are positioned below the objective lens. Both are used to magnify and invert the image created by the objective lens, producing a secondary image. The diffraction lens is focused on the back focal plane of the objective lens and the intermediate lens is focused on the image created by the objective lens. The lens that is used determines what is displayed on the viewing screen, camera or detector system, either the diffraction pattern or real space image. A set of projector lenses are then used to further magnify the secondary image/diffraction pattern and project it onto the imaging device.

Aberrations

Ideally electromagnetic lenses would be free from imperfections and focus electrons to the same point in the Gaussian image plane (Figure 3.6a). However, aberrations occur in all electromagnetic lenses which decrease the obtainable resolution to more than a hundred times less than the theoretical resolution limit. In TEM and STEM the main types of aberration that occur are spherical and chromatic.

If a lens contains spherical aberrations (C_s) electron rays that pass through the lens at an appreciable distance away from the optic axis are focused more strongly (Figure 3.6b) as compared to electron rays that are parallel and close to the optic axis which focuses at the Gaussian image plane. The plane of least confusion is where the smallest image of a point object is formed with the minimum disk radius. At the Gaussian image plane a larger disk is formed which reduces the ability to resolve more fine details in the image causing it to appear blurred or distorted. It is possible to correct for C_s in TEM and STEM by using multi-pole

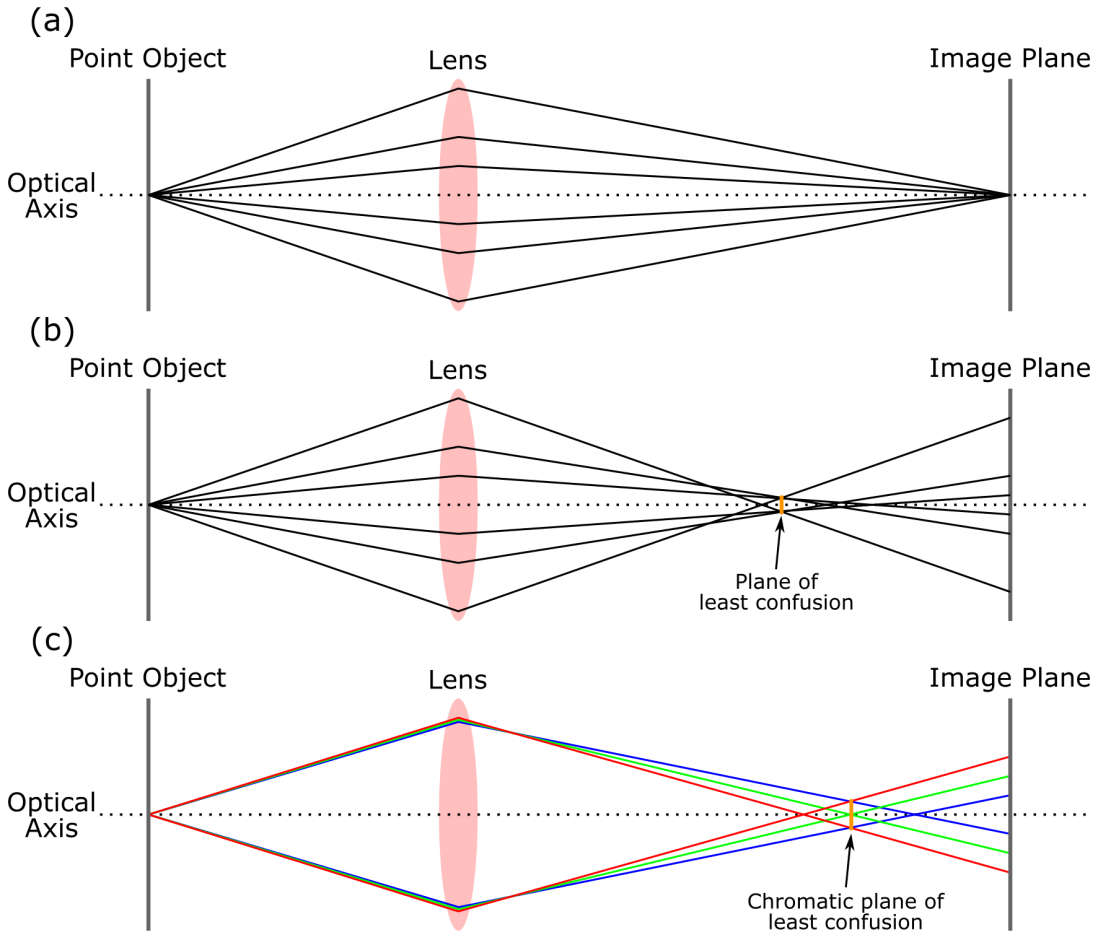

Figure 3.6: (a) Aberration-free lens that focuses point object at the Gaussian image plane (b) Spherical aberration caused by imperfections in the lens focusing rays further away from the optical axis strongly (c) Chromatic aberration caused by electrons of lower energies being focused more strongly.

lenses controlled by a computer to spread the off-axis beams out and re-converge them into a single point at the Gaussian image plane.

Chromatic aberrations (C_c) are caused due to the lens being unable to focus electrons of different energies to the same point (Figure 3.6c). Lower energy electrons are more strongly focused than higher energy electrons. The point at which these effects are minimised is called the chromatic plane of least confusion. Electrons may possess different energies as a result of the energy spread from the

electron source, fluctuations in the potential applied to accelerate the electrons and energy loss from inelastic scattering between the incident electrons and the specimen. Relatively thick samples produce a larger number of inelastically scattered electrons making chromatic aberrations more problematic for these samples. Chromatic aberrations can be reduced by using an electron source with small energy spread (i.e. Schottky FEG and cold FEG) or by using a monochromator to filter electrons of specific energies.

3.2.6 Contrast Mechanisms

Not only is resolution important, the contrast (difference in intensity between the object and background) also needs to be high enough so different points may actually be detected. The electron waves can change in both amplitude and phase as they travel through the specimen with both giving rise to different types of image contrast. All images are collected as intensity results from an amplitude change. In amplitude contrast these changes are direct, while in phase contrast the phase alters such that interference results in a change in amplitude. In most situations, both types of contrast contribute to the image although under select conditions one tends to dominate. To accurately interpret TEM and STEM images the origin of different contrast mechanisms need to be understood.

Amplitude Contrast

Atoms within the sample will cause some incident electrons to be incoherently elastically scattered to high angles (Rutherford scattering). Areas that are denser cause more electrons to be scattered at higher angles these are then blocked by certain apertures and the physical limitations in the microscope column. If the sample has a uniform thickness but different elemental compositions areas containing atoms with a higher atomic number (Z) will cause electrons to scatter to higher angles leading to a change in mass contrast. Similarly, if a sample has the same elemental composition but non-uniform thickness, thickness contrast will show a difference in intensity between the thicker and thinner areas, due to the increase in scattering to high angles. In bright field microscopy, areas corresponding to the highly scattered electrons appear as reduced amplitude/intensity

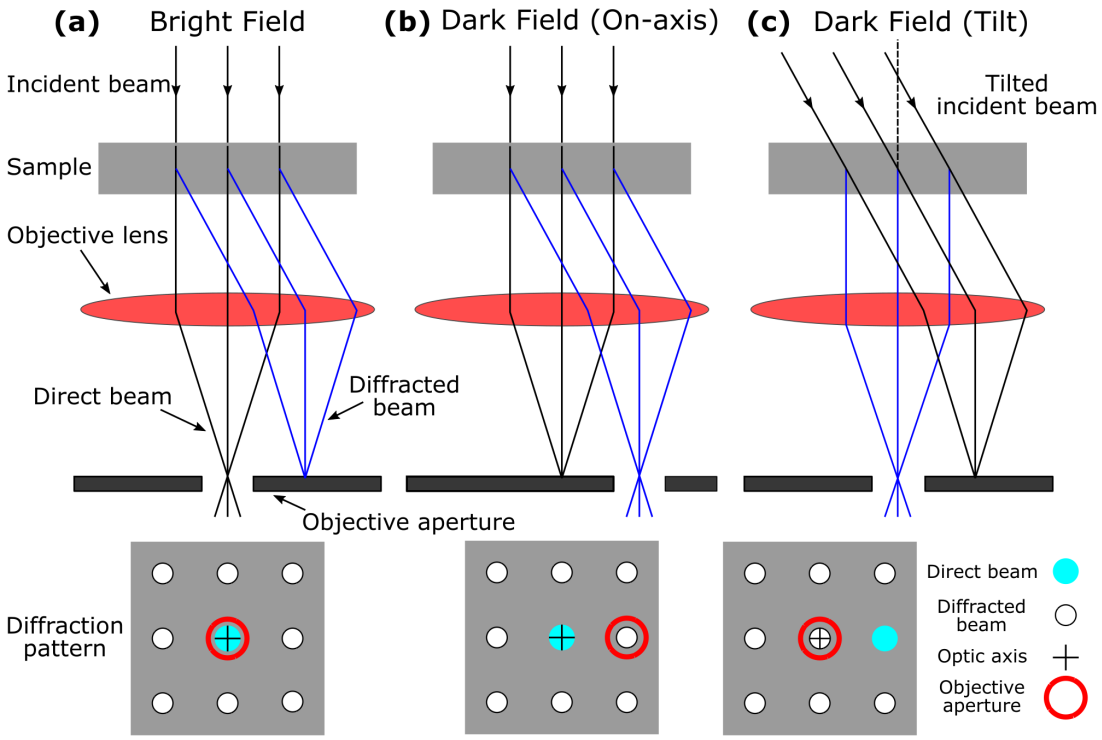

Figure 3.7: (a) Bright field microscopy, highly scattered electrons are blocked and appear dark against a bright background (b) Dark field microscopy, the direct beam is blocked with an objective aperture and the image formed is from certain diffracted beams (c) Tilted dark field, the electron beam is tilted so the diffracted beam is along the optical axis.

(darker) and the background (electrons with smaller scattering angles or from the direct beam) appear light. Figure 3.7a shows a bright field image formed by blocking highly scattered diffracted electron beams.

In crystalline samples, Bragg scattering causes electrons to be strongly diffracted at particular angles depending on the crystallographic structures present. This results in diffraction contrast where corresponding areas appear darker in the bright field image. Images can be formed from these diffracted beams in dark-field microscopy. Here an objective aperture is used to block the direct beam of electrons allowing only certain scattered electrons through. This can be carried out either by adjusting the objective aperture and keeping the direct beam along the optical axis (Figure 3.7b) or by tilting the electron beam so as to bring a

diffracted beam on to the optical axis (Figure 3.7c). Dark field images have a dark background and areas related to the diffracted beam selected will appear bright. A higher electron fluence is required to provide sufficient signal compared to bright field due to fewer electrons being used to form the image, however contrast is much improved.

When electrons are scattered off-axis to low angles ($< 5°$) mass-thickness and diffraction contrast will contribute to the amplitude/intensity observed in the final image, although when diffraction contrast is present it will tend to dominate. At higher scattering angles ($> 5°$) Bragg scattering is normally negligible and the low intensity incoherent elastically scattered electrons are dependent on only the Z of the atoms in the sample. This is referred to as Z-contrast imaging and is used in high angle annular dark field (HAADF) imaging in STEM.

Phase Contrast

Structural information is contained within the phase of the electron waves. However, practically only the amplitude is recorded as intensity (amplitude^2). Phase contrast occurs any time more than one diffracted beam contributes to the image. The phase of the electron wave will change when it passes through the specimen ($\pi/2$ from thin specimens, using the weak phase object approximation) and the interaction between the resulting electron waves of different phase will produce an interference pattern related to the spatial frequencies of the associated diffracted beams (Figure 3.8). This affects the overall intensity of the image and provides phase-related structural information.

Contrast may be further enhanced by adding an additional phase shift to the diffracted electron waves by changing the defocus of the objective lens. This is the basis for high-resolution imaging and can allow lattice images and individual atomic columns to be resolved using phase contrast at high magnification. The optimum level of defocus is determined by the objective lens' contrast transfer function (CTF) and is known as Scherzer defocus and can be calculated for an objective lens given C_s (spherical aberration coefficient) and electrons of wavelength λ.

$$\Delta f_{sch} = -1.2(C_s\lambda_e)^{0.5} \tag{3.7}$$

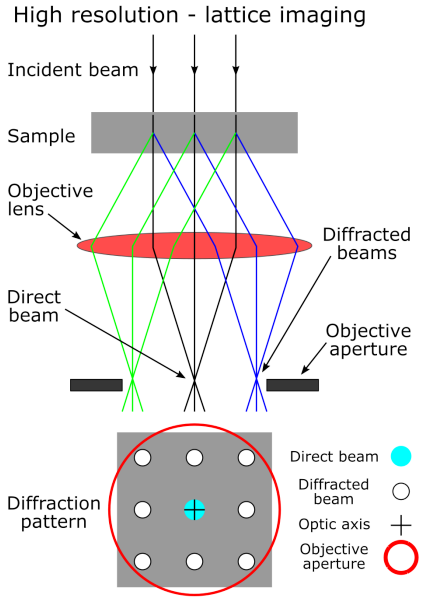

Figure 3.8: Interference patterns produced from several selected diffracted beams provides phase contrast in high-resolution images.

3.2.7 Selected Area Electron Diffraction

When an electron beam interacts with a material consisting of a periodic array of atoms, like that of a crystal, the atomic planes in the sample act as a diffraction grating, which produces an interference pattern constructed from the diffracted electron waves. This diffraction pattern is brought into focus in the back focal plane of the objective lens and can be used to provide information on the crystal structure of the sample.

In single crystal samples, points in the diffraction pattern where the Bragg condition is satisfied will produce constructive interference and can be seen as a series of bright spots that relate to the spatial arrangement of atoms within the unit cell. The distance between a diffracted spot and the zero-order beam (unscattered electron beam) is inversely proportional to the corresponding lattice spacing in the sample. This information can be used to deduce the crystal orientation, real-space position of atoms and ultimately the crystal structure of a sample.

In polycrystalline materials, rather than well-defined diffraction spots that are

observed in single crystal patterns the diffraction pattern consists of a series of bright rings centred around the zero order beam. These rings are a result of the diffraction patterns of thousands of randomly orientated crystals superimposed on top of each other blurring together to create the rings. Similarly to how the distance between single diffraction spots and the zero order beam gives lattice information the radius of the polycrystalline rings can be used to calculate lattice spacings.

Finally, in amorphous samples there is no periodic long-range order within the material. Therefore, the diffraction pattern consists of diffuse rings centred around the zero order beam relating to the average interatomic distances within the specimen.

When carrying out electron diffraction in TEM a selected area aperture positioned in the image plane of the intermediate or projector lens is generally used to select a specific area of interest. This aperture only allows the selected area within an error governed by spherical aberrations to contribute to the diffraction pattern and is known as selected area electron diffraction (SAED).

3.2.8 Energy Dispersive X-ray Spectroscopy

Energy dispersive X-ray (EDX) spectroscopy also known as EDS provides elemental analysis and chemical composition in TEM, STEM and SEM. Each element has a unique atomic structure that leads to a set of characteristic X-ray emissions that can be measured to identify elements and used to estimate the relative abundance. In SEM and STEM EDX mapping can be used to spatially resolve the position of certain elements within the sample.

Characteristic X-rays are produced in a specimen during irradiation by the electron beam when incident electrons excite atomically bound inner shell electrons (e.g. K or L shell). The excited inner shell electrons has an increased amount of energy causing it to then move to a higher energy shell or removing the electron from the atom. Either case will produce an electron-hole that is then filled by an atomic electron relaxing from a higher energy shell. When this transition occurs the electron from the high energy shell will lose energy equal to the energy difference between the higher energy shell and the inner shell. This

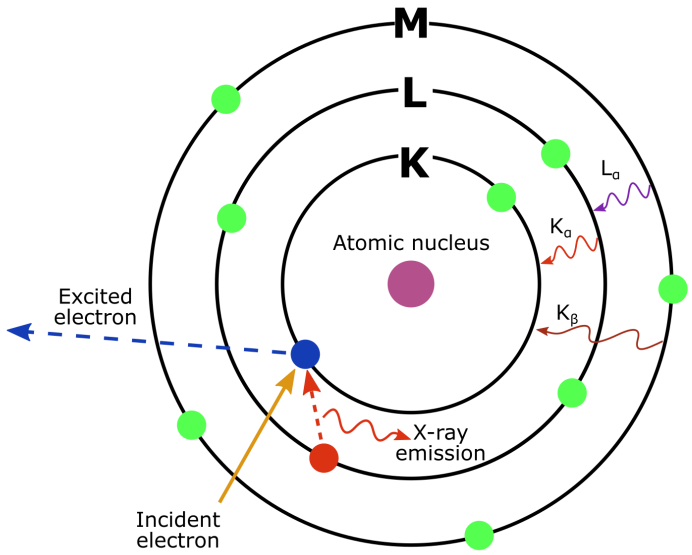

Figure 3.9: Principle of EDX illustrated showing ionisation of an inner shell electron. A higher energy electron then fills the respective hole and emits an X-ray of energy which is characteristic to the elements and electron transition.

loss of energy is given off in the form of a photon with a particular energy that for inner shell ionisation typically falls within the energy range of X-rays. A diagram of this principle is given in Figure 3.9. An energy dispersive spectrometer is used to measure the energy of the emitted X-rays which are characteristic of specific atoms and electron energy shell transitions within that atom.

3.2.9 Scanning Transmission Electron Microscopy

The principal difference between STEM and conventional TEM is that the electron beam is highly focussed to a small nanometre sized probe which is then rastered across the specimen area by the scanning coils. In microscopes that can function as both a TEM/STEM the condenser lenses demagnify and focus the electron beam with the upper objective lens providing the final and largest demagnification step. Scanning coils are situated after the condenser system to raster the probe across the sample area. Once the electrons pass through the sample the electrons can be collected by a set of different detectors without the

need for an objective lens. A bright field detector produce images from electrons scattered to small angles while annular dark field (ADF) and high angle annular dark field (HAADF) detectors are used to image electrons that have been scattered to higher angles. Mass thickness and diffraction contrast can be seen in both BF and ADF images which can make them harder to interpret compared to HAADF images which contain only Rutherford scattered electrons. This results in the image only containing mass-thickness contrast or Z contrast and depending on the probe diameter and the sample, it is possible to resolve individual atoms.

The magnification in STEM is controlled by the scan dimensions of the specimen rather than the lenses. This means no chromatic aberrations occur from the imaging lenses that limits the resolution in TEM, although spherical aberrations still occur in the probe formed by the condenser lens system limiting the resolution. Some STEM systems include C_s aberration correctors in the probe forming lens to further increase the resolution.

3.2.10 Scanning Electron Microscopy

In SEM the condenser lens system is used to demagnify and converge the electron beam. The objective lens then further demagnifies it and focuses the electron beam into a small probe at the sample surface. This focused probe is controlled by a set of scanning coils which rasters it across the sample. Different signals are generated from the sample surface that provides information on the surface and sub-surface structure and elemental composition of the sample.

There are two major categories of interaction that can occur, elastic and inelastic. Elastic scattering is the result of the incident electron being deflected by an atomic nucleus. The electrons scatter to high angles and little or no energy is lost during these collisions. If the scattering angle of the electron is $> 90\,^{\circ}$ then the electron will be backscattered out of the sample, towards the lens/detectors. These are called backscattered electrons (BSE). Heavier elements cause more backscattered electrons due to the higher atomic number nucleus, with areas that contain more of these elements appearing brighter; provided the specimen surface is flat. BSE provides information on composition and topography.

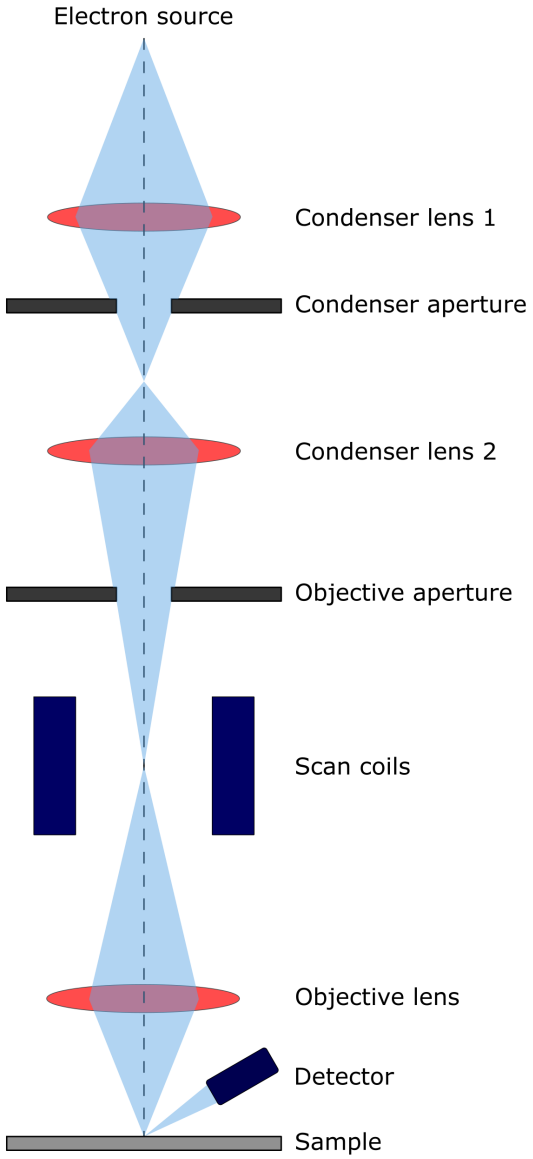

Figure 3.10: Schematic of SEM construction.

In inelastic scattering energy is transferred from the primary beam electrons to the electrons and atoms within the sample. The incident electrons can ionise atoms leading to secondary electrons (SE) being emitted from the surface of the sample. These SE have very low energies on average < 50 eV which means they can only escape the sample from regions a few nanometers away from the surface. Images produced using SE provide surface topographic information about the sample.

There are other signals which are produced when the sample is exposed to electrons, shown in Figure 3.11. One of the most useful being EDX which is previously mentioned when discussing TEM and STEM. In SEM samples tend to be much thicker and the interaction volume of the incident electrons for X-rays is gathered from regions deep within the sample.

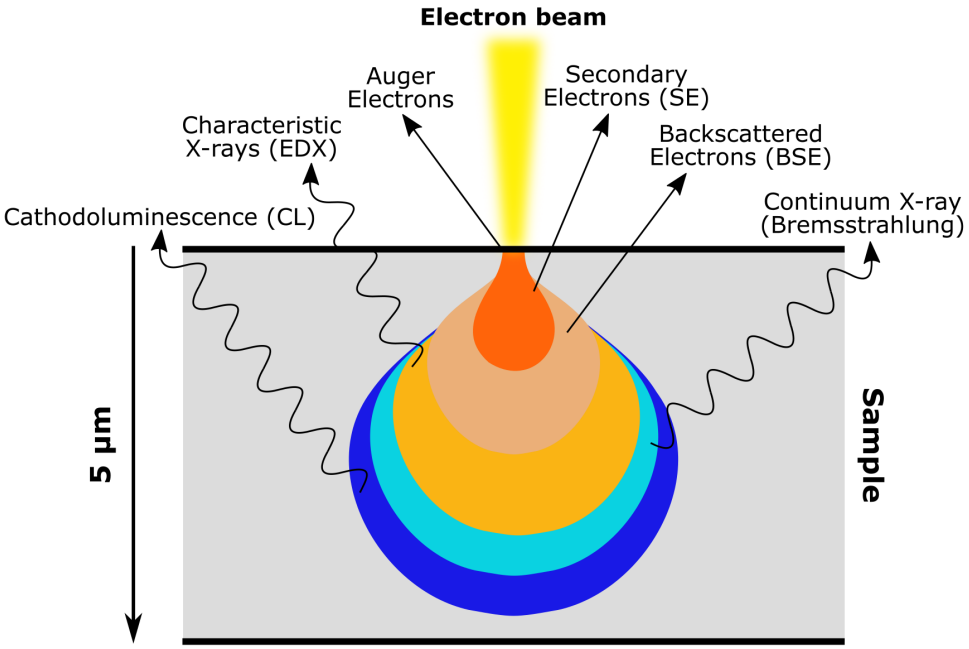

Figure 3.11: Illustration showing the signals that are generated when electrons interact with the sample and where these signals originate.

3.3 Powder X-ray Diffraction

X-ray diffraction is a characterisation technique used to identify the crystalline structure of a sample. Incident X-rays interact strongly with electrons in an atom which causes the incident beam to be scattered from the original direction of travel. If the sample is a crystal, where the atoms are arranged in a periodic array, at specific angles the scattered X-rays will constructively interfere with one another due to the exit waves being in phase. This leads to well-defined X-rays leaving the sample at specific angles or wavelengths (depending which is varied in the experiment) to different inter-planar distances (d_{hkl}) known as lattice spacings or d-spacings. Amorphous materials contain no long-range order and when the X-rays are scattered the combined exit waves are out of phase, leading to destructive interference and no well-defined peaks.

Bragg's law, shown in Equation 3.8, can be used to calculate the angle at which constructive interference from X-rays scattered by parallel planes of atoms will produce a diffraction peak. The derivation for Bragg's law is shown in Figure 3.12. The scattering points, shown in Figure 3.12 as red circles, can refer to any

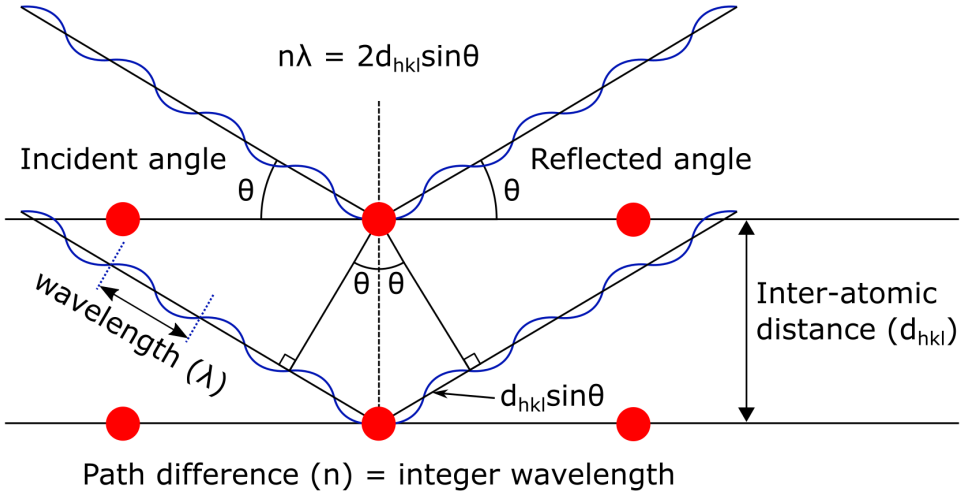

Figure 3.12: Schematic representation of the derivation for Bragg's law, $n\lambda = 2d_{hkl}sin\theta$. Two incident X-rays are in phase and at a specific incident angle of θ for a given inter-atomic spacing (d_{hkl}) the scattered rays interfere constructively to give a peak in the pXRD pattern.

periodic distribution of electron density such as molecules, polymers and proteins.

$$n\lambda = 2d_{hkl}sin\theta \tag{3.8}$$

Here, this technique was used to find which polymorph was present in APIs and compare the results with the data acquired by SAED. It was also used to check for any crystallinity that may be present within different solid dispersions and in Chapter 6 to measure the percentage crystallinity of amorphous solid dispersions that have been stored at high humidity levels.

3.4 Fourier Transform Infra-red Spectroscopy

Infra-red spectroscopy is an analysis technique based on measuring the vibrational frequency of atomic bonds within a molecule and can be used to identify compounds or provide information on bonding and chemical species present. In FTIR spectroscopy the infrared (IR) radiation is emitted from a glowing black-body source which is passed through an aperture to control the amount of energy. The beam then enters an interferometer, shown in Figure 3.13, consists of a beam-splitter, fixed mirror and a moving mirror.

The beam-splitter reflects approximately half of the incident beam towards the fixed mirror while the other half is transmitted towards the moving mirror Both beams are then reflected back towards the beam-splitter by the two mirrors, where each are again half reflected and half transmitted. One half of each beam travels towards the source while the other half travels towards the sample and the detector. An interference pattern, or interferogram, is generated by the beams heading towards the detector that varies with the displacement of the moving mirror. Absorption of IR radiation will occur in the sample at specific wavelengths relating to the energy that chemical bonds within the sample vibrate under irradiation. This vibration can take the form of many different vibrational modes e.g. bending, symmetrical and asymmetrical stretching. Although the vibration itself needs to have a net change in the dipole moment (a separation of charge) as it vibrates. The intensity of the interferogram for the wavelength at which absorption occurred will decrease and the altered interferogram is collected

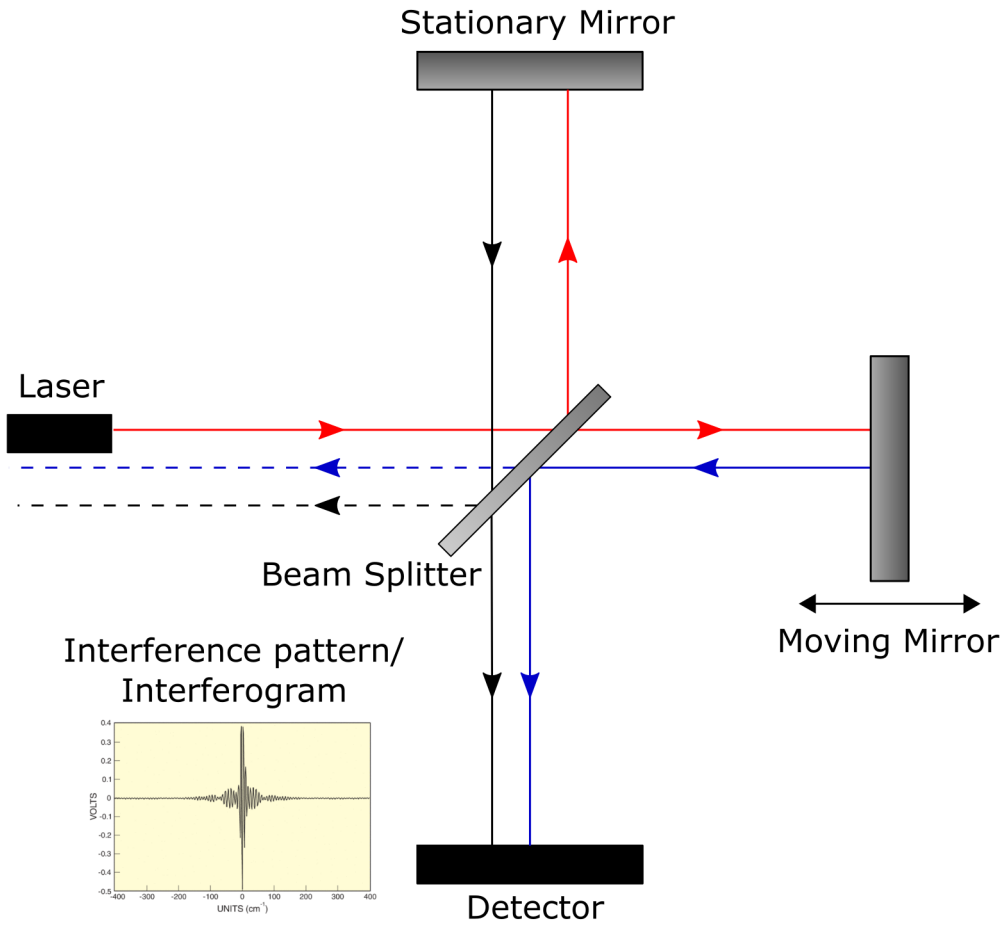

Figure 3.13: Michelson interferometer.

by a detector. A Fourier transform is carried out by a computer to convert the intensity versus mirror displacement (time domain) to a plot of intensity versus frequency (frequency domain). Producing the final spectrum of absorption or transmittance versus wavenumber, measured in cm^{-1} (analogous to frequency).

The three most commonly used sampling methods for FTIR include transmission, reflectance and attenuated internal reflection (ATR). ATR-FTIR is the most common method used due to the ease of use on a variety of samples and was used here, an example of an ATR-FTIR is shown in Figure 3.14. In ATR-FTIR a crystal with high refractive index, such as ZnSe (n = 2.4), Ge (n = 4) or diamond (n=2.4) is used and when the crystal is in close contact with a sample that has

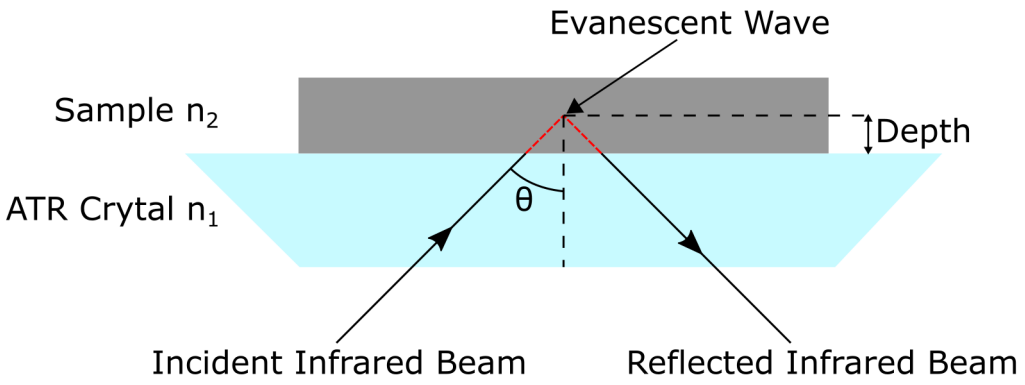

Figure 3.14: Schematic of attenuated total reflectance Fourier transform infra-red spectroscopy

a relatively low refractive index, total internal reflection occurs. This creates an evanescent wave that penetrates a few microns into the sample. The penetration depth depends on the wavelength of the IR beam, the angle of incidence and the refractive index of the crystal. The sample selectively absorbs radiation at specific wavelengths/frequencies and the evanescent wave is attenuated/altered; the energy of this wave is passed back to the IR beam and collected by the detector. The resultant attenuated radiation is measured and plotted as a function of wavenumber and gives rise to the absorption spectral characteristics of the sample.

3.5 Differential Scanning Calorimetry

Differential scanning calorimetry (DSC) is a commonly used thermal analysis technique due to the ease of use and wide range of applications. It can be used to determine the temperature and heat flow of different material transitions and thermal events as a function of time and temperature. There are two different configurations of DSC, known as heat flow or power-compensated DSC and heat flux DSC, a diagram of both is shown in Figure 3.15.

In power-compensated DSC the sample material, approximately $1 - 10$ mg, is weighed out into a sealed pan, this and an empty reference pan are placed into separate furnaces containing individual heating elements. Both pans are

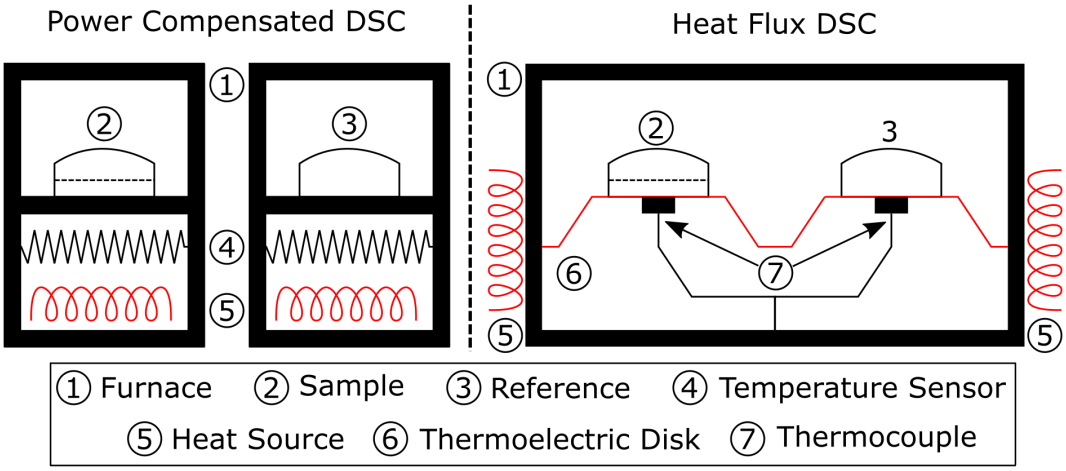

Figure 3.15: Schematic of two common differential scanning calorimetry set-ups

maintained at the same temperature and the difference in thermal power needed to maintain the temperature is measured, providing a graph of heat flow as a function of temperature. For heat flux DSC both the sample and reference pans are prepared in the same way as power-compensated DSC, but are placed into a single furnace onto thermoelectric disks which transfers the heat to both the sample and reference as the temperature of the furnace is increased. There will be a difference in temperature between the sample and reference due to the different heat capacities (C_p). The temperature difference is measured by thermocouples and the heat flow can be calculated using equation 3.9, where q is the heat flow from the sample, ΔT is the temperature difference between the sample and reference and R is the resistance of the thermoelectric disk.

$$q = \frac{\Delta T}{R} \tag{3.9}$$

To prevent any unwanted reactions occurring and to remove volatile compounds that may be produced during heating, the furnace is kept under an inert atmosphere or with a suitable gas flow such as N_2.

The heat flow will change when the sample absorbs or releases heat during different thermal events occurring such as melting, crystallisation, phase transitions, chemical reactions and many other processes. Changes occurring to the sample

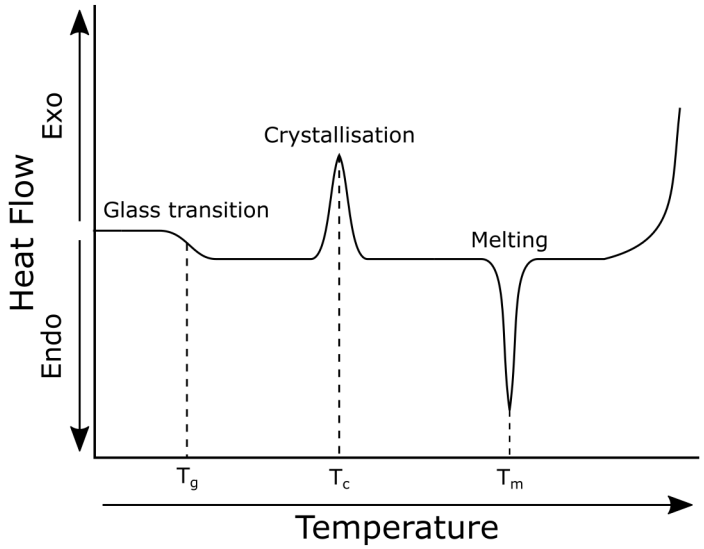

Figure 3.16: Example of a differential scanning calorimetry thermogram

can be identified by the thermogram, such as endothermic peaks (melting, solvent loss, phase transitions), exothermic peaks (crystallisation, phase transitions) or even small steps in the graph due to the glass transitions of amorphous materials which occur due to a change in the C_p (2nd order phase transformation), some of which are shown in Figure 3.16.

3.6 Chapter Summary

This chapter has outlined the use of different bulk characterisation techniques that are applicable for amorphous solid dispersion samples including pXRD, FTIR and DSC. These were used to benchmark samples in Chapters 5 and 6 to confirm the bulk crystallinity within an API, the molecular bonding environment and miscibility between the API and polymer.

Electron microscopy techniques are used in the following chapters to firstly determine the electron beam stability of a variety structurally different APIs and to investigate the number of crystalline areas within amorphous solid dispersion samples. Chapters 6 and 7 use several more specialised electron microscopy techniques not discussed in this chapter including conical/hollow cone dark field, focused ion beam (FIB), scanning moiré fringes (SMFs) and nanodiffraction/scanning electron diffraction (SED) details of how these methods work will be presented in the later sections as they appear.

Specific experimental parameters used for each techniques and data analysis methods are detailed in the following chapters.

Chapter 4

Critical Electron Fluence Measurements and Predictions for Poorly Soluble APIs

When studying electron beam sensitive materials it is important to understand the effects of electron beam damage and the electron fluence limits that the material can withstand before a loss of useful information occurs. This chapter measures the critical electron fluence (C_F) of 20 chemically diverse, poorly water-soluble active pharmaceutical ingredients (APIs) by selected area electron diffraction (SAED) to determine the electron beam stability of these compounds, then discusses the decay profiles and effects of d-spacing on the measured C_F.

To further understand how the chemical structure of individual API affects the C_F measurements, principal component analysis (PCA) is used to determine if any of the molecular descriptors correlate strongly to C_F. The descriptors that provide either a positive or negative correlation to C_F are then used to generate the best fitting multiple linear regression (MLR) model to attempt to predict the C_F for other poorly water-soluble drugs when using 200 kV accelerating voltage at room temperature. The molecular descriptors that are highlighted by PCA and the validity of the MLR model are then discussed.

The effects of temperature on C_F are also measured at 160 K and compared to room temperature to determine if lowering the temperature provides a large improvement to the C_F and the achievable resolution for use in later experiments.

4.1 Transmission Electron Microscopy

4.1.1 Operating Conditions and Method

All the crystalline APIs were prepared for TEM by grinding the powder and dispersing in water; the crystal references and compound data are shown in Appendix A. Water was used to form powder suspensions to prevent the samples from readily dissolving and causing any suspension induced changes to the crystal form. Approximately $3-4$ drops of the suspended powder was placed onto a 400 mesh continuous carbon coated copper grid. The samples were examined in a Tecnai F20 TEM/STEM operated at an accelerating voltage of 200 kV, equipped with a field emission gun using an extraction voltage of 4.5 kV. The images were captured using a Gatan Orius CCD camera.

The electron flux (J), which is the rate of electrons passing through the sample per unit area, was controlled by altering the C1 condenser lens by selecting different spot sizes, generally between 7 and 9, and by defocusing the C2 condenser lens to lower the intensity of the electron beam. Selected area electron diffraction (SAED) patterns were acquired using an aperture size of 1.1 μm diameter at the image plane from crystal areas that appeared relatively thin.

In some cases, the crystals were fairly large (0.5 - 2 μm) and thick allowing very few electrons to pass through. These areas were mostly avoided when acquiring SAED patterns. The exact size and thickness of crystals varied depending on the sample. All of the crystals were randomly orientated, sometimes with several crystals sitting above or below each other. Successive SAED patterns were collected at approximately $15-30$ second intervals until no diffraction spots were visible. An example diffraction series for the API griseofulvin is displayed in Figure 4.1. The time between the initial exposure and collection of the first diffraction pattern was also recorded. A minimum of five electron diffraction time series were taken for each compound, resulting in an average of approximately 80 diffraction spots per compound. However, in some samples it was only possible to obtain 8 - 30 spots. While in others, where more than five series were taken, over 150 separate diffraction spots were analysed using a custom made MATLAB script; detailed later on.

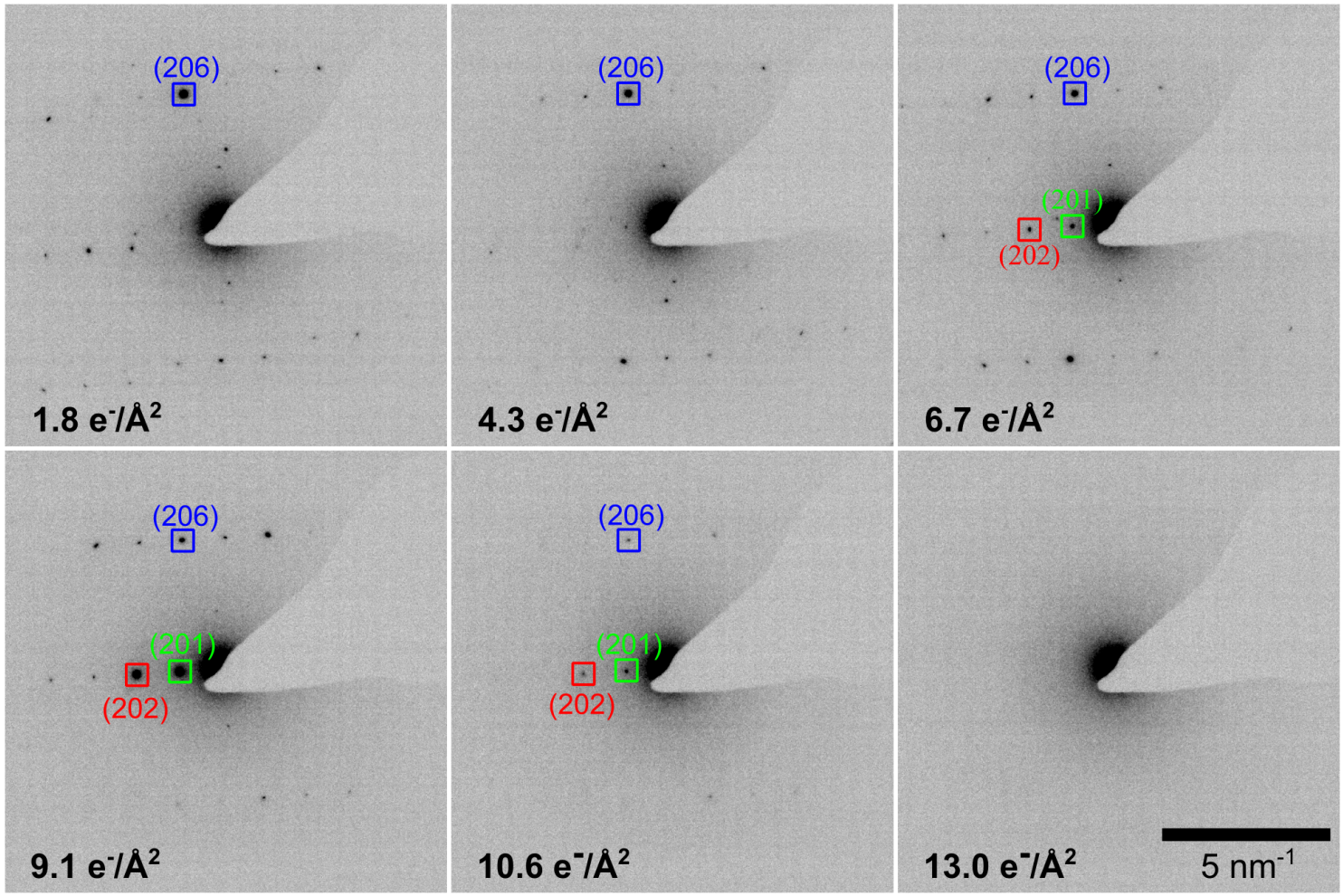

Figure 4.1: Example of an electron diffraction pattern time series of griseofulvin acquired using an electron flux of 0.02 $e^-/(Å^2\ s)$. The (206) reflection gradually reduces in intensity as the cumulative electron fluence increases until it is no longer visible, indicating loss of crystallinity. The cumulative electron fluence for each image is shown in the bottom left.

4.1.2 Cooling Experiments

In addition to measuring C_F at room temperature, three APIs were selected to determine the affects of decreasing the temperature via a cooling holder on the C_F and the resulting dose-limited resolution. The APIs selected were felodipine, griseofulvin and probucol.

The temperature of the sample was reduced by filling a dewar attached to the holder with liquid nitrogen. This gradually decreased the temperature. Over time the liquid nitrogen boiled off requiring the dewar to be topped up with liquid nitrogen every 5 - 10 minutes. A temperature of 155 - 165 K was reached in approximately 30 minutes. Once the experimental temperature was reached the method and operating conditions used to carry out the experiments were identical to the room temperature experiments, the only difference being the need to refill the dewar periodically.

4.1.3 Calculation of Electron Fluence

Before calculating electron fluence (F) it was assumed that the damage occurring within the sample was due to the cumulative F and was independent of J. This has been shown to be true for organic compounds when low values of J (< 0.2 $e^-/(Å^2\ s)$) are used (Egerton and Rauf, 1999). An electron flux between 0.01 - 0.03 $e^-/(Å^2\ s)$ was used for the experiments reported here and was calculated using equation 4.1. This equation estimates the probe current using a calibration curve provided by the microscope manufacture (FEI, now ThermoFisher Scientific) based on the measured brightness (i.e. exposure time) incident onto the phosphor fluorescent screen. J is then calculated by multiplying by the electron beam area.

$$J(e^-/(Å^2 s)) = \frac{a \times b \times \epsilon}{T_e \times C_s \times e} \times \frac{M^2 \times 10^{-20}}{\pi \times r^2} \tag{4.1}$$

where a is a calibration constant (1.875 x 10^{-15}), b is a constant relating to the accelerating voltage (1.3 at 200 kV), ϵ is the emulsion setting which relates to the sensitivity of the TEMs phosphor viewing screen (equal to 2 during TEM operation), C_s is the screen correction factor specific to the phosphor screen used

in the microscope (in this case equal to 1.2) and e is the elementary charge of an electron (1.6×10^{-19} C). The exposure time (T_e) can be read from the exposure meter on the TEM phosphor screen and is dependent on the C1 and C2 condenser excitation, the source extraction voltage and size of the condenser aperture. To acquire the most accurate reading of the screen current the beam must be within the diameter of the screen with no sample in the field of view and no objective aperture inserted. M is the magnification at the viewing screen and r is the radius of the projected electron beam on the screen, in meters, and is controlled using the C2 condenser lens. The cumulative F can then be calculated by multiplying the time the sample has been exposed to the electron beam by J (Equation 4.2).

$$F(e^-/\text{Å}^2) = J \times (t_0 + t) \tag{4.2}$$

where t_0 is the time between the area first being exposed to the electron beam and the time taken to record the first diffraction pattern and t is the subsequent acquisition time of the following diffraction patterns, both in seconds.

Beam current estimations using the phosphor screen provide a good approximation of the J, particularly when larger values of J are used. However, a Faraday cup provides the most accurate method of measurement for the electron beam current and should be used when available.

4.1.4 Data Analysis

Custom made MATLAB scripts were written to assist and automate parts of the data analysis and C_F measurements of the APIs. This was due to the large amount of data collected from the number of images acquired during a diffraction series (5 - 50), the number of series collected for each API (5 - 10) and then number of API examined. The general work flow and details for each step carried out by the MATLAB scripts are elaborated on below:

1. **Import data and create image stack** - The diffraction pattern series were imported into MATLAB using the ReadDMFile function written by Sigworth (2013). The imported images were then stored into a three-dimensional matrix to create an image stack. A median filter was then applied to each image to remove some of the noise within each image.

2. **Create a mask of diffraction spots** - A mask was created from the entire image stack to show areas that contained diffraction spots. This was done by creating a single image from the maximum intensities for each pixel across all images, an example is displayed in Figure 4.2a. The resulting image was then normalised to the maximum pixel intensity and an adaptive threshold was applied using the "imbinarize" function. An adaptive threshold was used since it takes into account changes in illumination due to the exponential background surrounding the zero order diffraction spot. A disk shaped morphological opening was used on the binary image to remove small objects within the foreground of the image which was due to noise within the original image. The threshold used and structure size in the morphology operations was manually changed to eliminate the identification of spots in the mask that was due to noise and to reduce the number of real diffraction spots that overlapped. An example of a resulting image mask is shown in Figure 4.2b.

3. **Measure d-spacings** - The d-spacings for each diffraction spot were calculated using the "regionprops" function which provides information on the different regions within the image. In this case, the centre of each of the diffraction spots was found and the distance between these values and the zero order spot (calculated finding the midpoint between a Friedel pair) was measured.

4. **Measure spot intensities** - The mask was applied to the first image in the image stack and the top 20 most intense pixels for each region in the image were measured and averaged. This value was then stored and the process repeated for each image in the stack, which resulted in a matrix containing raw pixel intensities of each diffraction spot in each image. The raw intensities were then normalised against the maximum intensity for each diffraction spot (I/I_{max}).

5. **Calculate Electron Fluence** - The acquisition time of each image was extracted from the metadata of the .dm3 file and then equations 4.1 and 4.2 were used to calculate cumulative electron fluence for each image.

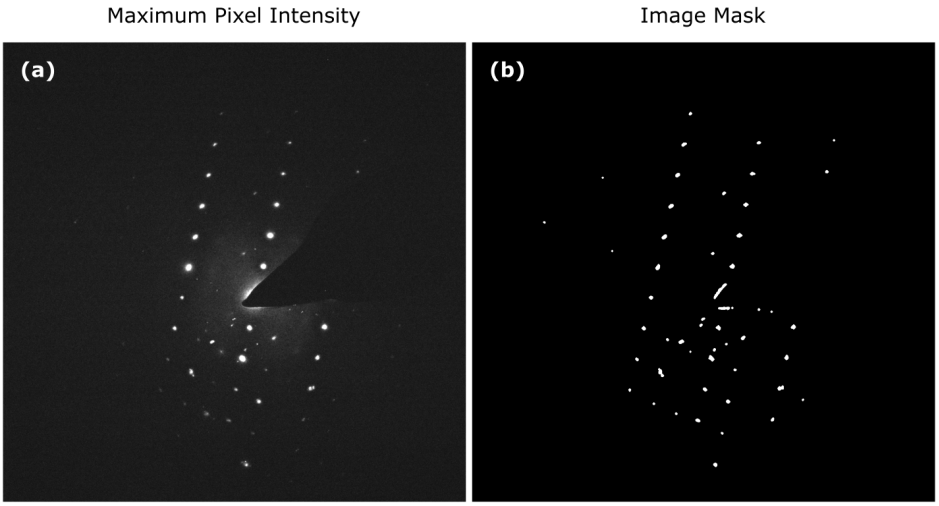

Figure 4.2: Example of the image mask creation from a diffraction pattern series of griseofulvin at 160 K (a) Image of the maximum pixel intensities across all images within the diffraction pattern series; (b) Image mask created by using an adaptive threshold to convert the previous image into a binary image and using morphological opening to remove noise.

6. **Calculate Critical Electron Fluence** - Critical fluence for each diffraction spot was calculated by plotting the electron diffraction spot decay curves of $\ln(I/I_{max})$ against F and fitting a linear function to approximate where I/I_{max} drops to e^{-1} (or -1 for $\ln(I/I_{max})$). The d-spacing and C_F were then stored together.

4.2 Principal Component Analysis

Principal component analysis is a method that is used to reduce the dimensionality of multidimensional data sets and to select a subset of variables from a larger set based on the correlation of the input variables with the principal component (Smith, 2002). To carry out PCA the original data matrix which contains n, number of observations and p, number of variables must first be prepared by subtracting the mean from each variable to produce the mean adjusted dataset (X) where the mean is equal to zero. The variance of each variable is then

scaled to unit variance, to convert all the variables into the same units. The covariance/correlation matrix is then calculated using Equation 4.3.

$$C = \frac{1}{n-1} X X^T \tag{4.3}$$

where C is the covariance matrix with dimensions $n \times n$ and X^T is the transpose matrix. C is then used to calculate the unit eigenvectors and eigenvalues for this matrix. This calculation is non-trivial for matrices larger than 3×3 and is carried out using a computer algorithm. The eigenvectors allow the data to be represented in terms of eigenvectors rather than xy coordinates with eigenvectors being orthogonal to each other. The eigenvalues are ordered from highest to lowest, with the highest values corresponding to the first principal component which accounts for the largest percentage of variance within the dataset, the second highest accounting for the second largest percentage variance and so on.

Dimensionality reduction is then performed by selecting fewer principal components than p. Some information will be lost, although, if the eigenvalues are small then the loss of information is minimal. The number of principal components are selected so that the majority of the variance in the data can be accounted for, generally $> 70\%$. The new data set is then calculated from Equation 4.4.

$$Y = AX \tag{4.4}$$

where Y is the new data set also known as the PCA scores and A are the PCA loadings/coefficients. The original data can be calculated by multiplying the transpose of A with Y and adding the subtracted mean. For the data presented in Table 4.2, the data was set to a mean of zero and unit variance and then using the "pca" function in MATLAB the covariance matrix, eigenvectors, eigenvalues, A and Y were all calculated.

A variety of molecular descriptors were selected as input parameters for PCA, based on them being easy to determine from the chemical structure and the possibility of them having an influence on the C_F, shown in Table 4.1. Hydrogen bond donors were defined as N, O, S atoms covalently bonded to at least one hydrogen atom and hydrogen bond acceptors were defined as N, O, S and halogen atoms with at least one lone pair. Rotatable bonds were considered as any single bonds

not within a ring, bound to any non-terminal heavy atom and conjugated carbons were taken to be any sp^2 hybridised carbon atom. Values for each molecular descriptor for each compound are shown in Table 4.2.

The selection of parameters used was based on readily obtainable values from the chemical structure and ones that have been shown previously to increase C_F (Clark et al., 1980; Isaacson, 1975; Kumar and Adams, 1990). The decision to only include parameters relating to chemical structure was so that the MLR model was applicable to APIs in the early stages of drug development and did not depend on parameters that may include information that was not available i.e. crystal structure.

Table 4.1: Input parameters used in the PCA consisting of molecular descriptors obtain from the chemical structure, parameters previously been known to affect C_F and the measured C_F values.

Parameters	**Meaning**
T_m	Melting temperature
M_w	Molecular weight
HB_d	Number of hydrogen bond donors
HB_a	Number of hydrogen bond acceptors
rotB	Number of rotatable bonds
$Ring_{arom}$	Number of aromatic rings
$Ring_{aliph}$	Number of aliphatic rings
nX	Number of halogens
C_c	Number of conjugated carbons
C_nc	Number of non-conjugated carbons
C_t	Total number of carbon atoms
$Atom_{nH}$	Number of non-hydrogen atoms
$Atom_H$	Total number of hydrogen atoms
$HB_{d:a}$	Number of hydrogen bond donor/acceptor ratio
$HB_{a:d}$	Number of hydrogen bond acceptor/donor ratio
$C_{c:nc}$	Number of conjugated/non-conjugated carbon ratio
$C_{c:ct}$	Number of conjugated/total carbons ratio
$C_{nc:ct}$	Number of non-conjugated/total carbons ratio
$Atom_{nH:H}$	Number of non-hydrogens to hydrogen ratio
C_F	Critical fluence

Table 4.2: Molecular descriptors used in PCA (not including the measured C_F). Each term is listed in table 4.1; all values except T_m are calculated from the chemical structures of each API. T_m was taken from data on https://www.drugbank.ca/.

Compounds	$\mathbf{T}_m$ **(°C)**	$\mathbf{M}_w$ **(g/mol)**	$\mathbf{HB}_d$	$\mathbf{HB}_a$	**rotB**	$\mathbf{Ring}_{arom}$	$\mathbf{Ring}_{aliph}$	**nX**	$\mathbf{C}_c$	$\mathbf{C}_{nC}$	$\mathbf{C}_t$	$\mathbf{Atom}_{nH}$	$\mathbf{Atom}_H$	$\mathbf{HB}_{d:a}$	$\mathbf{HB}_{a:d}$	$\mathbf{C}_{c:nc}$	$\mathbf{C}_{c:ct}$	$\mathbf{C}_{nc:ct}$	$\mathbf{Atom}_{nH:H}$
Amcinonide	254	503	1	8	4	0	6	1	0	21	28	36	35	0.1	8.0	0.0	0.0	0.8	1.0
Bicalutamide	194	430	2	9	5	2	0	4	12	5	18	29	14	0.2	4.5	2.4	0.7	0.3	2.1
Celecoxib	160	381	1	3	4	3	0	3	15	2	17	26	14	0.3	3.0	7.5	0.9	0.1	1.9
Ciclesonide	205	541	1	6	6	0	6	0	0	24	31	39	44	0.2	6.0	0.0	0.0	0.8	0.9
Cilostazol	159	369	1	5	7	2	2	0	7	12	20	27	27	0.2	5.0	0.6	0.4	0.6	1.0
Drospirenene	199	367	0	2	0	0	7	0	0	20	24	27	30	0.0	0.0	0.0	0.0	0.8	0.9
Dustasteride	249	529	2	8	2	1	4	6	6	17	27	37	30	0.3	4.0	0.4	0.2	0.6	1.2
Efavirenz	137	316	1	5	1	1	2	4	6	7	14	21	9	0.2	5.0	0.9	0.4	0.5	2.3
Felodipine	145	384	1	5	6	1	1	2	6	6	18	25	19	0.2	5.0	1.0	0.3	0.3	1.3
Griseofulvin	143	353	0	6	3	1	2	1	6	7	17	24	17	0.0	0.0	0.9	0.4	0.4	1.4
Indapamide	168	366	2	5	3	2	1	1	12	3	16	24	16	0.4	2.5	4.0	0.8	0.2	1.5
Indomethacin	158	358	1	4	4	3	0	1	14	3	19	25	16	0.3	4.0	4.7	0.7	0.2	1.6
Lopinavir	92	628	4	5	15	3	1	0	18	16	37	46	48	0.8	1.3	1.1	0.5	0.4	1.0
Nandrolone	124	274	2	3	5	0	4	0	0	15	18	20	26	0.7	1.5	0.0	0.0	0.8	0.8
Nifedipine	173	346	1	7	5	1	1	0	6	5	17	25	18	0.1	7.0	1.2	0.4	0.3	1.4
Nimodipine	125	418	1	6	10	1	1	0	6	9	21	30	26	0.2	6.0	0.7	0.3	0.4	1.2
Nisoldipine	148	388	1	7	7	1	1	0	6	8	20	28	24	0.1	7.0	0.8	0.3	0.4	1.2
Probucol	126	517	2	4	8	2	0	0	12	19	31	35	48	0.5	2.0	0.6	0.4	0.6	0.7
Simvastatin	139	419	1	3	7	0	3	0	0	19	25	30	38	0.3	3.0	0.0	0.0	0.8	0.8
Tolnaftate	110	307	0	2	3	3	0	0	16	3	19	22	17	0.0	0.0	5.3	0.8	0.2	1.3
Furosemide	206	331	4	8	5	3	0	1	11	1	12	21	11	0.5	2.0	11.0	0.9	0.1	1.9

4.3 Multiple Linear Regression

Multiple linear regression (MLR) was used to quantify the relationship between several predictor variables and a dependent variable, providing an equation that could be used to predict C_F. A multiple linear regression model can be represented as:

$$y = \beta_0 + \beta_1 x_1 + \beta_2 x_2 ... + \beta_k x_k \tag{4.5}$$

where k is the number of predictor variables, β_0 is a constant, β_1, β_2, , β_k are the regression coefficients and y is the dependent variable (C_F).

The parameters that were shown to have an influence on C_F during PCA were used as the predictor variables to create a number of MLR models. In order to select the best and simplest model without overfitting, MLR was carried out using the "steplm" function in MATLAB, this function adds or removes variables to increase or decrease the value of certain selection criteria, these being: adjusted R^2, Bayesian Information Criterion (BIC) and Akaike Selection Criterion (AIC) (Akaike, 1974; Schwarz, 1978). The adjusted R^2 value is a statistical diagnostic tool used to determine the percentage of the variability of the dependent variable explained by the variation of the independent variables and takes into account the number of variables in the model. A larger adjusted R^2 suggests that the model provides a better fit. AIC and BIC are both information criteria which are used to measure the goodness of fit, by calculating the difference between a given model and the true underlying model. The difference between AIC and BIC is how additional parameters that are included in the model are penalised. Smaller values calculated by AIC and BIC indicate that a model is closer to the "true" model. Therefore a smaller value suggests a more accurate model. By using these selection criteria, the stepwise regression method can add or remove variables in order to improve the model over that expected by random chance.

4.4 Results and Discussion

4.4.1 Critical Fluence Measurements

Figure 4.3 shows the decay curves of the natural log of the relative diffraction spot intensity ($\ln(I/I_{max})$) against cumulative F for the inter-planar spacings 2.35 Å (206), 5.78 Å (111) and 4.10 Å (202) of the API griseofulvin, showing various decay profiles with different forms found during the C_F calculations. In all plots a section of the decay is approximated to a linear function with an adjusted R^2 of > 0.90. As mentioned earlier this is used to calculate the C_F which it should be noted varies by < 0.1 when adding or removing any datum point on any of the plots (generally adjusted R^2 shifts by approximately 0.01 - 0.03 in these circumstances). In Figure 4.3a the intensity is at its maximum within the first two data points, corresponding to an electron fluence of < 2 $e^-/Å^2$. The intensity then decays and can be approximated to a linear function until $\ln(I/I_{max})$ is equal to -1.5 (22% of the maximum intensity). At this point the diffraction spot is below e^{-1} of the maximum intensity and the C_F can be calculated from the linear function. The spot continues to decrease in intensity until around 10 $e^-/Å^2$ where the intensity plateaus and becomes similar to the background level, no longer visible in the electron diffraction pattern. Previous studies have observed similar decay profiles in other materials (Clark et al., 1980; Knapek et al., 1984; Kumar and Adams, 1990; Leijten et al., 2017; Li and Egerton, 2004; Reimer and Spruth, 1982). Similar profile shapes were seen for the majority of diffraction spots from each sample. In some cases small fluctuations in the intensity of the first few data points could be seen, where there was an initial increase in intensity before the decay. This may be attributed to a rapid loss of mass upon irradiation, reorientation or conformational changes occurring in the sample, producing a structure that is more stable to the electron beam (Clark et al., 1980; Grubb, 1974; Howitt and Thomas, 1977; Stenn and Bahr, 1970). Decreases in intensity are due to damage of both the chemical and crystal structure and in most cases it appears that both occur simultaneously (Stenn and Bahr, 1970). However, it has been demonstrated in phthalocyanines that the crystal structure is lost before the

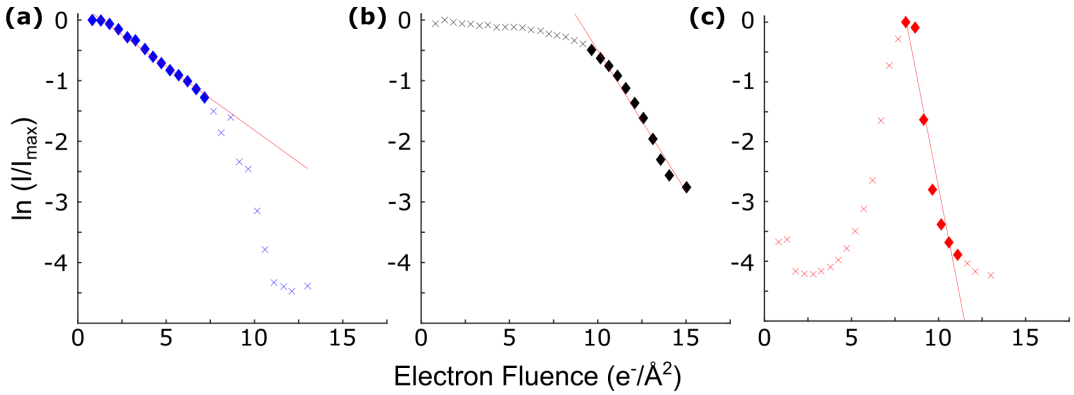

Figure 4.3: Intensity curves of griseofulvin that demonstrate the different decay profiles observed, the linear sections of each graph are fitted using a straight line to calculate C_F (a) Linear decay of 2.35 Å spacing, equal to a (206) reflection; (b) latent decay of 5.78 Å spacing, equal to a (111) reflection; (c) enhanced intensity effect followed by linear decay of the 4.10 Å spacing, equal to a (202) reflection.

chemical structure while studies on tetracene show that the chemical structure is destroyed first (Stenn and Bahr, 1970).

In Figure 4.3b the decay profile exhibits an initial plateau, between an electron fluence of 0 - 6 $e^-/Å^2$ here the spot intensity remains above 90% of the maximum before following a linear decay, at an electron fluence >9 $e^-/Å^2$, similar to the one shown in Figure 4.3a but at an increased rate. This plateau is unexpected at room temperature and, as well as being observed for griseofulvin (5.78 Å) plateaus were also observed in other compounds: dutasteride (3.31 Å and 6.62 Å) and in six different spacings in tolnaftate (3.07 Å, 3.33 Å, 3.43 Å, 3.97 Å, 4.15 Å and 5.25 Å). Such a plateau has been referred to as latent decay by Siegel and Wade and is typically observed in samples that are studied at cryogenic temperatures (Siegel, 1972; Wade and Pelissier, 1982). A proposed explanation for this decay profile was put forward by Siegel; the diffusion rate of damaged fragments decreases at low temperatures, preventing a change in the crystalline order (Siegel, 1972). Once the number of fragments reaches a critical concentration, the fragments are able to diffuse away, no longer preventing changes to the structure and hence decreasing order at the corresponding diffraction intensities (Reimer and Spruth,

1982; Wade, 1984; Wade and Pelissier, 1982). The reason for a similar decay profile being apparent at room temperature is not clear but it may be caused by steric hindrance preventing fragments from diffusing. The occurrence of a thermally activated reverse reaction or a healing effect may prevent a proportion of the damage. Allowing for the structure to stay intact until the cumulative damage is too great and the structure finally breaks down.

In Figure 4.3c, the decay profile starts with the diffraction spots at low intensities and as the fluence increases the intensity initially increases. At approximately 8 $e^{-}/Å^{2}$ the spot is at its maximum brightness and there is then a rapid decay in intensity levels. This has been referred to as the enhanced intensity effect and is thought to occur in relatively thin samples (<100 nm) with a high density of lattice defects (Knapek et al., 1984; Wade, 1984; Wade and Pelissier, 1982). Some defects may be present before electron beam exposure but the majority of lattice defects i.e. point defects are likely to be caused during irradiation (Stenn and Bahr, 1970). When there is a high density of lattice defects electrons that pass through the sample encounter strain fields causing the intensity of the diffracted beam to increase; leading to the enhanced intensity seen in the electron diffraction pattern (Koehler, 1959; Wilkens and Rapps, 1977). In addition, reconfiguration or orientation into a more stable structure occurs via the production of radiation induced derivatives or mechanical movement of the crystal causing it to tilt off the original axis and can increase the relative intensities (Knapek et al., 1984).

Seemingly random and erratic changes in intensity have also been seen in other studies where there are multiple peaks in the decay curves and are thought to occur in relatively thick samples (multiple hundreds of nm). The decay profiles of these samples have been shown to follow the movement of bend contours in bright field TEM images (Wade and Pelissier, 1982). This is due to a combination of mechanical movement and structural changes within the crystal altering the lattice orientation relative to the electron beam (Grubb, 1974; Siegel, 1972; Wade, 1984; Wade and Pelissier, 1982).

Due to the limited amount of time available before damage occurred in the current materials it was not possible to tilt a particular crystalline particle onto a recognisable zone axis.

Table 4.3: Mean critical fluence and standard deviation for each compound, calculated from diffraction pattern data. C_F when all measured diffraction spots are included are shown and the number of spots used in these averages. Columns 2, 3, 4 and 5 separate the diffraction spots based on d-spacing and show the calculated values when only spots within those chosen ranges are included in the average. All units are in $e^-/Å^2$.

API	**d < 2Å**	**2 - 4 Å**	**4 - 6 Å**	**d > 6 Å**	**All d-spacings**	**Total number of spots averaged**
Amcinonide	1.0 ± 0.1	1.1 ± 0.2	1.4 ± 0.3	1.5 ± 0.4	1.3 ± 0.3	42
Bicalutamide	1.6 ± 0.2	2.9 ± 0.7	3.1 ± 0.6	4.4[1]	2.9 ± 0.8	51
Celecoxib	3.8 ± 1.4	5.2 ± 1.2	5.8 ± 0.7	6.0 ± 3.4	4.5 ± 1.6	161
Ciclesonide	-	-	0.6 ± 0.1	0.7 ± 0.1	0.6 ± 0.1	8
Cilostazol	1.6 ± 0.5	2.1 ± 0.9	2.5 ± 0.9	3.7[1]	2.1 ± 0.9	166
Drospirenene	0.8 ± 0.3	0.9 ± 0.3	0.9 ± 0.3	1.2 ± 0.3	0.9 ± 0.3	105
Dutasteride	1.9 ± 0.4	2.1 ± 0.4	2.5 ± 0.6	2.7 ± 0.4	2.2 ± 0.5	70
Efavirenz	-	0.5 ± 0.1	0.4 ± 0.1	0.9 ± 0.1	0.5 ± 0.1	25
Felodipine	1.8 ± 0.7	2.1 ± 0.9	2.7 ± 1.2	2.0 ± 0.3	2.1 ± 0.9	67
Griseofulvin	4.4 ± 2.2	5.8 ± 3.1	7.6 ± 3.6	6.1 ± 3.4	5.3 ± 2.9	111
Indapamide	2.7 ± 1.0	4.8 ± 1.9	5.0 ± 2.0	6.1 ± 2.2	4.5 ± 2.0	103
Indomethacin	2.8 ± 1.6	2.8 ± 2.0	2.8 ± 2.4	3.9 ± 2.7	2.9 ± 1.9	241
Lopinavir	-	0.5 ± 0.1	0.7 ± 0.3	0.5 ± 0.1	0.6 ± 0.2	25
Nandrolone	1.3 ± 0.2	1.4 ± 0.3	1.5 ± 0.2	1.3[1]	1.4 ± 0.2	85
Nifedipine	0.7 ± 0.1	0.7 ± 0.2	0.7 ± 0.3	0.9 ± 0.1	0.7 ± 0.2	60
Nimodipine	2.1 ± 0.8	3.0 ± 0.7	2.7 ± 0.9	-	2.7 ± 0.8	65
Nisoldipine	-	0.3 ± 0.1	0.2 ± 0.0	-	0.3 ± 0.1	14
Probucol	0.1 ± 0.1	0.1 ± 0.0	0.2 ± 0.1	0.1 ± 0.0	0.1 ± 0.1	61
Simvastatin	0.6 ± 0.2	0.7 ± 0.2	0.7 ± 0.2	-	0.7 ± 0.2	45
Tolnaftate	8.4 ± 4.6	13.8 ± 4.7	15.2 ± 3.8	14.6 ± 1.7	13.0 ± 5.1	165

[1] Only data from one diffraction spot available.

This means the crystals were randomly orientated and the majority of diffraction patterns showed different inter-planar spacings making it difficult to provide a representative C_F for a particular inter-planar spacing.

Most previous studies examined thin crystals with preferred orientations which provide easily comparable diffraction pattern series via selection of a single first-order diffraction spot in order to calculate C_F (Kumar and Adams, 1990; Reimer and Spruth, 1982; Wade, 1984; Wade and Pelissier, 1982). Instead of selecting one spot to provide a measurement for C_F, in this work an average of all the spots measured was taken to give an overall measurement of C_F, hence crystallinity will be assessed in random orientations (Table 4.3). This average includes higher order spacings that are not generally included in C_F measurements.

It is observed that diffraction spots with smaller d-spacings generally fade faster, corresponding to a loss of high-resolution information and short-range order, while the general molecular packing and long-range order (large d-spacings) remain intact even though the molecules are fragmenting and losing their short-range order (Kolb et al., 2010). Including the smaller d-spacings within the average C_F measurement generally provides a smaller value of C_F, shown in Table 4.3, where the diffraction spots have been grouped into d-spacing ranges (<2 Å, 2 - 4 Å, 4 - 6 Å and >6 Å). The majority of samples follow the trend of smaller spacings corresponding to smaller values of C_F, however for griseofulvin the spacings >6 Å have a lower average C_F compared to the spacings within the range 4 - 6 Å; there is also a larger spread of measured fluence as can be seen from the standard deviation. This may be a result of preferential damage along certain crystal planes, causing the intensity of these spots to fade irrespective of their inter-planar spacing. The large standard deviation may also be a result of sample thickness which was not taken into consideration during this study due to the difficulties associated with measuring this in powder samples. Thickness has been shown to provide a linear dependency to the C_F of the sample, with thicker samples providing larger C_F values; as a result of heating, charging effects and the rate of outward diffusion of damage fragments being more significant in thin samples (Egerton et al., 2004; Fryer, 1984).

4.4.2 Principal Component Analysis

Using the molecular descriptors from Table 4.2 and the experimentally determined average of C_F for all measured diffraction spots, PCA was carried out to determine if a correlation exists between the selected descriptors and C_F. The results showed that 86% of the total variance in the input parameters could be explained using four principal components (PCs), where 40%, 24%, 14% and 8% of the variance is explained by PC1, PC2, PC3 and PC4 respectively, shown by the scree plot in Figure 4.4. The PC loadings were then used to find a correlation between each molecular descriptor and C_F. This was achieved by plotting PC loadings against each other and measuring the component angle between C_F and

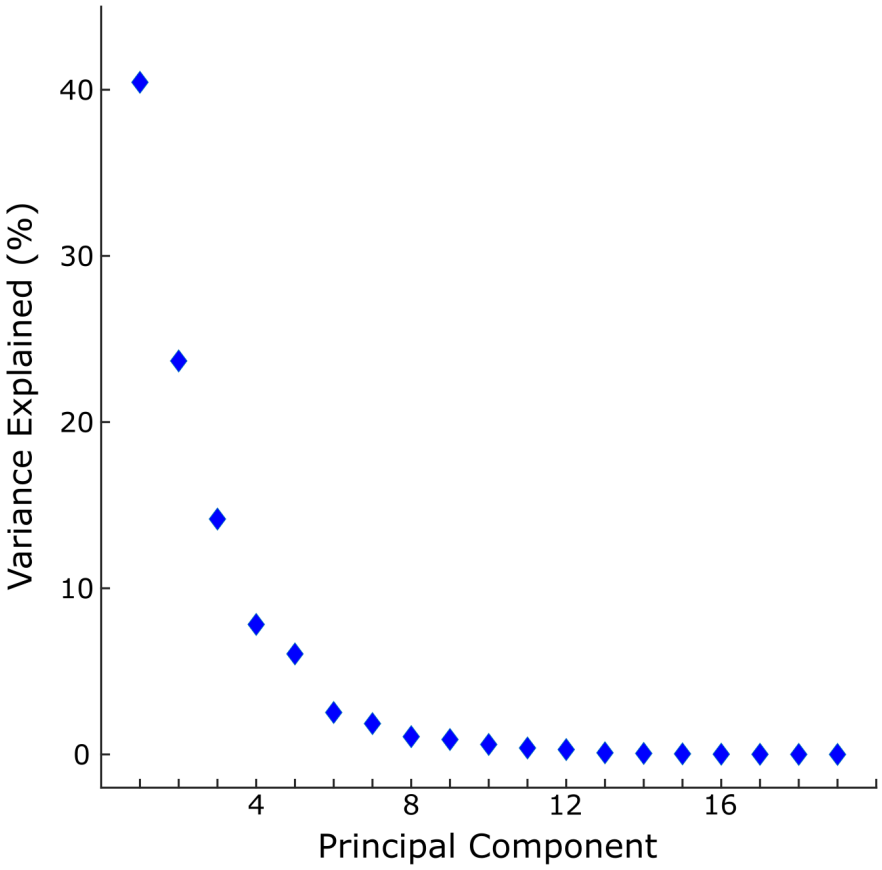

Figure 4.4: Scree plot of variance explained against principal component for PCA; used to select the number of PCs to reduce the dimensionality of the dataset.

each molecular descriptor. The graphs and an example of one of the component angles being measured can be seen in Figures 4.5a and 4.5b. A value of cos θ of approximately 1 suggests that the molecular descriptor influences C_F positively, if cos θ is approximately -1 it suggests a negative correlation and if cos θ is approximately 0 then the molecular descriptor is independent of C_F. For there to be an overall correlation between the molecular descriptor and C_F the sample relationship must hold true in both PC1 vs PC2 (θ_{PC1-2}) and PC3 vs PC4 (θ_{PC3-4}). The graph of θ_{PC3-4} against θ_{PC1-2} in Figure 4.5c shows clearly the descriptors that are positively correlated, negatively correlated and independent when considering all four PCs.

From the 19 molecular descriptors entered into the PCA, 9 were shown to be either positively or negatively correlated to C_F, these being the number of hydrogen bond donors (HB_d), the number of hydrogen bond acceptors (HB_a), the number of rotatable bonds (rotB), the number of aromatic rings ($Ring_{arom}$), the number of conjugated carbons (C_c) and the ratio of number of hydrogen bond donors to acceptors ($HB_{d:a}$), the ratio of number of hydrogen bond acceptors to donors ($HB_{a:d}$), the ratio of number of conjugated to non-conjugated carbons ($C_{c:nc}$) and the ratio of number of conjugated carbons to total number of carbons ($C_{c:t}$). It should be noted that using the C_F for different d-spacing ranges, as opposed to the overall average, gave little or no difference to the final PCA results.

The molecular descriptors which gave a positive correlation to C_F were $Ring_{arom}$, C_c, $C_{c:nc}$ and $C_{c:t}$. It was expected that $Ring_{arom}$ would give a positive correlation since previous studies have suggested that the delocalisation of electrons in a ring allows the energy deposited from the electron beam to be shared and dissipated more effectively which then decreases the formation of damaging radicals (Fryer, 1987; Fryer et al., 1992; Isaacson, 1975; Li and Egerton, 2004). The presence of benzene rings has been suggested to influence the delocalisation of electrons up to twelve atoms away from the ring (Alexander and Charlesby, 1954).

The molecular descriptors which gave a negative correlation to C_F were HB_d, HB_a, rotB, $HB_{d:a}$, $HB_{a:d}$. The rotB relates to the number of different structural configurations the molecules can undertake and in this study the greater number

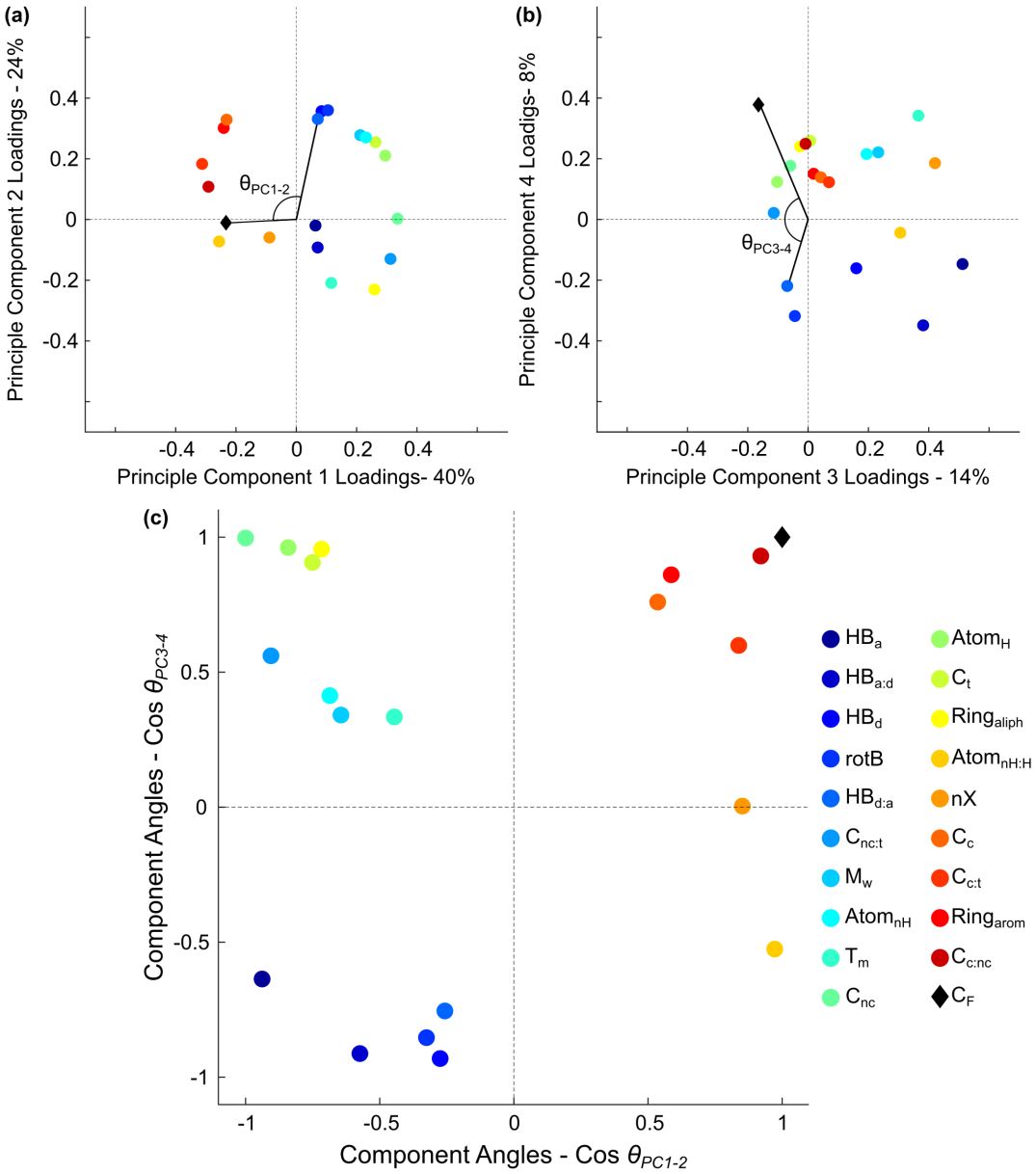

Figure 4.5: (a) PCA loadings for principal component 1 and 2; (b) PCA loadings for principal component 3 and 4. (c) Angles between critical fluence and other molecular descriptors calculated from graphs a and b. Points in the top right quadrant are positively correlated in all principal components, points in the bottom left quadrant are negatively correlated in all principal components and all the other molecular descriptors are independent of critical fluence (which we demonstrate here correlates to itself, as expected.)

of rotB lead to a lower C_F. Surprisingly factors that related to hydrogen bond donors/acceptors all appeared to give a negative correlation to C_F.

This was initially unexpected since organic crystals are held together by weak intermolecular forces such as van der Waals bonding, hydrogen bonding and $\pi-\pi$ stacking of aromatic rings and it was assumed that if more hydrogen bonds were present then the crystal would be more stable i.e. requiring a higher electron fluence before damage occurred. If a crystal is mainly stabilised through hydrogen bonding removal of the hydrogen-bonded atoms by the electron beam may cause disruption to the crystal structure at an increased rate as compared to structures that are mainly stabilised through van der Waals or $\pi-\pi$ stacking. The hydrogen atoms may be removed via knock-on damage, where the electron collides with the hydrogen atom directly and due to the low binding energy the atom is removed from the structure (Egerton et al., 2004). However, no correlation between the overall number of hydrogen atoms and C_F was found. Alternatively, the hydrogen atoms may be removed through radiolysis where the covalent bond between the hydrogen atom and another atom (C-H, O-H, N-H etc.) is broken and due to the size of the hydrogen atom, it can diffuse away preventing reformation of the covalent bond (Stenn and Bahr, 1970). When hydrogen bonding is present the adjacent covalent bond is weakened making it more susceptible to damage by radiolysis (Conroy et al., 2017). The weakening of the adjacent covalent bond was demonstrated in a study by Conroy et. al. using liquid cell TEM where the mineral boehmite (γ-AlOOH), a layered material that is structurally stabilised through hydrogen bonds, was exposed to electron irradiation and layers of the material were found to delaminate and dissolve (Conroy et al., 2017). In comparison, a similar mineral, gibbsite (γ-$Al(OH)_3$), showed no delamination or dissolution suggesting that in boehmite the hydrogen bonding network breaks down.

Further evidence supporting the weakening of adjacent covalent bonds comes from gamma irradiation experiments that showed significantly more hydrogen was released for boehmite as compared to gibbsite (Westbrook et al., 2015). This was also consistent with corresponding measurements of O-H stretch frequencies in IR spectroscopy, which indicated that the O-H bonds strength was weaker (i.e. lower wavenumber) in boehmite (3290 - 3085 cm^{-1}) compared to gibbsite (3463

- 3468 cm^{-1}), but the hydrogen bonding between structural units was stronger (Ingram-Jones et al., 1996; Ross and DeVore, 2008). This effectively implies that strong hydrogen bonding between molecular units weakens the neighbouring covalent bond (O-H, N-H etc.) making it more susceptible to radiolysis and break down of the structure leading to a negative correlation with the C_F. This could in principle be correlated to C_F for compounds in this study by determining the strength of O-H and N-H bonds of each compound.

Melting temperature (T_m) which had previously been shown to be correlated to the C_F for polymers was not correlated to C_F for these 20 compounds (Kumar and Adams, 1990). Previously, significant deviations for conjugated systems were observed when comparing C_F to T_m due to the fact that conjugated systems have little effect on increasing the T_m directly (which is related to the flexibility and mobility of a molecule), whereas conjugation increases the radiation resistance of a molecule (Kolb et al., 2010; Kumar and Adams, 1990). The majority of samples measured here contained at least one conjugated ring, possibly explaining why this set of data do not follow the same trend.

The number of halogens (nX) has also been previously shown to increase C_F; in the study by Clark et al. all hydrogens in copper phthalocyanine were substituted by F or Cl and the halogenated compounds showed increases in C_F (Clark et al., 1980). The substitution was thought to create a caging effect where the F and Cl atoms, due to their much larger size compared to hydrogen, sterically hindered the diffusion of molecules preventing/delaying radiation damage. Here no correlation was found between nX and C_F, possibly because the compounds that possessed either F or Cl (amcinonide, bicalutamide, celecoxib, dutasteride, efavirenz, felodipine, griseofulvin, indapamide and indomethacin) contained very few of these (between 1 and 6) compared to the number of hydrogens (9 - 35).

4.4.3 Multiple Linear Regression Model

From the molecular descriptors shown to be correlated to C_F, several MLR models were constructed using stepwise regression and judged based on the selection criteria mentioned in Section 4.3. This was done to generate potential models that would then be tested further to provide the best prediction for C_F. For each

Table 4.4: MLR equations to predict C_F for the most commonly generated models through stepwise regression when excluding one sample on each iteration. The MLR coefficients shown are averaged across all iterations. The RMSE and adjusted R^2 show how well each model compares.

Model	Equation	RMSE	Adjusted R^2	Frequency
1	$3.20 - 3.19HB_{d:a} - 0.27HB_{a:d} + 0.47C_{c:nc}$	1.91	0.47	36
2	$3.11 - 0.03rotB - 3.51HB_{d:a} - 0.28HB_{a:d} + 0.49C_{c:nc}$	1.89	0.44	12
3	$3.09 + 0.14C_c - 4.14HB_{d:a} - 0.26HB_{a:d}$	2.08	0.37	2
4	$1.08 + 0.50C_{c:nc}$	2.38	0.29	2
5	$2.15 - 0.34HB_d - 0.13HB_{a:d} + 0.48C_{c:nc}$	2.14	0.34	2
6	$0.32 - 1.58HB_d + 0.69HB_a + 3.90HB_{d:a} - 0.46HB_{a:d} + 0.53C_{c:nc}$	2.04	0.32	2

criterion, 20 different models were generated where one sample was excluded at each iteration. By excluding one sample during the iteration process the best-derived model equation sometimes changed, due to fitting a slightly different dataset.

The models that were derived more than once during each iteration are shown in Table 4.4. To find which of these gave the best fit for C_F. Further models were generated using the 'fitlm' function in MATLAB with the 'RobustOpts' turned on, in order to reduce the effects of extreme data points such as tolnaftate which has a C_F more than twice as large as the next highest compound. The root mean squared error (RMSE) and adjusted R^2 was then used to judge which of these models gave the best prediction for C_F. Out of all the potential models generated model 1 occurred most frequently and gave the best fit (adjusted R^2 0.49) along-side one of the smallest error values (RMSE 2.35). Three predictor variables are used in this model all of which are ratios; hydrogen bond donors to acceptors ($HB_{a:d}$), hydrogen bond acceptors to donors ($HB_{d:a}$) and conjugated carbons to non-conjugated carbons $C_{c:nc}$. Model 2 included rotB in addition to $C_{c:nc}$, $HB_{d:a}$ and $HB_{a:d}$. This gave a similar RMSE value to model 1 but decreased the adjusted R^2 value indicating a worse fit. $C_{c:nc}$ or C_c appeared in

every equation suggesting it is important to include information on conjugation when predicting C_F, although $C_{c:nc}$ did not provide an adequate prediction on its own, as shown in model 4 which had the highest RMSE (3.00) and lowest adjusted R^2 (0.28). Model 6 included a total of 5 predictor variables and had a higher RMSE and lower adjusted R^2 than models 1 and 2 which suggests that adding too many variables decreases the effectiveness of the model and that a sufficiently good prediction for C_F can be achieved using the predictor variables in model 1. The plot of predicted C_F against the experimental C_F using the equation for model 1 is shown in Figure 4.6a.

The three compounds that showed the highest error in predicted C_F (red points in Figure 4.6b) all contain no hydrogen bond donors, with tolnaftate having an experimental C_F of 13.0 $e^-/Å^2$ whilst being predicted at 5.7 $e^-/Å^2$. The

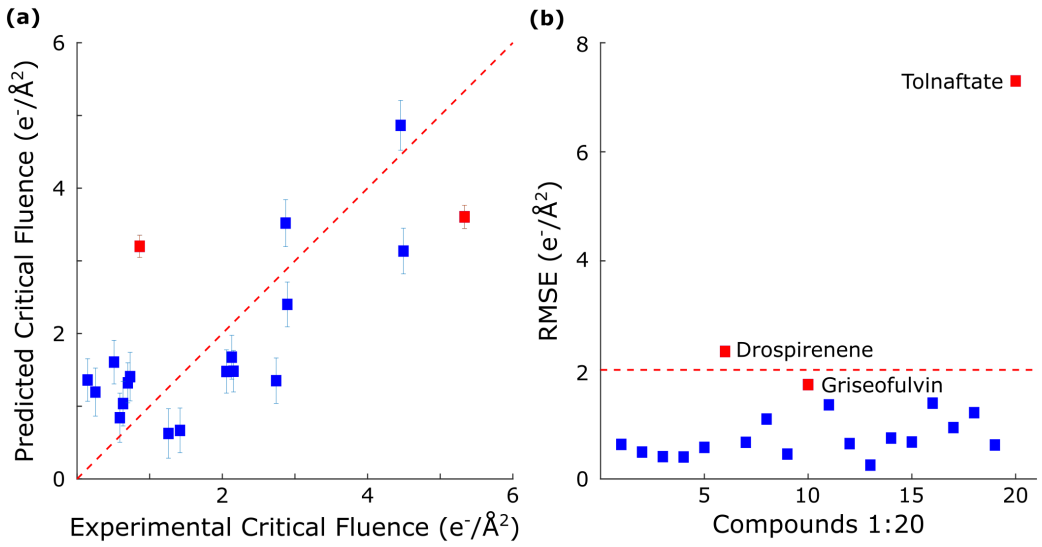

Figure 4.6: (a) Predicted C_F of each API, calculated using the regression equation in model 1 (Table 4.4) against experimental C_F. The error bars represent the standard error of the mean. Points shown in red are two of the APIs that are poorly predicted. The data point for tolnaftate is not shown on the graph as the experimental C_F is twice as large as the next highest compound. The red line is for y = x and shows how closely the model predicts C_F. (b) Root mean squared error of each compound for model 1, the points above the red dotted line are predicted outside an RMSE of ±2 and all contain no hydrogen bond acceptors.

relatively high electron beam stability of tolnaftate compared to other compounds may be due to a lack of hydrogen bonds and the presence of two fused benzene rings, only seen in tolnaftate, promoting large-scale charge and heat delocalisation across the whole molecule. The work presented here was only carried out with a limited number of samples most of which had C_F <5 $e^-/Å^2$ providing a very small representation of compounds that have a C_F >5 $e^-/Å^2$. This may be due to a disproportionate number of poorly water-soluble drugs having low C_F making it unlikely that less electron beam sensitive compounds would have been selected. The predictive model was tested on one other available poorly-water soluble compound, furosemide. Here the C_F was predicted at 6.2 $e^-/Å^2$ and found to be close to the subsequently determined experimental value of 7.1 $e^-/Å^2$, however, more compounds would be required to further determine the accuracy of the model on unseen APIs.

To improve the predictive capabilities of the model and to make it more widely applicable to other APIs, not just poorly water soluble, a larger sample that contained an even larger range of chemically diverse compounds would be required to build the model. In addition, descriptor variables that provide more detailed information regarding crystal structure, intermolecular bonding present and the reactivity of radicals that form during irradiation, may account for more variability within the data. This could provide further insights into the mechanisms/damage products of damage for individual APIs and a more accurate prediction of C_F, although the robustness of the predictive model would decrease due to the information required prior to the prediction regarding the API such as crystal structure.

4.4.4 Cooling Experiment

The results of the cooling experiments demonstrated an increase in C_F when measured at 160 K as opposed to room temperature, shown in Figure 4.7a. Compared to the C_F at room temperature, the electron beam stability of probucol increased by a factor 5, while felodipine and griseofulvin increase by a factor of

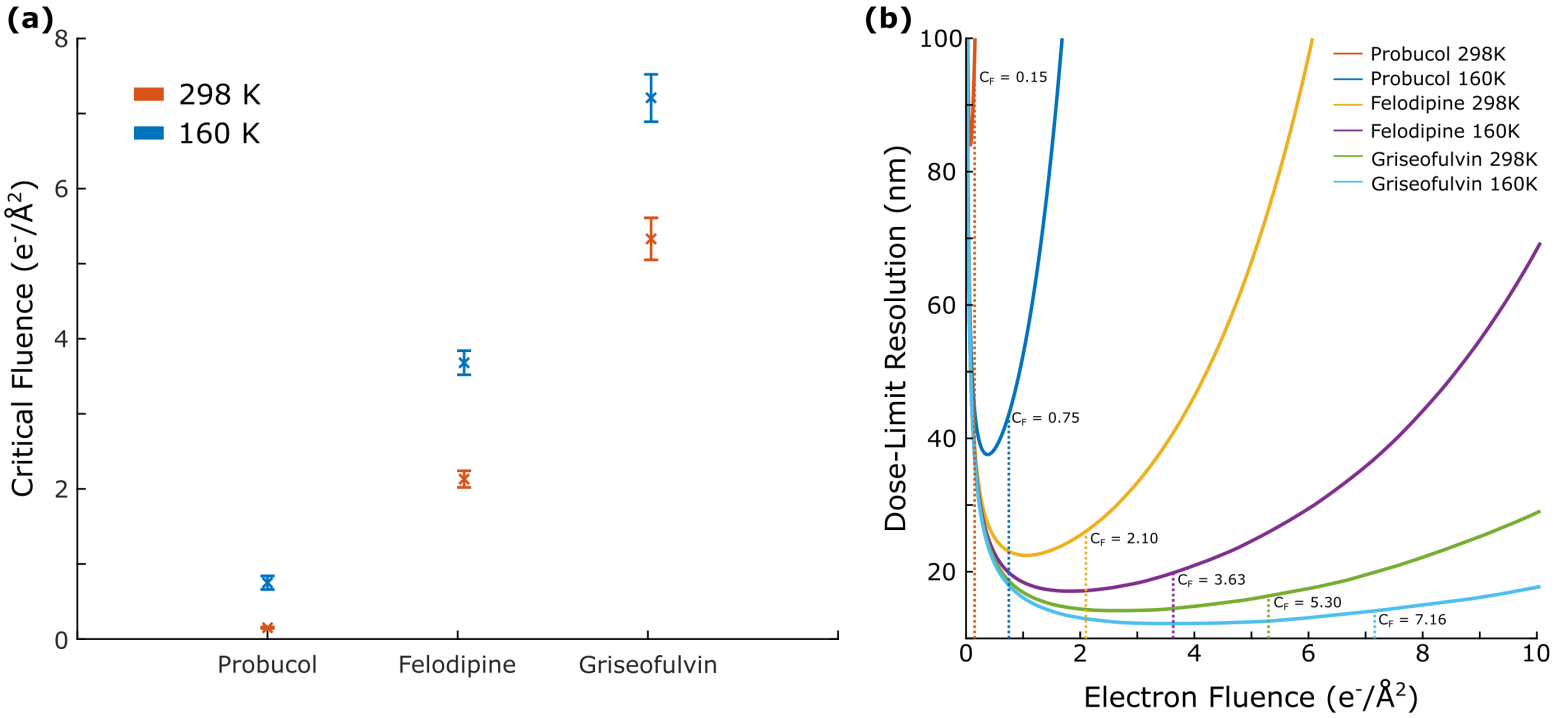

Figure 4.7: (a) Comparison of measured C_F and standard error of the mean for probucol, felodipine and griseofulvin at room temperature and cooled to 160 K. (b) Dose-limited resolution for each compound at room temperature and cooled to 160 K.

1.73 and 1.35 respectively. The increased stability due to lower temperatures are known to vary depending on the material and the experimental technique used to measure C_F (mass-loss, electron diffraction or EELS) (International Experimental Study Group, 1986). Although for more electron beam sensitive samples lower temperatures appear to provide a larger protection factor, which was observed here with probucol having a much higher cryoprotection factor than felodipine or griseofulvin (Egerton, 2013).

The energy transferred to the sample is known to be independent of the temperature (Egerton et al., 2004). Therefore reduced temperatures affect the chemical reactions that take place after primary electron excitation and diffusion of chemical species. Molecular fragments are produced by inelastic scattering of primary electrons and at reduced temperature the diffusion rate of these fragments decreases. The fragments may then become trapped by the slow diffusion of surrounding molecules (Knapek and Dubochet, 1980). The probability of a fraction of the broken bonds to reform between molecular fragments and the sites of breakage increases due to the slow diffusion rate, improving the healing effect of some of the broken covalent bonds (Knapek and Dubochet, 1980). It has been shown by Siegel (1972) and Egerton (1980) that the effects of cryoprotection are temporary and after heating the sample to room temperature further damage occurred without additional irradiation; most likely due to an increase in diffusion of these fragments that did not reform covalent bonds leading to mass loss.

The usefulness of increasing the C_F of a sample by decreasing the temperature can be shown by considering the dose-limited resolution (DLR), this being the maximum bright field TEM image resolution that is achievable for a thin sample exhibiting low contrast. When determining the dose-limited resolution many factors are involved, one of which is the C_F, shown in Equation 4.6.

$$DLR = (SNR)(DQE)^{-\frac{1}{2}}(FC_F/e)^{-\frac{1}{2}}(2)^{\frac{1}{2}}/|C| \tag{4.6}$$

$$F = e^{\frac{-t}{\lambda_e}} \tag{4.7}$$

where SNR is the signal to noise ratio and must equal or exceed some chosen background value, typically above 3 or 5σ to satisfy the Rose criterion; DQE is

the detector quantum efficiency and relates to the noise generated by the detector and signal from the sample; F is the collection efficiency of incident electrons to detected electrons (Equation 4.7), which depends on the sample thickness (t) and the mean free path of electrons (λ_e); e is the elementary charge of an electron and C is the contrast (Egerton, 2014). The contrast of a sample will generally decrease from the initial contrast (C_0), as seen from the fading of diffraction spots, causing δ to vary as the cumulative fluence increases. This change, in C, is generally approximated to an exponential decay, like the majority of diffraction spots measured here; the equation to calculate C when assuming an exponential decay is shown in Equation 4.8.

$$C = C_0 e^{\frac{Fluence}{C_F}} \tag{4.8}$$

DLR is also dependant on t and as seen in the equation for collection efficiency (F, Equation 4.7), when t is very thin ($<$ 10 nm) then F will be close to 1 and as t increases F becomes exponentially small. However, the increased amounts of elastic scattering event occurring in thick samples increases C and as t continues to increase C will remain relatively moderate compared to F. Therefore there is a balanced between F and C where a particular t will provide the best resolution. The optimum resolution also depends on the accelerating voltage since at higher accelerating voltages there is weaker elastic scattering (Egerton, 2014). This results in higher accelerating voltages providing more contrast in thicker samples, for example Egerton (2014) calculated that at 300 kV the optimum contrast is given at approximately 1μm. Lower accelerating voltages provides higher contrast for thin samples, however, the amount of damage will increase due to the increased inelastic scattering cross-section.

The DLR for all three compounds measured at both room temperature and at 160 K are shown in Figure 4.7b; this was calculated using their respective C_F at each temperature and the following values: SNR = 5; DQE = 0.5; C_0 = 0.1; t = 100 nm and λ_e = 150 nm. For probucol, the achievable resolution increased by approximately 45 nm while both felodipine and griseofulvin increased by approximately 5 nm and 2 nm respectively. In addition to increasing the DLR, increasing the C_F via cooling also increased the range of electron fluence values

where the resolution is at or close to the maximum. Assuming J is kept the same, more time is then available to acquire data, alternatively, it allows for a larger J to be used, increasing the brightness of the image. This is true for all samples but is most noticeable in probucol.

Although cooling increases the C_F and therefore resolution limits, it also introduced some experimental difficulties these being: an increased amount of sample drift due the temperature stability of the holder, a temperature differential exists between the hold and the rest of the vacuum column causing images to blur and the samples to drift outside the selected area aperture or field of view; vibrations caused by refilling the liquid nitrogen dewar, sometimes caused the holder to vibrate due to the liquid nitrogen boiling and reduced efficiency at collecting large amounts of data due to the time needed for the sample to reach the desired temperature and constantly requiring to refill the dewar to keep the temperature relatively stable. Therefore, depending on the aims of the experiment being conducted cooling is not always favourable; however, if resolution is the most important factor then cooling will both increase the dose-limited resolution and the time available for imaging.

The quality of the electron diffraction patterns and detection of diffraction spots against the background may effect the resulting measurements for C_F. Two strategies to improve these include the use of an imaging filter and the use of the latest generation of electron detectors, more specifically direct electron detectors; both of which may affect the observed intensity decay and lengthen the life of the crystal relative to the background signal. In the former case the imaging filter can eliminate or significantly reduce the effects of inelastic scattering in the electron diffraction pattern, which is particularly problematic for low Z materials such as these APIs. Yonekura et al. (2002) has previously used a imaging filter to remove the effects of inelastic scattering in 2-D proteins crystals. In the latter case improvements in the DQE of the detector will increase the signal-to-noise ratio (SNR) against the background allowing easier identification of diffraction spots at low electron fluence, also increasing the DLR for bright field images.

4.5 Chapter Summary

The aim of this chapter was to determine the C_F of a range of poorly water-soluble APIs and relate these measurements to the chemical structure. Thus allowing the creation of a predictive model that can be used to predict the C_F of other poorly water-soluble APIs through easy to obtain information on the chemical structure without relying on crystallographic information that may not be available for all APIs. From the results and discussion, it was found that:

- The C_F of 20 APIs were successfully measured using SAED with the majority having an average C_F below 5 $e^-/Å^2$, the most electron beam stable API, tolnaftate, had a C_F of 13 $e^-/Å^2$.
- The molecular descriptors with the highest positive correlation to C_F, found by PCA, were the number of aromatic rings, the number of conjugated carbons and the ratio of conjugated carbons to non-conjugated carbons.
- Descriptors that included hydrogen bond donors, hydrogen bond acceptors and rotatable bonds displayed the highest negative correlation.
- The negative correlation to C_F may be due to the removal of hydrogen atoms, via radiolysis causing destabilisation of hydrogen bonding networks within the crystal and loss of structural integrity.
- The number of halogen atoms and melting temperature which had previously been suggested to be correlated with C_F were shown to have no correlation for this set of compounds.
- The model that provided the best prediction of C_F included three predictor variables, these being ratios of conjugated carbons to non-conjugated carbons, the ratio of hydrogen bond donors to acceptors and the ratio of hydrogen bond acceptors to donors.
- Samples which contained no hydrogen bond acceptors gave the largest error when predicting C_F, which may be due to the lack of predictor variables that account for other potential mechanisms of electron beam damage.

- To further improve the accuracy of the predictive model a larger set of APIs could be included into the model, since the MATLAB scripts significantly reduces the data analysis time required for each API. Control over the sample thickness and use of imaging filters and direct electron detectors could provide more accurate measurements for C_F, which would then result in a more accurate model.

- Reducing the temperature of the sample increased the C_F and dose-limited resolution, with more sensitive APIs gaining a large cryoprotection factor than less beam sensitive compounds; however, the experimental method reduces the number of area/samples that can be analysed.

This chapter presents a robust model for predicting the C_F of poorly water-soluble drugs, without requiring crystallographic data, and is important for the establishment of electron fluence limits of the different APIs, mainly felodipine which is used in the following chapters. Knowing the C_F is important to ensure that low-levels of crystalline material, if present, are not destroyed before they can be detected by TEM and for determining the DLR. The following chapters will examine the use of TEM for the detection of low levels of crystallisation in amorphous solid dispersions prepared by both hot-melt extrusions and spraying at different drug loading levels, comparing the results to FTIR, DSC and pXRD.

Chapter 5

Comparison Between Preparation Methods and Drug Loadings in Amorphous Solid Dispersions

This chapter investigates four different amorphous solid dispersions (ASDs) in an attempt to detect nascent crystallinity occurring from the ASDs and understand the effects of preparation method and drug loading on the amount of recrystallisation that can be identified. The model system examined here was comprised of the API felodipine, previously examined in Chapter 4, and the copolymer copovidone. More information on these materials are detailed in sections 3.1.2 and 3.1.2 respectively. Hot-melt extrusion (HME) and spray drying (SD) were the two preparation methods used to produce ASDs at 15% and 30% drug loadings. Powder X-ray diffraction (pXRD), Fourier transform infrared spectroscopy (FTIR), differential scanning calorimetry (DSC) and TEM were all used to investigate chemical interactions between the API and polymer and if any amount of crystalline felodipine could be detected.

5.1 Sample preparation

5.1.1 Hot-Melt Extrusion

Amorphous solid dispersions of 15:85 and 30:70 w/w% of felodipine and copovidone were prepared via HME. Components were weighed on an analytical balance and added to a small sterilin pot. The API and polymer were then blended on a Turbula blender at 23 rpm for 4 minutes. Extrusion was carried out on a Thermofisher Haake Minilab II hot melt extruder using a barrel temperature and screw speed of 130°C and 30 rpm. The extrudate exited the extruder as a long rod which were cut into smaller sections and milled using a pepper grinder to form a powder. Each powder was then dried under vacuum and stored in a desiccator prior to use.

5.1.2 Spray Drying

Solvent based ASDs were prepared via SD. Two different solutions of felodipine and copovidone were formed by dissolving 15:85% w/w and 30:70% w/w of felodipine and copovidone in a mutually compatible solvent system of 20:80 v/v% of acetone and methanol.. Spray drying was performed using a Büchi Mini Spray Dryer B-290. The API/polymer solutions were spray dried using: an inlet temperature of 100°C; the aspirator and air flow set to 100% and the pump speed set to 30%. The spray dried solid dispersion material was isolated and dried in a vacuum oven at 40°C overnight and then stored in a desiccator prior to use.

5.2 Methods of analysis

5.2.1 Powder X-ray Diffraction

Each sample was mounted onto a silicon wafer and analysed using a PANalytical CubiX PRO diffractometer ($\lambda = 1.5418$ Å). Samples were measured in reflection geometry in θ - 2θ configuration over a 2θ scan range of 2° to 40° with 25 second exposure per 0.02° increment. The X-rays were generated by a copper long-fine focus tube operated at 45 kV and 40 mA. The samples were spun at 30

rpm to improve counting statistics. Powder diffraction patterns were collected to determine if any difference occurred between each ASD and as a method to check for crystallinity in general.

5.2.2 Fourier Transform Infrared Spectroscopy

A Thermo Scientific NicoletTM iSTM FTIR ATR spectrometer was used to collect all the FTIR spectra. Samples were placed onto the ATR crystal and pressed down using a clamp to provide good contact between the sample and crystal. Backgrounds were collected every 15 minutes and the spectra were obtained in % transmission mode between 600 - 4000 cm^{-1} at a resolution of 2 cm^{-1}. Data collection was repeated in triplicate for each sample. During analysis, the % transmission was converted to absorbance by using equation 5.1 to increase the ease of identifying weak signals in the presence of much stronger signals.

$$Absorbance = 2 - log(Transmission\%) \tag{5.1}$$

5.2.3 Differential Scanning Calorimetry

A Mettler Toledo DSC was used to collect all the data. Approximately 10 mg of sample was added to a 100 μl aluminium pan and was hermetically sealed. An empty aluminium 100 μl pan was used as a reference. Samples were heated from 30°C up to 200°C and then cooled back to 30°C under a nitrogen atmosphere using a temperature ramp rate of 10°C/min. This was carried out in triplicate. Measurements to determine melting temperatures plus the onset and midpoint of the glass transition temperature (T_g) of the dispersions was carried using the Mettler STARe evaluation software.

5.2.4 Transmission Electron Microscopy

Each sample was prepared by grinding the powder dry in a pestle and mortar to further reduce the size of the coarsely ground particles. The ground powder was then added to a 400 mesh continuous carbon-coated copper grid by gently touching the powder onto the grid. All samples were examined in a Tecnai F20

TEM/STEM operated at an accelerating voltage of 200 kV, equipped with a field emission gun using an extraction voltage of 4.5 kV. The images were captured using a Gatan Orius CCD camera with an exposure time of 2 - 3 seconds to increase the signal to noise ratio. Energy dispersion X-ray (EDX) spectra were collected using an Oxford Instrument 80mm X-Max SDD detector and processed using the AZtec software

A relatively large number of different areas (> 50) were examined for each sample in an attempt to try quantify and provide statistical analysis on the number of areas found to be crystalline and amorphous. Areas that had not been exposed to the electron beam were examined to limit any damage that occurred; an electron flux (J) between 0.014 and 0.023 $e^-/(Å^2\ s)$ was used. From the previous work felodipine had a C_F of $2.1 \pm 0.9\ e^-/Å^2$, therefore using the J previously stated each sample had approximately $60 - 150$ seconds of electron beam exposure before the C_F was reached.

Areas that appeared thin or containing diffraction contrast were examined, typically located on the edges of larger particles that were 500 nm - 3μm in size. A selected area aperture with a diameter of 1.1μm at the image plane was inserted around the region that visually appeared to be thin or diffracting and selected area electron diffraction (SAED) patterns were then acquired to identify if the sample was crystalline. Provided the sample had not damaged excessively, dark field (DF) images were collected by inserting an 2.9 mrad radius objective aperture around the most intense diffraction spot in the electron diffraction pattern. Once the diffraction pattern had completely faded J was increased to provide enough signal for EDX spectra to be collected to confirm the presence of felodipine via observation of a $Cl_{K\alpha}$ peak at 2.62 keV. In some cases the increased flux caused the particles to disappear from the field of view.

5.3 Results and Discussion

5.3.1 Powder X-ray Diffraction

Figure 5.1 shows a comparison between the experimentally measured diffraction pattern of felodipine (Figure 5.1a) and the simulated powder diffraction patterns of each of the known polymorphic forms (Figure 5.1 b-e). The software CrystalMaker was used to simulate each of the diffraction patterns. The measured pattern shows a number of sharp and distinct peaks most notably at 2θ angles of: 10.27°, 10.91°, 16.39°, 20.57°, 23.35°, 24.61°, 25.49°, 26.55°, 29.57° and 32.77°. These can be index to the 011, $\bar{1}11$, $\bar{1}21$, $\bar{2}21$, $\bar{3}12$, $12\bar{3}$, $22\bar{3}$, $\bar{3}21$, $13\bar{3}$ and 321 diffraction spacings in felodipine form I respectively.

Figure 5.2 shows the resulting powder diffraction patterns from pure copovidone and all of the ASDs. Copovidone exhibits two broad peaks at 2θ angles of 11.85 and 21.97, similarly the ASDs have an average peak position and standard deviations of $12.18 \pm 0.37°$ and $21.26 \pm 0.38°$. The characteristic peaks of crystalline felodipine were not observable in the samples prepared by HME or SD at all drug loading levels. This suggests that the crystalline felodipine starting material completely transforms into amorphous felodipine and is prevented from recrystallisation due to stabilisation from the polymer. However, if particles are microcrystalline or smaller the diffraction peaks broaden making it difficult for pXRD to differentiate between amorphous and microcrystalline materials; hence the need for further characterisation methods that can determine these differences such as DSC (Johari et al., 1990; Yu, 2001).

There is little difference between the diffraction patterns for each of the solid dispersions, although, the relative intensity in the second broad peak of the 30% SD mixture appears lower in comparison to the rest. When measured this peak has a relative intensity of 0.80 compared to 0.97, 0.92 and 0.94 for 30% HME, 15% SD and 15% HME respectively. This change in shape has previously been attributed to an increase in amorphous drug content by Bikiaris et al. (2005) when studying diffraction patterns of Hesperetin and PVP and comparing to physical mixtures where no change in shape was found.

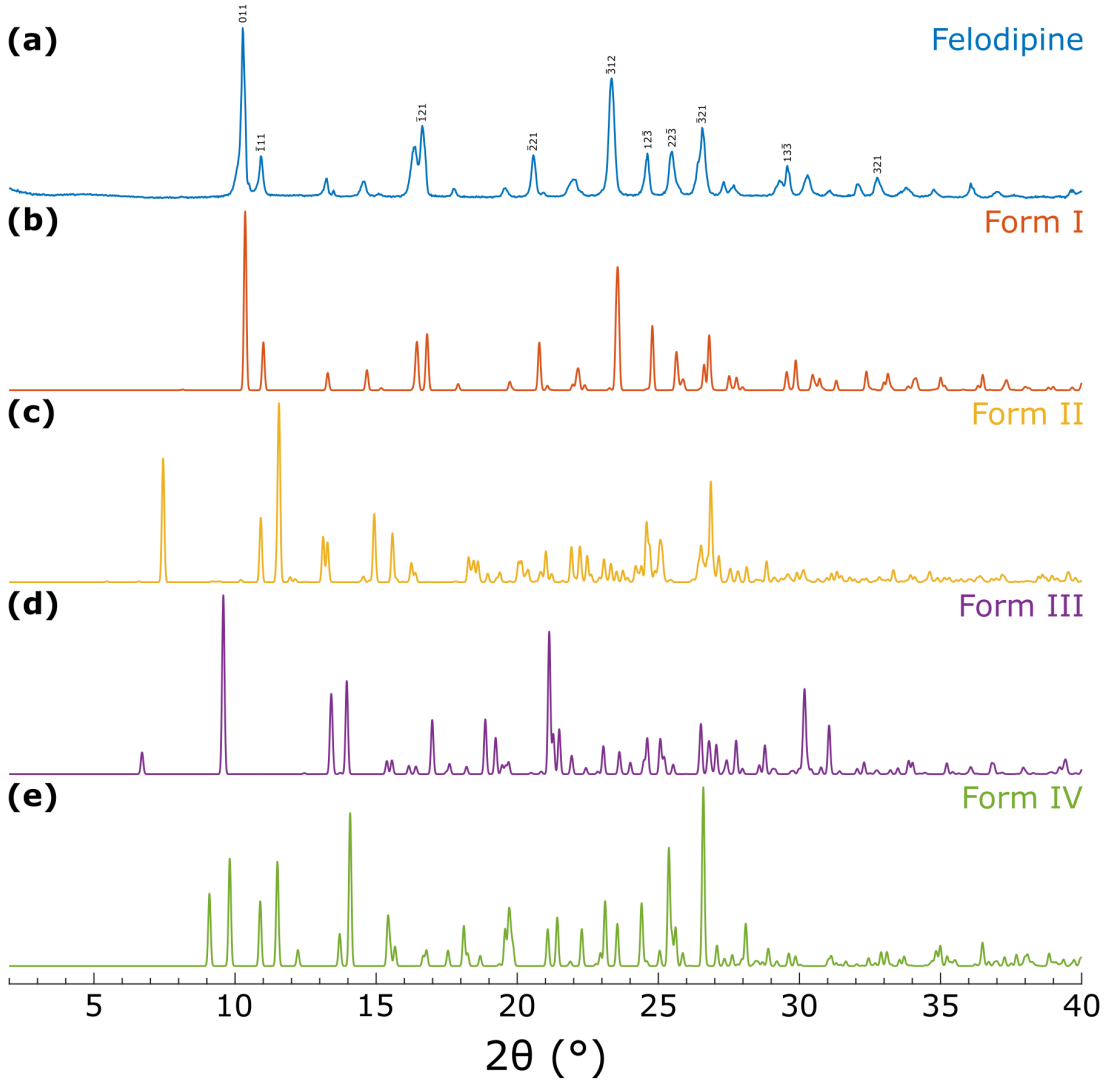

Figure 5.1: Diffractogram of pure crystalline felodipine and simulated powder diffraction patterns of each of the known polymorphs: (a) experimental data indexed to form I; (b) Most thermodynamically stable polymorph, form I; (c) form II; (d) form III; (e) form IV.

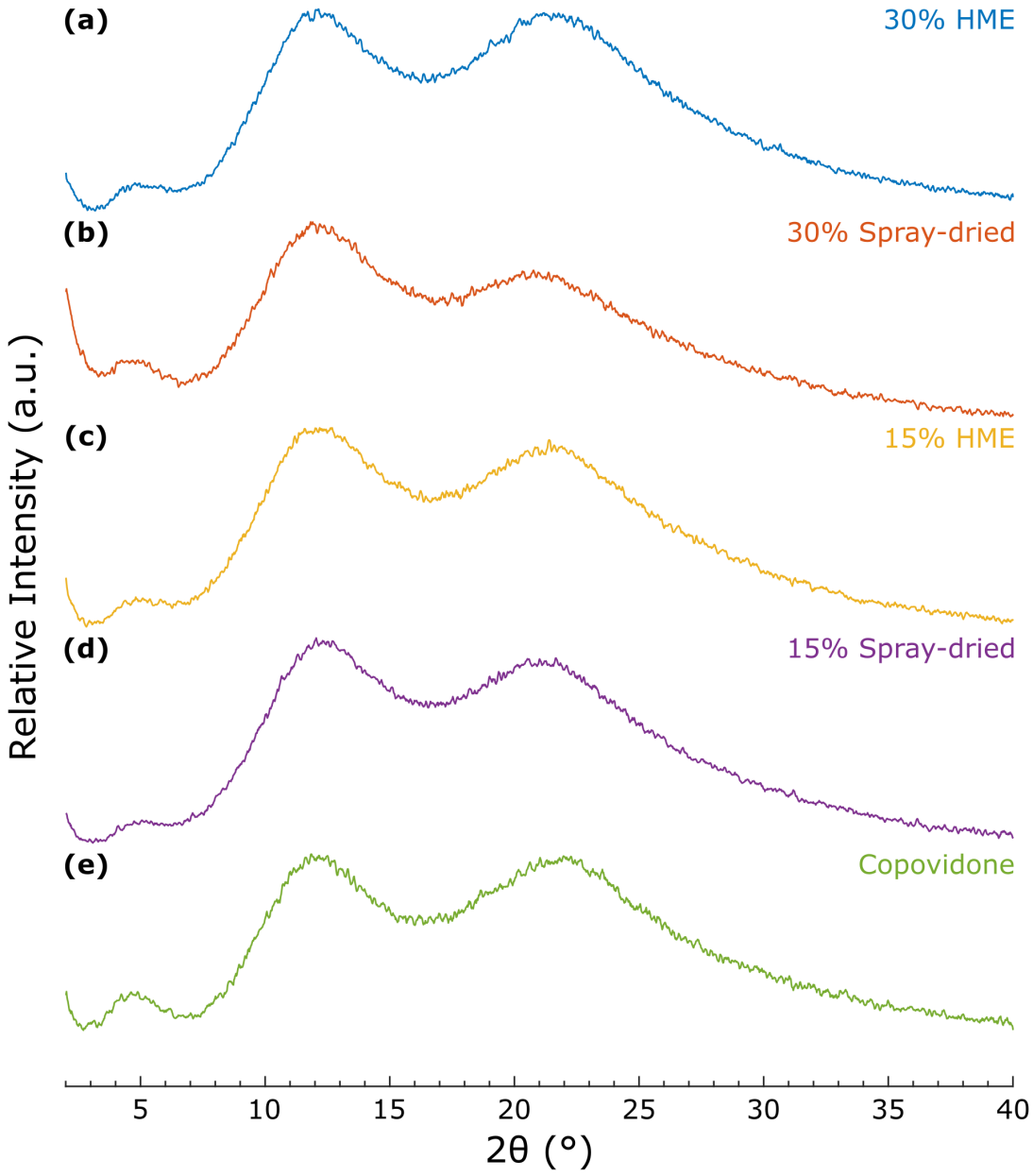

Figure 5.2: Diffractogram of copovidone and each ASD sample (a) 30% drug loading HME; (b) 30% drug loading SD; (c) 15% drug loading HME; (d) 15% drug loading SD; (e) copovidone.

5.3.2 Fourier Transform Infra-Red Spectroscopy

FTIR spectra were collected as a method to check for evidence of recrystallisation within the ASDs, differences between each sample and to examine the intermolecular interactions that occur between felodipine and copovidone. Felodipine contains a secondary amine group (N-H) and a carbonyl (C=O) group that are capable of acting as hydrogen bond donor and acceptor respectively, while copovidone contains C=O groups within the pyrrolidone ring and acetate group. Previous studies have shown that the N-H, O-H and C=O stretches are all sensitive to the strength of the hydrogen bond that is formed (Tang et al., 2002). Therefore, a detailed analysis of both the O-H/N-H and C=O regions of the spectra can be used to provide information regarding the interactions that are occurring between felodipine and copovidone in each ASD. Identifiable peaks for each sample were manually assigned to their corresponding bond vibration and are shown in Table 5.1.

Figure 5.3 shows the absorbance spectra against wavenumber between 3700 - 2700 cm^{-1} (O-H and N-H stretch region) for crystalline felodipine, copovidone and HME and SD at 15% and 30% drug loadings. A sharp peak in crystalline felodipine can be seen at 3367 cm^{-1} indicating a stretch in the N-H bond and has previously been shown to occur at 3370 cm^{-1} and 3373 cm^{-1} (Konno and Taylor, 2006; Pandey et al., 2016). Generally, a free N-H group that is not involved in any intermolecular interactions would be seen at around 3420 cm^{-1}, this red-shift of

Table 5.1: Identified peaks in the FTIR spectra for felodipine, copovidone (PVP/VA), 15% SD, 15% HME, 30% SD and 30% HME. All units are in cm^{-1}.

Vibration	Mode	Typical Range	FEL	PVP/VA	15% SD	15% HME	30% SD	30% HME
O-H	Stretch	3200 - 3500	-	3460	3444	3446	3437	3442
N-H	Stretch	3300 - 3400	3367	-	3295	3304	3295	3306
C-H	Stretch	$>$ 3000	3099	-	3099	3091	3093	3091
C-H	Stretch	$<$ 3000	2951	2953	2962	2949	2951	2951
C-O	Stretch	1735 - 1750	1687	1730	1732	1732	1732	1732
C-O	Stretch	1640 - 1690	-	1664	1659	1662	1659	1659
C-H	Bending	1350 - 1500	1493	1493	1495	1495	1495	1495
C-N	Stretch	1200 - 1350	1275	1232	1236	1236	1236	1236
C-Cl	Stretch	550 - 850	798	-	796	796	796	796

50 cm^{-1} indicates that the N-H group is part of a different bonding environment i.e. hydrogen bonding between the N-H and C=O groups (Skrovanek et al., 1985). Other studies have examined the FTIR spectra of amorphous felodipine which has a N-H stretch at 3340 cm^{-1} suggesting that the amorphous phase actually has, on average, stronger hydrogen bonds than the crystalline phase (Kestur and Taylor, 2010; Konno and Taylor, 2006; Song et al., 2013; Tang et al., 2002). This has been observed for a number of other compounds and has been suggested that the difference between crystalline and amorphous hydrogen bonding is due to constraints that the crystal packing imposes (Eerdenbrugh and Taylor., 2011).

Copovidone and all the ASD systems exhibit a broad absorption band approximately between 3700 - 3100 cm^{-1}, this band is similar to the O-H stretch that is observed when O-H groups are involved in hydrogen bonding. However, neither felodipine or copovidone contain O-H groups. This can be explained due to copovidone being hygroscopic, meaning it tends to absorb moisture from the air and the absorption bands are a result of latent water that has been absorbed by the polymer. The maxima for these bands are at 3460, 3444, 3446, 3437 and 3442 cm^{-1} for copovidone, 15% SD, 15% HME, 30% SD and 30% HME respectively, and are shown in Table 5.1. Each sample shows a different maximum peak for the O-H stretch which decreases by 13 - 18 cm^{-1} between copovidone and the ASDs. A red-shift in peak position suggests that a stronger bond is present and, in this case, it indicates an increase in strength of the hydrogen bonds formed by the O-H group. Smaller differences in peak position also occur between the different drug loading levels and preparation methods, with the higher drug loadings and spray-dried samples causing the largest red-shift.

Another broad, but weakly absorbing peak can be seen on the shoulder of the O-H band in the ASD samples, towards the lower wavenumber side, at approximately 3300 cm^{-1}. This peak can be attributed to the N-H stretch in the solid dispersions and red-shifts, by 35 - 45 cm^{-1} in relation to the amorphous felodipine - felodipine hydrogen bonds, indicating the N-H group forms stronger hydrogen bonds between felodipine - copovidone. The 15% and 30% SD mixtures exhibit peaks at 3295 cm^{-1} while the HME samples display peaks at 3304 cm^{-1} and 3306 cm^{-1} for drug loadings of 15% and 30% respectively, suggesting that the SD solid dispersion possesses a slightly stronger hydrogen bond.

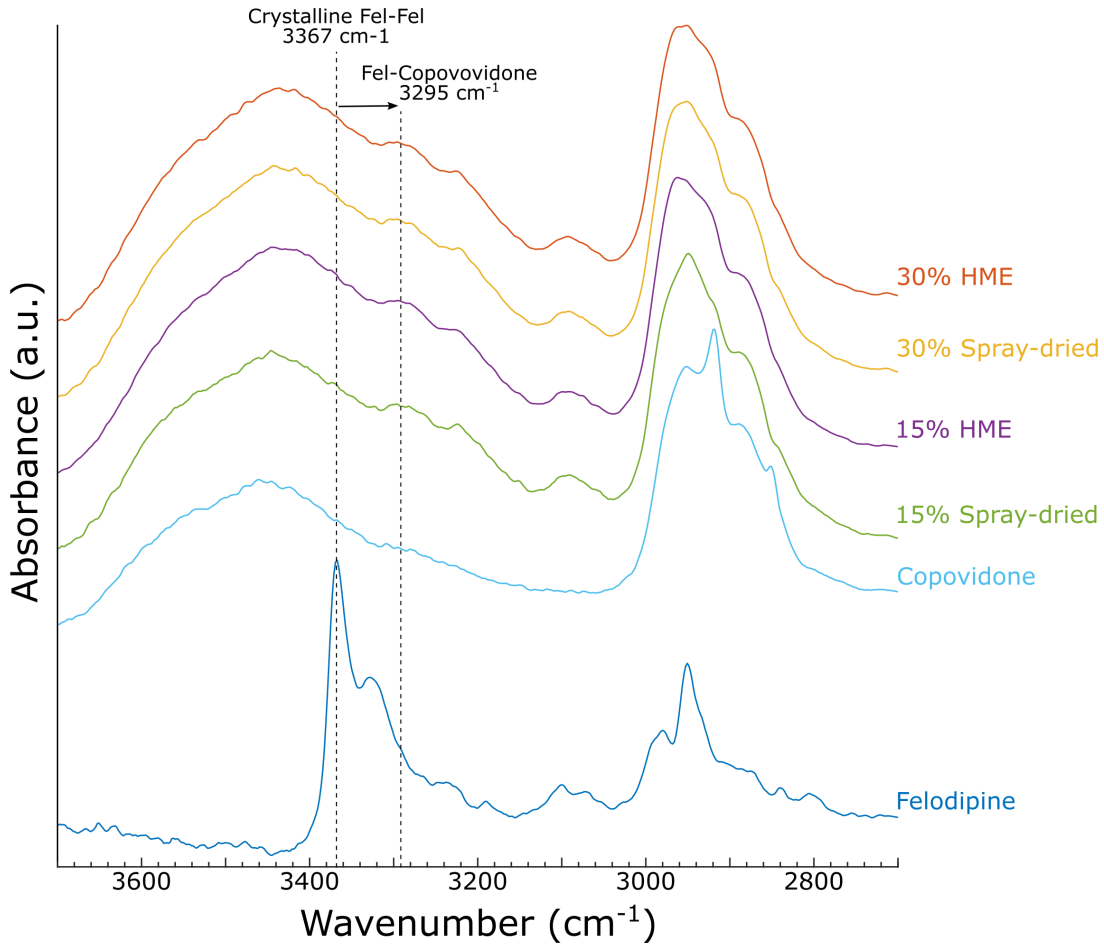

Figure 5.3: Absorbance spectra of felodipine, copovidone and amorphous solid dispersions between 2700 - 3700 cm^{-1}. Crystalline felodipine shows an N-H stretch at 3367 cm^{-1}, this peak is shifted to 3295 cm^{-1} in the solid dispersion samples.

A study by Konno and Taylor (2006) demonstrated that this peak at approximately 3300 cm^{-1} increased in absorbance as the concentration of PVP was varied between 0% and 70%. Similarly Kestur and Taylor (2010) showed in the felodipine/copovidone system prepared by rotary evaporation that as the polymer concentration increased the 3340 cm^{-1} peak from the amorphous felodipine-felodipine interactions decreased in intensity and broadened towards the lower wavenumber side and the shoulder peak at around 3290 cm^{-1} increased in inten-

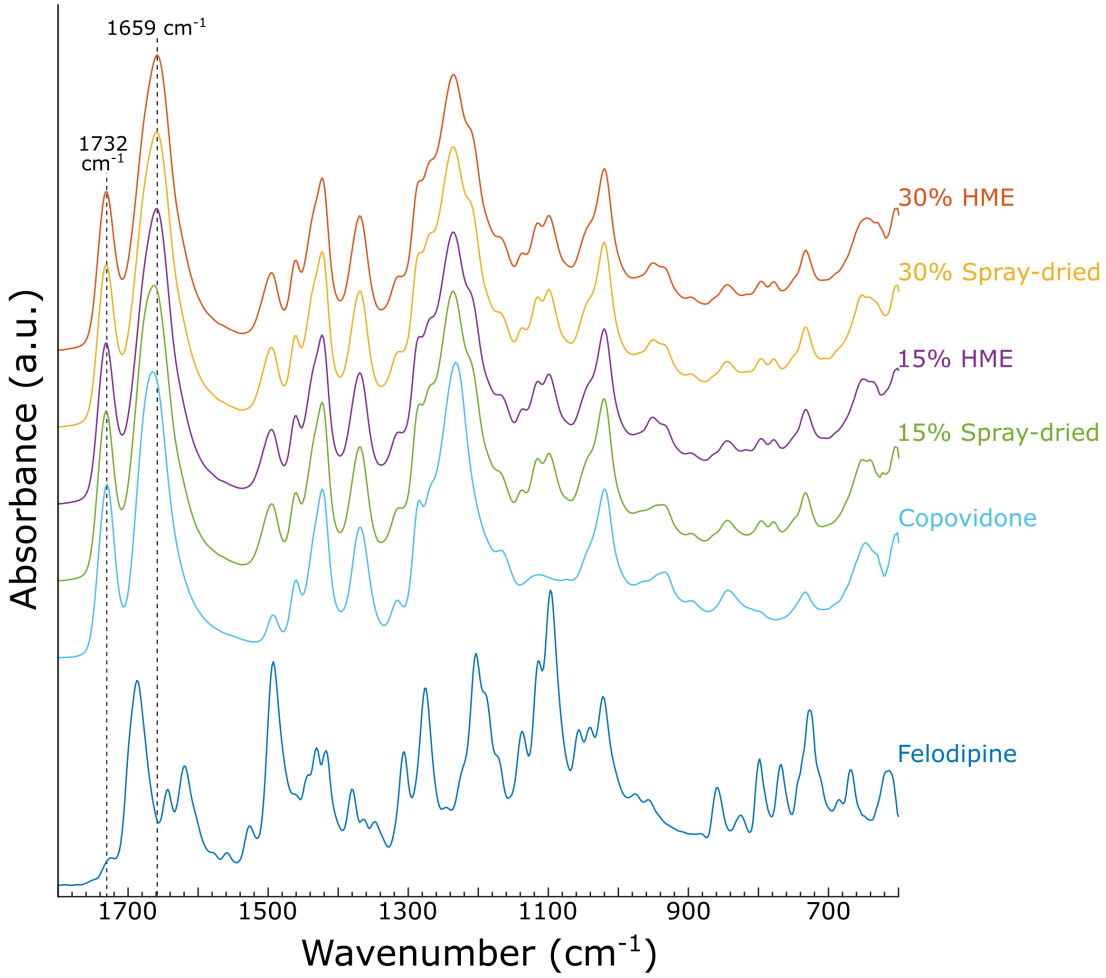

Figure 5.4: Absorbance spectra of felodipine, copovidone and amorphous solid dispersions between 600 - 1800 cm^{-1}.

sity. Here the 3340 cm^{-1} absorption is not observed in any samples suggesting that all the felodipine is bonded with copovidone, or that the broad O-H band is obscuring this peak. Although there is a small broad peak on the shoulder of the N-H stretch in felodipine at 3320 cm^{-1} which was not characterised to any specific bond vibration and is not observed in other spectra for felodipine. The intensity of the felodipine-copovidone interaction does not vary much with increased polymer concentration and is similar for all samples, despite the change in polymer concentration.

In the C=O bond range shown in Figure 5.4, felodipine shows a single peak at 1687 cm^{-1}. This peak is due to the C=O stretch from the ester groups and is typically seen between 1735 - 1750 cm^{-1} but is red-shifted due to hydrogen bonding. In copovidone there are two strongly absorbing broad peaks at around 1732 cm^{-1} and 1659 cm^{-1}, these peaks are derived from the C=O groups in the acetate and pyrrolidone ring structure respectively. Both act as hydrogen bond acceptors, however, the N-H group in felodipine should preferentially form hydrogen bonds with the C=O in the pyrrolidone ring due to this being a stronger hydrogen bond acceptor compare to the acetate group (Kestur and Taylor, 2010; Song et al., 2013; Taylor et al., 2001). There is a small red-shift between the ASDs and copovidone (2 - 5 cm^{-1}) but due to the broad absorption peak of copovidone in this region the peak is obscured, similar to the findings of previous studies examining the same drug/polymer system (Karavas et al., 2008; Kestur and Taylor, 2010; Song et al., 2013).

5.3.3 Differential Scanning Calorimetry

DSC traces were collected as a method to detect evidence of recrystallisation and miscibility between API/polymer mixtures by examining the thermal events that occur. If the sample is crystalline a sharp endothermic peak will be detected indicating a crystalline solid melting. Whereas if the sample is amorphous this peak will be absent and a glass transition (at a temperature T_g) will be be observed as a step change from the baseline across a broad range of temperatures; due to a change in the specific heat capacity and T_g being a second order phase transition. If two components in the same sample are miscible then a single T_g is regarded as evidence for the formation of a glassy material. The T_g of a miscible API and polymer will be found at an intermediate value between the T_g of the pure API and the polymer. When two T_g features are present the samples are phase separated and are not miscible, the two T_g values correspond to the separated polymer rich and API rich domains (Karavas et al., 2005).

Figure 5.5a shows the first DSC traces for each of the ASD samples and felodipine. Felodipine displays a strong endothermic peak at 149.7°C, this is similar to the value of 145°C previously reported by Song et al. (2013) as the

melting point of felodipine. In the 30% SD, 15% SD, 30% HME and 15% HME a broad and large endothermic peak is visible at 82°C, 83.3°C, 80°C and 82°C respectively. These peaks appear to be larger in both of the 15% drug loading samples when compared to the 30% sample. This is most likely due to the increase in polymer concentration allowing a larger quantity of water vapour to be absorbed by the polymer, which is then evaporated off as the temperature increases; also obscuring the T_g. In the subsequent scans (Figure 5.5b and c) these peaks are no longer visible suggesting that the majority of the absorbed water had been removed from the sample.

Upon the second heating of felodipine the melting point at 149.7°C was no longer apparent, indicating a phase transformation from crystalline to amorphous. An apparent melt of felodipine occurred at 49.8°C, although, this is more likely a result of an enthalpy relaxation around the T_g of amorphous felodipine. This relaxation peak can occur due to stress in the material due to processing, handling, storage or thermal history as the material is heated through its glass transition temperature (Thomas, 2015). The T_g of amorphous felodipine can be measured in runs two and three at 45.0°C, which is the same as found in previous studies (Song et al., 2013). All solid dispersion samples in runs two and three exhibited a single T_g, between the T_g of amorphous felodipine (49.8°C) and copovidone (106°C measured by Patterson et al. (2008)) suggesting the two materials are miscible. The T_g midpoint for each sample was measured at 95.1 ± 0.5°C, 88.3 ± 0.1°C, 98.4 ± 0.3°C and 88.7 ± 0.2°C in the 15% HME, 30% HME, 15% SD and 30% SD, respectively, indicating that amorphous felodipine and copovidone are intimately mixed into a single phase. All measured T_g values can be found in Table 5.2. The difference in the T_g between different drug loadings can be modelled by the Gordon-Taylor equation (Equation 5.2). Here the T_g of a two-component system is estimated based on the weight fraction (w_1 and w_2) of each component and their respective T_g values. This prediction assumes that the two components are miscible and the free volumes of the components are additive (Gordon and Taylor, 1952; Simha and Boyer, 1962)

$$T_{g(mix)} = \frac{w_1 T_{g1} + K w_2 T_{g2}}{w_1 + K w_2} \tag{5.2}$$

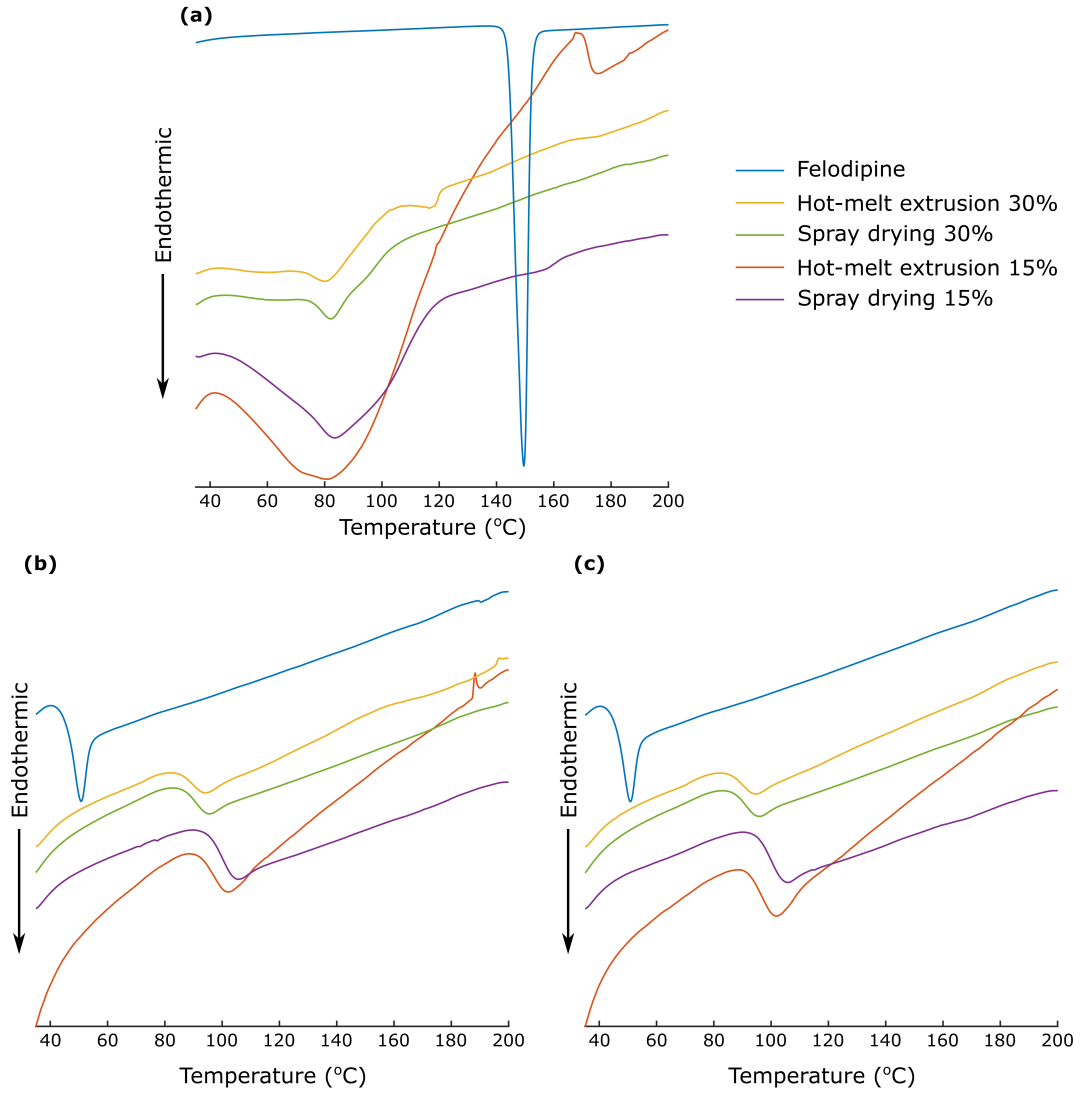

Figure 5.5: DSC traces for felodipine, 30% drug loading HME, 30% drug loading SD, 15% drug loading HME and 15% drug loading SD (a) first run; (b) second run; (c) third run.

The constant K is calculated from the equation shown in Equation 5.3; here the product of the density (ρ) and the T_g of the two components one and two are taken as ratios to calculate K.

$$K = \frac{T_{g1}\rho_1}{T_{g2}\rho_2} \tag{5.3}$$

Table 5.2: Onset, midpoint and predicted T_g for each solid dispersion and pure felodipine. All T_g are reported in °C.

Drug loading (%)	Hot-melt extrusion		Spray drying		G-T Pred
	T_g Onset	T_g Mid	T_g Onset	T_g Mid	T_g
0	-	106*	-	106*	-
15	88.6 ± 0.0	95.1 ± 0.5	92.1 ± 0.6	98.4 ± 0.3	89.5
30	82.6 ± 0.4	88.3 ± 0.1	83.5 ± 0.2	88.7 ± 0.2	77.1
100	44.7 ± 0.1	45.0	44.7± 0.1	45.0	-

* T_g of copovidone reported by Patterson et al. (2008).

$T_{g(mix)}$ was calculated as 89.5°C and 77.0°C for the 15% and 30% drug loading mixtures respectively using previously reported values for: T_g of copovidone measured by Patterson et al. (2008) as 106°C; the density of amorphous felodipine measured by Konno and Taylor (2006) as 1.33 g/cm^3 and the density of copovidone measured by Six et al. (2004) as 1.19 g/cm^3. The measured T_g for each sample deviates positively with the values predicted by the Gordon-Taylor equation by approximately 10°C in each drug loading. Deviations between the calculated and measured T_g values for different API/polymer mixtures has been previously reported by Forster et al. (2001); Patterson et al. (2007); Taylor and Zografi (1998). From these results, Patterson et al. (2007) indicated the deviation from the predicted T_g is compound specific and occurred irrespective of the preparation technique employed. The direction and amount of deviation that arises have been attributed to intermolecular hydrogen bonds between the polymer and API and the number/strength of these bonds, suggesting a change in stability of the amorphous felodipine (Patterson et al., 2007; Taylor and Zografi, 1998).

5.3.4 Transmission Electron Microscopy

15% Hot-melt extrusion

Two regions of crystalline felodipine were identified out of a total of 55 that were examined in the 15% HME sample, the results are shown in Figure 5.6 and 5.7. Figure 5.6a shows the region of interest of the first crystalline area to be identified and the selected area that the electron diffraction pattern was collected

from. This region appears to contain a number of smaller particles that had agglomerated together with dimensions of approximately 2 μm × 3 μm. The SAED pattern in Figure 5.6b was collected using an electron flux of 0.014 $e^-/(Å^2$ s) and is polycrystalline indicating that multiple crystals in different orientations are present.

The d-spacings were measured using the radial profile plugin in ImageJ, which produces a profile plot of normalised integrated intensities as a function of the radial distance around a concentric circle from a point in the image. In this case, the centre was the zero order diffraction spot. From the radial profile (Figure 5.6c) nine distinct d-spacings can be identified, all of which can be assigned to d-spacings in felodipine form I, II or IV. The radial distances are also shown on the SAED pattern with ring one being the nearest to the centre and ring nine the furthest. Two additional diffraction spots with d-spacings of 1.05 nm and 0.84 nm, similar to $\bar{1}12$ and $22\bar{3}$ spacings in form II or $\bar{1}01$ and 012 spacings in form IV appear to be present within the diffraction pattern. However, these were not identifiable by the radial profile due to their low intensity against the high-intensity background signal. The radial distances, measured d-spacings, theoretical d-spacings of forms I, II and IV felodipine and their respective hkl values are summarised in Table 5.3.

Although all the measured spacings possessed similar values to ones within form I (average error of 1.2%), the percentage error between the measured and theoretical values ranged by a total of 6%. When compared to forms II and IV the error varied between 1% in form II and 0.9% in form IV, suggesting that the sample is more likely to be either form II or IV rather than form I due to the narrower error range. This is interesting considering form I is the most thermodynamically stable of the all the polymorphs at ambient conditions (Surov et al., 2012). Forms II and III are known to be less stable and have a monotropic relationship with form I, meaning that once a transformation occurs it is irreversible. While forms I and IV are enantiotropic and can reversibly change between the two; form IV is more stable at conditions above 87.6°C (Surov et al., 2012; Wang et al., 2015).

After the sample had been exposed to an electron fluence of approximately 3 - 3.5 $e^-/Å^2$ the diffraction spots completely faded (Figure 5.6e). At increased

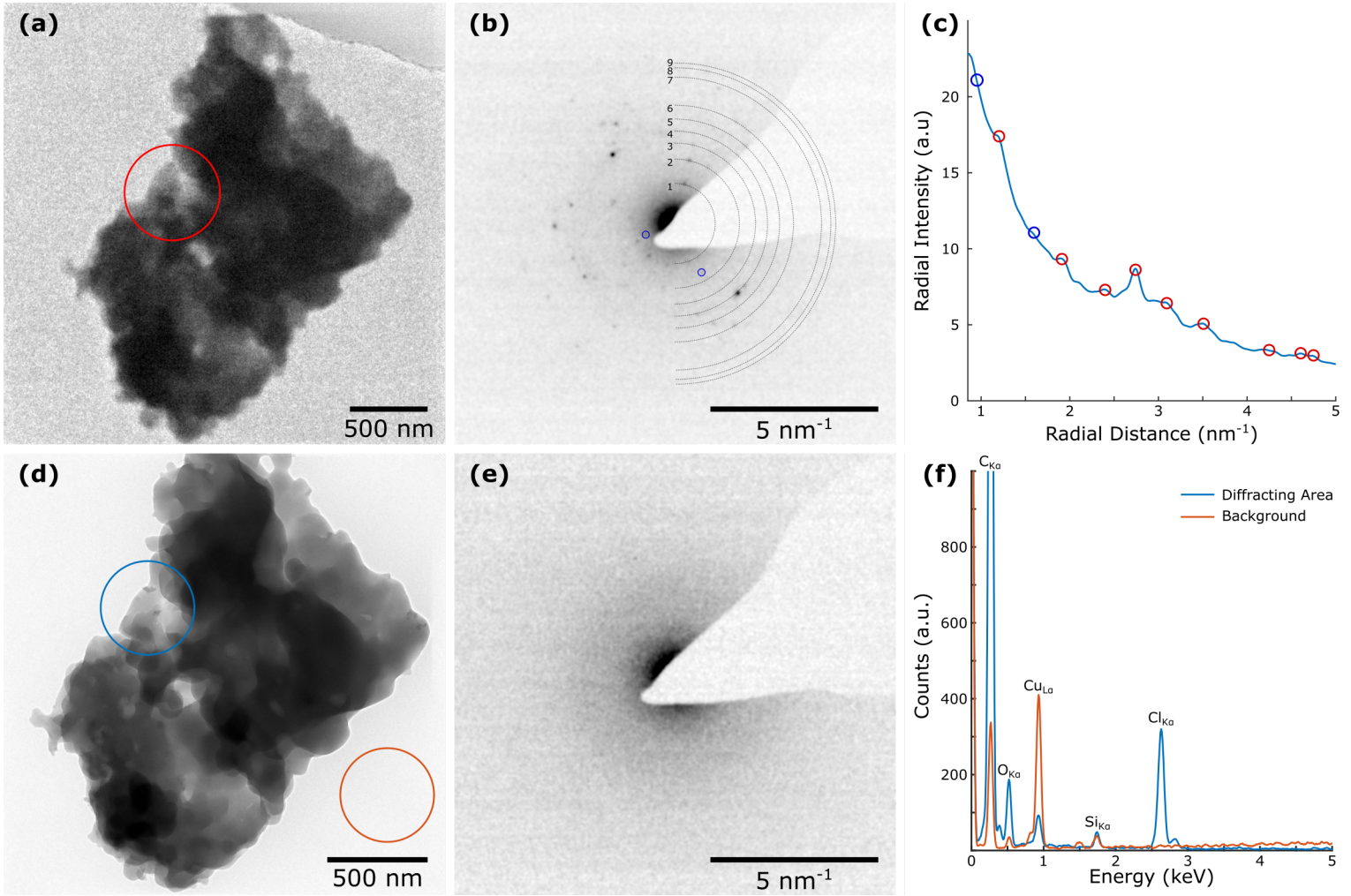

Figure 5.6: (a) Low fluence BF image of 15% HME sample taken using an electron flux of 0.014 $e^-/(Å^2\ s)$; (b) SAED of highlighted region,showing the radial distances of each diffraction spot; (c) Radial profile around the zero order diffraction spot; (d) BF image captured of the same region using higher electron flux; (e) Faded SAED of the same area showing loss of crystalline structure; (f) EDX spectra of diffracting area and the carbon film background.

Table 5.3: Radial profile measurements from Figure 5.6c comparing to possible spacings in felodipine forms I, II and IV. Average percentage error between the measured and theoretical values are 1.2 ± 1.2, 8.5 ± 0.3 and 8.1 ± 0.4 for forms I, II and IV respectively.

Spot	**Distance** (nm^{-1})	**d-spacing** (nm)	**d-spacing (nm)**			**hkl**		
			I	II	IV	I	II	IV
-	0.95*	1.05	1.09	0.96	0.97	100	$\bar{1}12$	$\bar{1}01$
1	1.19	0.84	0.85	0.77	0.77	011	$\bar{2}21$	$\bar{1}11$
-	1.60*	0.63	0.60	0.57	0.57	020	$22\bar{3}$	012
2	1.91	0.52	0.53	0.48	0.49	120	224	$\bar{2}02$
3	2.39	0.42	0.43	0.39	0.38	022	$\bar{8}02$	$\bar{2}22$
4	2.74	0.37	0.36	0.33	0.33	$\bar{1}23$	$\bar{5}16$	$\bar{2}31$
5	3.09	0.32	0.32	0.30	0.30	212	137	$\bar{1}24$
6	3.50	0.29	0.29	0.26	0.26	$\bar{4}11$	916	$\bar{1}34$
7	4.33	0.23	0.23	0.21	0.21	$\bar{5}04$	848	431
8	4.60	0.22	0.22	0.20	0.20	500	882	045
9	4.74	0.21	0.21	0.19	0.19	412	71 11	244

* low radial intensity difficult to distinguish from the high intensity background close to the zero order diffraction spot (highlighted as blue circles) .

electron fluence the same area also shrunk in size from 3.08 μm^2 to 2.38 μm^2 in Figure 5.6a and in Figure 5.6d respectively. This further indicates damage to the sample and suggests the potential for mass loss of lighter elements. Figure 5.6d was obtained utilising a greater electron flux, improving the signal to noise ratio and allowing small particles with an average height and width of 55 ± 16 nm and 39 ± 7 nm to be identified. These particles can be observed within the diffracting area and the right-hand-side edge of the larger agglomerated area.

Figure 5.6f shows the EDX spectra from the diffracting area (blue circle), that contained a number of the small particles and confirms that this area contained felodipine, due to the $Cl_{K\alpha}$ peak at 2.62 keV. Whereas the background spectrum taken from the carbon film displayed no $Cl_{K\alpha}$ peak (red circle).

Figure 5.7a displays a low fluence BF image of the region of interest of the second crystalline area taken with an electron flux of 0.014 $e^-/(Å^2\ s)$. This region contains a particle with dimensions of approximately 2 $\mu m \times 0.75$ μm and appears less agglomerated than the previous region. Similar to the first area, the diffraction pattern in Figure 5.7c, is polycrystalline producing multiple diffuse spots with high intensities. The radial profile for this diffraction pattern is

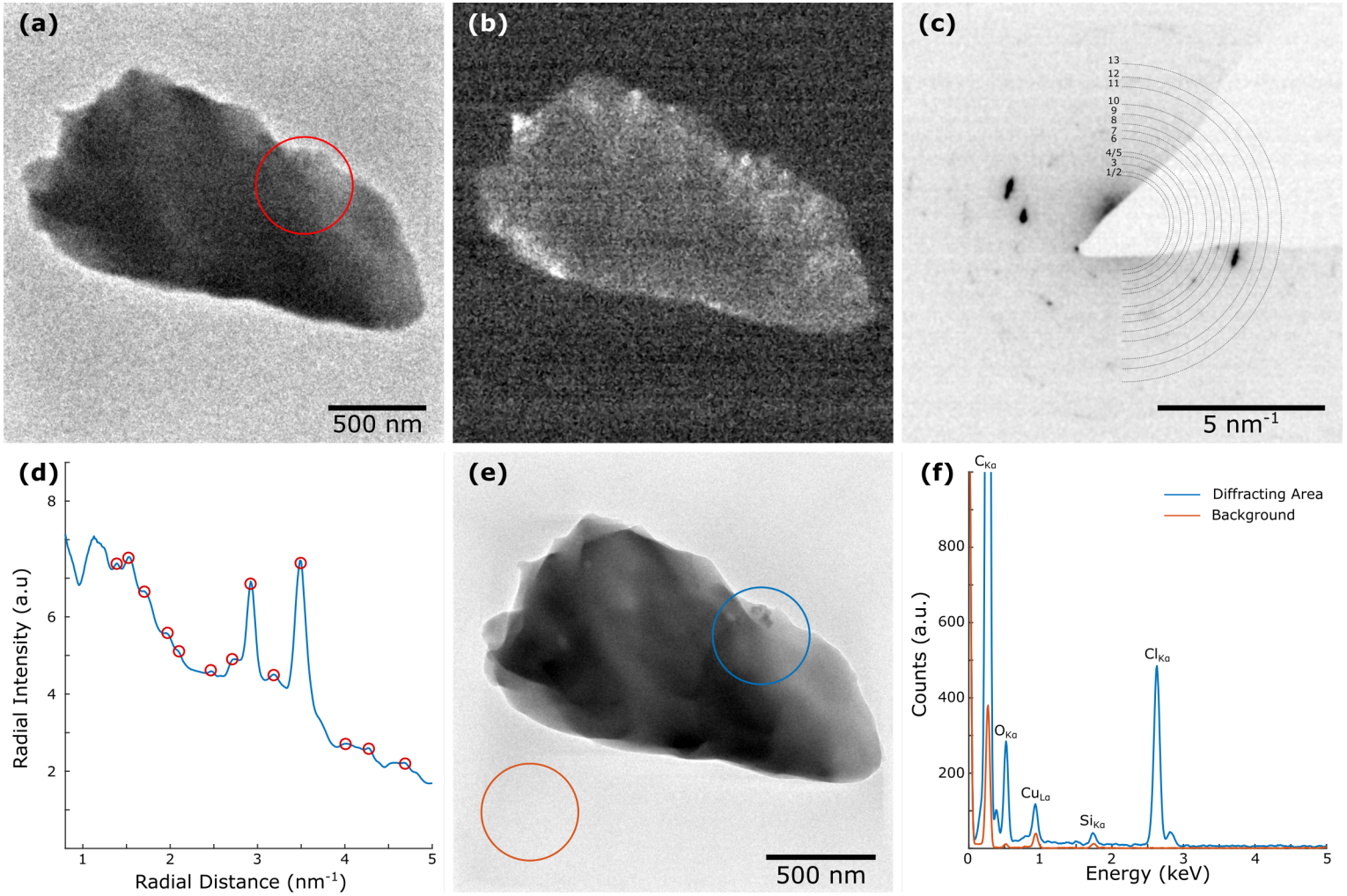

Figure 5.7: (a) Low fluence BF image of 15% HME sample taken using an electron flux of 0.014 $e^-/(Å^2\ s)$; (b) DF image; (c) SAED of highlighted region,showing the radial distances of each diffraction spot; (d) Radial profile around the zero order diffraction spot; (e) high fluence BF image; (f) EDX spectra of diffracting area and the carbon film background.

Table 5.4: Measurements taken from the radial profile from Figure 5.7d comparing to possible spacings in felodipine forms II, III and IV. Average percentage error between the measured and theoretical d-spacings are 7.9 ± 0.3, 2.0 ± 0.6 and 1.6 ± 0.6 for forms II, III and IV respectively.

Spot	**Distance** ($\mathbf{nm^{-1}}$)	**d-spacing** (nm)	**d-spacing (nm)**			**hkl**		
			II	III	IV	II	III	IV
1	1.39	0.72	0.66	0.71	0.72	402	200	101
2	1.53	0.65	0.60	0.63	0.65	313	$\bar{1}11$	002
3	1.73	0.58	0.53	0.57	0.57	$\bar{3}31$	111	$\bar{1}12$
4	1.98	0.51	0.47	0.49	0.50	620	$\bar{2}12$	$\bar{2}11$
5	2.10	0.48	0.44	0.47	0.47	711	112	121
6	2.48	0.40	0.37	0.40	0.40	150	310	031
7	2.73	0.37	0.34	0.36	0.36	$\bar{1}53$	311	131
8	2.92	0.34	0.32	0.34	0.33	317	$\bar{3}14$	$\bar{2}23$
9	3.20	0.31	0.29	0.31	0.31	933	221	311
10	3.49	0.29	0.26	0.28	0.28	$\bar{6}62$	313	042
11	4.01	0.25	0.23	0.24	0.24	082	$\bar{6}04$	$\bar{1}50$
12	4.29	0.23	0.22	0.23	0.23	773	125	$\bar{2}51$
13	4.69	0.21	0.20	0.21	0.21	$\bar{6}85$	331	333

presented in Figure 5.7d and rings eight and ten correspond to these high-intensity spots with d-spacings of 0.34 nm and 0.29 nm respectively. Likewise in the first crystal, the measured d-spacings can be indexed to multiple polymorphs of felodipine; in this case forms II, III and IV provide the best match with the smallest consistent percentage errors. The radial distances, d-spacings and hkl values for forms II, III and IV are all summarised in Table 5.4. Total loss of diffraction spot intensities occurred after the area had been exposed to a cumulative electron fluence of 3 - 3.5 $e^-/Å^2$. The overall area of the larger particle also decreased from 1.679 μm^2 to 1.387 μm^2 between image 5.7a and 5.7e, suggesting a loss of mass from lighter elements.

In the BF image obtained at an increased electron flux (Figure 5.7e), small particles can again be seen within the selected area. Figure 5.7b displays a DF image of the second crystal with bright areas indicating crystals that are in similar orientations; highlighting these small particles. Most crystalline areas appear on the edges of the larger particle, possibly due to an increase in thickness toward the centre or the preferential nucleation and growth of the crystals along the edges. The size distribution of the particles identifiable in the DF image varies

between 33 ± 23 nm $\times$ 36 ± 27 nm, similar to the size of the crystals found in the first area. Furthermore, parts of the larger particle in the higher fluence BF image (Figure 5.7d) appear faceted, suggesting crystallinity, although any crystal structure that was previously present would have been destroyed by the electron beam exposure. The EDX spectra in Figure 5.7f confirms the presence of the $Cl_{K\alpha}$ peak within the selected area, suggesting this area contained felodipine.

15% Spray-dried

Within the 15% SD solid dispersion two crystalline regions were identifiable out of the 55 areas that were sampled. In the first region, shown in Figure 5.8a, the area selected for electron diffraction is a section of a particle approximately 1.2 μm in size; adjacent are multiple larger particles that are not completely in view. Two diffraction spots can be identified in the first SAED (Figure 5.8b) which was collected using an electron flux of 0.019 $e^-/(Å^2\ s)$. The two diffraction spots have d-spacings of 0.24 nm and 0.21 nm and can be matched to multiple spacings in all forms of felodipine. The distance between these d-spacings was 0.75 nm and assuming the area corresponds to a single crystal this distance is similar to; (200) and (101) within forms III and IV as well as multiple spacings within form II. Form I possessed no spacings that could match 0.75 nm. After an additional electron fluence of 0.93 $e^-/Å^2$ the 0.24 nm and 0.21 nm diffraction spots disappeared, however another spot with a spacing of 0.24 nm appeared on the opposite side of the SAED pattern (Figure 5.8c). This faded after the sample was exposed to an additional electron fluence of 1.05 $e^-/Å^2$ (Figure 5.8e). A clear $Cl_{K\alpha}$ peak is displayed in the EDX spectra in Figure 5.8d from the selected area, suggesting felodipine was present.

A second crystalline area in the 15% spray-dried sample is displayed in Figure 5.9a. Part of the particle was obscured due to it being positioned adjacent to a copper grid bar. An electron diffraction pattern was taken from the edge of the particle using an electron flux of 0.019 $e^-/(Å^2\ s)$. The pattern is polycrystalline with five different d-spacings, identifiable by taking the radial profile around the zero order diffraction spot (Figure 5.9b and c). Two other diffraction spots, that were difficult to identify in the radial profile due to the high background intensity, are highlighted by the blue circles, all measured spacings can be assigned to

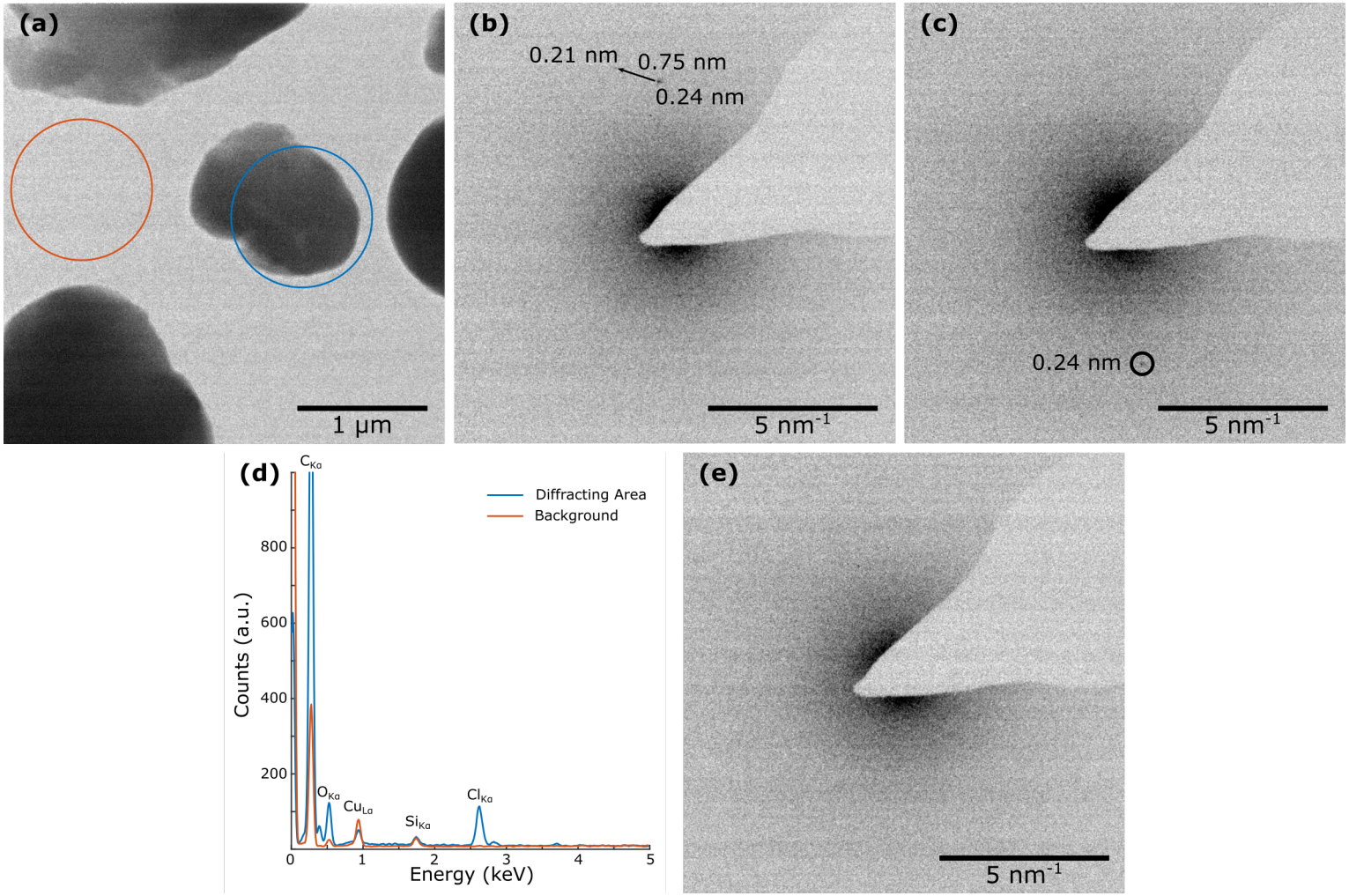

oire

Figure 5.8: (a) Low fluence BF image of 15% SD sample taken using an electron flux of 0.019 $e^-/(Å^2\ s)$; (b) SAED of highlighted region in blue; (c) SAED after an additional electron fluence of 0.93 $e^-/Å^2$ after image b; (d) EDX spectra of diffracting area and the background; (e) SAED after an additional electron fluence of 1.98 $e^-/Å^2$ after image b.

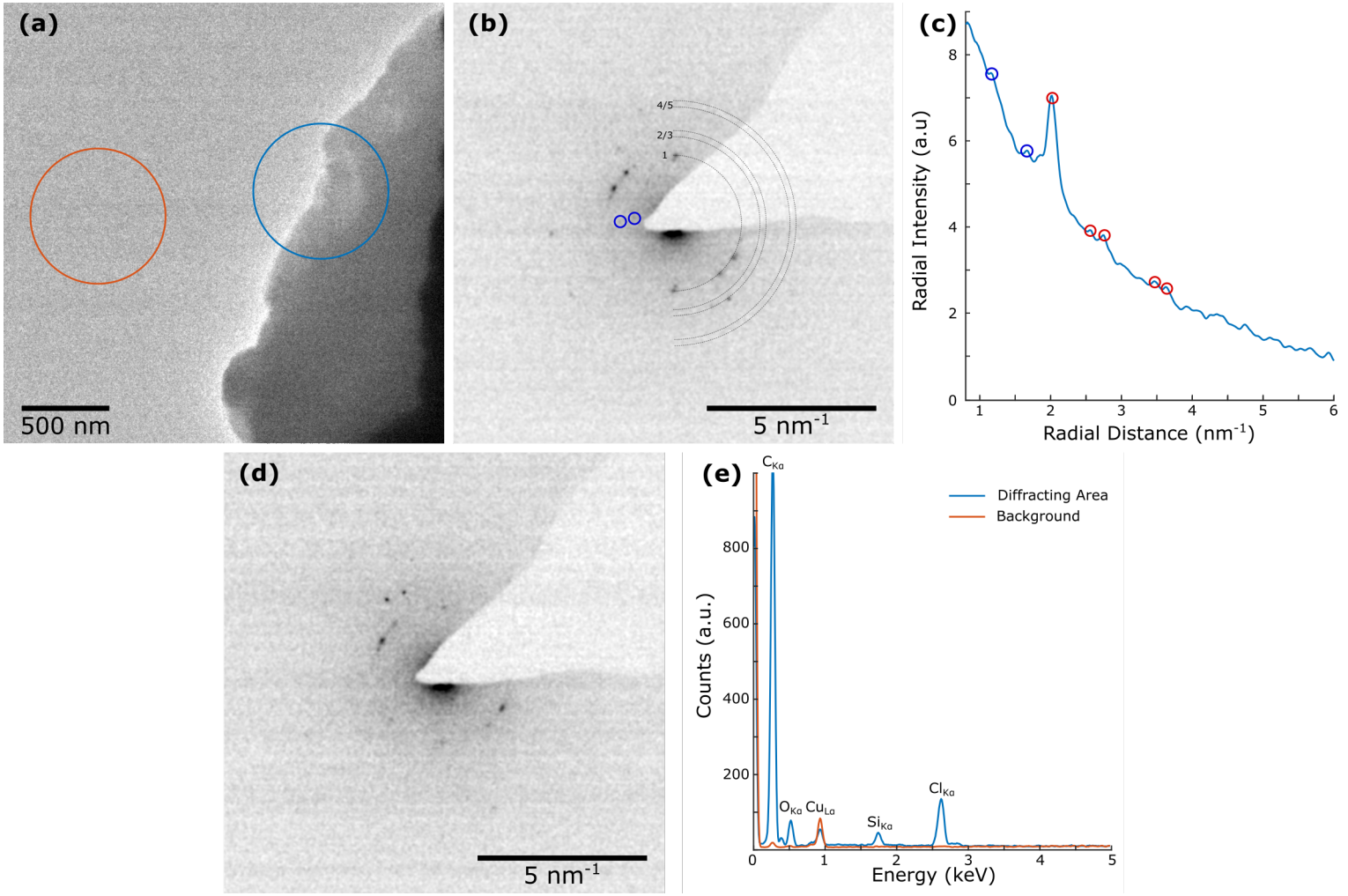

Figure 5.9: (a) Low fluence BF image of 15% SD sample taken using an electron flux of 0.019 $e^-/(Å^2\ s)$; (b) SAED of highlighted region in blue; (c) (e) Radial profile of the diffraction pattern, indexable to all polymorphs of felodipine; (d) SAED after an additional electron fluence of 0.95 $e^-/Å^2$; (e) EDX spectra of diffracting area and the background.

Table 5.5: Measurements taken from the radial profile from Figure 5.9f comparing to possible spacings in felodipine forms I, II, III and IV. Average percentage error between measured and theoretical d-spacings equal to 0.5 ± 0.6, 5.6 ± 0.003, 5.3 ± 0.2 and 5.1 ± 0.4 for form I, II, III and IV respectively.

Ring No.	Radial Distance (nm^{-1})	d-spacing (nm^{-1})	d-spacing (nm)				hkl			
			I	II	III	IV	I	II	III	IV
-	1.17	0.86	0.85	0.81	0.81	0.81	011	220	002	110
-	1.66	0.60	0.60	0.57	0.57	0.57	020	$\bar{2}23$	111	$\bar{1}12$
1	2.02	0.50	0.49	0.47	0.47	0.47	210	040	112	121
2	2.57	0.39	0.40	0.37	0.37	0.37	031	$\bar{1}51$	$\bar{1}14$	$\bar{3}01$
3	2.75	0.36	0.36	0.34	0.34	0.34	300	911	$\bar{1}05$	$\bar{3}12$
4	3.46	0.29	0.29	0.27	0.27	0.27	$\bar{1}41$	$\bar{8}44$	321	232
5	3.64	0.27	0.27	0.26	0.26	0.26	$\bar{1}42$	370	223	410

d-spacings in all forms of felodipine, shown in Table 5.5. Figure 5.9d is obtained after the selected area had been exposed to an additional electron fluence of 0.95 $e^-/Å^2$ and shows that the pattern was beginning to decay, the total extinction of the diffraction spots occurred after a cumulative electron fluence of 3 - 3.5 $e^-/Å^2$.

Figure 5.9e shows the EDX spectra taken from the selected area and background carbon film. The diffracting area exhibited a $Cl_{K\alpha}$ peak, providing further evidence that felodipine is present.

30% Hot-melt Extrusion

TEM was able to identify two different crystalline regions in the 30% solid dispersion prepared via HME from the 55 areas sampled. Figure 5.10a displays the first region, here an isolated particle with dimensions of approximately 850 × 360 nm and the edges of multiple larger particles that are partially out of the field of view are evident. The electron diffraction pattern was obtained using an electron flux of 0.023 $e^-/(Å^2\ s)$ and appeared to be a single crystal, however very few diffraction spots were present. The spots are identified in Figure 5.6b; spots 1, 2 and 3 are part of a systematic row with a d-spacing of 0.60 nm, 0.30 nm and 0.20 nm respectively. Spots 4, 5 and 6 run parallel to this row and have d-spacings of 0.19 nm, 0.19 nm and 0.17 nm. An attempt was made to index this pattern by correlating the measured d-spacings and the angles between the row containing spots 1, 2 and 3 with the remaining spots to theoretical values. However, similar sized spacings and angles to the measured values exist in felodipine forms I, III

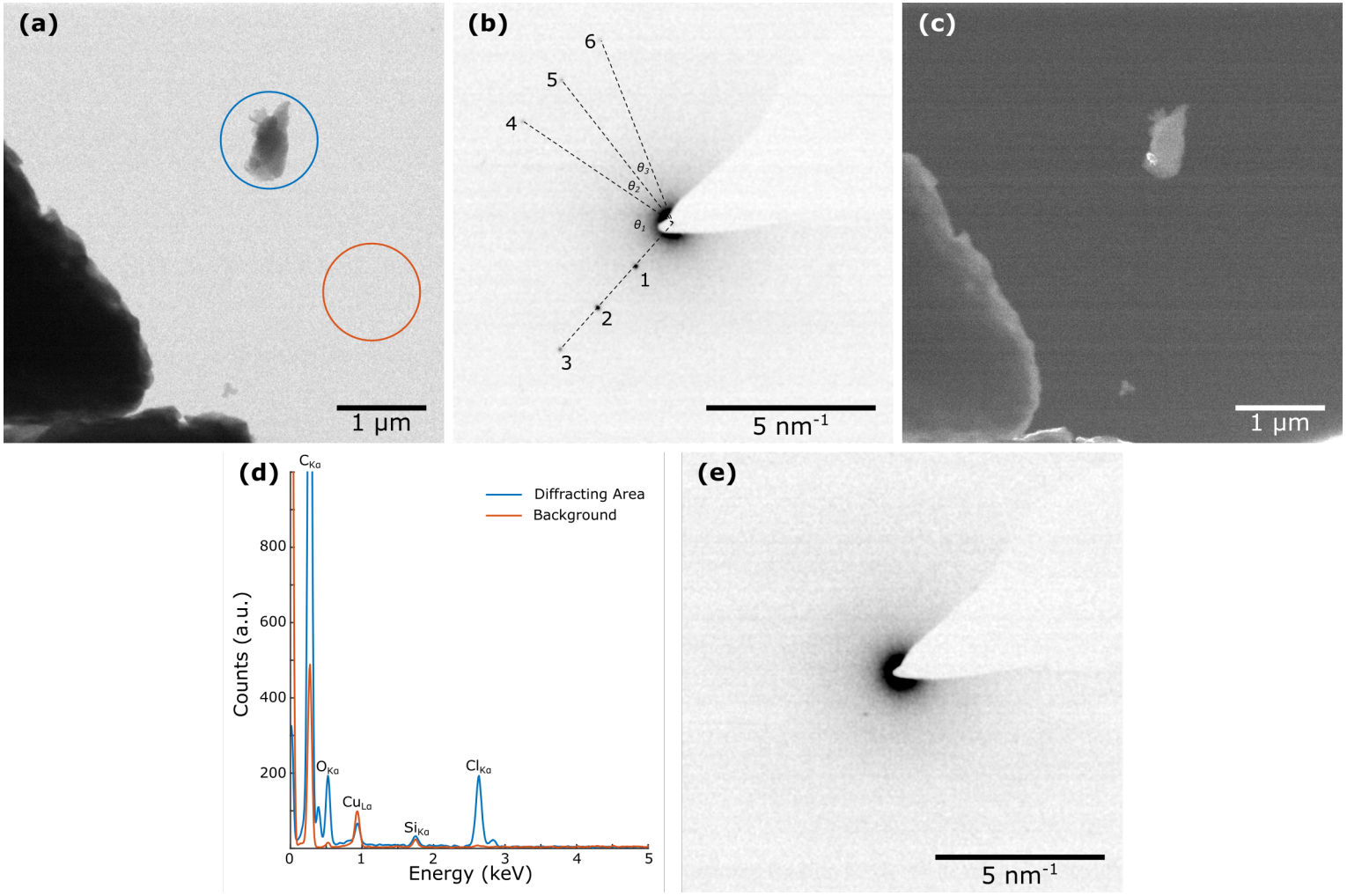

Figure 5.10: (a) Low fluence BF image of 30% HME sample taken using an electron flux of 0.023 $e^-/(Å^2\ s)$; (b) SAED of highlighted region in blue; (c) DF image showing the location of crystals present; (d) EDX spectra of diffracting area and the background; (e) Faded diffraction pattern, acquired after an electron fluence of.3 - 3.5 $e^-/Å^2$.

Table 5.6: Measured d-spacings of each diffraction spot in Figure 5.10b compared to possible spacings in felodipine forms I, III and IV. Average percentage errors between measured and theoretical values are equal to 0.9 ± 0.01, 3.4 ± 0.01 and 3.6 ± 0.4 for form I, III and IV respectively.

Spot	**Distance** ($\mathbf{nm^{-1}}$)	**d-spacing** (nm)	**d-spacing (nm)**			**hkl**		
			I	III	IV	I	III	IV
1	1.68	0.60	0.60	0.58	0.57	002	$10\bar{3}$	012
2	3.36	0.30	0.30	0.29	0.29	004	$20\bar{6}$	024
3	5.04	0.20	0.20	0.19	0.19	006	$30\bar{9}$	035
4	5.33	0.19	0.19	0.18	0.18	$62\bar{2}$	$72\bar{1}$	$5\bar{3}1$
5	5.37	0.19	0.19	0.18	0.18	$62\bar{4}$	622	$54\bar{1}$
6	5.81	0.17	0.17	0.16	0.16	$62\bar{6}$	525	$55\bar{3}$

Table 5.7: Measured angles between the systematic row and spots 4, 5 and 6 for the potential d-spacings in Table 5.6 in felodipine forms I, III and IV.

Angle	**Measured Angle** (°)	**Theoretical Angle (°)**		
		I	III	IV
θ_1	82.3	81.6	82.1	81.4
θ_2	100.4	99.6	100.2	99.5
θ_3	116.6	115.9	116.5	115.9

and IV presenting difficulty in determining the exact polymorph/s that was/were present. Possible matches for each of these polymorphs are summarised in Tables 5.6 and 5.7. Figure 5.10e shows the electron diffraction pattern after an electron fluence of 3 - 3.5 $e^-/Å^2$ had been exposed to this region, demonstrating electron beam damage.

Before the crystal had completely damaged a DF image (Figure 5.10c) was collected by inserting an objective aperture around the 0.60 nm diffraction spot. Crystalline areas that are similarly orientated and contain spacings close to 0.60 nm appear bright; a smaller particle with dimensions of 150 × 75 nm can be seen within the selected area used during electron diffraction. Further bright regions are apparent along the edges of the particle toward the bottom of the image.

Figure 5.10d shows the EDX spectrum taken from the selected area and background carbon film. The EDX spectra from the diffracting area exhibits the $Cl_{K\alpha}$ peak, providing further evidence that felodipine is present.

The second crystalline region in the 30% hot-melt extruded sample is displayed

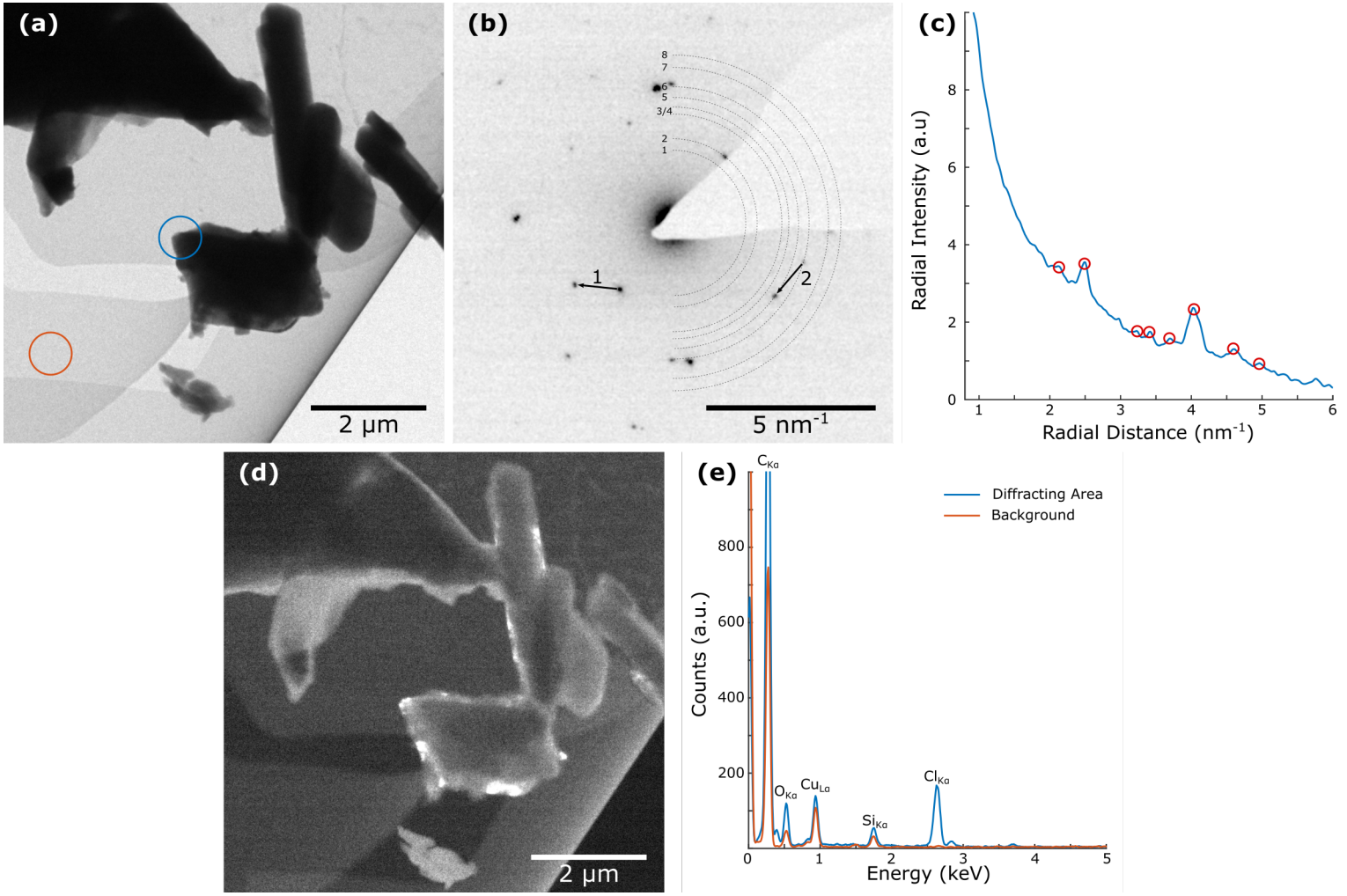

Figure 5.11: (a) Low fluence BF image of 30% HME sample taken using an electron flux of 0.018 $e^-/(Å^2\ s)$; (b) SAED of highlighted region in blue; (c) Radial profile taken from the SAED pattern around the zero order diffraction spot; (d) DF image showing where other crystals are located; (e) EDX spectra of diffracting area and the background.

Table 5.8: Summary of the measured d-spacings of the radial profile from Figure 5.11f comparing to felodipine form III. Average percentage error between the measured and theoretical values is equal to 0.4 ± 1.6.

Ring No.	**Radial Distance (nm^{-1})**	**d-spacing (nm)**	**d-spacing (nm)** Form III	**hkl** Form III
1	2.13	0.47	0.47	122
2	2.49	0.40	0.41	$31\bar{2}$
3	3.23	0.31	0.31	$\bar{2}15$
4	3.43	0.29	0.29	$32\bar{2}$
5	3.71	0.27	0.27	$51\bar{3}$
6	4.03	0.25	0.25	$51\bar{5}$
7	4.61	0.22	0.21	$51\bar{7}$
8	4.96	0.20	0.20	$62\bar{4}$
$\overrightarrow{1}$	1.34	0.75	0.72	010
$\overrightarrow{2}$	1.21	0.83	0.81	002

in Figure 5.11a. Multiple particles are apparent ranging between 1 - 5 μm in size. The electron diffraction pattern in Figure 5.11b was collected using an electron flux of 0.018 $e^-/(Å^2\ s)$ and is polycrystalline. The radial profile around the central diffraction spot is shown in Figure 5.11c. These spots were indexable to felodipine form III which provided the best match compared to all other polymorphs. Table 5.8 summarises the measured and theoretical d-spacings, including the distance between spots that appeared to be from the same single crystal (represented on the diffraction pattern). The $\overrightarrow{1}$ and $\overrightarrow{2}$ measured at 0.75 nm and 0.83 nm and closely resembles the 010 and 002 d-spacing of form III respectively. After the area was exposed to a cumulative electron fluence of 3 - 3.5 $e^-/Å^2$, the diffraction spots were no longer visible.

Dark field images were obtained before the sample lost all signs of crystallinity and revealed a number of additional crystalline regions (Figure 5.11d). After applying a threshold to the image a total of seventeen particles were identified. The particle size distribution varied with the majority (eleven) possessing dimensions under 100 nm, these being 80 ± 40 nm × 80 ± 30 nm on average. Five particles were measured at being between 100 nm and 250 nm in size, on average 145 ± 50 nm × 165 ± 30 nm. The final particle was much larger than the rest and measured as having a width of 620 nm and a height of 270 nm.

Figure 5.11e shows the EDX spectra taken from the selected area and background carbon film. The diffracting area exhibits the characteristic $Cl_{K\alpha}$ peak, providing further evidence that the particles identified are felodipine.

30% Spray-dried

Within the 30% drug loading sample prepared via SD, no crystalline regions were identified within the 55 areas sampled. Examples of two different amorphous regions and their respective SAED patterns and EDX spectra are shown in Figure 5.12. The first BF image displays SD particles that appear spherical with diameters of approximately 500 nm and uniform contrast. While the particle in the second image is between 2 - 3 μm in length with a completely different morphology. The contrast within this particle varies with the two ends appearing much lighter compared to the central section. This may be caused by spherical particles crumpling or buckling under the high vacuum or as a result of grinding by the pestle and mortar during sample preparation, resulting in non-spherical morphologies. The EDX spectra for both areas contain the characteristic $Cl_{K\alpha}$ peak indicating felodipine was present.

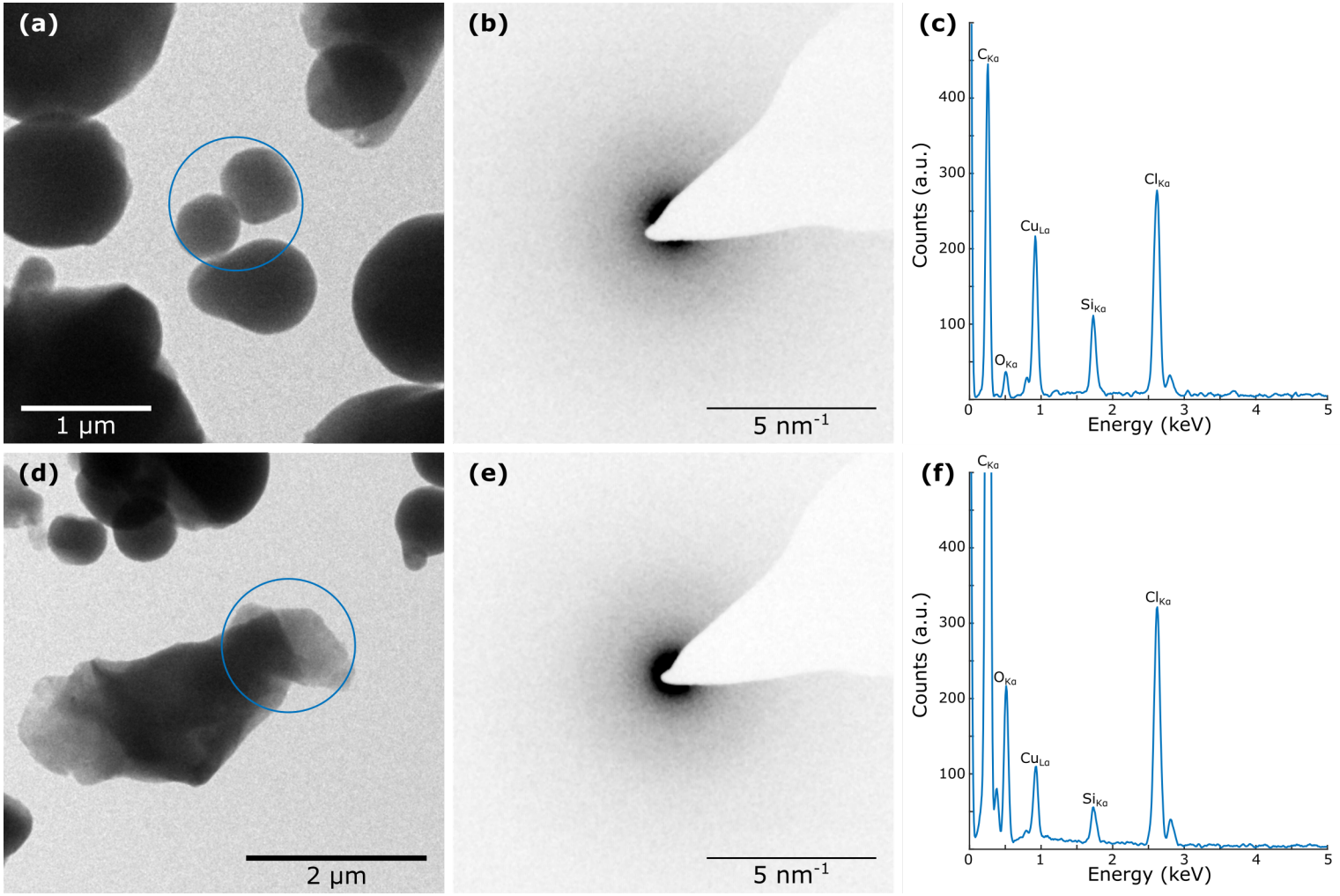

Figure 5.12: (a) Low fluence BF image of one area in the 30% SD sample taken using an electron flux of 0.018 $e^-/(Å^2\ s)$; (b) SAED of highlighted region in blue; (c) EDX spectra of the same area; (d) Low fluence BF image of another area in the 30% SD sample; (e) SAED of highlighted region in blue; (f) EDX spectra of the same area.

5.3.5 Comparison of characterisation methods

From the pXRD results, all samples appeared amorphous and very little discernible difference between the ASDs was evident. Both FTIR and DSC were unsuccessful in identifying crystallinity within any of the ASDs. The FTIR results, however, showed a red-shift in the N-H stretch between preparation methods, suggesting stronger hydrogen bonds were formed between felodipine and copovidone in the SD samples. Between drug loading levels no appreciable difference was found in the SD samples; 15% HME samples showed a redshift of 2 cm^{-1} compared to the 30% sample. For a drug to be molecularly miscible in a particular polymer, some level of drug-polymer interaction is required. The extent of these drug-polymer interactions in providing a physically stable mixture is not fully known but is thought to play an important role in the miscibility of the two materials (Tang et al., 2002). An increase in drug-polymer interactions through either specific (i.e. hydrogen bonding) or non-specific (i.e. van der Waals forces) are thought to reduce the molecular mobility and cause a delay in inhibiting the onset kinetics and extent of crystallisation in the API (Konno and Taylor, 2006; Mistry et al., 2015; Mistry and Suryanarayanan, 2016). Essentially this increases the activation energy for amorphous phase separation and recrystallisation to occur (Janssens and Van den Mooter, 2009b). Therefore the FTIR data suggest stronger interactions and an increase in activation energy for crystallisation when prepared by SD.

DSC also demonstrated a difference between preparation methods, most prominently in the 15% drug loading where the SD mixture exhibited a T_g 3°C higher than HME samples. An increase in T_g between ASDs containing the same binary system and drug loading suggests interactions between the polymer and drug are greater in number and/or strength than the interactions between like molecular species (Konno and Taylor, 2006). This suggests that SD provides greater drug-polymer mixing which is in contrast to Guns et al. (2011) and Tian et al. (2013b) who both found HME to provide higher degrees of mixing and improved physical stability. A review by Huang and Williams (2018) concluded that solvent base preparation methods (i.e. spray drying) are chemically more stable but suffer from less physical stability (more prone to recrystallising) due to being

negatively affected by residual solvent, high surface area, potential crystal nuclei, and molecular relaxation. Drug loading has a significant effect on the T_g due to an increased polymer concentration causing an anti-plasticising effect that immobilises the drug, increasing intermolecular interactions and decreasing molecular mobility (Frank and Matzger, 2018; Kothari et al., 2015a,b; Wegiel et al., 2013). This effect has been shown by Kothari et al. (2015b) to be a potential factor in increasing the physical stability of ASDs comprised of PVP and nifedipine, an analogue of felodipine.

Based on the pXRD, FTIR and DSC results presented it was the expectation that TEM would not identify any crystalline regions and if they were present, samples prepared via HME containing higher drug loadings would be the most likely candidates for crystallisation. The number of crystalline regions that could be identified as crystalline felodipine by TEM is summarised in Table 5.9, showing that 2 regions (or 4% of the regions sampled in all but the 30% spray dried mixtures) were crystalline.

This is unexpected since, as mentioned earlier, an increase in polymer concentration is thought to improve the physical stability. However Rumondor et al. (2011), Duong et al. (2015) and Frank and Matzger (2018) found that higher polymer concentrations may lead to phase separation or crystallisation in hygroscopic polymers. This is due to water causing a plasticising effect that reduces T_g and disrupts intermolecular bonding leading to an increase in molecular mobility and a decrease in physical stability (Konno and Taylor, 2008; Marsac et al., 2010; Rumondor and Taylor, 2010b; Rumondor et al., 2011; Ueda et al., 2014; Xiang and Anderson, 2017). Higher concentrations of lipophilic drugs have been shown to be inversely proportional to the hygroscopicity of the ASDs (Andronis

Table 5.9: Summary of amorphous, crystalline and percentage of regions found to be crystalline within ASDs .

	15% Hot-melt extrusion	30% Hot-melt extrusion	15% Spray-dried	30% Spray-dried
Amorphous	53	53	53	55
Crystalline	2	2	2	0
Crystalline (%)	4	4	4	0

et al., 1999; Chen et al., 2015; Ueda et al., 2014). In this case, the hygroscopicity of higher polymer concentrations in 15% SD samples may lead to a plasticising effect and induce increased molecular mobility and crystallisation. If water was causing a plasticising effect, a decrease in T_g would be observable via DSC as even low levels of water can reduce T_g by more than 10° (Guo et al., 2013). However, the DSC results presented in the second and third run show T_g being higher than expected when compared to the Gordon-Taylor equation. This discrepancy may be due to water evaporating off during the first run and consequently being removed by the N_2 gas flow, therefore, no plasticising effect is observed.

Aside from the 30% SD ASD potentially being more physically stable, another possibility explaining the absence of crystalline areas could be a result of an inadequate number of areas sampled. The probability of finding crystalline areas can be modelled using a Poisson distribution (Equation 5.4) assuming there is: an equal probability of crystallisation occurring in each sample; each area has an equal probability of crystallising and each crystallisation event is independent of one another.

$$P(x;\lambda) = \frac{\lambda^x e^{-\lambda}}{x!} \tag{5.4}$$

P is the probability of x amount of crystalline regions being identified and λ is the expected number of crystallisation events to occur within 55 areas, in this case, 1.5. This results in the probability of finding one or more crystalline areas as 0.78; in the instance of sampling 100 areas the probability of not observing any crystallisation events are 0.065. However, manually sampling a large number of areas is time-consuming. Alternative prolonged electron beam exposure eradicating crystals in the sample could also explain the lack of crystallinity in the 30% SD mixture. As mentioned earlier FTIR shows that stronger hydrogen bonds are present in the SD samples and all the ASDs compared to crystalline felodipine. From the predictive model in Chapter 4 the ratio of hydrogen bond donors/acceptors and vice versa were shown to negatively correlate to electron beam stability, suggesting that ASD may be more electron beam sensitive than the pure crystalline form. To confirm this further studies measuring the C_F of crystals within solid dispersion would be required.

When attempting to index the electron diffraction patterns the majority of crystals found appeared to be metastable forms of felodipine, although, the exact form present was ambiguous requiring higher quality single crystal electron diffraction patterns to be recorded. If the metastable forms are present this suggests that during crystallisation within solid dispersions amorphous felodipine converts into the one or more of the metastable polymorphs before reaching the most thermodynamically stable form. This may be due to a lower activation energy barrier between the amorphous phase and one or more of the metastable polymorphs, leading to cross-nucleation between polymorphs. Another study examining the crystallisation of nifedipine, an analogue of felodipine, from a drug/polymer melt and observed the crystal growth of the metastable β polymorph due to preferential growth from a polymer additive (Gunn et al., 2012). Other studies have also shown that polymer additives or polymer rich domains can seed nucleation and prevent or slow down the simultaneous transformation to the more stable form (Tao and Yu, 2006). Therefore if phase separation occurs within the solid dispersions polymer rich phases may result in heterogeneous nucleation lowering the activation energy for metastable polymorphs to form (Frank and Matzger, 2017, 2018).

Only the particle size of crystals in the hot melt extruded solid dispersions was identifiable via either BF and/or DF images. These were found to be under 100 nm, approximately 10 - 60 nm in both 15% HME sample areas, while particles varied in size between 40 - 200 nm in the 30% HME sample. The majority of these particles were, however, less than 100 nm. These small differences in particle size distribution suggest that crystal growth had occurred within the higher drug loading. Crystallisation can be separated into two associated processes; nucleation and crystal growth (Andronis and Zografi, 2000). Both processes require molecular motion allowing molecules to rearrange to create stable nuclei or to attach for crystal growth. For organic molecules, crystal growth starts to occur when the critical nucleation diameter is typically between 10 and 20 nm.(Ricarte et al., 2015). The molecular mobility of solid dispersions is an important factor in both the nucleation and growth; the global mobility/α-relaxation of an amorphous material is directly related to the T_g (Huang and Williams, 2018; Ke et al., 2012; Meng et al., 2015). When the sample is stored below the T_g

the global mobility decreases dramatically and the amorphous solid dispersion is generally kinetically stabilised. However crystallisation has been observed in systems stored well below T_g where the global mobility is considered to be negligible. The cause of this crystallisation is thought to be due to the occurrence of β-relaxation, which is a localised motion that has much lower energy barrier than α-relaxations. Since the T_g for felodipine/copovidone systems are much higher than the storage temperature the start of crystallisation is most likely due to these β relaxations allowing felodipine molecules to form critical nuclei. Once formed the local concentration of felodipine would decrease as the crystal grows, further growth would then be mediated by the global mobility. The differences in T_g between both drug loading levels may explain the increased size of crystalline particles in 30% drug loaded sample as the global mobility is higher leading to more crystal growth. In addition dust or shed particles during processing such as from extruder during HME or milling could allow sites for heterogeneous nucleation to occur (Qi et al., 2011).

TEM has previously been used to analyse ASD. A study by Ricarte et al. (2015) examined SD ASD of griseofulvin and HPMCAS and found TEM to be more sensitive when compared to FTIR, DSC and wide angle X-ray scattering (WAXS) data. While other studies have applied TEM to investigate phase separation in ASD via contrast differences used to determine the position of heavier atoms i.e. S and Cl (Bhardwaj et al., 2018; Marsac et al., 2010). The results presented here demonstrate TEM as a more sensitive technique for the detection of low-levels of crystallinity, despite electron beam damage limitations. However quantification of the exact amount of crystallisation is difficult to evaluate via the nature of the method.

5.4 Chapter Summary

The aim of this chapter was to identify the presence of nascent crystallisation in ASD, by TEM and other characterisation methods, prepared using HME and SD at 15% and 30% drug loadings. This was to determine if there was a difference between preparation methods and drug loadings and to improve the understanding of the physical stability of the ASD. From the results and discussion presented it was learnt that:

- pXRD, FTIR and DSC can distinguish between amorphous and crystalline felodipine, however, they were unable to identify any amount of crystalline felodipine within the ASDs studied.
- From FTIR and DSC results preparation via SD appeared to produce more intimately mixed dispersions as compared to HME.
- TEM is capable of detecting very low amounts of crystalline felodipine within the 15% and 30% HME and the 15% SD samples (two areas in each). While no obvious signs of recrystallisation were found in the 30% SD mixture, although this may be the result of a low sample number.
- Crystals present appeared to be a mixture of the stable polymorph (form I) and metastable polymorphs of felodipine (forms II, III and IV). The collection of higher quality single crystal diffraction patterns is required to confirm this.
- Quantitative assessment of the amount of crystallinity through the use of SAED and the sampling of different regions was difficult in TEM due to the lack of robustness of the statistical sampling.
- Information obtained by TEM offered complementary data to bulk techniques and may provide insight into the growth mechanism of API crystals in a solid dispersion.

In this chapter the sensitivity of TEM compared to other characterisation techniques has been demonstrated. The following results chapters will build on

the work presented thus far by examining ASD exposed to high humidity to induce ageing of the sample. This will allow the recrystallisation of the amorphous drug to be examined over a shorter period of times. Preliminary experiments regarding promising electron microscopy techniques are then used to determine if they are applicable to electron beam sensitive samples and provide mechanistic insight into recrystallisation and information regarding size, shape, form and defects within crystals and were in the solid dispersion they occur.

Chapter 6

Transmission Electron Microscopy of Aged Amorphous Solid Dispersion

This chapter investigates the effects of accelerated ageing of amorphous solid dispersions (ASD) by storage at elevated relative humidities (RH) in an attempt to understand the mechanism of crystal nucleation and growth through analysis by TEM. Initially, the ASD system selected for examination was 95:5 w/w % of indomethacin and copovidone, however, difficulties occurred when preparing by hot-melt extrusion (HME) and rotary evaporation; either the ASD did not form or the sample crystallised before starting the experiment. Based on previous literature, crystallisation of amorphous indomethacin should have taken more than 21 days at this drug loading level and 75% RH (Crowley and Zografi, 2003; Yoshioka et al., 1995). Therefore an alternative ASD system was examined, this being a 50:50 w/w % felodipine and copovidone prepared by HME. This sample had been prepared at the same time as the 15% and 30% HME samples used in Chapter 5. pXRD, FTIR and DSC were all used as methods to provide complementary analyse of bulk crystallinity, while TEM was used to investigate the local structure.

6.1 Sample preparation

6.1.1 Indomethacin Amorphous Solid Dispersion

Hot-melt extrusion of indomethacin

An amorphous solid dispersion of 95:5 w/w % of indomethacin and copovidone was prepared via HME. Each component was weighed using an analytical balance and blended using a Turbula blender operated at 23 rpm for 4 minutes. Extrusion was carried out on a Thermofisher Haake Minilab II hot melt extruder using a barrel temperature and screw speed of 170°C and 30 rpm. Prior experiments demonstrated that copovidone was easily extruded at 170°C and that the API melted at 160-162°C and would not degrade up to temperatures of at least 180°C. Zero torque was measured during extrusion at this temperature and no sample left the extruder. The melt was assumed to be of such low viscosity that the extruder could not push it out. This was confirmed when the equipment was stopped and opened.

A new batch was attempted at a temperature and screw speed of 160°C and 30 rpm. The recorded torque was 300 Ncm and the screw speed registered as 5 rpm. The batch appeared not to be molten or soft enough for successful extrusion. The temperature was increased to 163°C. This resulted in material leaving the extruder in the form of small dark brown beads rather than long thin rods. The high shear force may have caused degradation of the extrudate. A final attempt was made to form the solid dispersion and the temperature was increased to 165°C. The resulting beads were lighter in colour however it is questionable as to whether this is really extruded material as it was still a thick liquid that ran out of the die. It appeared that the operating window for extrusion of indomethacin is very narrow (virtually solid at 160°C but liquid at 163°C). Due to the uncertainty of whether the final product was extruded material rotary evaporation was used as an alternative preparation method.

Rotary evaporation of indomethacin

Rotary evaporation was another method used to create ASDs of indomethacin and copovidone. Here the indomethacin was converted to the amorphous form by

heating at 180°C for approximately 5 minutes, followed by quench cooling to room temperature. Copovidone was dried at 120°C for 12 hours before use. An ASD containing 95:5 w/w % of indomethacin and copovidone was prepared by rotary evaporation by dissolving both components in 100 mL of anhydrous methanol at 70°C. The solvent was then removed using a rotary evaporator at 50°C. The resulting powder was extracted and dried in a vacuum oven at room temperature for 24 hours. pXRD was used after drying to assess the crystallinity of the samples and they were found to be crystalline. The experiment was repeated using the same conditions, which again resulted in crystallisation of the indomethacin. Since the preparation of 95% indomethacin, ASDs were unsuccessful via multiple preparation methods it was decided that a 50:50 w/w % felodipine and copovidone prepared via HME would be used instead.

6.1.2 Felodipine Amorphous Solid Dispersion

Amorphous solid dispersions containing 50/50 w/w % felodipine and copovidone were prepared via HME. Components were weighed on an analytical balance and blended using a Turbula blender at 23 rpm for 4 minutes. Extrusion was carried out on a Thermofisher Haake Minilab II hot melt extruder using a barrel temperature and screw speed of 130°C and 30 rpm. The resulting extrudate left the extruder as long rods that were separated into small pieces and milled using a pepper grinder to form a coarse powder. The powder was then dried in a vacuum oven at 30°C and stored in a desiccator prior to use.

Before conducting the ageing study the solid dispersion was checked for crystallinity by pXRD. This particular 50% HME sample had been prepared at the same time as the samples examined in Chapter 5 and had not been freshly prepared. However, it had been stored in a desiccator and appeared amorphous by pXRD before carrying out the ageing study. The humidity was controlled and maintained by creating a humidity chamber containing a saturated salt solution inside a desiccator. Two sets of experiments were carried out, one at 85% RH and the other at 75% RH. To achieve these RH values a saturated solution of KCl was used to prepare a RH of 85%, while NaCl was used for a RH of 75% (Greenspan,

1977). The RH value was confirmed using a hygrometer stored within the humidity chamber. The temperature was not controlled or closely monitored but was assumed to be at approximately room temperature.

6.2 Methods of analysis

6.2.1 Transmission Electron Microscopy

Samples were prepared by grinding the dry powder in a pestle and mortar to further reduce the size of the coarsely ground particles. The ground powder was then added to a 400 mesh continuous carbon-coated copper grid by gently touching the powder onto the grid. All samples were examined in a Tecnai F20 TEM/STEM operated at an accelerating voltage of 200 kV, equipped with a field emission gun using an extraction voltage of 4.5 kV. The images were captured using a Gatan Orius CCD camera with an exposure time of 2 - 3 seconds to increase the signal-noise ratio. EDX spectra were collected using an Oxford Instrument 80 mm X-Max SDD detector and processed using the AZtec software.

Areas that had not been exposed to the electron beam were examined and to limit any damage that occurred an electron flux of 0.0175 $e^{-}/(Å^2\ s)$ was used. To try and maximise the number of crystalline areas found, conical dark field (DF) was used to more clearly highlight areas that contained crystalline regions (more information is provided on conical DF in the following section). A 2.9 mrad radius objective aperture was inserted and aligned around the optical axis; the electron beam was tilted by 5.5 mrad and precessed at a frequency of 10 Hz per full rotation. The combination of this sized objective aperture and beam tilt allows for diffraction spacings between 3 Å and 9.6 Å to be sampled. Constantly bright regions or regions that oscillated between bright and dark, due to the path of the electron beam, indicated that crystals were present. A DF video was captured as the electron beam was precessed showing areas of potential crystallinity for approximately 10 - 30 seconds. Selected area electron diffraction (SAED) patterns were then collected by inserting the selected area aperture with a diameter of 1.1 μm at the image plane to further identify each crystal. Once the diffraction pattern had completely faded the electron flux was increased to provide enough

signal for an EDX spectrum to be collected to confirm the presence of felodipine via observation of a $Cl_{K\alpha}$ peak at 2.62 keV.

6.2.2 Conical Dark Field

Dark field microscopy has already been used for identification of crystalline APIs within formulations by Ricarte et al. (2015). It was previously mentioned that while this method allowed identification of crystalline regions only certain diffraction spots within the sampled region are included in image formation, thereby some crystalline regions will be missed.

Conical DF, also known as hollow cone DF, is a method that has previously been used for orientation mapping, defect analysis and grain size measurements in

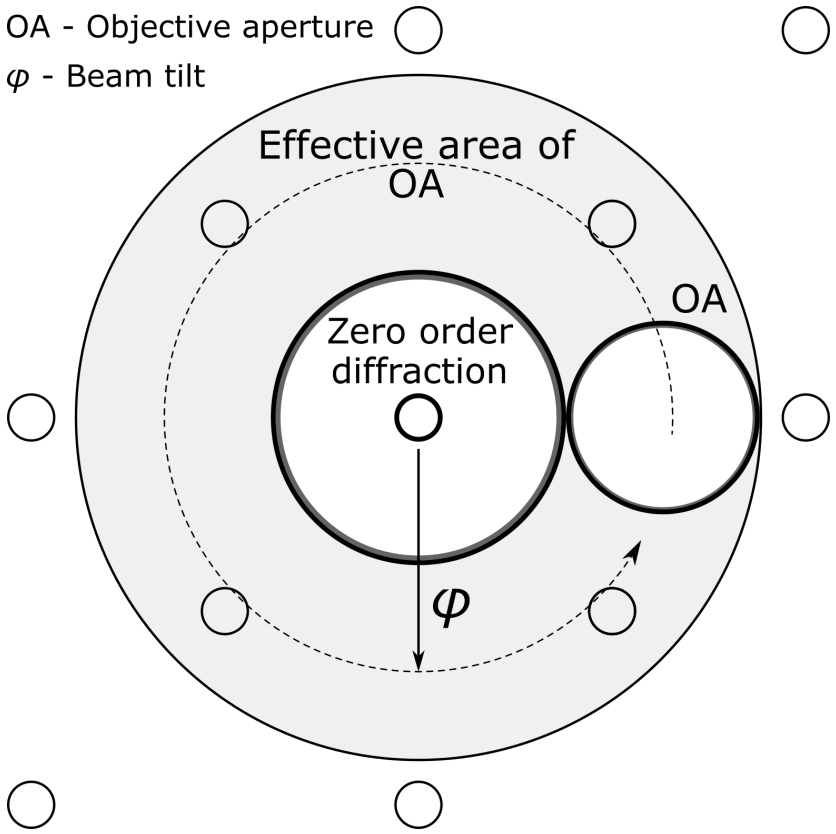

Figure 6.1: Schematic of region sampled within the back focal plane using conical DF.

inorganic materials but has also been used for single particle 3D reconstruction of proteins and identification of inorganic nanoparticles in biological systems (Klein et al., 2015; Tsai et al., 2016; Wu and Zaefferer, 2009; Yao et al., 2010). Here it is used as a method to overcome the problem of only sampling specific diffraction spacings/orientations in standard DF imaging, to increase the contrast between crystalline and amorphous regions, resulting in a higher probability of finding crystals and to measure the size of crystalline areas. In this method, a small objective aperture is centred around the optical axis and the zero-order diffraction beam is tilted by an angle φ, this is then precessed using the deflection coils to drive the tilted electron beam in a circular path. Figure 6.1 shows the effective reciprocal space area that the objective aperture will sample as the electron beam moves.

Preliminary results using conical DF were generated on pure crystalline felodipine. Figure 6.2 shows different times points collected from a conical DF video of felodipine. The intensity of certain areas changes as the electron beam is precessed and different diffraction spots fall within the objective aperture. After an electron fluence of approximately 1.87 $e^{-}/Å^{2}$ the intensity of these areas are similar to the background, indicating the sample has been damaged by the electron beam.

The video was processed using ImageJ, firstly by applying a rolling ball background subtraction (between 10 - 30 pixels) to remove large light regions that appeared due to sample thickness. A single image was then generated that showed the maximum intensity for each pixel across the entire data series by using the z-projection function to show all areas that are diffracting within a single image. The histogram was then assessed to find the standard deviation (σ) of the pixel intensity and a threshold was applied that was between 4 - 6 σ. The Rose criterion states that in order for a feature in an image to be detectable, the object must exceed 3 - 5σ above the background pixel values (Rose, 1973). This provided an outline for identifying where the diffracting particles were positioned (Figure 6.3). In some cases certain areas would visibly change in intensity during the dark field video, indicating crystallinity, however due to the low intensity of these diffracting areas they were not always identified when thresholding. When these areas were identifiable the mask was manually adjusted to incorporate them in to

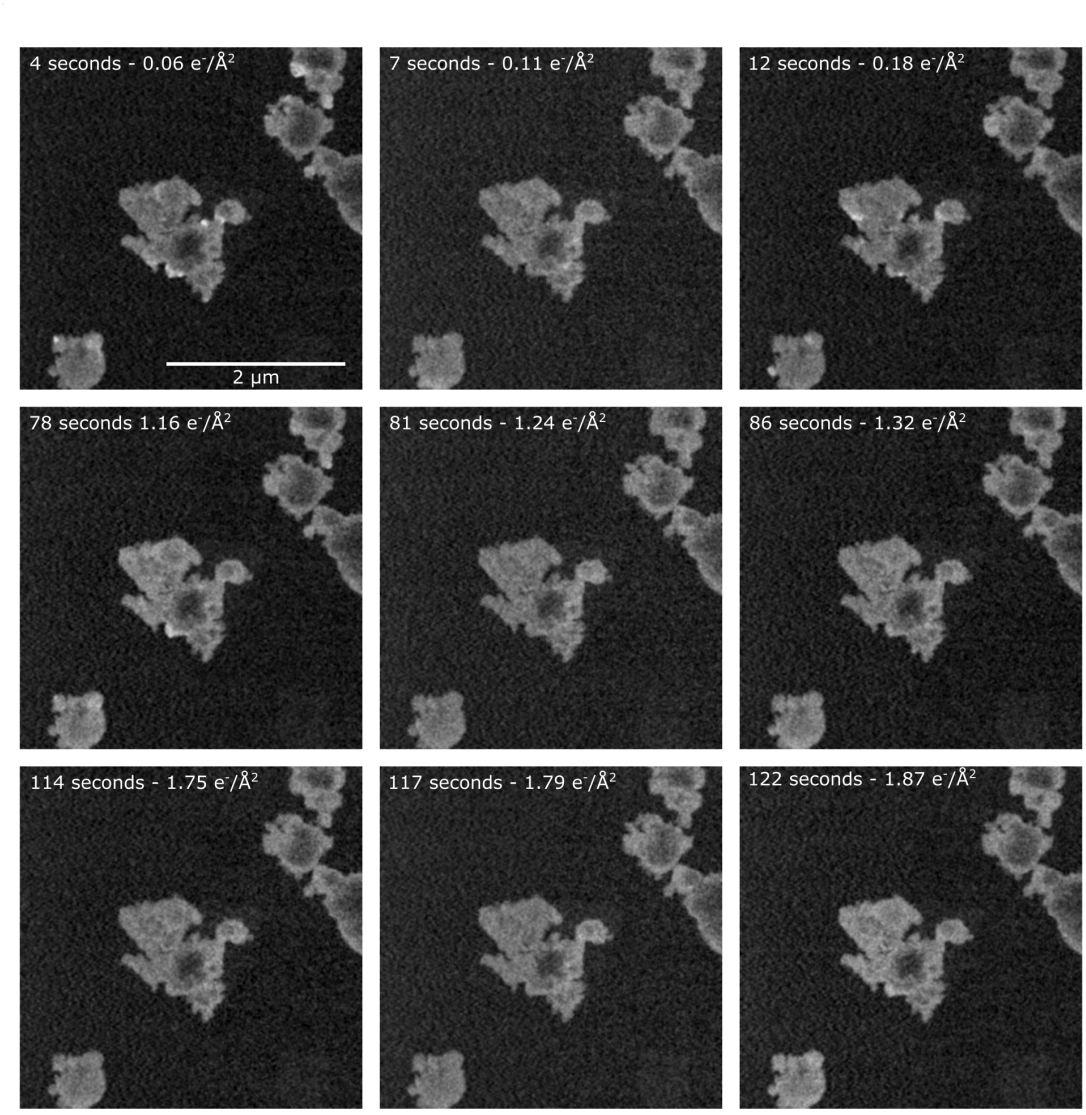

Figure 6.2: Different time points extracted from the recorded conical DF video of crystalline felodipine, demonstrating how the intensity changes as the electron beam is precessed and the electron fluence increases. The scale bar is constant for each image.

image. Particle size analysis was then carried out on the thresholded image. The same image processing was carried out for all the conical DF videos collected for the ASD samples.

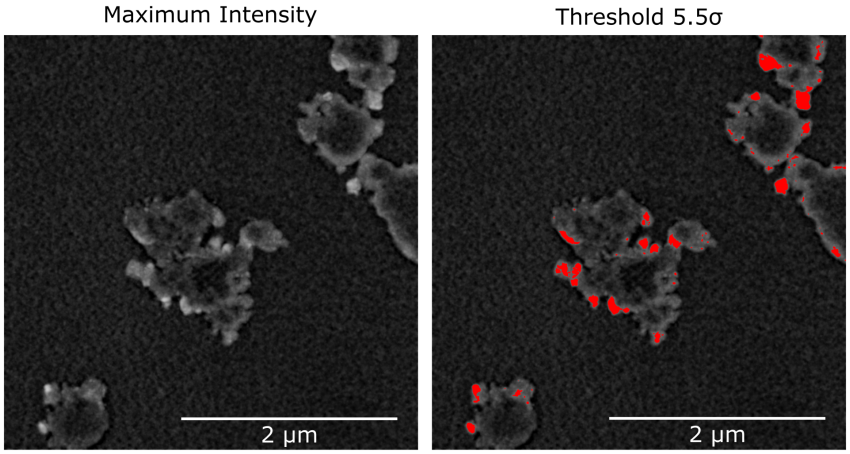

Figure 6.3: Processed conical DF image showing the z-projection for maximum intensity and the applied threshold showing the areas that appear crystalline.

6.2.3 Powder X-ray Diffraction

Each sample was mounted onto a silicon wafer and analysed using a Philips X'Pert diffractometer ($\lambda = 1.5418$ Å). Samples were measured in reflection geometry in θ - 2θ configuration over a 2θ scan range of 2° to 40° with 25 second exposure per 0.02° increment. The X-rays were generated by a copper long-fine focus tube operated at 40 kV and 40 mA. The samples were spun at 30 rpm to improve counting statistics. Powder diffraction patterns were collected to check for bulk crystallinity and determine how the crystallinity changed over time.

The % crystallinity of each day was calculated for each diffractogram using Equation 6.1 (Rumondor and Taylor, 2010a; Shah et al., 2006).

$$\%\ Crystallinity = \frac{A_c}{A_c + A_a} \times 100 \tag{6.1}$$

Here A_c is the total area under each crystalline diffraction peak and A_a is the total area under the amorphous regions. A_c and A_a were found using High-Score Plus by manually removing the background and then fitting two amorphous peaks. The visible crystalline peaks are then fitted and the area of each amorphous and crystalline peak can then be taken from the software and % crystallinity calculated from Equation 6.1.

6.2.4 Fourier Transform Infra-red Spectroscopy

A Thermo Scientific NicoletTM iSTM FTIR ATR Spectrometer was used to collect all the FTIR spectra. Samples were placed onto the ATR crystal and pressed down using a clamp to provide good contact between the sample and crystal. Backgrounds were collected every 15 minutes and the spectra were obtained in % transmission mode between 600 - 4000 cm^{-1} at a resolution of 2 cm^{-1}. Data collection was repeated in triplicate for each sample. During analysis, the % transmission was converted to absorbance by using equation 6.2 to increase the ease of identifying weak signals in the presence of much stronger signals.

$$Absorbance = 2 - log(Transmission\%) \tag{6.2}$$

6.2.5 Differential Scanning Calorimetry

A power compensated Mettler Toledo DSC was used to collect all the data. Approximately 10 mg of sample was added to a 100 μL aluminium pan and was hermetically sealed. An empty aluminium 100 μL pan was used as a reference. Samples were heated from 30°C up to 200°C and then cooled back to 30°C under a nitrogen atmosphere using a temperature ramp rate of 10°C/min. This was carried out in triplicate. Measurements to determine melting temperatures plus the onset and midpoint of the T_g of the dispersions was carried using the Mettler STARe evaluation software.

6.3 Results and Discussion

6.3.1 85% Humidity

The first ageing experiment was carried out at 85% RH and room temperature and was used to study the crystallisation of felodipine over the course of two weeks using pXRD, FTIR, DSC and TEM. The time points that data were collected on were days 1, 3, 7 and 14.

Powder X-ray diffraction

Crystallisation was noticeable in pXRD within the first 3 days of analysis. A single diffraction peak is visible on day 1 at 29.5°; this is similar to the $40\bar{2}$ d-spacing in form I, however this peak was not visible on subsequent days. The diffractogram from day 3 showed multiple diffraction peaks appearing, these being the 011, $20\bar{2}/\bar{1}21$, $\bar{2}21$, $\bar{3}11$, $12\bar{3}$, $22\bar{3}$, $\bar{3}21$, $13\bar{3}$ and $\bar{4}12$ peaks of form I felodipine. By day 7 the intensities of these peaks had increased and further peaks of felodipine form I were observed; $\bar{1}11$, $\bar{1}02$, 002, $21\bar{3}$, 321, 400, $\bar{4}14$, 223 and $50\bar{2}$. The diffractograms and indexed peaks for each day can be seen in Figure 6.4, no measurement was taken on day 14 due to equipment failure.

The amount of crystalline form I was quantified by calculating the % crystalline for each day these were found to be 0%, 6.1% and 11.3% for days 1, 3 and 7 respectively.

Fourier transform infrared spectroscopy

Form I crystalline felodipine exhibits a sharp absorbance peak at 3367 cm^{-1} indicating a stretch in the N-H bond of two felodipine molecules hydrogen bonded together while amorphous felodipine features a broad absorbance peak at 3340 cm^{-1}. Therefore the presence of the 3367 cm^{-1} peak would indicate crystallisation of the ASD had occurred and a peak at 3340 cm^{-1} would suggest amorphous-amorphous phase separation both due to the increased RH. Figure 6.5 displays the absorbance spectra against wavenumber between 3700 - 2700 cm^{-1} (O-H and N-H stretch region) and 600 - 1800 cm^{-1} (C=O stretch region) for the aged ASD sample stored at room temperature and 85% RH. Crystalline or amorphous felodipine peaks were not observed during analysis on day 1; a broad absorbance peak at 3294 cm^{-1} was visible. This peak has previously been assigned to the N-H stretch in the ASDs due to the hydrogen bond interactions between felodipine and copovidone. The position of this peak has red-shifted, by 46 cm^{-1} and 73 cm^{-1} in relation to the N-H stretch found between felodipine - felodipine hydrogen bonds in the amorphous phase (3340 cm^{-1}) and crystalline form I (3367 cm^{-1}); indicating the N-H group forms stronger hydrogen bonds between felodipine and copovidone.

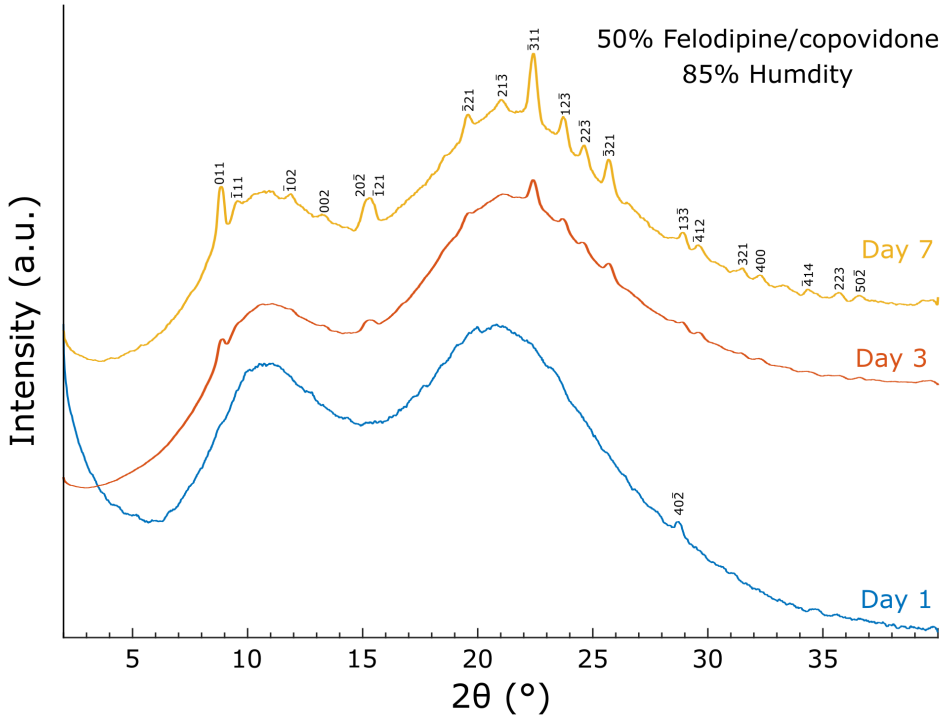

Figure 6.4: pXRD results of 50:50 felodipine and copovidone ASD prepared via HME and stored at 85% RH and room temperature. The crystalline peaks are indexed to form I felodipine.

A small peak began to emerge at 3367 cm^{-1} from the results on day 3 and increases in absorbance on subsequent days, similar to the diffraction peak intensities found in pXRD results (Figures 6.4 and 6.5 respectively). The presence of this peak indicates that felodipine has crystallised from the ASD due to the presence of atmospheric water. The intensity of the crystalline felodipine peak at 3367 cm^{-1} appears to increase at the expense of the felodipine-copovidone peak at 3294 cm^{-1}. This suggests that the higher RH disrupts either the strength or number of felodipine-copovidone interactions, possibly due to water displacing the API within the amorphous matrix causing the API to phase separate and crystallise. Due to the lack of an amorphous felodipine peak, amorphous-amorphous phase separation does not appear to occur unless low concentrations that cannot be detected are present, similarly no amorphous felodipine peak was found in

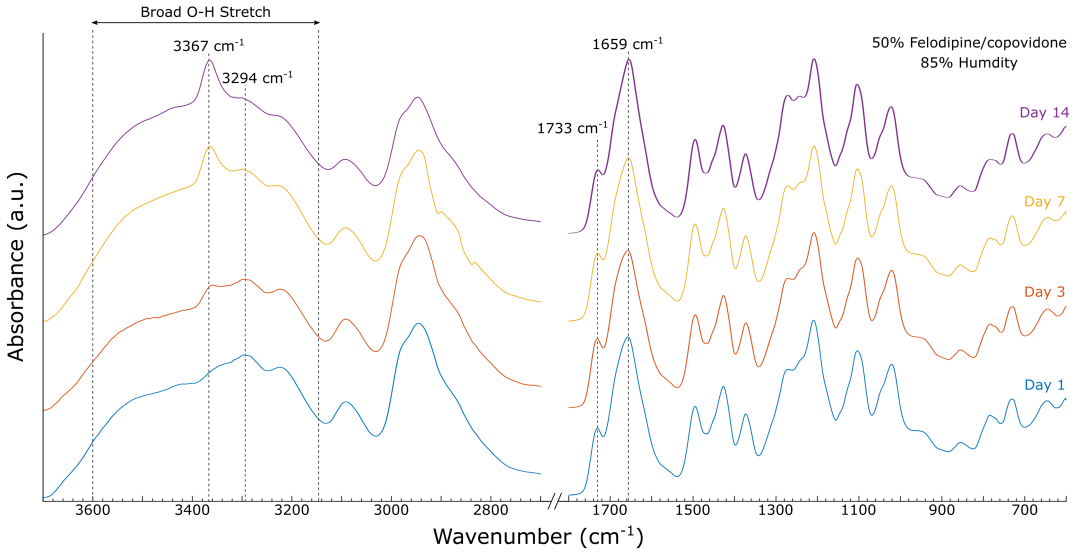

Figure 6.5: Absorbance spectra between 2700 - 3700 cm^{-1} and 600 - 1800 cm^{-1} of 50:50 felodipine and copovidone ASD prepared by HME, stored at room temperature and 85% RH.

Figure 5.3 in Chapter 5. It seems likely that the phase separated drug, no longer stabilised by the polymer, crystallises rapidly due to thermodynamic and kinetic instability, resulting in the crystalline peak observed. The thermodynamic and kinetic effects of the addition of water into the binary system of felodipine and copovidone are discussed later.

Two broad, strongly absorbing peaks can be found within the C=O regions at 1733 cm^{-1} and 1659 cm^{-1}, these peaks are derived from the two C=O groups of copovidone in the acetate and pyrrolidone ring structure respectively. Both act as hydrogen bond acceptors, however, the N-H group in felodipine should preferentially form hydrogen bonds with the C=O in the pyrrolidone ring due to this being a stronger hydrogen bond acceptor compared to the acetate group (Kestur and Taylor, 2010; Song et al., 2013; Taylor et al., 2001). The increased RH does not appear to have any affect on either the absorbance or the positions of these two peaks.

Differential scanning calorimetry

The effects of atmospheric water on solid dispersions are known to cause amorphous-amorphous phase separation and/or crystallisation. These are detectable by DSC from the occurrence of two T_gs, due to a polymer rich and a drug-rich phase and by an additional endothermic peak due to the melting of crystalline regions.

The results of the DSC analysis are shown in Figure 6.6 for days 1, 3, 7 and 14. Broad and large endothermic peaks are visible at 72°C, 63°C, 71°C and 77°C during the first heating of the sample for days 1, 3, 7 and 14 respectively. This has previously been suggested to be due to water vapour being absorbed by the polymer, which is then evaporated off as the temperature increases obscuring the mixed or phase separated T_gs. However, there appears to be no correlation between the position of these peaks or the intensity as the storage time at 85% RH increases. In addition days 1 and 14 exhibit small endothermic peaks at 46°C similar to the T_g of amorphous felodipine, while day 7 has a similar peak at 48°C; no peak is present from the results on day 3. Another endothermic peak can be seen on days 7 and 14 at 118°C. The cause of these peaks are not clear as the T_g for pure copovidone has been reported to be 106°C and the addition of amorphous felodipine to the copovidone would reduce the T_g. In the subsequent scans, the broad peaks and peaks around 45°C and 118°C are no longer visible. Indicating the removal of adsorbed water by the polymer and potentially causing the phase separated regions to reform into a single phase.

On subsequent heatings a single T_g was found for all samples except day 3, where two T_gs were observed at 75.2°C and 101.7°C. The measured T_g for days 0, 1, 7 and 14 were 74.6°C, 74.8°C, 72.5° and 72.6° respectively. Using the Gordon-Taylor equation (Equation 5.2) the T_g for a 50/50 mixture of felodipine/copovidone is predicted to be 64.6°C, although this prediction does not take into account the weight fraction of water that has been absorbed by the polymer. To include water into the Gordon-Taylor equation it would be necessary to measure the amount of water absorbed and recalculate the weight fraction of each component and use the following reworked Gordon-Taylor equation for ternary

systems (Gordon and Taylor, 1952; Lu and Zografi, 1998):

$$T_{g(mix)} = \frac{w_p T_{g,p} + K_{p,d} w_d T_{g,d} + K_{p,w} w_w T_{g,w}}{w_p + K_{p,d} w_d + K_{p,w} w_w} \tag{6.3}$$

$$K_{p,d} = \frac{\rho_p T_{g,p}}{\rho_d T_{g,d}} \; ; \; K_{p,w} = \frac{\rho_p T_{g,p}}{\rho_w T_{g,w}} \tag{6.4}$$

where w, T_g and ρ are the weight fractions, glass transition temperature in Kelvin, and density of the pure components respectively for the polymer (p), water (w) and drug (d). The amount of water absorbed was not measured here

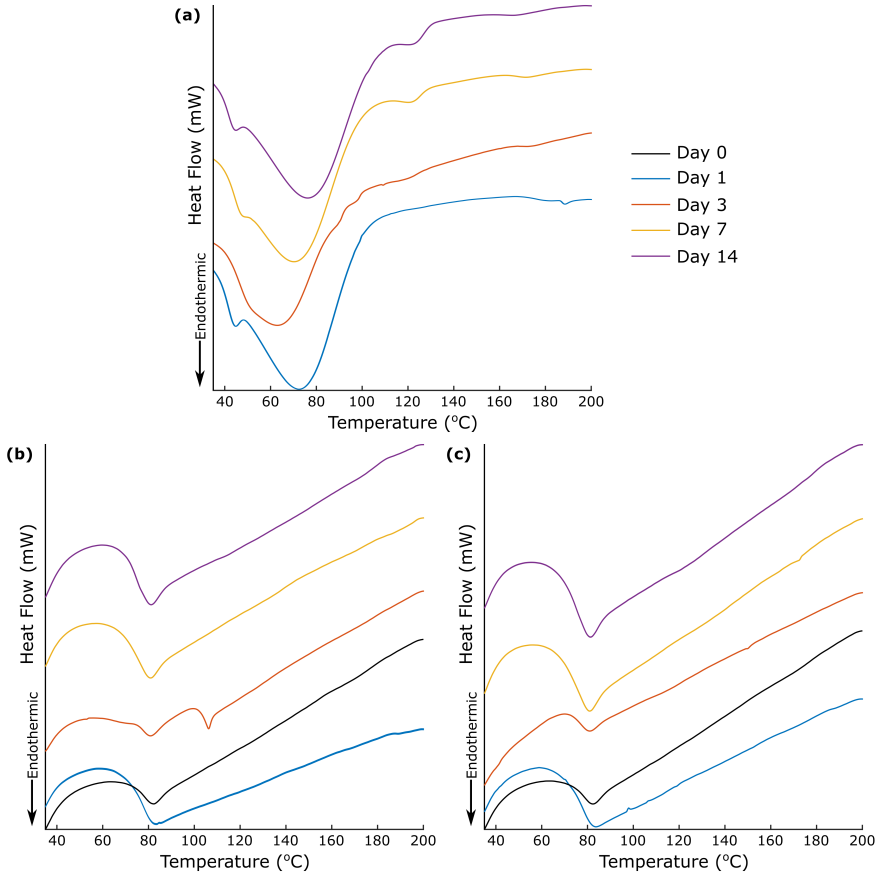

Figure 6.6: DSC of 50% felodipine/copovidone solid dispersion prepared via hot melt extrusion and stored at room temperature and 85% relative humidity (a) run one; (b) run two; (c) run three.

but water is known to cause a plasticising effect which would decrease the ternary predicted T_g from that of the binary system prediction. The direction and amount of deviation from the predicted T_g have been associated with the intermolecular hydrogen bonds between the polymer and drug and the number/strength of these bonds (Patterson et al., 2007; Taylor and Zografi, 1998). The small decrease in T_g between days 3 and 7 suggests a slight change in stability or decrease in the intermolecular bonding strength/number between the amorphous felodipine and copovidone, although not enough to cause amorphous phase separation or crystallisation. Furthermore, the plasticising effect of water was not observed by DSC since a previous measurement on a sample not stored at increased RH also showed a single T_g at 74.6°C (runs two and three shown in Figure 6.6).

Transmission electron microscopy

Bright field (BF) images, conical DF videos, SAED patterns and EDX spectra were all collected on multiple regions that appeared to be crystalline in TEM on days 1, 3, 7 and 14. All the images and indexed diffraction patterns not shown in this section from each region that was analysed can be found in Appendix B.

During day 1 of storage at 85% RH, a single crystalline region of felodipine was identified from a total of 11 regions that were analysed. Two diffraction spots can be seen in the electron diffraction pattern in Figure 6.7. These diffraction spots appear to be from the same systematic row with a single crystal and match either the (011), (220), (002) or (110) d-spacings within felodipine forms I, II, III and IV respectively. The conical DF results were unable to identify or resolve any particles that may be the origin of these diffraction spots. If the diffraction spot intensities are low then the resulting contrast in the conical DF will also be low making it difficult to distinguish crystalline particles from the background. Furthermore, the size of a single pixel in the DF image is approximately 8 nm in size, therefore particles similar in size or smaller are unresolvable. Although the BF image shows various darker particles that are approximately 50 - 250 nm in size, possibly the origin of diffraction.

During day 3 of storage at 85% RH, 5 different crystalline regions were identified from a total of 9 regions examined. Two of these regions contained single

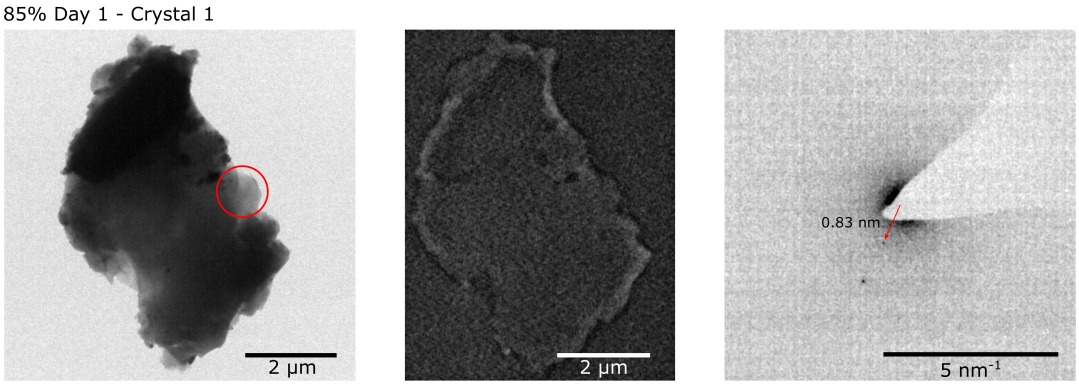

Figure 6.7: Crystalline area 1 examined on day 1 of storage at 85% relative humidity. The d-spacing of 0.83 nm can be indexed to either (011), (220), (002) or (110) spacings within felodipine forms I, II, III and IV respectively.

crystals, 2 were polycrystalline and 1 was crystalline in the conical DF video but appeared amorphous by SAED; most likely due to extended electron beam exposure and fading of the electron diffraction pattern. An example of a single crystal region is shown in Figure 6.8. The diffraction spots that are from the same single crystal are shown by the red arrows while spots circled in blue appear to be from different crystals. Spots 1, 2 and 3 and the angles between these spots are indexable to all forms of felodipine, summarised in Table 6.1. The DF image displays two crystals within the area selected for electron diffraction; these particles are 450 × 250 nm and 100 × 50 nm in size. A polycrystalline region is shown in Figure 6.9. From the DF image the particle at the top, where the selected area aperture was positioned, can be seen to contain multiple crystalline areas. The SAED pattern agrees with the DF image as the pattern consists of multiple randomly orientated crystals. The measured d-spacings can be assigned to multiple d-spacings within all forms of felodipine some of these spacings are shown in Table 6.2.

During day 7 of the ageing study 8 different regions were analysed by TEM, however, no crystalline regions were found after processing the DF videos or from the SAED patterns. The final measurements were taken after ageing for 14 days, here 4 different crystalline regions were identified from a total of 9. Three of

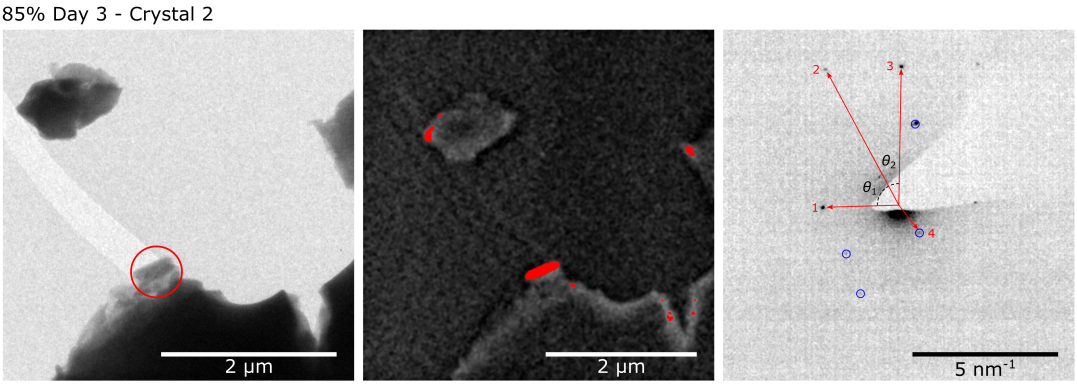

Figure 6.8: Crystalline area 2 examined on day 3 of storage at 85% RH. Indexable to all crystalline forms of felodipine. Spots circled in blue are from a different crystal.

Table 6.1: Crystalline area 2 examined on day 3 of storage at 85% RH. Measured d-spacings and angles compared to theoretical values for felodipine polymorphs for the diffraction pattern shown in Figure 6.8. Average percentage errors between measured and theoretical values are equal to 0.8 ± 0.3, 0.9 ± 0.8, 6.0 ± 0.6 and 4.2 ± 0.5 for forms I, II, III and IV respectively.

Spot	**Distance (nm^{-1})**	**d-spacing (nm^{-1})**	**d-spacing (nm)**				**hkl**			
			I	II	III	IV	I	II	III	IV
1	2.60	0.39	0.38	0.39	0.36	0.40	013	533	$21\bar{4}$	031
2	5.27	0.19	0.19	0.20	0.18	0.20	260	14 $\bar{4}$4	041	116
3	4.74	0.21	0.21	0.21	0.20	0.22	$25\bar{3}$	$9\bar{7}1$	$\bar{2}35$	$1\bar{2}5$
4	1.16	0.86	0.85	0.87	0.81	0.90	011	311	002	011
θ_1	-	64°	63°	65°	65°	63°	-	-	-	-
θ_2	-	30°	30°	30°	30°	30°	-	-	-	-

these regions contained single crystals while 1 contained four d-spacings that could be matched to d-spacings within all forms of felodipine. The measured angles between respective diffraction spots did not match the theoretical angles between the potential hkl values suggesting the SAED was formed from multiple crystals (Figure B.4). Figure 6.10 shows an example of a single crystal region. The bright field image shows a faceted particle within the selected area, while the DF image only shows a single crystal face diffracting. The diffraction spots within the SAED electron diffraction pattern can be assigned to either felodipine form I or II (Table 6.3) with percentage errors of 1.2 ± 0.2 and 0.9 ± 0.3 respectively.

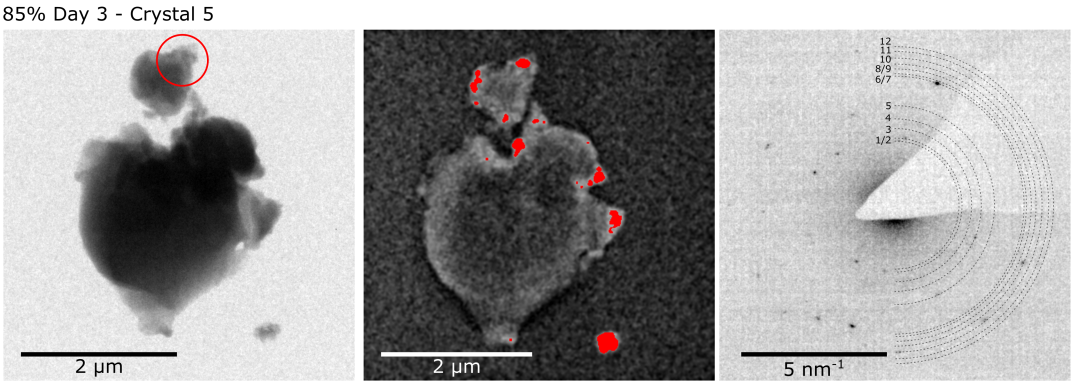

Figure 6.9: Crystalline area 5 examined on day 3 of storage at 85% RH. Indexable to all crystalline forms of felodipine.

Table 6.2: Crystalline area 5 examined on day 3 of storage at 85% RH. Measured d-spacings and angles compared to theoretical values for felodipine polymorphs for the diffraction pattern shown in Figure 6.9. Average percentage errors between measured and theoretical values are equal to 1.3 ± 0.8, 0.1 ± 0.6, 0.6 ± 0.6 and 1.2 ± 1.4 for forms I, II, III and IV respectively.

Spot	**Radial Distance** (nm^{-1})	**d-spacing** (nm^{-1})	**d-spacing (nm)** I	II	III	IV	**hkl** I	II	III	IV
1	2.20	0.45	0.45	0.45	0.45	0.45	102	115	211	$21\bar{2}$
2	2.30	0.43	0.43	0.44	0.43	0.42	$22\bar{1}$	042	013	211
3	2.63	0.38	0.38	0.38	0.38	0.38	$31\bar{2}$	802	$40\bar{2}$	$21\bar{3}$
4	2.96	0.34	0.33	0.34	0.34	0.34	023	$73\bar{3}$	$31\bar{4}$	$22\bar{3}$
5	3.42	0.29	0.29	0.29	0.29	0.29	$12\bar{4}$	$15\bar{5}$	$32\bar{2}$	141
6	4.42	0.23	0.22	0.23	0.23	0.22	$43\bar{4}$	539	132	$24\bar{4}$
7	4.51	0.22	0.21	0.22	0.22	0.21	$44\bar{2}$	084	026	422
8	4.67	0.21	0.21	0.21	0.21	0.21	$51\bar{5}$	$97\bar{1}$	232	431
9	4.84	0.21	0.20	0.21	0.21	0.21	520	683	126	$13\bar{5}$
10	5.04	0.20	0.20	0.20	0.20	0.20	$61\bar{4}$	65 10	$13\bar{5}$	$13\bar{6}$
11	5.27	0.19	0.19	0.19	0.19	0.19	$44\bar{5}$	15 $1\bar{6}$	523	530
12	5.43	0.18	0.18	0.18	0.18	0.18	261	16 $4\bar{2}$	$53\bar{4}$	$12\bar{7}$

All the EDX spectra from each area analysis characterised to have crystalline felodipine appeared to be similar and contained the characteristic $Cl_{K\alpha}$ at 2.62 keV within the area selected for electron diffraction (EDX spectra not shown). This further confirms the presence of felodipine.

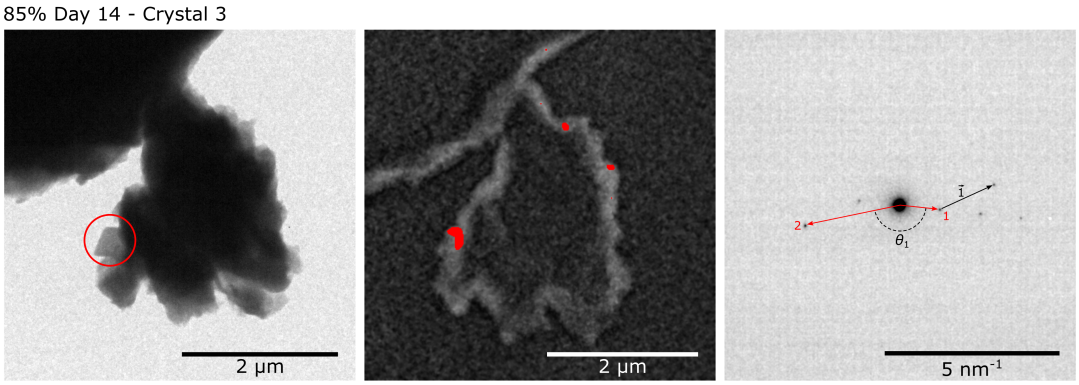

Figure 6.10: Crystalline area 3 examined on day 14 of storage at 85% RH. Indexable to forms I and II felodipine.

Table 6.3: Crystalline area 3 examined on day 14 of storage at 85% RH. Measured d-spacings and angles compared to theoretical values for felodipine polymorphs for the diffraction pattern shown in Figure 6.10. Average percentage errors between measured and theoretical values are equal to 1.2 ± 0.2 and 0.9 ± 0.3 for forms I and II respectively.

Spot	**Distance** ($\mathbf{nm^{-1}}$)	**d-spacing (nm)**	**d-spacing (nm)**		**hkl**	
			I	II	I	II
1	1.16	0.87	0.85	0.87	011	021
2	2.75	0.36	0.36	0.37	122	044
$\vec{1}$	1.68	0.60	0.59	0.60	111	023
θ_1	-	162°	162°	163°	-	-

6.3.2 75% Humidity

Another ageing study was carried out at 75% RH and room temperature and was again used to study the crystallisation of felodipine, however a lower RH was used in an attempt to reduce the rate or crystallisation to allow more detailed analysis of the earlier time points. Here only pXRD and TEM were used to maximise the amount of time available for TEM analysis. The time points that data were collected on were days 0, 1, 2, 4 and 7.

pXRD

No signs of crystallinity was found in the pXRD results on day 0. During day 1 of storage several diffraction peaks began to emerge from the amorphous background, these being the 011, $\bar{3}11$, $12\bar{3}$, $21\bar{3}$, $\bar{3}21$ and 321 of form I felodipine. The intensity of these peaks began to increase on subsequent days (days 2, 4 and 7) and more diffraction peaks of form I felodipine became visible ($\bar{1}11$, $10\bar{2}$, 002, $20\bar{2}$, $\bar{1}21$, $\bar{2}21$, $22\bar{3}$, $13\bar{3}$, $\bar{4}12$, 400, $\bar{4}14$, $\bar{1}14$, 223 and $50\bar{2}$).

The amount of crystalline form I was quantified by calculating the % crystalline for each day these were found to be 0%, 3.2%, 4.8%, 7.3% and 9.6% for days 0, 1, 2, 4 and 7 respectively.

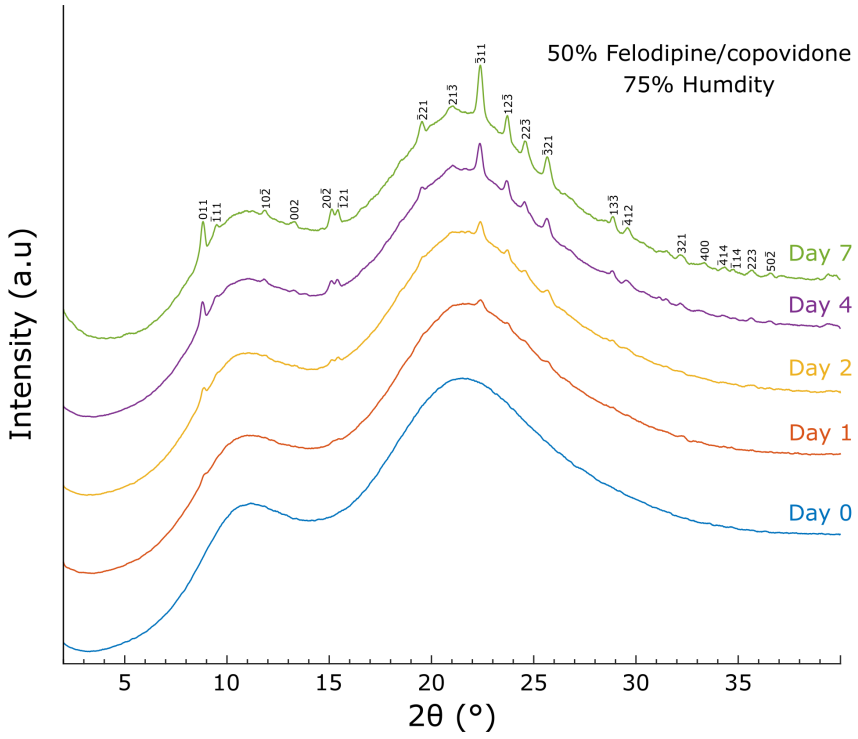

Figure 6.11: pXRD of 50% felodipine/copovidone solid dispersion stored at 75% humidity.

TEM

Bright field images, conical DF videos, SAED patterns and EDX spectra were all collected on multiple regions that appeared to be crystalline by TEM on days 0, 1, 2, 4 and 7. All the images and indexed diffraction patterns not shown in this section from each region that was analysed can be found in Appendix B.

The crystallisation was apparent by TEM from day 0, where 2 crystalline regions were found from the 8 examined. A low fluence BF image, diffraction pattern and high fluence BF image of this area are shown in Figure 6.12. The first BF image showed a large particle, approximately 4 μm in length and 1.5 μm across; much larger than any particle previously in Chapter 5 and the current chapter. From the SAED pattern a single crystal can be identified that contains d-spacings of 0.36 nm, 0.82 nm and 0.39 nm, these can be indexed to $31\bar{1}$, 011 and $\bar{3}02$ d-spacings in felodipine form I (3.64 ± 0.42) and is along the [233] zone axis. The hkl of $\bar{3}35$, 220 and $5\bar{1}\bar{5}$ in form II felodipine along the $[\bar{5}5\bar{6}]$ zone axis can also be assigned to the diffraction spots (1.48 ± 0.28); the results are summarised in Table 6.4.

Six diffraction spots, highlighted by blue circles, are visible within the diffraction pattern that was not indexable to the same crystal/zone axis, this shows that more than one crystal is present within the selected area. When acquiring a higher magnification image at increased electron flux the crystal deformed by bending and rounding at one end that was previously faceted, clearly showing

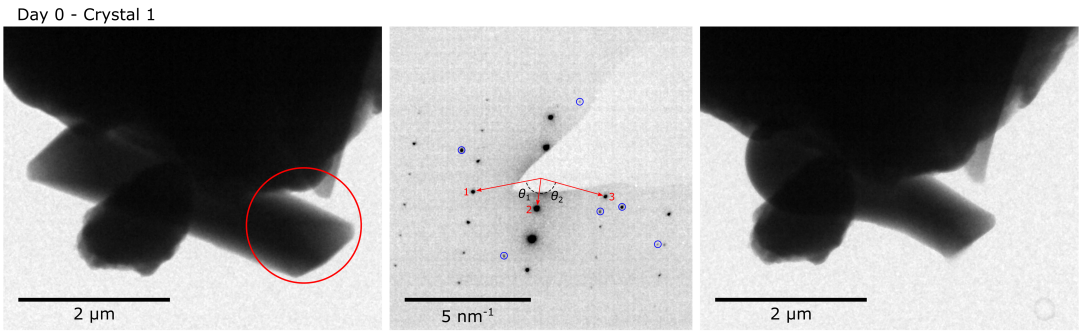

Figure 6.12: Crystalline area 1 examined the day before starting the ageing study at 75% RH. Indexable to felodipine forms I and II.

Table 6.4: Crystalline area 1 examined the day before starting the ageing study at 75% RH. Measured d-spacings and angles compared to theoretical values for felodipine polymorphs for the diffraction pattern shown in Figure 6.12. Average percentage errors between measured and theoretical values are equal to 3.6 ± 0.4 and 1.5 ± 0.3, forms I and II respectively.

Spot	**Distance** (nm^{-1})	**d-spacing** (nm)	**d-spacing (nm)** I	II	**hkl** I	II
1	2.75	0.36	0.38	0.36	$31\bar{1}$	$\bar{3}35$
2	1.22	0.82	0.85	0.81	011	220
3	2.60	0.39	0.40	0.38	$\bar{3}02$	$5\bar{1}\bar{5}$
θ_1	-	70°	71°	70°	-	-
θ_2	-	83°	83°	84°	-	-

the effects of electron beam damage.

The second crystalline region found during day 0 is shown in Figure 6.13. The diffraction spots in the electron diffraction pattern are much fainter in comparison to the previous pattern and can be indexed to forms II (zone axis, [938]), III (zone axis, [301]) and IV (zone axis, [613]), with percentage errors measured as 3.6 ± 1.2, 4.0 ± 0.7 and 5.4 ± 1.7 respectively. It is not clear from the BF image where the diffraction is originating from however, one area appears much darker potentially due to it being crystalline and causing diffraction contrast. If this is the case the particle is approximately 0.4 × 0.2 μm. No conical DF video was

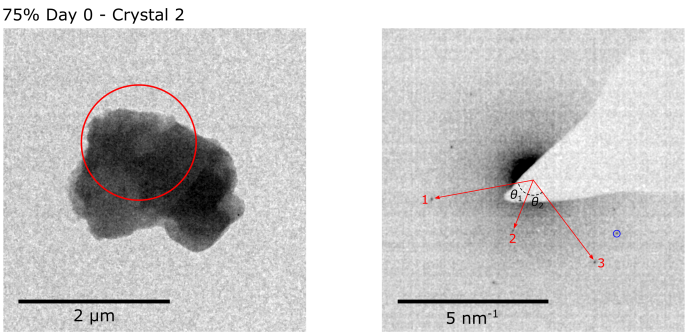

Figure 6.13: Crystalline area 2 examined the day before starting the ageing study at 75% RH. Indexable to forms II, III and IV.

Table 6.5: Crystalline area 2 examined the day before starting the ageing study at 75% RH. Measured d-spacings and angles compared to theoretical values for felodipine polymorphs for the diffraction pattern shown in Figure 6.13. Average percentage errors between measured and theoretical values are equal to 3.6 ± 1.2, 4.0 ± 0.7 and 5.4 ± 1.7, forms II, III and IV respectively.

Spot	**Distance** ($\mathbf{nm^{-1}}$)	**d-spacing** (nm)	**d-spacing (nm)**			**hkl**		
			II	III	IV	II	III	IV
1	3.39	0.30	0.30	0.31	0.31	$6\bar{2}\bar{6}$	$1\bar{2}\bar{3}$	311
2	1.80	0.56	0.57	0.58	0.57	$22\bar{3}$	$10\bar{3}$	012
3	3.44	0.31	0.31	0.31	0.31	$\bar{2}60$	$\bar{1}23$	$\bar{3}13$
θ_1	-	58°	57°	58°	56°	-	-	-
θ_2	-	59°	58°	58°	58°	-	-	-

acquired in either crystalline areas on day 0.

During day 1 of storage at 75% RH 6 different crystalline regions were found out of a total of 12 that were examined. An example of one of these crystalline regions is shown in Figure 6.14. Here the SAED pattern consists of two systematic rows assumed to be part of the same single crystal and diffraction spots from several other crystals. The systematic rows could be indexed to the 110 and $0\bar{1}1$ in felodipine form I (0.3 ± 0.9) and were part of the [111] zone axis. From the DF

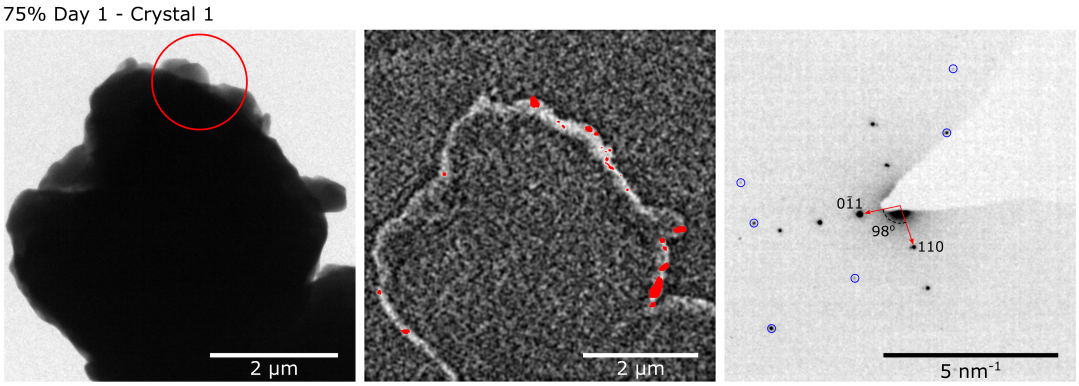

Figure 6.14: Crystalline area 1 examined on day 1 of storage at 75% RH. Indexable to form I felodipine, average percentage errors between measured and theoretical values are equal to 0.3 ± 0.9.

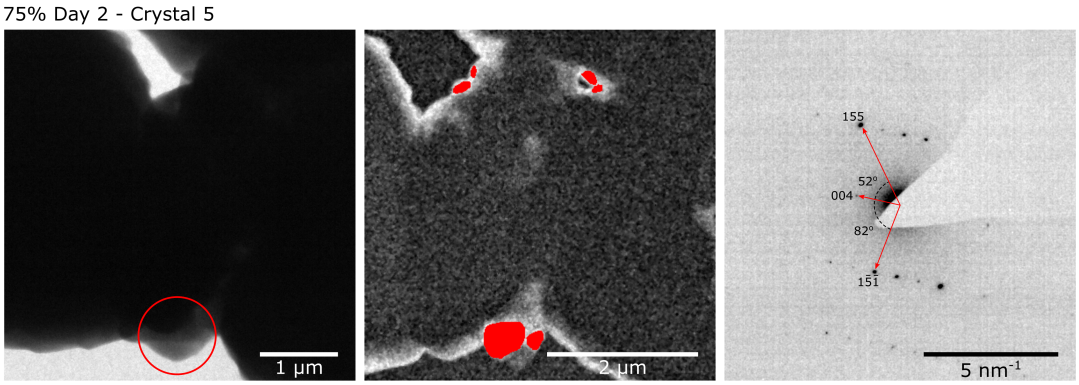

Figure 6.15: Crystalline area 5 examined on day 2 of storage 75% RH. Indexable to form II felodipine, average percentage errors between measured and theoretical values are equal to 3.0 ± 0.7.

image, only one crystalline area (160 × 210 nm in size) can be seen suggesting there may be smaller crystalline particles present that could not be identified due to the low electron fluence and magnification used to capture the images. Other areas that appeared crystalline were identified from the processed conical DF video; crystalline regions varied in size between 80 - 350 nm and tended to occur on the edge of larger particles.

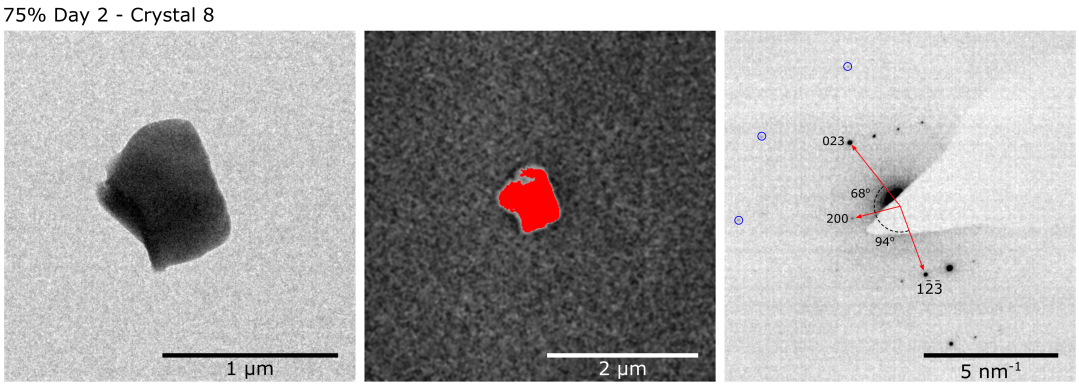

Figure 6.16: Crystalline area 8 examined on day 2 of storage 75% RH. Indexable to form I felodipine, average percentage errors between measured and theoretical values are equal to 1.5 ± 1.0.

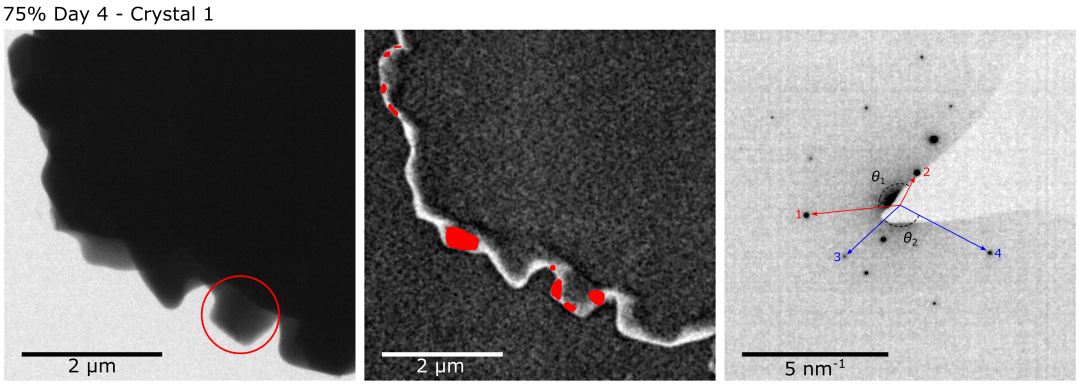

Figure 6.17: Crystalline area 1 examined on day 4 of storage 75% RH. Two single crystal patterns can be seen and d-spacings 1 and 2 are from one crystal and d-spacings 3 and 4 from the other crystal and can be indexed to felodipine form I and II.

Table 6.6: Crystalline area 1 examined on day 4 of storage 75% RH. Measured d-spacings and angles compared to theoretical values for felodipine polymorphs for the diffraction pattern shown in Figure 6.17. Average percentage errors between measured and theoretical values are equal to 1.6 ± 3.1 and 2.1 ± 1.0, forms I and II respectively.

Spot	**Distance** ($\mathbf{nm^{-1}}$)	**d-spacing** (nm)	**d-spacing (nm)**		**hkl**	
			I	II	I	II
1	3.24	0.31	0.30	0.31	$3\bar{1}1$	445
2	1.28	0.78	0.80	0.77	$\bar{1}\bar{1}0$	$\bar{2}\bar{2}1$
3	2.57	0.39	0.40	0.38	220	$44\bar{2}$
4	3.45	0.29	0.30	0.28	$00\bar{4}$	$3\bar{5}\bar{5}$
θ_1	-	122	122	121	-	-
θ_2	-	110	109	108	-	-

During day 2 of analysis, 8 crystalline regions were identified from a total of 14 that were examined. An example of one of these crystalline regions is shown in Figure 6.15. The SAED pattern displays a single crystal that can only be indexed to felodipine form II (3.0 ± 0.7) and sit along the [510] zone axis. From the DF image, two bright regions can be seen from the selected area measured at 250 and 500 nm in size. The BF image shown was acquired at a higher electron fluence and the crystalline area has decreased in size compared to the DF image

due to exposure to the electron beam.

Another crystalline region from day 2 is shown in Figure 6.16. This is an isolated particle approximately 800 nm in size. The SAED displays single crystal pattern that can only be indexed to felodipine form I (1.5 ± 1.0) and sits along the [032] zone axis. Three other diffraction spots are highlighted by blue circles that are not part of the same zone axis/crystal.

During day 4 of analyse, 5 crystalline regions were identified from a total of ten that were examined. Figure 6.17 displays an example of one of the regions analysed. A particle that appeared faceted can be seen in the bright field image. When compared to the DF image four bright regions can be seen from the selected area and are measured at 100 - 350 nm in size. Additional crystalline areas can be found along the edges of the much larger particle. The SAED pattern appears to contain two separate single crystals. The measured d-spacings and angles between diffraction spots can be assigned to the $3\bar{1}1$ and $\bar{1}\bar{1}0$ for one crystal and 220 and $00\bar{4}$ for the other crystal in felodipine form I (1.6 ± 3.1) corresponded to the [114] and [110] zone axes. The d-spacings 445 and $\bar{2}\bar{2}1$ in felodipine form II (2.1 ± 1.0) can also be assigned to one of the crystals and corresponds to the [110] zone axis, while the other crystal can be assigned to the $44\bar{2}$ and $3\bar{5}\bar{5}$ spacings and sits along the [15 7 16] zone axis. The results are summarised in Table 6.6.

All the EDX spectra from each area analysis and characterised as crystalline felodipine appeared to be similar and contained the characteristic $Cl_{K\alpha}$ at 2.62 keV within the area selected for electron diffraction (EDX spectra not shown). This further confirms the presence of felodipine.

In addition to the identified crystalline regions, days 1 and 4 displayed areas that appeared to demonstrate amorphous phase separation between felodipine and copovidone. These areas are shown in Figure 6.18. Here the BF images display dark particles that varied in size between each area. On day 1 the phase separated 'particle' size was normally distributed and the mean size was measured at 65 nm with a standard deviation of ±25 nm (Figure 6.18a). On day 4 a large dark area on the right-hand side of the bright field image is displayed, with smaller particles on the left (Figure 6.18b). The particle size distribution was non-normal and skewed towards the smaller particle size, the median value was measured at 156 nm, lower quartile at 122 nm and the upper quartile at

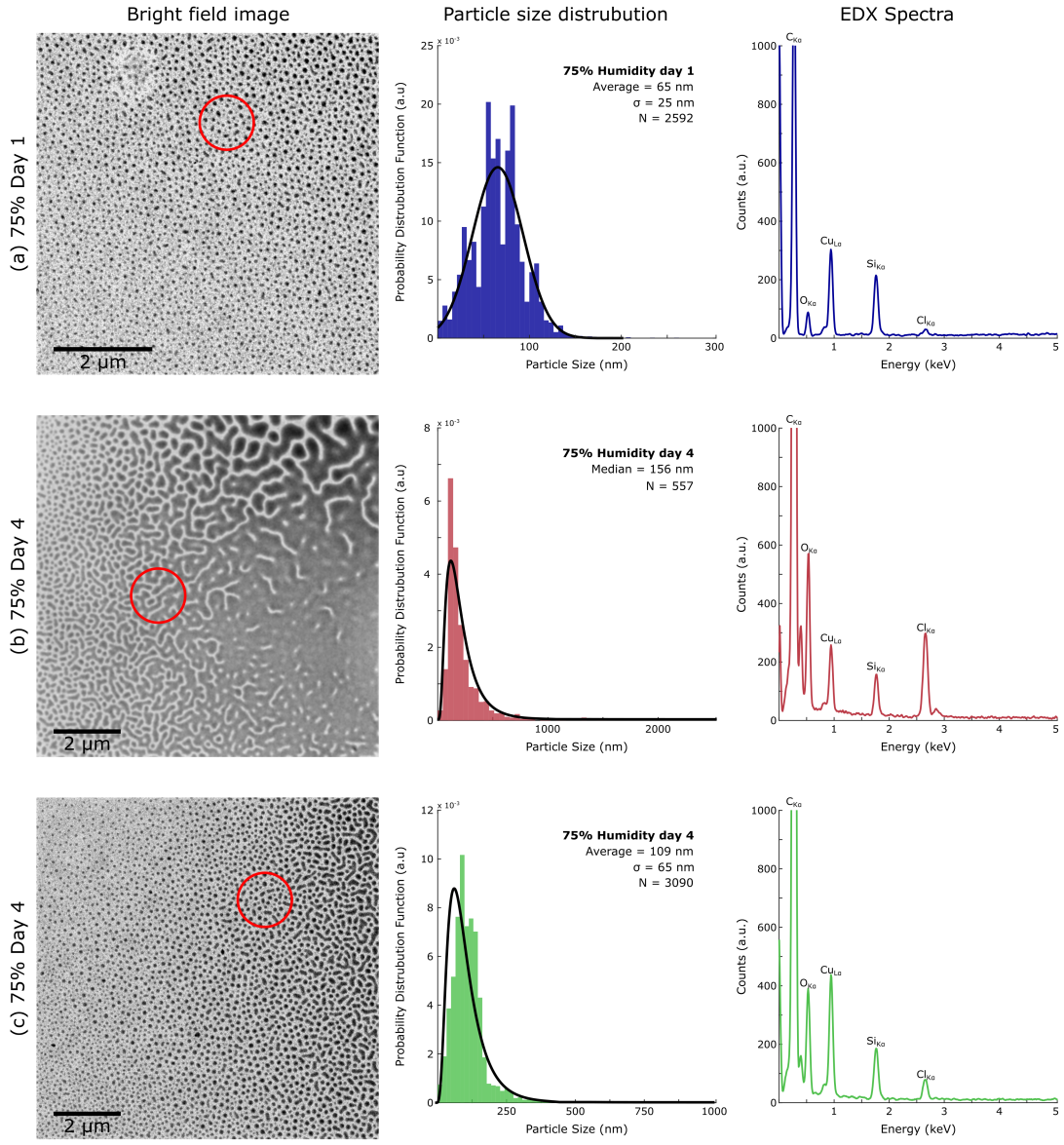

Figure 6.18: Apparent phase separation of three areas showing the BF image of the area, particle size distrubution and EDX spectrum for (a) day 1 stored at 75% humidity; (b) day 4 stored at 75% humidity, large area was sensitive to the electron beam; (c) day 4 stored at 75% humidity.

244 nm. When operating the microscope this large area appeared to decrease in size as the electron flux/fluence was increased suggesting the formation of these

particles may be a beam induced effect rather than phase separation, however further investigation to reproducibly find these areas would be required. The final region in Figure 6.18c was from a different area but the same grid square as Figure 6.18b. Here the particle size is normally distributed and the mean size is measured at 109 nm with a standard deviation of ±65 nm. If these areas are not artefacts of electron beam damage then the size of the particle increases between days 1 and 4. No SAED pattern was captured to detect for crystallinity as it was assumed that if any crystallinity existed it would have been destroyed by the electron beam. Assuming the particles are amorphous this shows evidence of amorphous-amorphous phase separation and suggests that the drug-rich regions are thermodynamically or kinetically stable (up to a point) without the presence of the polymer. All of these areas contained the characteristic $Cl_{K\alpha}$ peak confirming the presence of felodipine. Similar areas were found in a study by Li et al. (2017) where they were examining the impact of water on amorphous solid dispersion films of a drug evacetrapib and two polymers, copovidone and HPMC. Amorphous phase separation was observable by TEM when the samples at various drug loading levels were stored at 50% RH and 97% RH. Larger phase separated domains were found in lower drug loading levels, most likely due to increases polymer concentration and therefore water absorption The phase separated particles appeared to contain the polymer and appeared lighter in contrast compared to the continuous phase that was thought to contain the drug, identified by EDX.

Figure 6.19 shows two other regions from days 1 and 4, where isolated near spherical particles approximately 1 μm in size are observed. These particles were only found on these days and weakly scattered the electron beam making them difficult to find. More examples of these particles are shown in Appendix B. The SAED patterns show a textured polycrystalline material with a d-spacing of 0.40 ± 0.02 nm. The polycrystalline ring generally faded after an electron fluence of approximately 5.5 $e^-/Å^2$, appearing slightly more stable than crystalline felodipine that has a critical fluence of 2.1 ± 0.9 $e^-/Å^2$. However, 5.5 $e^-/Å^2$ is the extinction fluence (electron fluence for the pattern to completely fade) rather than the critical fluence. From the EDX spectrum acquired in all regions containing these particles a small $Cl_{K\alpha}$ can be seen, higher than the background levels

from the carbon film. This indicates that small amounts of felodipine are contained within these areas, although it is not clear if copovidone is also present. If copovidone is present these particles may be polymer-rich phases containing a low level of semi-crystalline drug or they could be partially solvated felodipine due to the increased atmospheric water content. These particles had not previously been observed in any other sample suggesting they are induced by the absorption of water by the solid dispersion. Similar spherical droplet like particles of nanosuspensions have been found previously by Harmon et al. (2016) and Lindfors et al. (2007) by cryo-TEM. In both cases the nanosuspensions were stabilised using a surfactant and an increase in surfactant concentration formed smaller droplets. Harmon et al. (2016) also prepared samples containing no surfactant and when HME ASD were added to a solution of water they formed amorphous scaffolds

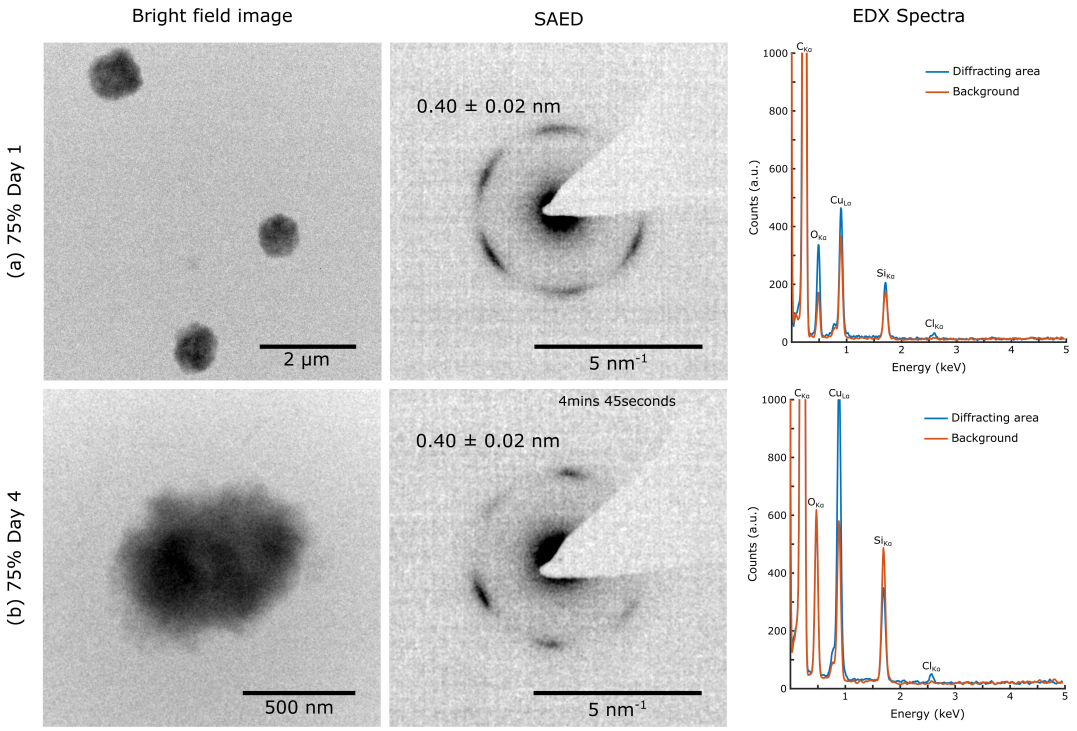

Figure 6.19: Bright field image of weakly scattering areas, SAED shows a textured polycrystalline pattern with a single ring at 0.40 ± 0.02 nm and corresponding EDX spectra revealing the presence of Cl (a) 75% humidity day 1; (b) 75% humidity day 4.

that converted to submicrometre particles. A more detailed analysis is required to further determine the exact nature of the particles here.

6.3.3 Further discussion

Adsorption of water within a binary ASD system is known to modify the thermodynamics and kinetics properties of the system (Purohit and Taylor, 2017). The addition of water influences the kinetics of a ASD by creating a plasticising effect that enhances the molecular mobility and in turn lowers the viscosity and T_g (Andronis et al., 1999; Shamblin and Zografi, 1999). The thermodynamics of ASD systems can be modelled using the Flory-Huggins equation and can evaluate the entropic and enthalpic changes due to the water (Flory, 1942; Zhang and Zografi, 2001).

$$\frac{\Delta G_{mix}}{RT} = n_w ln\Phi_w + n_d ln\Phi_d + n_p ln\Phi_p + n_w\Phi_d\chi_{wd} + n_w\Phi_p\chi_{wp} + n_d\Phi_p\chi_{dp} \quad (6.5)$$

where ΔG_{mix} is the Gibbs free energy of mixing, R is the universal gas constant equal to 8.314 J/(mol K), T is the temperature in Kelvin, n the number of moles, Φ is the volume fraction and χ is the interaction parameter/Flory-Huggins parameter. Subscripts w, p and d denote the water, polymer and drug respectively. The first three terms in the equation represent the entropic contribution due to the addition of water, which reduces the free energy as a result of the increased number of moles and the higher randomness added to the system. The latter three terms are the enthalpic contributions between d-p, p-w and d-w. Values of $\chi > 2$ indicate highly unfavourable interactions between the two components, values < 2 including zero and negative values indicate favourable/not highly unfavourable interactions. Large χ values occur between hydrophobic drugs and water due to the immiscibility between the two components while hygroscopic polymers and water favourable mix resulting in a small χ value. If $\Delta\chi$, the difference between χ_{wd} and χ_{wp} is large then it will be thermodynamically favourable for the system to phase separate into a drug-rich phase and polymer rich phase, this is called the $\Delta\chi$ effect (Robard et al., 1977). The thermodynamic effects

and the kinetic effects (discussed later on) can be used to explain the observed results.

It was expected that the DSC results would clearly demonstrate a decrease in T_g between the sample stored at day 0 and when exposed to increased relative humidity, due to the plasticising effect of water. However, T_g appeared relatively constant between days 0, 1 and 3 and only decreased by 2.7° between days 3 and 7 suggesting the water had little effect on the amorphous solid dispersion. The discrepancy between the results presented here and literature may be due to the sample not being freshly prepared and sufficient water already being present within the system, therefore all measured T_gs contained the plasticising effect. Furthermore, two T_gs are expected if moisture-induced phase separation had occurred; the second run on day 3 of storage was the only sample that exhibited two obvious T_gs these being at 75.2°C and 101.7°C. The T_g of a drug-rich phase would be expected to decrease due to the increase in drug concentration relative to the polymer concentration, however, the first T_g is similar to the measured T_g on none aged 50% drug loading samples on day 1 of storage. The second T_g noticeable increases and is approximately 5° lower than the T_g of pure copovidone, suggesting a polymer-rich phase or unreacted copovidone. The possibility of phase separation within the ASDs being present is reinforced by the TEM results shown Figure 6.18, this was observed much less frequently than crystalline areas, suggesting in some cases the amount occurring may be below the limits of detection for DSC.

Both the pXRD and FTIR results for storage at 85% RH and the pXRD for 75% RH demonstrate crystallisation of form I felodipine from the ASDs much faster than expected. Previous results by Rumondor et al. (2009c) showed that crystallinity in a 50:50 felodipine and PVP ASD system prepared by rotary evaporation and stored at 75% RH and room temperature was detectable by pXRD after 29 days of storage, resulting in approximately 10% crystallinity and plateaued at 40% crystallinity after 114 days. The same system stored at 85% RH crystallised within 10 days and appeared to be approximately 30% crystalline and plateaued at 70% crystallinity after 50 days. Compared to the results presented here for the first week of ageing; storage at 85% RH and room temperature on days 1, 3, and 7 showed 0%, 6.1% and 11.3% crystallinity respectively and storage

at 75% RH and room temperature showed % crystalline of 3.2%, 4.8%, 7.3% and 9.6% on days 1, 2, 4 and 7; showing similar crystallinity values and growth rates at both storage conditions Solid dispersions prepared using copovidone are known to be less hygroscopic and absorb less water than ASDs prepared using PVP. The weight fraction between adsorbed water and pure PVP has been measured at 0.26 and 0.36 for 75% and 85% RH respectively, compared to 0.17 and 0.24 for pure copovidone (Prudic et al., 2015; Taylor et al., 2001). The larger amount of water absorbed has been shown to increase the rates of amorphous phase separation and recrystallisation; therefore, amorphous phase separation and crystallisation would be expected to occur more in the felodipine/PVP. If the measurement of crystallinity was extended for a longer period of time in the copovidone system it would be reasonable to expect that the overall amount of recrystallisation to occur would be less than PVP; due to less water being absorbed and the stronger intermolecular bonds between the drug and polymer preventing the majority of the solid dispersion from demixing (Rumondor et al., 2009b). However the felodipine that does demix from the polymer then rapidly crystallises. Thus the majority of strongly interacting copovidone and felodipine bonds remain intact but the minority of unmixed material transforms rapidly, this is consistent with the TEM results that suggest that in most cases once the material demixes crystals are then formed.

A recent study by Luebbert and Sadowski (2017) examined moisture induced phase separation and recrystallisation in two different APIs; felodipine and ibuprofen mixed with either PVP, PVAC or copovidone prepared by spray drying. It was found that when stored at 40° and 75% RH the onset of crystallisation of amorphous felodipine from copovidone would occur after 42 days in 60% drug loading and 314 days for 40% drug loading, suggesting for a freshly prepared sample at 50% drug loading recrystallisation would occur at some point between 42 and 314 days for spray dried samples. However, here the onset of crystallisation occurred after between 1 to 3 days of storage. Different preparation methods were used between this study and Luebbert and Sadowski (2017), from Chapter 5 it was suggested that HME more readily crystallises than spray dried samples, which would result in more rapid crystallisation. The sample examined here had not been freshly prepared which may have influenced the stability of the ASD

despite it being found to be amorphous by pXRD before beginning the ageing study. Storage below the T_g is known to inhibit the global molecular mobility and therefore crystal growth, kinetically stabilising the ASD, storage at low RH decreases the water absorption from the air which can lead to the plasticising effect reducing the T_g. However, the ASD remains thermodynamically unstable. β-relaxations which are the local molecular motions between molecules in the solid dispersion have a low energy barrier and could form very small crystal nuclei or phase separated regions but are prevent from growing larger due to the polymer and low global molecular mobility. Upon exposure to the humid atmosphere, the absorbed water then reduces the global mobility by preferentially bonding with copovidone allowing crystal growth to occur more rapidly than in a freshly prepared sample.

The particles size of all the crystal areas found during each day of the ageing study was measured and fitted using a log-normal distribution; this type of distribution has been shown to generally fit the distrubution of crystallite size (Ungár et al., 2001). The median particles size and lower and upper quartiles were measured at 80 nm ($Q_{0.25}$ = 60 nm, $Q_{0.75}$ = 130), 90 nm ($Q_{0.25}$ = 60 nm, $Q_{0.75}$ = 210) and 180 nm ($Q_{0.25}$ = 100 nm, $Q_{0.75}$ = 280) on day 1, 2 and 4 when stored at 75% RH respectively. When stored at 85% RH the median particle size and lower and upper quartiles were measured at 60 nm ($Q_{0.25}$ = 50 nm, $Q_{0.75}$ = 130) and 110 nm ($Q_{0.25}$ = 90 nm, $Q_{0.75}$ = 150) for days 3 and 14 respectively. The data are skewed towards the smaller particle sizes for all days and storage conditions, as can be seen from Figure 6.20 and from the interquartile range between the median and $quartile_{0.25}$ being smaller than the interquartile range between $quartile_{0.75}$ and the median. The median particle size increases between each day (for the separate storage conditions) and the upper quartile also increased while the lower quartile either stayed the same or increased. This indicates that the area of the crystalline material is increasing in size over time and crystal growth is occurring, as indicated by pXRD (Figures 6.4 and 6.11). It is difficult to determine the rate of crystal growth from the data and the effects of differences in RH on the growth rates due to the limited number of data points and the number of areas that can be found during analysis on each day.

Multiple crystalline forms can be identified by TEM, these are summarised in Tables 6.7 and 6.8 which show the possible crystalline form of felodipine that match to the measured d-spacings and angles between the diffraction spots when a single crystal is present. The tables also show when one or more polymorph provides a smaller error/error range than other polymorphs. In some cases a single polymorph provides a better match to the observed diffraction pattern, Figure 6.21 shows a bar graph of the possible occurrences for each polymorph and the number of occurrences when a single polymorph provides a better match than any other. From this graph form II appears to occur the most often followed by form I, while forms III and IV match some diffraction patterns better than the other polymorphs but not as frequently as forms I and II. The appearance of forms II, III and IV in TEM is in contrast to both the pXRD and FTIR results which only identified felodipine form I. It fairly well established that the phase

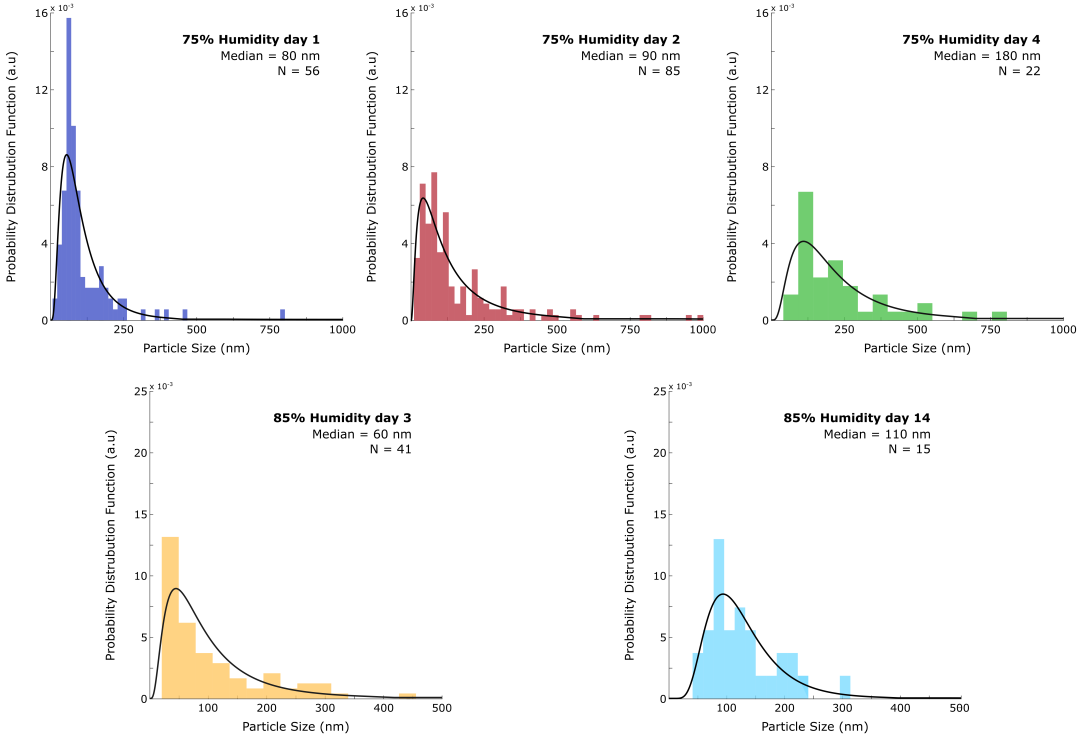

Figure 6.20: Particle size distributions measured by conical dark field for each day that crystalline areas were found. Fitted using a log normal distrubution.

that nucleates first tends to be the one with the lowest free-energy barrier of formation and closest Gibbs energy to the initial state rather than the overall most stable (Stranski and Totomanow, 1933; Turnbull, 1981). This suggests that form II may be thermodynamically more favourable to form from the amorphous phase than form I meaning a lower activation energy barrier needs to be overcome to form the crystal nuclei. The activation energy barrier of nucleation for classical nucleation theory is shown in Equation 6.6 (Turnbull and Fisher, 1949).

$$\Delta G^* = \frac{16\pi\sigma^3}{3\Delta G_v^2} \tag{6.6}$$

Where ΔG^* is the activation energy barrier, ΔG_v is the Gibbs energy difference between the amorphous and crystalline phases and σ is the interfacial energy between the crystal-amorphous phase. Larger values of ΔG_v relates to a higher tendency for nucleation and increased rate and is always higher for more thermodynamically stable polymorphs. While larger values for σ indicates a higher interfacial energy between the crystal and amorphous phase requiring more energy and lowering the rate of nucleation. Crystal forms where the structure is more similar to the amorphous phase will have a lower σ value and therefore increase the rate of nucleation. Therefore form II may be more structurally related to the amorphous phase or requires less energy to form the correct configuration of molecules. Kinetically, as mentioned earlier the addition of atmospheric water increases the molecular mobility and may cause rapid crystallisation, metastable polymorphs tend to preferentially form when crystals are formed quickly compared to slow crystallisation that favours the more thermodynamically stable polymorph (Duong et al., 2018; Lee et al., 2011). Form II is also thought to be a precursor nuclei to form I since they are stabilised by similar synthons and both contain similar 1D hydrogen bonding chains between the N-H group and carbonyl group of the methyl ester along the [110] zone axis (Lou et al., 2009). However, the exact pathway that results in the most stable polymorph forming is unclear since form I could occur from transitions via multiple polymorphs. Indexable patterns to forms III and IV suggests crystallisation might be due to multiple stages and that form II may be the most kinetically stable of these and therefore higher

Table 6.7: Polymorphic forms found in aged samples stored at 85% relative humidity.

Day	Area	Crystal form	Best match
1	1	I, II, III, IV	I, II, III, IV
3	1	I, II, III, IV	II, III
3	2	I, II, III, IV	I
3	3	I, II, III, IV	II, IV
3	4	I, II, III, IV	II, III
14	1	I, II, III, IV	IV
14	2	I, II, III, IV	II, III
14	3	I, II	I, II
14	4	I, II, III	II, III

Table 6.8: Polymorphic forms found in aged samples stored at 75% relative humidity.

Day	Area	Crystal form	Best match
0	1	I, II	II
0	2	II, III, IV	III
1	1	I	I
1	2	I, II, IV	IV
1	3	I, II, III, IV	II, III
1	4	I, II, IV	I, II, IV
1	5	I, II, III	II
1	6	I, II, III, IV	I, II, III, IV
2	1	II, III	II
2	2	II	II
2	3	I, IV	I
2	4	I	I
2	5	II	II
2	6	I, II, III, IV	I, II, III, IV
2	7	I, II	II
2	8	I	I
4	1	I, II, III, IV	II
4	2	I, II	I, II
4	3	I, II, III, IV	I, II
4	4	I, II, III, IV	I, II, III, IV
4	5	II, IV	II

number of areas can be assigned. Alternatively, cross nucleation of polymorphs could result in a mixture of different polymorphs.

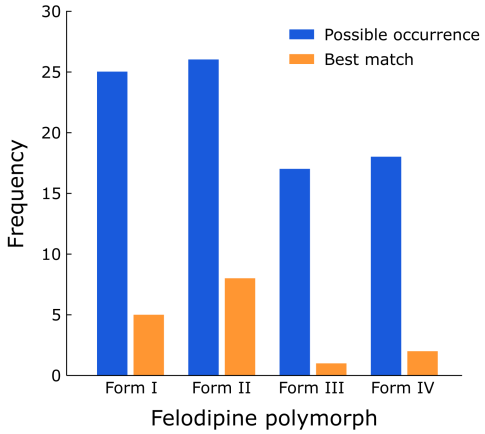

Figure 6.21: Occurrences of overall possible polymorphs found and best matches where a single polymorph provides a smaller error/error range than the rest.

Crystals are consistently found either on the edge of larger particles or larger crystals can be found isolated. A study by Chen et al. (2018) found that the chemical composition of ASD at the surface when exposed to 95% RH change from the original 40% drug loading to 69%. This suggests that the addition of water into the binary system causes the hydrophobic drug to diffuse to the solid-air interface creating a non-homogenous dispersion with different compositions to the surface and bulk. The concentration of the drug is then higher at these surfaces and can lead to supersaturation and homogeneous nucleation. Surface diffusion is also 10^6 - 10^7 times faster than bulk diffusion enabling faster crystal growth at the free surface (Cai et al., 2011; Ishida et al., 2007; Yu, 2016). Previous work by Qi et al. (2011) has studied the crystallisation and phase separation of aged felodipine/Eudgrait® E PO ASD via ATR-FTIR and various AFM techniques. They identified forms I and II within different sections of the extrudate, with form II mainly found within the cross-section of the 50% drug loading sample. This was explained by the centre containing higher drug loading due to thermal expansion of the polymer when leaving the extruder and resulted in homogeneous nucleation of form II. Form I was mainly found at the surfaces of the extrudate and thought to be due to heterogeneous nucleation from dust particles or particles shed from processing.

6.4 Chapter Summary

The aim of this chapter was to investigate the recrystallisation process of amorphous from a 50:50 ASD of felodipine/copovidone prepared via HME. To induce ageing of the ASD it was stored at room temperature and at 85% and 75% RH and analysed at different time points during the crystallisation process. TEM was the main method of analysis and was used to investigate the crystalline areas, identify the polymorph of felodipine that was present and measure particle size. From the results presented it was learnt that:

- TEM is a more sensitive technique than pXRD, FTIR and DSC as it identified crystalline material either on days 0 or 1 of analysis of both the 75% and 85% RH materials.
- FTIR results of the sample stored at 85% RH showed crystallisation on day 3 indicated by the absorbance peak at 3367 cm^{-1} and no amorphous phase separation of felodipine and copovidone was found.
- pXRD identified crystalline form I felodipine as early as day 1 in the sample stored at 75% RH and day 3 for 85% RH.
- Crystallisation occurs in the 50:50 felodipine/copovidone prepared via HME more rapidly but with less overall transformation then previously identified in felodipine/PVP systems prepared by rotary evaporation and felodipine/copovidone systems prepared by spray drying. This may be due to inhomogeneous mixing of copovidone and felodipine.
- Diffraction patterns acquired can be indexed to form I and II, and in some cases diffraction patterns can be indexed to multiple forms of felodipine making it difficult to determine which form is present. However, the sample appears to be a mixture of the metastable polymorphs, predominately form II and the stable form I.
- After image processing conical dark field was useful in both identifying crystals and for measuring the particle/area. The area distribution for

crystalline regions increase in size over time. Consistence with pXRD and FTIR.

- TEM also suggests nucleation and growth occurs at edges of particles as might be expected for water induced transformations.

The final results chapter will build on the work presented thus far by employing promising and complementary electron microscopy techniques to provide mechanistic insight into recrystallisation and information regarding size, shape, form and defects within crystals and were in the solid dispersion they occur.

Chapter 7

Advanced Microscopy Techniques

This chapter is split up into three different microscopy experiments: dual beam focused ion beam scanning electron microscope (FIB-SEM) cross sectioning, scanning moiré fringes (SMFs) in STEM and scanning electron diffraction (SED) in STEM. These techniques have been employed as potentially useful methods of analysis for amorphous solid dispersions and pharmaceuticals in general and can potentially identify and quantify (size, phase and location) in the early stages of crystallisation. The results shown are from one or two days of preliminary experimentation and require further work to fully realise the potential of these techniques.

Focused ion beam was used to cut a cross-section in the sample which was then imaged by SEM of an amorphous solid dispersion (ASD) of 50/50 felodipine and copovidone prepared by hot-melt extrusion (HME). The section was part of the resulting material that left the extruder in the form of rod-like shapes and had not yet been ground into a powder.

Scanning moiré fringes were collected in STEM for asbestos to determine the rotation between the selected area electron diffraction (SAED) patterns, collected in TEM using the CCD, and the bright field (BF) STEM detector. The measured SMFs of asbestos were compared with the predicted values and used to refine the method required in obtaining SMFs before examining more electron beam sensitive materials. This method was then carried out on pure crystalline felodipine to demonstrate detection of crystalline defects within an active pharmaceutical ingredient (API) and potentially quantify the frequency/density of defects.

Scanning electron diffraction was carried out in STEM on pure crystalline felodipine initially as a proof of principle that it was possible to obtain diffraction data without destroying the crystal structure. An ASD of 50/50 felodipine and copovidone prepared via HME that had been stored at 75% humidity for 7 days was then examined to provide further information on the size, phase and location of crystalline particles in the ASD. This sample had previously been examined by TEM during days 0, 1, 2 and 4 of storage and the results were discussed within Chapter 6.

7.1 Focused Ion Beam Cross-Section

Focused ion beam microscopy is a similar technique to SEM, but a beam of ions are used instead of electrons. The greater mass of these charged particles allows material to be removed from the sample via sputtering and enables cross-sections (< 100 nm) of a sample to be cut which can then be imaged by SEM or cut to a lamella and lifted out for analysis by TEM. If gas is injected into the system near the impact points between the ions and sample then material can be deposited on to the sample surface. Dual beam systems combine FIB and SEM to enable high-resolution SEM imaging of the modified sample surface without requiring sample exchange.

7.1.1 Method

A 50/50 felodipine/copovidone ASD was prepared by HME using the same conditions described in Chapters 5 and 6. The resulting extruded product formed rough rod-like shapes as it exited the extruder and were cut into approximately 20 mm sections. In Chapters 5 and 6 these rods were ground to form a powder. Instead of forming a powder one of the rods was resin embedded so the sample could be microtomed using a diamond knife to attempt to cut thin sections for TEM analysis. This was carried out dry to prevent water from interfering with the surface of the solid dispersion. The sectioning was unsuccessful, although, this left a large section with the cross-section of the extruded material exposed. The base of the large section was ground down to form a flat surface which was

then mounted onto an aluminium stub and used as the sample. Before inserting the sample into the FIB-SEM the sample was coated using a 5 nm Ir to reduce charging effects. Iridium was used rather than gold or platinum due to the smaller grain size which are not visible at high magnifications. An FEI Helios G4 CX DualBeam FIB was used to cut a cross-section from the sample of the ASD to determine if there was any evidence of phase separation or crystallisation within the cross-section of the extruded rod by secondary electron and back scattered electron imaging.

7.1.2 Results and Discussion

The results are shown in Figure 7.1 and demonstrate no evidence of phase separation or crystallisation within the ion beam milled section. It would be expected that if phase separation or crystallisation had occurred it would be identifiable by differences in contrast or identification of small denser particles being present. A previous study by Qi et al. (2011) identified that there were differences in the homogeneity of the surface and a cross-section of an aged felodipine/Eudgrait® E PO ASD prepared via HME. The meta-stable polymorph, form II, was mainly found within the cross-section of the 50% drug loading sample and this was thought to be a result of the centre containing a higher drug loading due to thermal expansion of the polymer when leaving the extruder. Lack of phase separation or crystallisation in the result here suggests the sample is homogeneously mixed within this cross-section. Using FIB-SEM to examining multiple areas from near the surface and further inside the cross-section could provide more information regarding where phase separation and crystallisation are occurring.

After ion milling the cross-section a thin lamella section was then prepared for analysis in TEM/STEM. However, when trying to mount the sample onto a TEM grid small bubbles and large vacancies started to appear within the lamella section, resulting in the sample falling off the micro-manipulator. This was a result of electron beam damage sustained to the sample, possibly due to radiolytic induced heating or electrostatic charging of the uncoated section.

Ideally, to prepare the section for TEM/STEM, cryogenic conditions would be used to prevent or reduce the effects of electron beam damage, such as electron

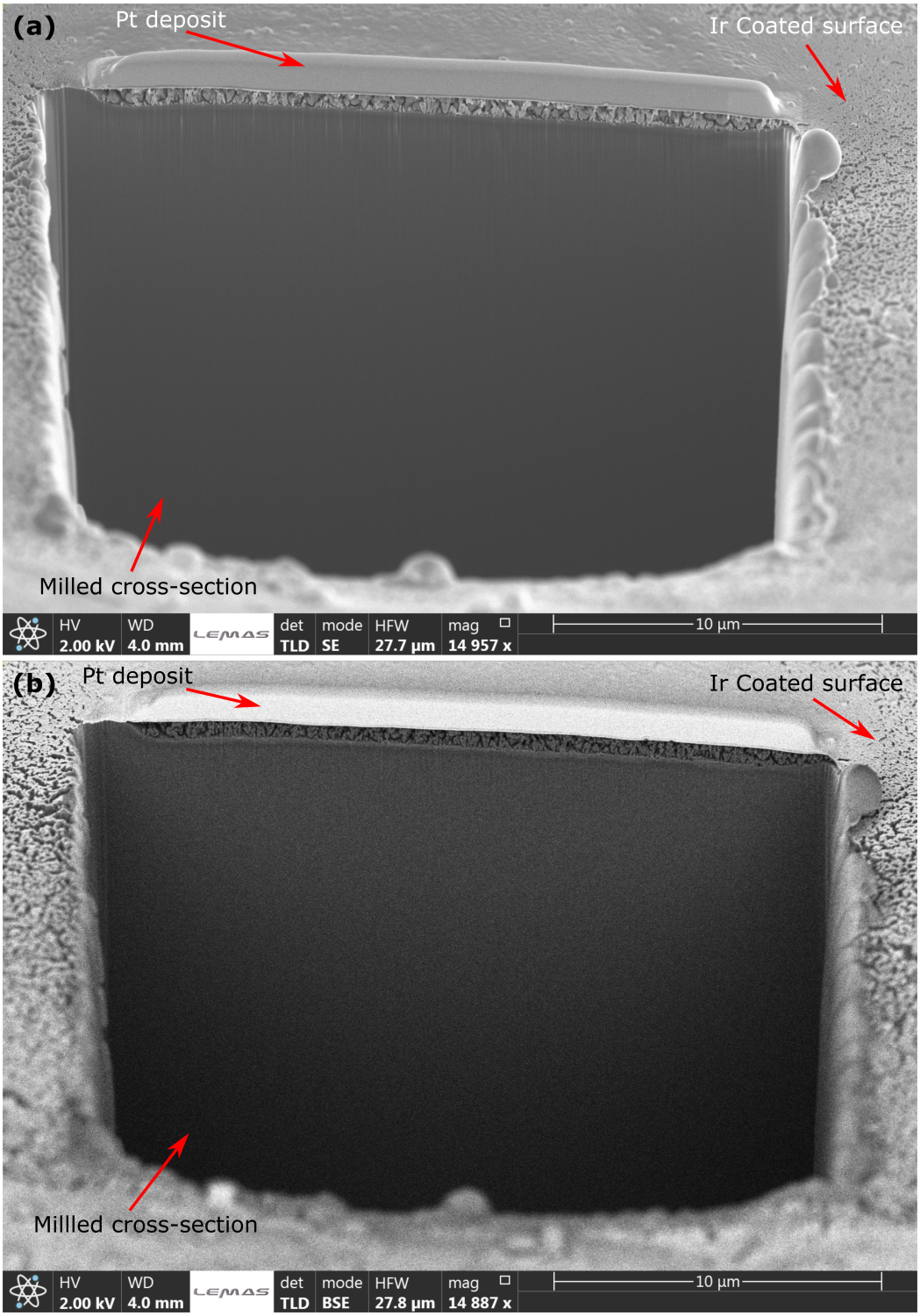

Figure 7.1: FIB-SEM cross-section of the inside of the extruded rod of 50/50 felodipine/copovidone ASD prepared by HME (a) SEM secondary electron image; (b) SEM backscattered electron image. Both images show no signs of phase separation or crystallisation.

beam heating, however, this was not possible at the time. After the section has been mounted onto a TEM grid it could then be cryogenically transferred into the cryo-TEM for analysing. However, this approach at examining beam sensitive materials is still in development here at Leeds and only been demonstrated in a few lab worldwide on biological samples (Mahamid et al., 2015; Parmenter et al., 2016; Rubino et al., 2012).

To further the use of this technique for investigating the homogeneity of extruded ASDs, samples that are known to readily phase separate or a well characterised aged sample could be used and compared to more stable amorphous solid dispersion/fresh samples. This would be helpful in determining the limitations of the technique.

7.2 Scanning Moiré Fringes

Moiré fringes occur due to the interference patterns produced by two similar but non-identical lattices. The difference between the lattices can be due to either size, rotation or a combination of both. In the case of STEM, SMFs are formed via the interference that occurs between the artificial scanned lattice produced by rastering the electron probe in STEM (d_s) and the real space lattice in the crystal being imaged (d_l).

The size of the observed SMFs are dependent on the magnification in STEM which determines the pixel size (alternatively known as the step size) and therefore d_s, the size of d_l and the relative angle (β) between d_s and d_l (Su and Zhu, 2010). If β is equal to zero the lattices form translational moiré fringes (d_{TM}), the size of which can be calculated from Equation 7.1 (Williams and Carter, 2009).

$$d_{TM} = \frac{d_s d_l}{|d_s - d_l|} \tag{7.1}$$

this equation shows that as d_s and d_l become more similar the difference approaches zero, resulting in the size of the SMF to tend towards infinity. When the difference in size between d_s and d_l increases then the resulting SMF decrease in size and are eventually unobservable. If there is an angle β between d_s and d_l

general moiré fringes (d_{GM}) are formed. The exact size can be calculated using Equation 7.2 (Williams and Carter, 2009).

$$d_{GM} = \frac{d_s d_l}{\sqrt{(d_s - d_l)^2 + d_s d_l \beta^2}} \tag{7.2}$$

this equation is similar to Equation 7.1. The additional term in the equation accounts for the rotation between the fringes and as β increases the resulting SMF will decrease. Schematics of both translational and general moiré fringes are shown in Figure 7.2.

This method has generally been developed to analyse large area strain measurements in semiconductors and functional oxides (Ishizuka et al., 2017; Kim et al., 2013a,b; Murakami et al., 2015; Naden et al., 2018; Su and Zhu, 2010; Wen et al., 2018). Scanning moiré imaging has also been used to examine the beam-sensitive mineral (Aquamarine: $Be_3Al_2Si_6O_{18}$:Fe^{2+}) and successfully recorded X-ray and core-loss images of the atomic structure (Kondo and Okunishi, 2014; Kondo et al., 2017).

For electron beam sensitive materials SMFs can effectively provide an image of the crystal lattice at lower magnifications than required to directly image the lattice by phase contrast, thereby reducing the electron fluence and electron beam damage. It is possible to identify the number/density of defects from the SMFs as they will disrupt the regular lattice, however, the type of defect that is observed can be difficult to determine. Lattice fringes can provide important information for pharmaceuticals by identifying the effects of pharmaceutical processing on API properties, such as milling which can introduce crystal defects into crystalline APIs (Byard et al., 2005; Koivisto et al., 2006). Crystal defects in APIs are known to be sites in which polymorphic transformations and hydrate formations are initiated and can have an impact on the solid-state behaviour of the API (Eddleston et al., 2010).

7.2.1 Asbestos

Crocidolite, one of six mineral forms of asbestos was used in a preliminary study to determine: the difference in rotation between the TEM CCD (used to identify real lattice spacings by SAED) and the BF-STEM detector; the effects of pixel size

and β on the measured SMFs compared to predicted values and finally to refine the method required to obtain SMFs before analysing electron beam sensitive materials. The sample was examined in an FEI Titan^3 Thermis operated at an accelerating voltage of 300 kV, equipped with a field emission gun using an extraction voltage of 4.5 kV and a monochromator. The images and diffraction patterns were captured using a Gatan OneView CCD and SMFs using the STEM BF detector.

Ideally, the angle between d_s and d_l is set to be equal to zero resulting in the formation of larger translational moiré fringes, which are easier to interpret than general moirés. Therefore before acquiring SMFs, the rotation that needs to be applied to the scan direction to align d_s and to the observed d_l (by TEM SAED) needs to be calculated. In addition to rotating the scan direction to align the lattice fringes there is a change in rotation between the CCD in TEM and the BF-STEM detector. This also needs to be accounted for when rotating the scan direction to align the fringes.

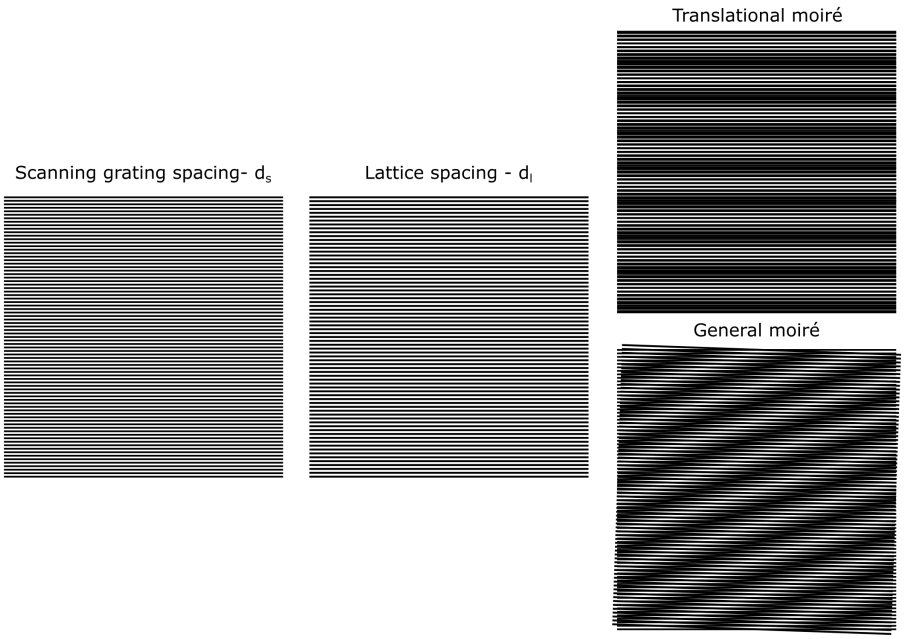

Figure 7.2: Schematic of translational and general moiré fringes created by the crystal lattice (d_l) and the scanning grating lattice (d_s) of similar sizes.

Detector Rotation Measurement

To find the rotation between the two imaging modes a SAED pattern was acquired from a suitable crystal to determine the angle between the vertical cross-section through the zero order diffraction spot and a first-order diffraction spot (θ_{SAED}). Figures 7.3a displays the SAED pattern and the measured θ_{SAED}, 8.5 ± 0.5°.

The microscope was then switched to STEM mode and aligned. A high-resolution lattice image was acquired at 2.39 MX magnification, corresponding to a pixel size of 0.041 nm and is shown in Figure 7.3b. An FFT of the high-resolution image was collected and the angle between the spacings (θ_{FFT}) corresponding to the same spacing examined by SAED and the centre was measured at 2.1 ± 0.2°. From this the difference in rotation between the CCD and BF-STEM detector can be calculated by subtracting θ_{SAED} and θ_{FFT}, resulting in a difference (θ_{diff}) of 6.4 ± 0.7°.

To then calculate the overall rotation required to align both sets of fringes θ_{SAED} is subtracted from θ_{diff}. For the series of images shown in Figure 7.3a, b and c, a clockwise rotation of -2 ± 1.2° is required to make β equal to zero and form translational moiré fringes. It should be noted the angles measured for θ_{SAED} and θ_{FFT} are measured in terms of clockwise rotation.

Therefore if the rotation required to align the diffraction spot or spacing in the FFT is anti-clockwise the angle should be taken as -θ°. An example of this is shown in the set of images in Figure 7.3d, e and f, where θ_{SAED} is equal to -17.3 ± 0.5° and θ_{FFT} is equal to -24.3 ± 0.2° (due to the anti-clockwise rotation) resulting in a θ_{diff} of 7.0 ± 0.7°. This then leads to scan rotation of 24.3 ± 1.2° so that β is equal to zero. For subsequent areas and samples, the average rotation difference between the detectors was taken as 6.7 ± 1.2°.

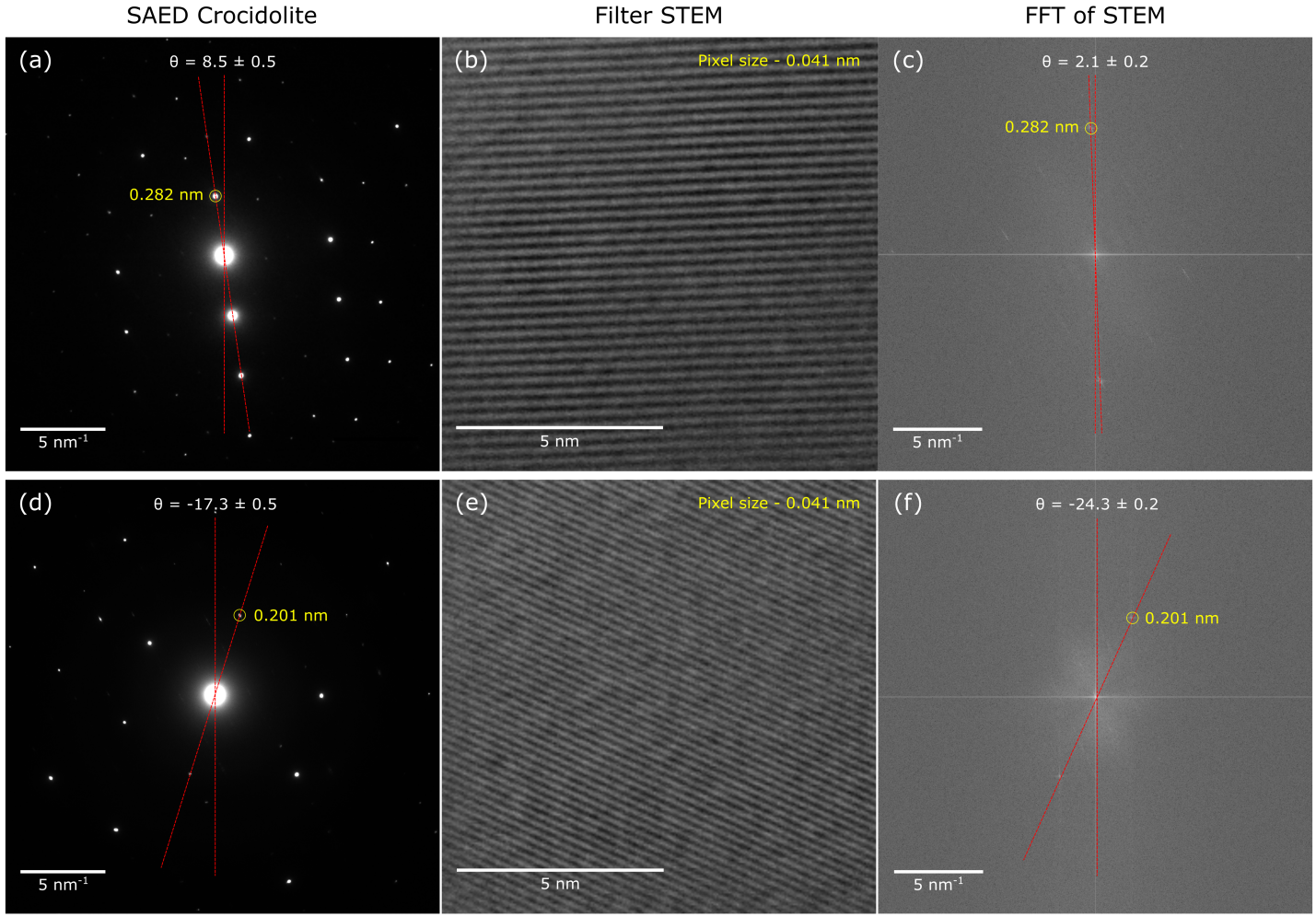

Figure 7.3: Rotation between TEM CCD and scan direction of STEM, a and d show the SAED patterns of different crystals and θ_{SAED}; b and e are high-resolution BF-STEM images of each crystal and c and f are the FFTs of the high-resolution images and θ_{FFT}. The angles measured in the FFT are different to the ones measured from TEM due to the difference in rotation between the TEM CCD and the BF-STEM detector.

Effects of Scan Direction and Pixel Size

After determining the rotation required to align d_s and d_l a series of SMFs were acquired with varying scan directions and magnifications/pixels size to determine how β and d_s affect the size of the measured SMFs. Figure 7.4 display a collection of SMF images that are a result of the interference between the 0.282 nm lattice spacing and a scanning lattice of pixel size 0.233 nm. The angle β was varied between 2.1° and - 2.9° and the resulting size of each SMF was measured via the FFT and are shown for each image. The largest spacing of 1.341 nm was found when β was equal to zero, as expected. A spacing of 1.283 nm was found when β was equal to -2.9°, this being the highest deviation from zero. Figure 7.6a demonstrates the predicted size of the SMF as a function of β, calculated from Equation 7.2. The measured SMFs for each β value were plotted and demonstrate good agreement between the predicted values and the SMF sizes measured via the FFT. The theoretical curve shows that small variations in β when close to zero (± 1°) have a relatively small effect on the size of the SMFs. However, as the angle deviates further from zero then the size begins to decrease. If the graph was extended beyond 5° then the SMF sizes would significantly decrease.

Figure 7.5 displays a collection of SMF images that resulted from the interference between the 0.203 nm lattice spacing and various STEM pixel sizes, these being 0.116 nm, 0.165 nm and 0.233 nm, corresponding to magnifications of 845, 593, 419 KX respectively. The scan direction for each image was adjusted so that β was equal to zero. The largest SMF was measured at 1.447 nm and found using a pixel size of 0.233 nm, the most similar to the lattice spacing of 0.203 nm. The SMF acquired using a 0.116 nm pixel size were 0.264 nm and are difficult to identify as they are only $2-3$ pixels in size, although, the FFT displays distinct spacings. Figure 7.6b demonstrates the theoretical size of the SMFs as a function of STEM pixel size, calculated from Equation 7.1. The measured SMFs for each pixel size value demonstrate a good agreement between the predicted values and the ones measured via the FFT. The theoretical curve shows that as the difference between pixel size and d_l (shown by the dotted line) approaches zero the size of the SMFs dramatically increases with small variations in pixel size and d_l; tending towards infinity.

Figure 7.4: Effect of scan direction in STEM on the size of the observed moiré fringes, the FFT is shown as an insert for each image and was used to measure the size of the SMFs. The angle β and fringe size are displayed for each image; the crystal lattice spacing and STEM pixel size used were equal to 0.282 nm and 0.233 nm respectively.

Figure 7.5: Effect of pixel size in STEM on the size of the observed moiré fringes for the 0.203 nm crystal lattice spacing; the FFT is shown as an insert for each image and was used to measure the size of the SMFs. The pixel size and fringe size are displayed for each image and the scan direction was adjusted so that β was close to zero.

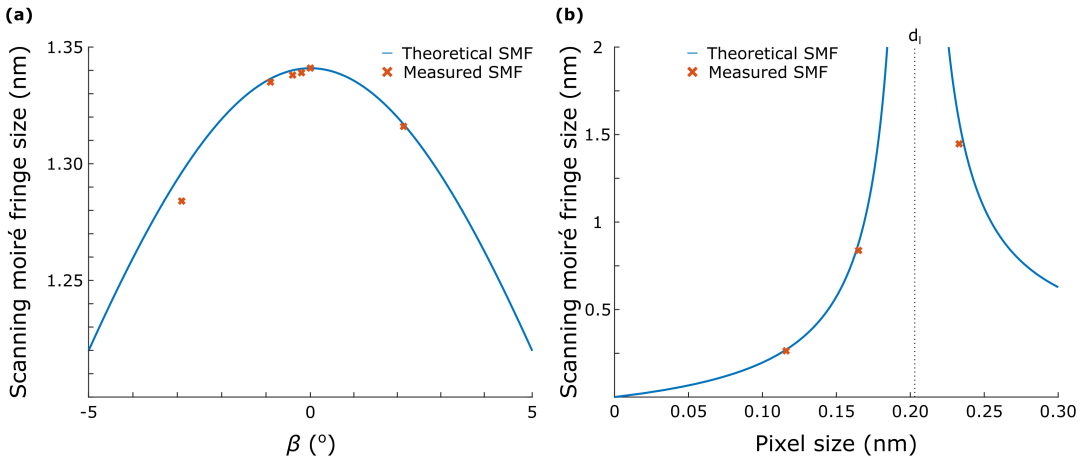

Figure 7.6: Graphs showing the comparison between the measured and calculated size of the SMF as a function of (a) β, calculated from Equation 7.2 and (b) STEM pixel size, calculated from Equation 7.1.

Therefore it is important to determine the pixel size and lattice spacings to relatively good accuracy; similar sized fringes with small measurement errors may lead to large discrepancies between the measured and predicted values.

7.2.2 Felodipine

Pure crystalline felodipine was used as a proof of principle to show that the SMF method could be used as a technique to determine the density/number of crystalline defects in electron beam sensitive organic crystals. The sample was prepared by drop casting approximately $3-4$ drops of the powder that had been suspended in water onto a 400 mesh continuous carbon-coated copper grid. The sample was examined in a FEI Titan^3 Thermis operated at an accelerating voltage of 300 kV, equipped with a field emission gun using an extraction voltage of 4.5 kV and a monochromator. BF images and diffraction patterns were captured using a Gatan OneView CCD and SMF using the STEM BF-detector. The electron beam current was reduced by adjusting the monochromator and the C2 condenser lens to provide an electron flux of approximately 0.1 $e^-/(Å^2\ s)$ in TEM. For STEM the electron fluence was controlled by using a probe current (I) of 5 pA, dwell

time (t) of 10 μs and a pixel size (d_s) of 0.933 nm, Equation 7.3 was used to calculate the electron fluence.

$$F(e^-/\mathring{A}^2) = \frac{I \times t}{e \times d_s^2} \tag{7.3}$$

To acquire SMFs, BF-TEM was used to identify areas that contained strongly diffracting regions. An objective aperture was inserted to increase the contrast while searching for areas. Once an area was identified a SAED pattern was acquired followed by a BF-TEM image. The electron beam was blanked so that the largest spacings within the diffraction pattern could be measured, this was to determine if any of the 10.85 Å 8.53 Å or 8.03 Å spacings of form I felodipine were present. If any of these spacings were found the area was then stored so it could be recalled later on. This process was repeated until several of these areas were found. The scan rotation required to align the two fringes was calculated by measuring θ_{SAED} and subtracting from the previously established 6.7°, before then operating the microscope in STEM mode. All areas were found in TEM before changing to STEM to reduce the time taken to switch back and forth between TEM and STEM.

Before acquiring the SMFs the stored area was recalled and the Ronchigram was focused on either a sacrificial area of the sample or on the carbon film next to a particle using a lower magnification than the one planned (<80 KX). Once the sample appeared to be in focus the magnification was increased to 80 KX and a BF-STEM image was captured. A magnification of 80 KX provided a pixel size of 0.93 nm and was closest in size to the first order diffraction spots in felodipine.

In some cases, this method was unsuccessful in producing SMF, possibly due to the cumulative electron fluence being too great and damaging the crystal or the sample being out of focus. One of the successful attempts to produce SMFs is shown in Figure 7.7. Figure 7.7a shows the SAED pattern of the [211] zone axis of felodipine form I. The scan direction was rotated by -1.8° so that β was equal to zero, although, during post-experimental analysis of the SAED pattern, it was found that a rotation of -3.3° was required and β was actually equal to 1.5°.

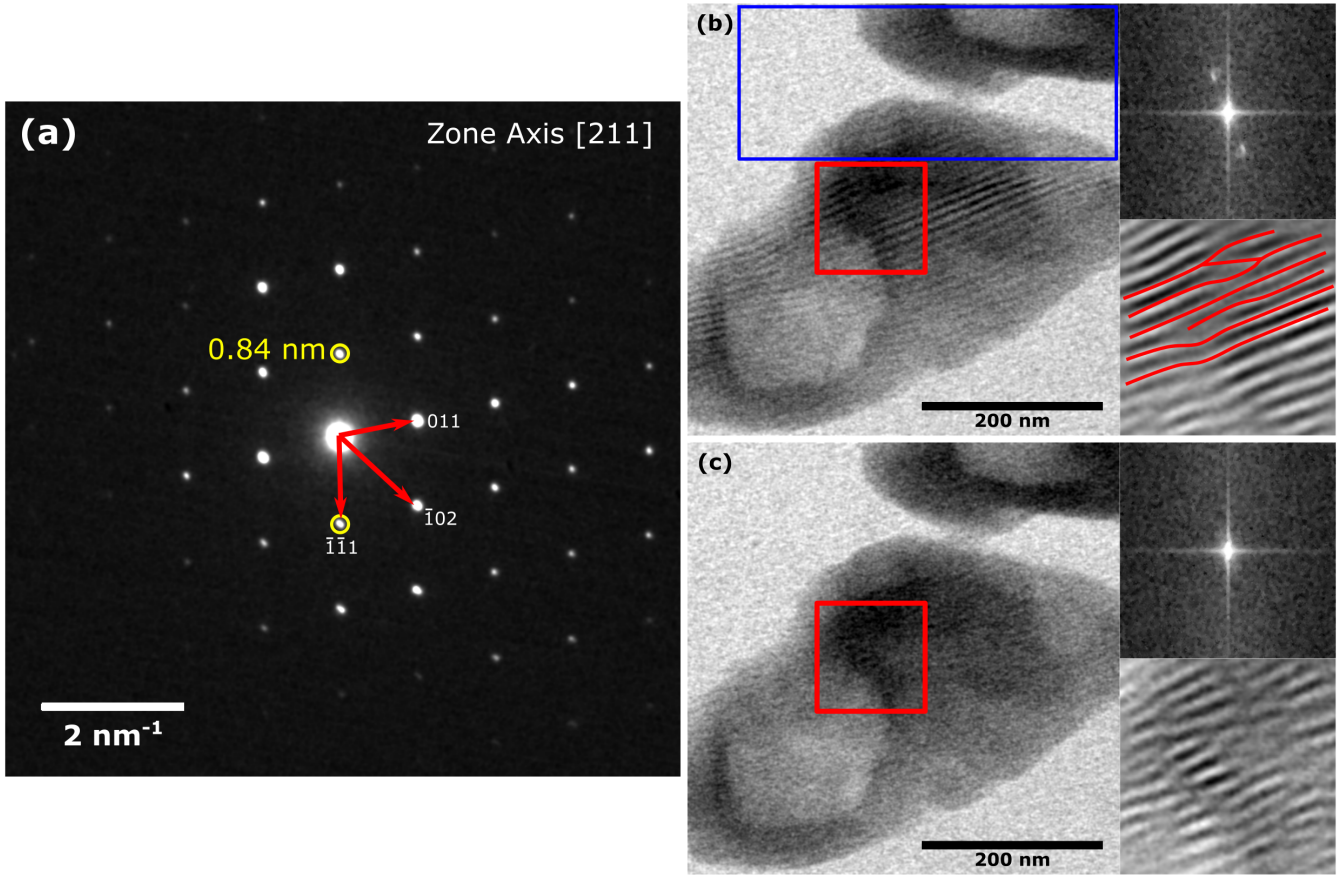

Figure 7.7: Scanning moiré fringes of crystalline felodipine form I (a) SAED pattern of [211] zone axis, the highlighted spots indicate the lattice fringe that contributed to the SMFs. (b) BF-STEM image of SMFs produced by using a pixel size of 0.93 nm and 0.84 nm d-spacing. From the FFT the average size of the SMFs was measured at 10.17 nm. Fourier filtered image from the area within the red box is also shown and highlights defects within the crystal. (c) Subsequent BF-STEM image of the same area showing the disappearance of the SMFs. The electron fluence in STEM for (b) and (c) was equal to 3.5 $e^-/Å^2$ and (d) 7.0 $e^-/Å^2$.

Figure 7.7b shows the crystalline particle, FFT of the red highlighted area and Fourier filtered image of the same area recorded at an electron fluence of approximately 3.5 $e^-/Å^2$. This electron fluence value does not include the electron fluence that the sample was previously exposed to during acquisition of the SAED pattern, bright field TEM or during focusing. A single spacing of 10.17 nm was measured from the FFT. The area highlighted by the blue box had previously been exposed to the electron beam in a prior scan and also demonstrated SMFs. During this previous scan (not shown), SMFs could be seen within this area with two spacings identifiable in the FFT at 7.95 nm and 4.00 nm. The value for the first order spacing at 7.95 nm was in close agreement to the predicted value of 8.00 nm, calculated using Equation 7.2 when d_s, d_l and β are equal to 0.93 nm, 0.84 nm and 1.5° respectively. The increase in the size of the SMFs between the first and second scan suggests that the average size of d_l had changed between scans, possibly due to electron beam effects. The increase in SMF spacing is due to the ratio between d_s and d_l being closer to one. If d_l is equal to 0.858 nm the resulting SMFs would be 10.17 nm, an increase of 0.02 nm to the average size of d_l. The Fourier filtered image shows areas within the red box that contains lattice irregularities, more of these defects could cause the average size of the SMFs to increase.

A subsequent BF-STEM image was acquired from the same area and is shown in Figure 7.7c. From the FFT no regular spacings were visible indicating that after a cumulative electron fluence of >7.0 $e^-/Å^2$ all signs of crystallinity were destroyed. The results demonstrate that it is possible to achieve real-space lattice information in STEM at a lower magnification than normally required, thereby reducing the total electron fluence and damage to the sample. Assuming that approximately 2 $e^-/Å^2$ was used to acquire the SAED pattern and bright field images (electron flux of 0.1 $e^-/(Å^2\ s)$ for 20 seconds) the total electron fluence that was applied to felodipine was approximately 5.5 $e^-/Å^2$, for the images where the SMFs could be seen, and 9 $e^-/Å^2$ after the crystal had damage. This is higher than the average C_F measured in Chapter 4, although 300 kV is used here, which would increase the electron beam stability compared to 200 kV.

Imaging in STEM using lower magnifications may also improve the electron beam stability of the sample. If the diameter of the probe is much smaller than

the size of the scan steps the resulting image will be undersampled, referred to as sparse scanning (Egerton, 2018). Assuming the sample damages via radiolysis, which is the case for felodipine, undersampling can be an effective way to reduce the electron fluence. When forming SMFs highly localised elastic scattering events occur entirely within the area irradiated by the probe while the majority of damage to the crystal will be due to delocalised inelastic scattering just outside this area (Egerton, 2018). The probability of delocalised inelastic scattering events to occur within a certain radius around the probe is known as the point spread function (Egerton, 2017). Provided that d_s is larger than the radius of inelastic scattering then, the probe will next sample an adjacent area that has not previously been damaged due to the delocalisation of radiolysis (Egerton, 2018). If the size of d_s was similar to the probe diameter then damaged areas would overlap destroying the crystal ahead of each dwell point. However, increasing d_s reduces the spatial resolution of the image and to sufficiently resolve features an increase in signal is required (Egerton, 2017, 2018). With SMFs the lattice is magnified and phase contrast is produced from the interference between d_s and d_l, both of which increases the information to damage ratio.

As discussed in the cooling experiments conducted in Chapter 4, an increase in the dose-limited resolution (DLR) can be a result of several different factors. The DLR can be calculated using the following equations:

$$DLR = (SNR)(DQE)^{-\frac{1}{2}}(FC_F/e)^{-\frac{1}{2}}(2)^{\frac{1}{2}}/|C| \tag{7.4}$$

$$F = e^{\frac{-t}{\lambda_e}} \qquad C = C_0 e^{\frac{Fluence}{C_F}} \tag{7.5}$$

where SNR is the signal to noise ratio and must equal or exceed some chosen background value, typically above 3 or 5σ to satisfy the Rose criterion; DQE is the detector quantum efficiency and relates to the noise generated by the detector and signal from the sample; F is the collection efficiency of incident electrons to detected electrons (Equation 7.5), which depends on the sample thickness (t) and the mean free path of electrons (λ_e); e is the elementary charge of an electron and C is the contrast (Egerton, 2014).

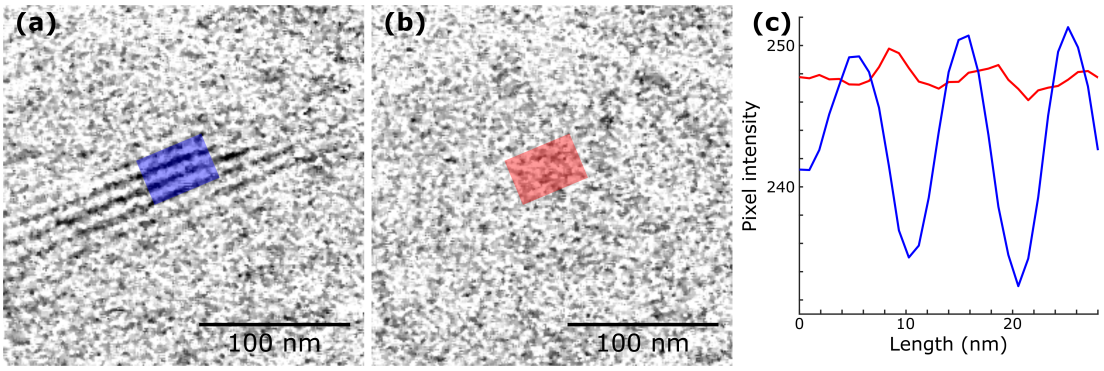

Figure 7.8: Processed SMF images using rolling ball background subtraction function in ImageJ and the position the line profiles (a) Background subtracted SMF image of Figure 7.7c; (b) Background subtracted SMF image of Figure 7.7d; (c) line profile of each area showing the difference in contrast. The subtracted background was approximately 25 for each image.

In the SMF method, the lattice fringes are magnified (in this case by an order of magnitude) making them easier to resolve, information to damage ratio is increased compared to higher magnifications and contrast in the image is increased due to the presence of phase contrast. Figure 7.8a and b shows the background subtracted images using the rolling ball background subtraction function in ImageJ from the images in Figure 7.7c and d. The mass-thickness contrast is essentially removed from the image leaving only the phase contrast due to the SMFs. Line profiles taken from the same areas are shown in Figure 7.8c and demonstrates the contrast between the two scans at 3.5 $e^-/Å^2$ and 7.0 $e^-/Å^2$. The contrast between bright and dark fringes can be approximately calculated by measuring the difference in intensity using a line profile and then dividing by the background intensity (approximately 25). When this is carried out in the same area in the image containing moiré fringes and the damaged image the average contrast value is approximately 0.6 and 0.1 respectively. Figure 7.9 demonstrates the effects of increasing C_0 from 0.1 to 0.6 when using: SNR = 5; DQE = 0.5; C_0 = 0.1; t = 100 nm, λ_e = 150 nm and C_F = 2.1 $e^-/Å^2$. It can be seen by increasing the initial contrast in the image the dose-limited resolution greatly improves and the total electron fluence available to image the sample before the loss of resolution also increases. In this case, the maximum dose-limited resolution

increases from 22.5 nm to 5.3 nm.

These preliminary experiments demonstrate that SMF increases the information to damage ratio and can be used to identify the number or density of crystalline defects within the sample which would be useful to apply to API analysis before/after pharmaceutical processing or to examine drugs within formulations to determine information regarding crystalline defects. Further improvements are required in both the data analysis to extract more information regarding the crystal structure and defects and the method to increase the robustness and consistency in identifying SMF.

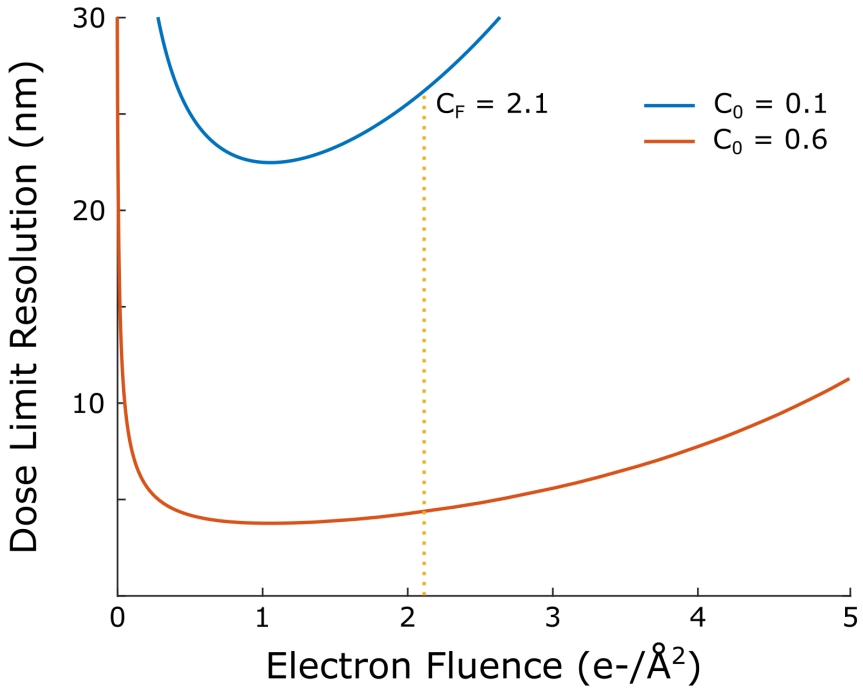

Figure 7.9: Graph demonstrating the effect of C_0 on the dose-limited resolution calculated by Equation 7.4, where SNR = 5; DQE = 0.5; C_0 = 0.1; t = 100 nm, λ_e = 150 nm and C_F = 2.1 $e^-/Å^2$.

7.3 Scanning Electron Diffraction

Scanning electron diffraction also referred to as nanobeam diffraction, is a method that rapidly scans an electron beam across the sample and collects a diffraction pattern from nanosized regions. The information collected results in a 4-D dataset that contains the probe positions and the diffraction data for each point. Virtual apertures can be digitally inserted into the diffraction pattern and altered to reconstruct dark field (DF) and bright field (BF) images from one or more diffracted beam. The electron beam can also be precessed to acquire higher quality diffraction patterns. More detailed analysis regarding crystal structure and defects can be acquired compared to conventional TEM as it does not rely on recording individual BF or DF images.

Applications of this techniques have previously been carried out on various metals, alloys and nanoparticles to obtain information regarding crystalline defects, orientation and phase maps (Cowley, 2004; Moeck et al., 2011). More beam sensitive materials have also been examined using this method including graphene oxide, polyethylene and semi-crystalline polymer blends (Eggeman et al., 2017; Kang et al., 2016; Panova et al., 2016).

7.3.1 Method

An FEI Tecnai F30 operated at an accelerating voltage of 300 kV, equipped with a field emission gun using an extraction voltage of 4 kV was used to examine the samples. After general alignments a 1μm condense aperture was inserted resulting in a convergence angle of 1 - 2 mrad. This reduced the electron beam intensity and formed small individual disks in the diffraction pattern.

Scanning and precession of the electron beam were controlled by a DigiSTAR Nanomegas which is an external piece of hardware, that is an add-on to the TEM. The hardware is connected to the deflector coils of the microscope and the software, Digistar control, was used to alter the scanning and precession parameter such as the scan area, precession angle and the scan step size (set between 5 and 15 nm). An external CCD camera was attached to the front of the viewing screen to capture the electron diffraction patterns as the electron beam was scanned across the sample. Using a dedicated external CCD camera allowed

for fast acquisition of the diffraction patterns (Moeck et al., 2011). This produced a 4-D dataset that consisted of the location of the scanning beam and then the diffraction pattern data corresponding to that location (Panova et al., 2016). A magnification of 5200 X was used to search for suitable areas and the exposure time measured from the viewing screen was >97 s when using a gun lens of 6 and spot size between 9 and 11.

Data Analysis

HyperSpy was used to analyse the acquired 4-D dataset. This is an open source Python library that has a large array of tools that can be used for data analysis for multi-dimensional datasets (de la Pena et al., 2018). A Python script written by Dr Alex Eggeman was used to analyse the data using functions from the HyperSpy library. The data can be opened in a navigation-signal window; the navigation window is a plot of the normalised intensity of each diffraction pattern (effectively the real-space object BF image) and the signal window is the diffraction pattern from the location selected in the navigation. The cursor in the navigation window can be moved around to view the diffraction data from different locations within the scanned area. A virtual aperture can be added to the diffraction patterns and positioned around a selected area to construct a virtual BF or DF image using the integrated intensity from the selected region. Multiple virtual apertures can be added to the diffraction patterns and summated to analyse more than one diffracted beam.

Multiple different crystals, orientations, phases and defects contribute to complex diffraction pattern data containing multiple different signals (Eggeman et al., 2015; Martineau and Eggeman, 2016). These signals can be decomposed using multivariate analysis to determine the individual diffraction signals of different factors by creating a subset of signals that can be combined in different proportion to describe the overall data. Using HyperSpy two methods of decomposition were applied here. PCA was carried out to determine the number of factors that represent the majority of the data to reduce the dimensionality and non-negative matrix factorisation (NMF) was then used to decompose the diffraction signal to identify the most significant crystalline signals and their location with the dataset.

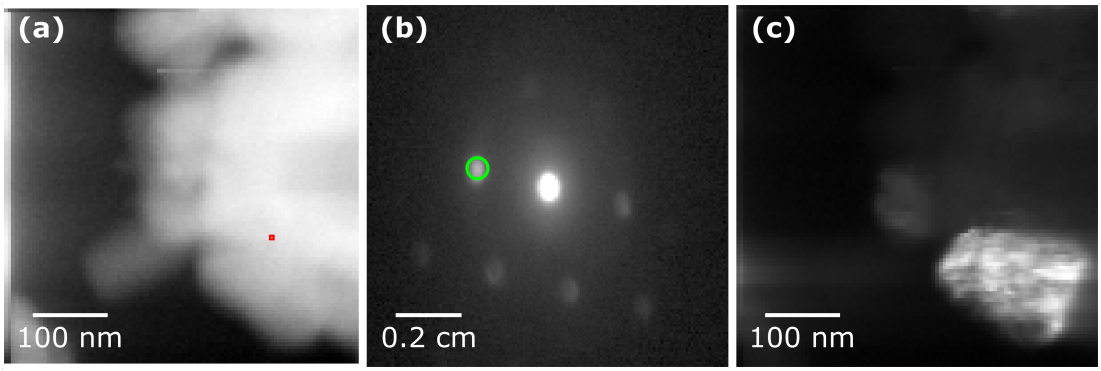

Figure 7.10: (a) Example of the navigation window from an area of pure felodipine, the red spot is the cursor that can be moved to access different diffraction patterns. (b) Signal window showing an example diffraction pattern from the location selected in the navigation. (c) Virtual dark field image created from the integrated intensities within the virtual aperture (the green circle in b).

7.3.2 Results and Discussion

Crystalline Felodipine

Felodipine was prepared by suspending in water to prevent the samples from readily dissolving and causing any suspension induced changes to the crystal form and placing approximately $3-4$ drops of the suspended powder onto a 400 mesh continuous carbon coated copper grid. Initially, the data were collected using a spot size of 9 and scan step size of 5 nm. One or two areas containing small crystals ($<$ 50 nm) were visible when moving the cursor in the navigation window until diffraction spots could be seen in the diffraction pattern. However, the majority of the scanned area appeared amorphous. After several data sets were collected the spot size was changed to 11 and more crystalline regions were then detected within the scanned area with relative ease, indicating that the crystals were previously damaging.

One of the crystalline areas was used as an example in Figure 7.10 displaying the navigation-signal windows and the reconstructed dark field image from the area selected using the virtual aperture. NMF decomposition was carried out on this dataset and the results for the first 12 NMF factors are shown in Figure 7.11.

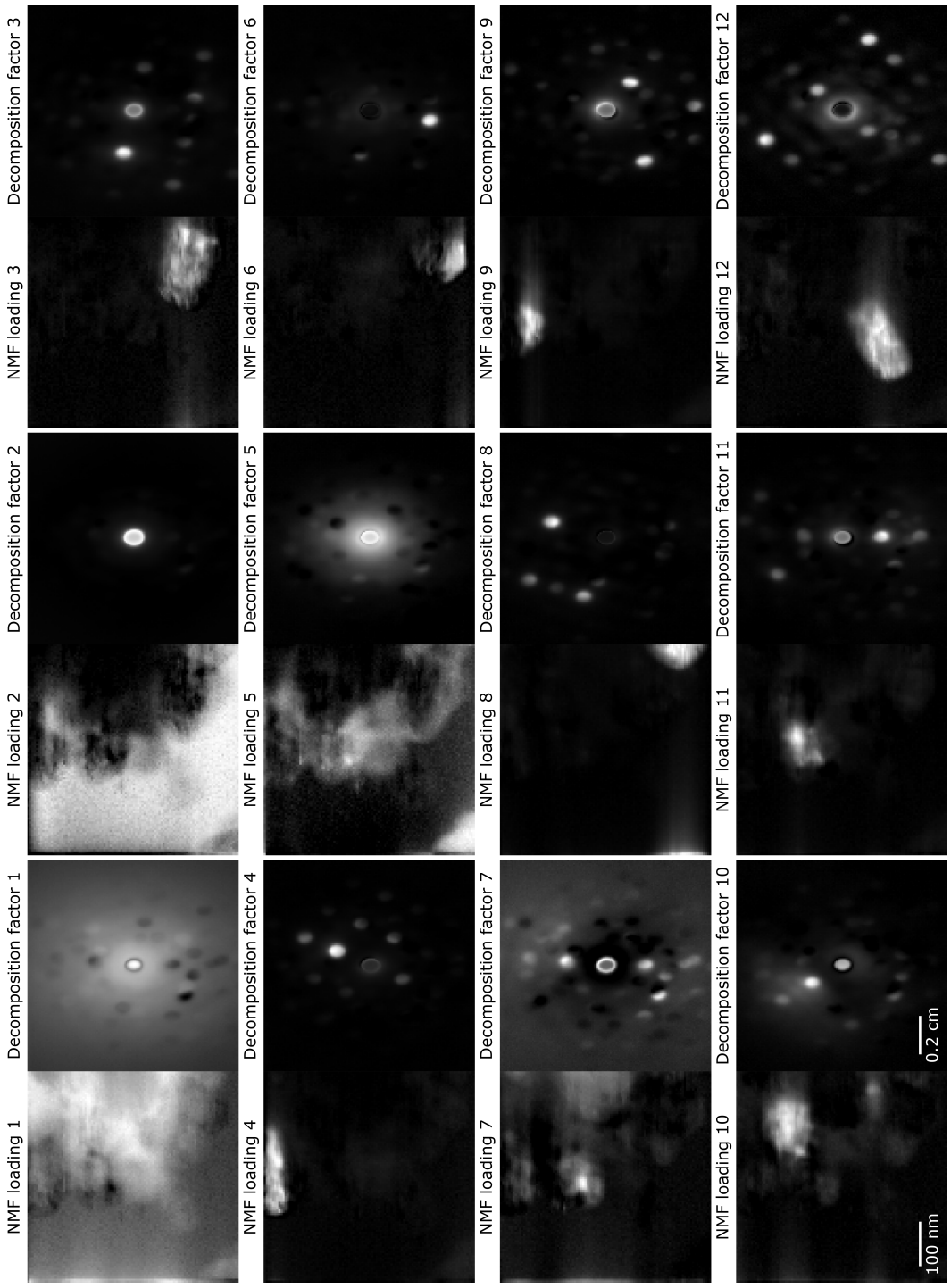

Figure 7.11: Scanning electron diffraction results that have been decomposed using non-negative matrix decomposition, showing the first 12 decomposition factors. The NMF loadings are the reconstructed image of the decomposed diffraction data.

The decomposition factors display the decomposed diffraction data signals and NMF loadings show the reconstructed images. The interpretation of what each factor means can be difficult, for example factors 1, 5, 7 and 10 do not appear to be showing a single diffraction signal. Factor 2 appears to show the BF image demonstrating diffraction contrast with the scanned area and factors 3, 4, 6, 8, 9, 11 and 12 show several DF images of individual crystalline particles.

Further analysis was not carried out on the electron diffraction patterns due to them being geometrically distorted as a result of recording the images using an external camera. This meant it was not possible to accurately measure the d-spacings, index the diffraction patterns or identify crystal orientations. The Digistar software does allow for the distortion to be corrected but access to the software was no longer available during the analysis. Provided with more time and access to the software indexing the patterns would be possible.

Amorphous Solid Dispersion

An ASD of 50/50 felodipine and copovidone prepared via HME that had been stored at 75% humidity for 7 days was then examined to provide further information on the size, phase and location of crystalline particles in the ASD. This sample had previously been examined by TEM during days 0, 1, 2 and 4 of storage and the results were discussed within Chapter 6. A TEM grid was prepared by grinding the stored powder in a pestle and mortar to reduce the size of the coarsely ground particles. The ground powder was then added to a 400 mesh continuous carbon-coated copper grid by gently touching the powder onto the grid.

The same method of analyse that was used to examine crystalline felodipine was carried out on the ASD sample, initially using a spot size of 11 and scan step of 5 nm. It was found that when using a scan step size of 5 nm it was difficult to identify any crystalline region, possibly due to electron beam damage, even though TEM had previously been successful in identifying crystals in similar samples (Chapter 6). To reduce the electron beam damage effects the scan step size was increased to 10 nm. After changing the step size, 3 crystalline regions were identified from a total of 6 scanned areas. The electron beam appears to

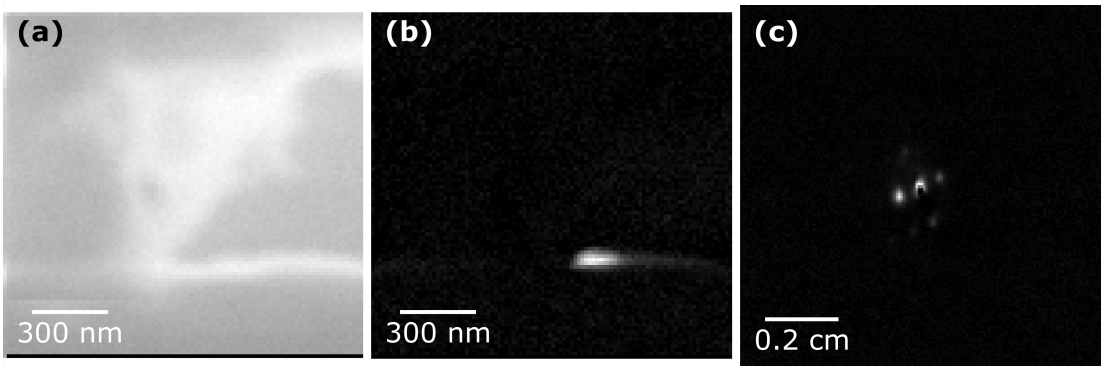

Figure 7.12: Felodipine/copovidone solid dispersion sample recorded using a scan step of 10 nm. (a) Reconstructed image of the scanned area; (b) NMF loading for factor 23, showing the area of the image that is crystalline; (c) corresponding decomposition signal showing diffraction spots present in the scanned area.

cause more damage to the sample when using a scan step of 5 nm compared to 10 nm. This is similar to changing the magnification in STEM where smaller scan steps result in increased damage due to crossover between delocalised inelastic scattering around the probe.

The BF reconstruction of the scanned area in which crystallinity is identified is shown in Figure 7.12a alongside the NMF loadings showing the size and area of the crystal region (Figure 7.12b). NMF factor 23 shows the decomposed signal (Figure 7.12c) relating to the only crystal region within this particular area. The previous factors appeared to show differences in thickness, regular noise within the images and other factors that were difficult to interpret. A larger number of crystals were found in the following area, shown in Figure 7.13, were NMF factors 2, 13, 27, 28 and 29 demonstrated areas that were decomposed into the respective individual crystals. The size of these crystals are approximately 120 - 750 nm in size, which is consistent with the particle sizes measured in Chapter 6 where the crystal size in the ASD varied between 10 - 750 nm. Again, previous factors appeared to show differences in thickness, regular noise within the images and other factors that were difficult to interpret.

The third crystalline area found exhibited a textured polycrystalline diffraction pattern (Figure 7.14a). A reconstructed DF image is shown in Figure 7.14b.

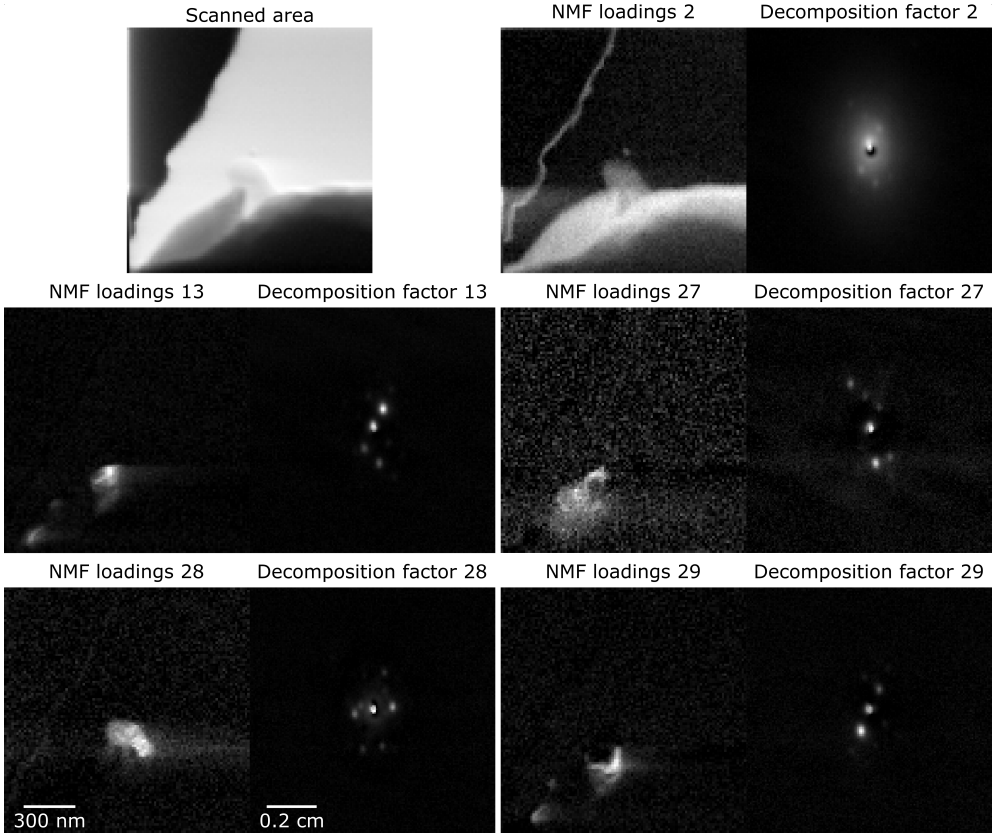

Figure 7.13: Felodipine/copovidone ASD sample recorded using a scan step of 10 nm, showing the scanned area and all the NMF decomposition factors that were decomposed into a single crystalline area.

The light areas correspond to the particle and the dark areas the carbon film. Figure 7.14c shows a diffraction pattern from the carbon background to compare against the textured pattern, demonstrating a clear difference between the two. The textured pattern appears similar to the one found in Chapter 6 and was thought to be due to either a polymer-rich phase with low drug concentration or a solvate of felodipine (although the spacing could not be measured in this case to compare).

From the results presented SED was able to detect crystal regions within the aged amorphous solid dispersions and measure the particle size. The data analysis carried out here was fairly simple due to the diffraction patterns not being calibrated and there is scope to extract further information from the data. For

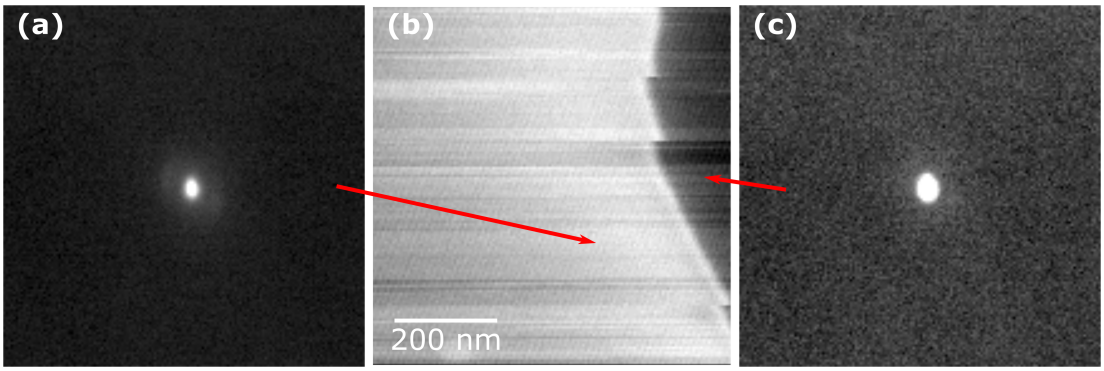

Figure 7.14: Felodipine/copovidone solid dispersion sample recorded using a scan step of 15 nm. (a) Text diffraction pattern showing one of the areas that exhibited this pattern; (b) Reconstructed dark field image of the scanned area, the light regions being the particle and the dark the carbon film; (c) amorphous diffraction pattern from the carbon film.

example orientation and phase maps could be produced to provide information on local degrees of crystallinity and areas containing various polymorphs within a aged solid dispersions. An example of this for a beam sensitive material has been demonstrated by Panova et al. (2016), where the local degree of crystallinity of a polymer blend containing poly(3-hexylthiophene-2,5-diyl) and polystyrene was found using SED.

SED is more dose-efficient than conventional TEM and STEM due to large amounts of data being collected simultaneously and the fact it provides information regarding the sample in reciprocal and real space. Ultimately the resolution of this technique is limited by electron beam damage and the convergence angle, therefore cryogenic conditions should be used when possible to maximise the time available for data collection and the resolution. The use of 300 kV accelerating voltage is also beneficial to reduce radiolysis damage and increase resolution for thick crystals.

7.4 Chapter Summary

This chapter shows the preliminary results from the three different microscopy techniques these being FIB-SEM, SMFs and SED. The aim was to use these techniques as ways to provide mechanistic insights into recrystallisation and information regarding size, shape, form and defects within crystals and where in a ASD they occur. From the results and discussion it was found that:

- SEM of a FIB cross-section did not identify any differences in contrast that would indicate phase separation or crystallisation towards the surface of a HME sample, suggesting the ASD was homogeneously mixed. More results from a less stable ASD that is known to readily phase separate or a well characterised aged sample could provide a better baseline for future work.
- Preparation of the thin lamella TEM samples using FIB was not possible due to electron beam damage. A repeat of this experiment at cryogenic conditions to reduce the effects of electron beam damage would be useful to determine if this sort of preparation is suitable to prepare thin cross-sections of extruded material for cryo-TEM analysis.
- SMF method is shown here to successfully obtain lattice information from beam sensitive materials by identifying the presence of defects within felodipine. This is achieved through the SMFs magnifying the real lattice making it possible to resolve at or inside the C_F for damage and increasing the information to damage ratio as a result of increasing contrast due to the presence of phase contrast.
- Interference between a lattice spacing of 0.838 nm in crystalline felodipine and scanning fringes of 0.93 nm produced SMFs between 8 - 10 nm in size, similar to the predicted value. The variation in size of the SMFs is due to the presence of defects affecting the average fringe size measured by FFT and can be identified in the STEM images. From the SMF images it is possible to identify numbers or density of defects in a processed API.

- SED was successful in identifying crystals of felodipine in both the pure drug and aged solid dispersion (including a polycrystalline area) and using NMF the diffraction signals could be decomposed into individual crystals. The crystals size and shapes identified i the aged ASD are consistent with the areas found in conventional TEM in Chapter 6. Using more advanced data analysis techniques and calibrating the diffraction pattern orientation and phase maps could be produced to provide information on local degrees of crystallinity and areas containing various polymorphs within an aged solid dispersions.
- SED is a dose-efficient method in acquiring diffraction and BF/DF images and the DLR of this technique could be further increased by using cryogenic conditions.

The results presented in this chapter demonstrate that nascent crystallinity in beam sensitive poorly water soluble APIs can be analysed using these methods. Future improvement in the methodology and data analysis can provide important information on length scales unobtainable with other characterisation techniques regarding the samples during drug development. One important factor that appears to be evident from previous chapters that requires further investigation is the nucleation pathways from the amorphous phase when in the presence of a polymer. These characterisation methods could provide insight into why these pathways occur and result in ways they might then be mitigated for future drug formulations.

Chapter 8

Conclusions and Future Work

8.1 Conclusions

In this thesis, the aim was to demonstrate the use of TEM in identifying and characterising crystallisation within amorphous solid dispersions (ASDs). Before examining any ASDs it was important to determine the electron fluence limits in TEM and understand why particular APIs were more prone to electron beam damage compared to others. Thus, allowing the prediction of APIs that are suitable for further TEM analysis.

Chapter 4 addressed this by measuring critical electron fluence (C_F) by TEM of a selection of 20 chemically diverse poorly water-soluble APIs using selected area electron diffraction (SAED). Principal component analysis (PCA) was then carried out to correlate a set of molecular descriptors (selected based on previous literature suggesting they improve electron beam stability) to the C_F. The results showed that the majority of APIs had C_F values below 5 $e^-/Å^2$ and the most stable 13 $e^-/Å^2$. These measurements indicate that poorly water-soluble drugs are very sensitive to the electron beam, producing similar electron fluence limits to biological samples. The number of hydrogen bond acceptors/donors and the ratios between the two were shown to have a negative influence on C_F, possibly due to the removal of hydrogen atoms via radiolysis causing destabilisation of the hydrogen bonding networks within the crystal and loss of structural integrity. The ratio of non-conjugated carbons to conjugated carbons positively influence C_F due

to the delocalisation of electrons within the molecule. Suggesting that molecular crystals that form mainly from $\pi - \pi$ stacking and Van der Waals bonds are more electron beam stable. Prior to these experiments melting temperature, the number of benzene rings and number of halogens atoms were thought to increase the electron beam stability, but for this set of materials only the conjugation from benzene rings had an effect.

By measuring the C_F at a temperature of 168 K it was shown cooling the sample increased the dose-limited resolution (DLR) and the time available to image at the DLR for a given API. These effects were more prevalent in APIs that were less electron beam stable, therefore, when practically possible and available the sample should be cooled to improve the lifetime and DLR.

Model ASDs containing felodipine and copovidone prepared via hot-melt extrusion (HME) and spray-drying (SD) at 15% and 30% drug loadings were examined in Chapter 5. The pXRD, FTIR and DSC results provide no indication that crystallisation had occurred within any of the ASDs. TEM was able to identify 2 crystalline areas from 55 in all but the 30% SD sample, demonstrating that TEM is more sensitive in detecting low levels of recrystallisation. The crystals present were potentially a mixture of the stable polymorph and metastable polymorphs, although higher quality single crystal diffractions patterns would be required to absolutely confirm this.

From the literature, interactions formed between felodipine and copovidone, mainly hydrogen bonding between N-H of felodipine and C=O of the pyrrolidone in copovidone, and the molecular mobility of the API are thought to be two of the most important factors in preventing recrystallisation. The FTIR suggests that the hydrogen bonds formed between felodipine and copovidone were stronger than that of pure felodipine and that the SD samples have slightly stronger hydrogen bonding compared to HME samples. The T_g measured by DSC showed a slight increase for SD samples. Therefore both characterisation methods suggest that SD ASDs formulations are more stable. TEM supports this claim, due to the lack of crystallisation identified in the 30% SD, although this could also be due to counting statistics.

Chapter 6 examined the effects of accelerated ageing conditions by increasing the relative humidity on a single ASD of felodipine and copovidone. From the literature, the addition of water into the system changes the thermodynamics of the ASD due to water more favourably mixing with copovidone than felodipine leading to phase separation and increasing the molecular mobility of the felodipine. Similarly to Chapter 5, the results show TEM to be more sensitive, able to identify moisture induced recrystallisation at earlier stages than pXRD, FTIR and DSC. Although due to the rate of crystallisation being faster than expected this was by one or two days. Conical dark field imaging allowed TEM to measure the size of crystal areas during the ageing process and showed a general increase in particle size over time. Nucleation and growth appeared to occur at the edges of particles, as might be expected for atmospheric water induced transformations.

Electron diffraction patterns showed suggested multiple forms of felodipine were present, similar to Chapter 5, in this case, the patterns consist of some single crystals of sufficient quality to be indexed. The majority being identified as forms I and II. This suggests that the sample recrystallises into a mixture of the stable and metastable polymorphs. A lower activation energy exists between amorphous felodipine and the metastable forms, in this case form II is the first to crystallise as it is most similar in energy to the amorphous phase. Over time this form then transforms into the more stable form I. A small number of areas that appear to be amorphous-amorphous phase separation or containing solvated felodipine were found and could indicate that in some cases phase separation occurred prior crystallisation; although these could be beam induced artefacts, requiring further investigation.

Chapter 7 examined the preliminary results for three different electron microscopy techniques, the first being dual beam FIB-SEM. Here, no observable difference in contrast was found by SEM of a FIB cross-section of an HME sample. Thin lamella were also unable to be prepared for TEM due to electron beam damage.

The scanning moiré fringe (SMF) method was successful in obtaining lattice information of beam sensitive materials and identifying the presence of defects, although the type of defect cannot be determined. The SMF lattice effectively

magnifies the real lattice allowing it to be resolved within the C_F and increasing the contrast of the image. Due to the difference in probe size compared to the scan step size (large in comparison to the probe size), the image is undersampled and the majority of damage occurs from the delocalised inelastic scattering, well within the pixel/scan step size. The scan step size results in the probe moving a sufficient distance where there is no overlap between the delocalised areas of damage, increasing the stability of the sample.

Finally, scanning electron diffraction (SED) was able to identify crystals before excessive damage occurred in crystalline felodipine and an aged ASD of felodipine and copovidone. Using decomposition methods the diffraction signal from the 4-D dataset could be decomposed into single crystals that can then be used to identify information regarding size and shape.

8.2 Final Comments

In summary, establishing the electron fluence limits for TEM of beam sensitive materials is important for determining suitable operating conditions for the sample and the DLR. Measurements of C_F for a range of APIs have been used to further the understanding of parameters that make a sample more stable in the electron beam and to predict the suitability of other APIs. TEM has been demonstrated as a more sensitive technique in identifying trace amounts of crystalline material in ASDs. Furthermore, it has provided information on the nucleation and growth of felodipine crystals in felodipine-copovidone in aged amorphous solid dispersions. Development in refining current and emerging electron microscopy techniques for electron beam sensitive samples could lead to a wealth of information being acquired at length scales inaccessible by other characterisation methods.

8.3 Future Work

To build off the work presented in this thesis several suggestions for future work have been outlined below:

Improving the predictive model. The development of the predictive model would benefit from incorporating a larger number of APIs to increase the accuracy of the predicted C_F and further validate the model. More sophisticated descriptors that include more information regarding crystal structure and bonding environments as input parameters in PCA could lead to further insight into factors that affect C_F and provide a more accurate predictive model. However, this would restrict the use of the model for APIs in the early stages of drug development since information regarding the crystal structure is not always readily available.

Improving electron diffraction data. The quality of the electron diffraction patterns and detection of diffraction spots against the background may affect the resulting measurements for C_F. By using an imaging filter and the latest generation of electron detectors, more specifically direct electron detectors, the observed intensity decay and lifetime of the crystal relative to the background signal could be improved. In the former case, the imaging filter can eliminate or significantly reduce the effects of inelastic scattering in the electron diffraction pattern, which is particularly problematic for low Z materials such as these APIs. In the latter case improvements in the DQE of the detector will increase the signal-to-noise ratio against the background allowing easier identification of diffraction spots at low electron fluence. Control of the crystal thickness would also reduce variations in C_F for a particular API and provide more accurate measurements.

Expanding amorphous solid dispersion study. Using a 300 kV microscope and cryogenic conditions would both extend the lifetime of the crystals by reducing radiolysis damage and increase the DLR. This would help to identify small crystals at the point of nucleation or nanosized areas of phase separation in the early stages of ageing in the ASD. It would be interesting to examine the effects of different polymers on the accelerated ageing of a particular drug at both low and high relative humidities over a longer period of time and to push the DLR. This could help to further understand how the drug interacts with the polymer and ultimately determine how they are mixed on the nanoscale.

Developing other electron microscopy techniques. For the preliminary experiments carried out using FIB-SEM, SMF and SED further development is required to achieve the full potential of these techniques. In all these methods cryogenic conditions would be favourable to reduce the electron beam damage.

For the FIB cross-sectioning, more results from a less stable ASD that is known to readily phase separate or a well characterised aged sample could provide a better baseline for future work and determining the limitations of the technique. The method for cutting thin lamella needs to be refined further for electron beam sensitive materials to successfully achieve suitable samples for TEM or STEM analysis.

Experiments utilising SMF could be carried out on a sample before and after milling to identify the change in the number/density of defects. Data analysis techniques could be applied to easily measure these defects automatically and the effect on the type of defect on the SMF could be modelled to provide information regarding the defect type. This could also be applied to solid dispersions to identify sites where defects are present that may influence the crystal growth of stable/metastable polymorphs.

For SED other decomposition methods could be attempted to find which provides the best interpretation of each decomposition factor. Experiments were the diffraction pattern is calibrated will allow orientation and phase maps to be created, which could provide useful information about the size of different phases and where they occur in the particles. The scan area is adjustable and given enough time and large enough storage SED data could be collected across areas 10s or 100s of μm in size which may allow for improved quantification of crystal areas.

By carrying out this future work TEM and other high resolution electron microscopy techniques have the potential to become a staple characterisation technique in the pharmaceutical industry by carefully managing the electron beam limitations.

Appendix A

List of compounds and their chemical and crystal structure

Table A.1: Compound name, IUPAC name, CAS number, crystal reference code/deposit number and chemical structure of all APIs used in the study.

API Name	IUPAC name	CAS number	Reference/Deposit number	Chemical Structure
Amcinonide	2-[(1S, 2S, 4R, 8S, 9S, 11S, 12R, 13S)-12'-fluoro-11'-hydroxy-9', 13'-dimethyl-16'-oxo-5', 7'-dioxaspiro [cyclopentane-1, 6'- pentacyclo [10.8.0.02,9.04,8.013,18] icosane]-4', 17'-dien-8'-yl]-2-oxoethyl acetate	51022-69-6	VAYJOW/ 867462	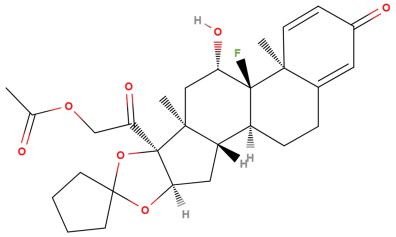
Bicalutamide	(RS)-N-[4-cyano-3-(trifluoromethyl) phenyl]-3-[(4-fluorophenyl) sulfonyl]-2-hydroxy-2-methylpropanamide	90357-06-5	JAYCES/ 289635	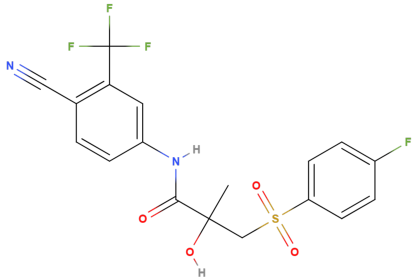
Celecoxib	4-[5-(4-Methylphenyl)-3-(trifluoromethyl) pyrazol-1-yl] benzenesulfonamide	169590-42-5	DIBBUL/ 139718	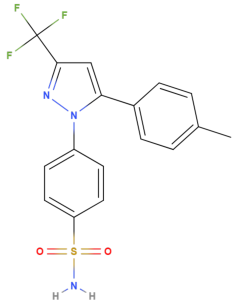

Ciclesonide	2-[(1S, 2S, 4R, 8S, 9S, 11S, 12S, 13R)-6-cyclohexyl-11-hydroxy-9, 13-dimethyl-16-oxo-5, 7-dioxapentacyclo [10.8.0.02,9.04,8.013,18] icosa-14, 17-dien-8-yl]-2-oxoethyl 2-methylpropanoate	126544-47-6	KOJPIJ/ 656903	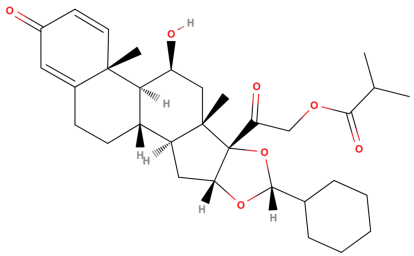
Cilostazol	6-[4-(1-Cyclohexyl-1H-tetrazol-5-yl) butoxy]-3, 4-dihydro-2 (1H)-quinolinone	73963-72-1	XOSGUH01/ 193455	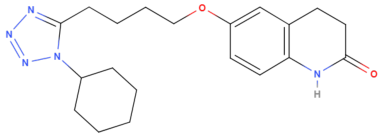
Drospirenone	(6R, 7R, 8R, 9S, 10R, 13S, 14S, 15S, 16S, 17S)-1, 3', 4', 6, 6a, 7, 8, 9, 10, 11, 12, 13, 14, 15, 15a, 16-Hexadecahydro-10, 13-dimetylspiro-[17H-dicyclopropa [6, 7:15, 16] cyclopenta[a]phenantrene-17, 2' (5'H)-furan]-3, 5' (2H)-dione	67392-87-4	XEZTON/ 903900	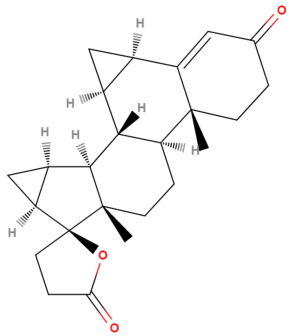
Dutasteride	(1S, 3aS, 3bS, 5aR, 9aR, 9bS, 11aS)-N-[2, 5-bis (trifluoromethyl) phenyl]-9a, 11a-dimethyl-7-oxo-1, 2, 3, 3a, 3b, 4, 5, 5a, 6, 9b, 10, 11-dodecahydroindeno [5,4-f] quinoline-1-carboxamide	164656-23-9	LATSIK/ 849482	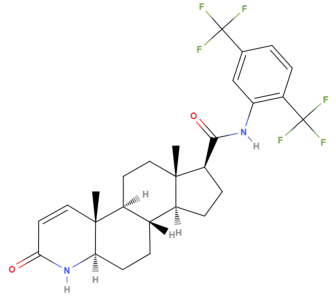

Efavirenz	(4S)-6-Chloro-4-(2-cyclopropylethynyl)-4-(trifluoromethyl)-2, 4-dihydro-1H-3, 1-benzoxazin-2-one	154598-52-4	AJEYAQ02/ 767883	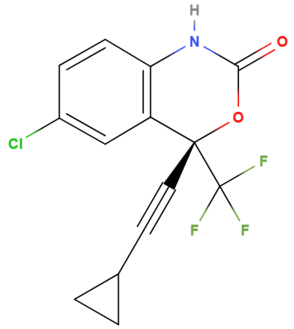
Felodipine	(RS)-3-ethyl 5-methyl 4-(2, 3-dichlorophenyl)-2, 6-dimethyl-1, 4-dihydropyridine-3, 5-dicarboxylate	72509-76-3	DONTIJ/ 1144175	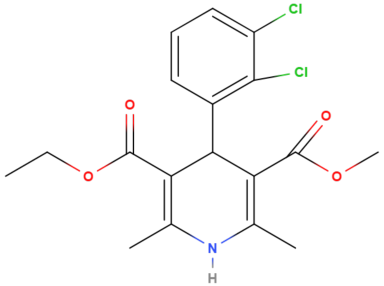
Griseofulvin	(2S, 6'R)-7-chloro-2', 4, 6-trimethoxy-6'-methyl- 3H, 4'H-spiro [1-benzofuran- 2, 1'-cyclohex[2]ene]- 3, 4'-dione	126-07-8	GRISFL/ 1170378	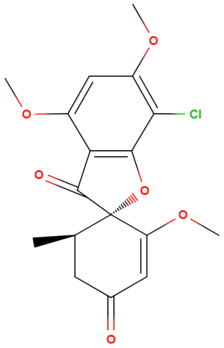

Indapamide	4-chloro-N-(2-methyl-2, 3-dihydroindol-1-yl)-3-sulfamoyl-benzamide	26807-65-8	VAGKUM/ 1448939 (HYDRATE)	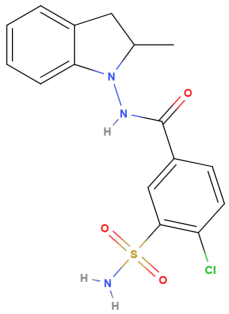
Indomethacin	2-1-[(4-Chlorophenyl) carbonyl]-5-methoxy-2-methyl-1H-indol-3-ylacetic acid	53-86-1	INDMET/ 1180373	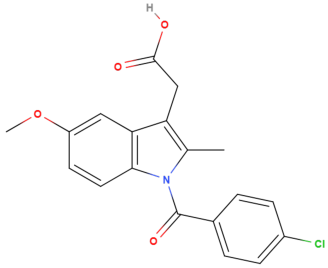
Lopinavir	(2S)-N-[(2S, 4S, 5S)-5-[2-(2, 6-dimethylphenoxy) acetamido]-4-hydroxy-1, 6-diphenylhexan-2-yl]-3-methyl-2-(2-oxo-1, 3-diazinan-1-yl) butanamide	192725-17-0	N/A	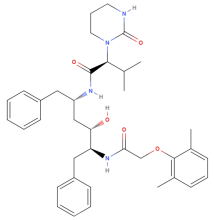
Nandrolone	(8R, 9S, 10R, 13S, 14S, 17S)-17-hydroxy-13-methyl-2, 6, 7, 8, 9, 10, 11, 12, 14, 15, 16, 17-dodecahydro-1H-cyclopenta[a]phenanthren-3-one	434-22-0	HEPDUE/ 1527597 (HYDRATE)	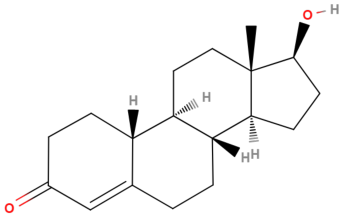

Nifedipine	3, 5-dimethyl 2, 6-dimethyl-4-(2-nitrophenyl)-1, 4-dihydropyridine-3, 5-dicarboxylate	21829-25-4	BICCIZ/ 1110171	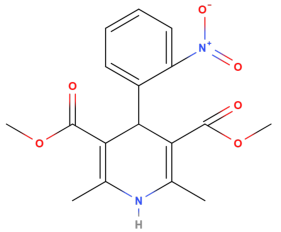
Nimodipine	3-(2-methoxyethyl) 5-propan-2-yl 2, 6-dimethyl-4-(3-nitrophenyl)-1, 4-dihydropyridine-3, 5-dicarboxylate	66085-59-4	VAWWEW/ 1280649	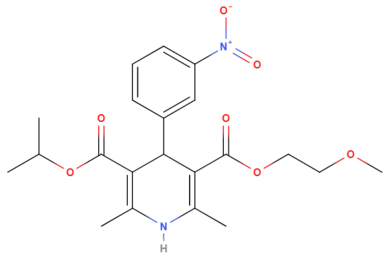
Nisoldipine	Isobutyl methyl 2, 6-dimethyl-4-(2-nitrophenyl)-1, 4-dihydropyridine-3, 5-dicarboxylate	63675-72-9	FULPAD/ 1161069	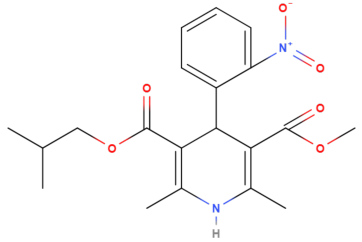
Probucol	4, 4'-[Propane-2, 2-diylbis(thio)] bis(2, 6-di-tert-butylphenol)	245-560-9	HAXHET01/ 1172913	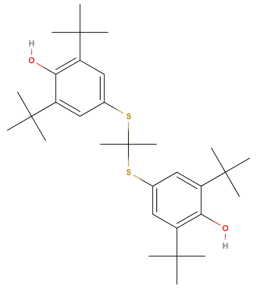

Simvastatin	(1S, 3R, 7S, 8S, 8aR)-8-2-[(2R, 4R)-4-hydroxy-6-oxotetrahydro-2H-pyran-2-yl] ethyl-3, 7-dimethyl-1, 2, 3, 7, 8, 8a-hexahydronaphthalen-1-yl 2, 2-dimethylbutanoate	79902-63-9	EJEQAL/ 219566	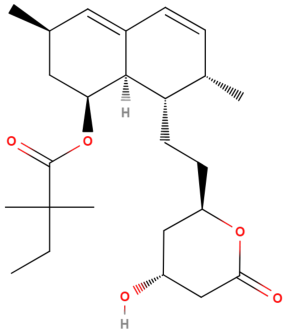
Tolnaftate	O-2-Naphthyl methyl (3-methylphenyl) thiocarbamate	2398-96-1	N/A	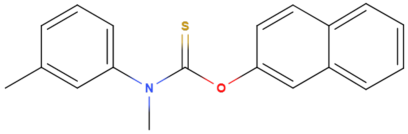
Furosemide	4-chloro-2 [(furan-2-ylmethyl) amino]-5-sulfamoylbenzoic acid	54-31-9	FURSEM13/ 761769	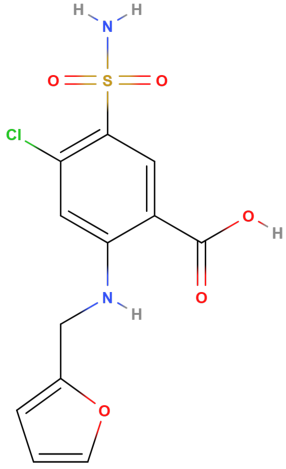

Appendix B

Images of crystalline areas found during ageing study and diffraction pattern analysis

The following figures show bright field images, the processed conical dark field videos and selected area electron diffraction patterns from both ageing studies at 85% humidity and 75% humidity at each day of analysis. The area selected for electron diffraction is shown as a red circle on the bright field image, and the particles that appear to be crystalline from the conical dark field videos via the masking process are outlined on the processed images. Each diffraction pattern has been indexed by matching to the measured d-spacings to similar d-spacings within each form of felodipine, if the pattern contained a single crystal the angles between diffraction spots were measured and taken into account. Diffraction spots that were not part of the measured single crystal were not indexed or used when calculating the error in the measurements; these are shown as blue circles on the SAED patterns.

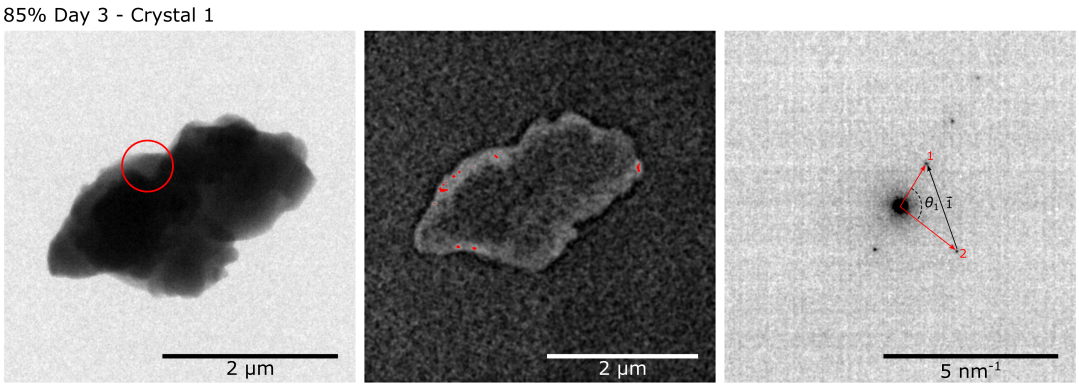

Figure B.1: Crystalline area 1 examined on day 3 of storage at 85% humidity.

Table B.1: Crystalline area 1 examined on day 3 of storage at 85% humidity. Measured d-spacings and angles compared to theoretical values for felodipine polymorphs for the diffraction pattern shown in Figure B.1. Average percentage errors between measured and theoretical values are equal to 3.2 ± 2.9, 3.9 ± 0.5, 6.0 ± 0.3 and 4.6 ± 2.4 for forms I, II, III and IV respectively.

Spot	**Distance** ($\mathbf{nm^{-1}}$)	**d-spacing** ($\mathbf{nm^{-1}}$)	**d-spacing (nm)**				**hkl**			
			I	II	III	IV	I	II	III	IV
1	1.42	0.70	0.67	0.73	0.66	0.72	$10\bar{2}$	312	$20\bar{2}$	101
2	2.05	0.49	0.50	0.50	0.46	0.53	$\bar{2}10$	$31\bar{4}$	$\bar{2}0\bar{2}$	$\bar{1}21$
$\overrightarrow{1}$	2.65	0.38	0.38	0.40	0.36	0.41	$3\bar{1}\bar{2}$	006	400	$2\bar{2}0$
θ_1	-	96°	97°	96°	98°	96°	-	-	-	-

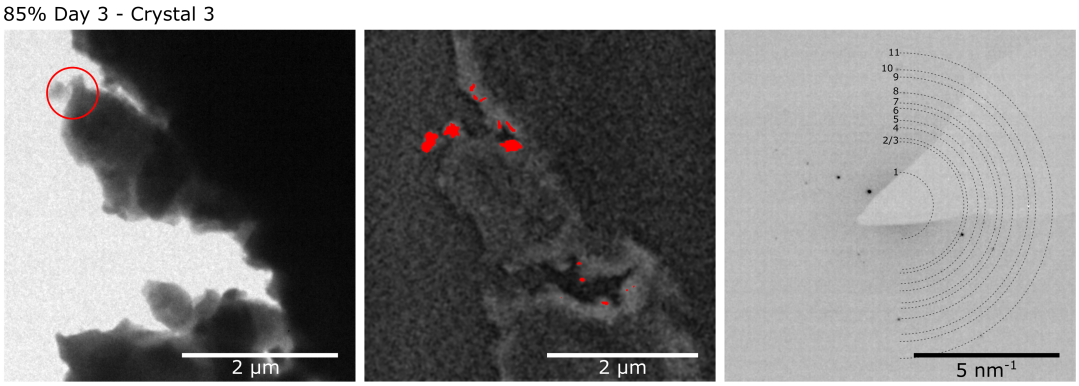

Figure B.2: Crystalline area 3 examined on day 3 of storage at 85% humidity.

Table B.2: Crystalline area 3 examined on day 3 of storage at 85% humidity. Measured d-spacings and angles compared to theoretical values for felodipine polymorphs for the diffraction pattern shown in Figure B.2. Average percentage errors between measured and theoretical values are equal to 1.6 ± 0.8, 1.2 ± 0.6, 6.6 ± 0.6 and 4.3 ± 0.5 for forms I, II, III and IV respectively.

Spot	**Radial Distance** ($\mathbf{nm^{-1}}$)	**d-spacing** ($\mathbf{nm^{-1}}$)	**d-spacing (nm)**				**hkl**			
			I	II	III	IV	I	II	III	IV
1	1.15	0.87	0.85	0.87	0.92	0.90	011	$31\bar{1}$	101	011
2	2.20	0.46	0.45	0.46	0.49	0.47	121	$04\bar{1}$	$21\bar{2}$	121
3	2.32	0.43	0.43	0.44	0.46	0.45	022	$62\bar{2}$	202	022
4	2.68	0.37	0.36	0.38	0.40	0.39	300	$42\bar{5}$	310	130
5	2.92	0.34	0.34	0.35	0.36	0.36	202	$91\bar{2}$	$21\bar{4}$	$31\bar{1}$
6	3.33	0.30	0.30	0.30	0.32	0.31	222	$92\bar{2}$	410	014
7	3.52	0.28	0.28	0.29	0.31	0.30	033	$93\bar{3}$	303	033
8	3.87	0.26	0.26	0.26	0.28	0.27	$31\bar{5}$	916	$51\bar{1}$	$41\bar{1}$
9	4.40	0.23	0.23	0.23	0.24	0.24	$20\bar{6}$	$91\bar{8}$	421	313
10	4.65	0.22	0.21	0.22	0.23	0.23	044	12 $4\bar{4}$	404	044
11	5.22	0.19	0.19	0.19	0.20	0.20	$43\bar{6}$	$39\bar{4}$	$33\bar{4}$	045

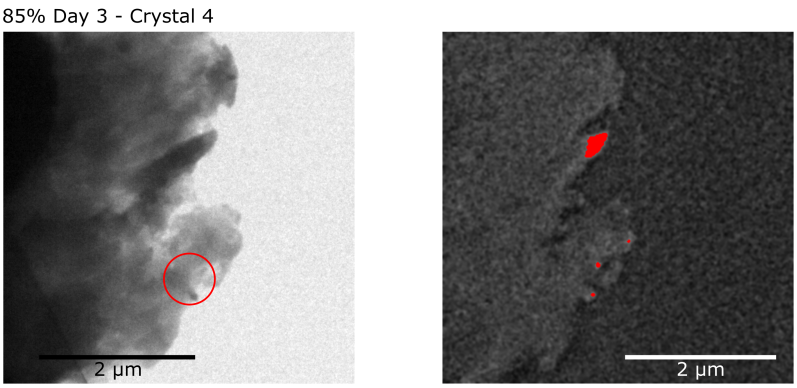

Figure B.3: Crystalline area 4 examined on day 3 of storage at 85% humidity.

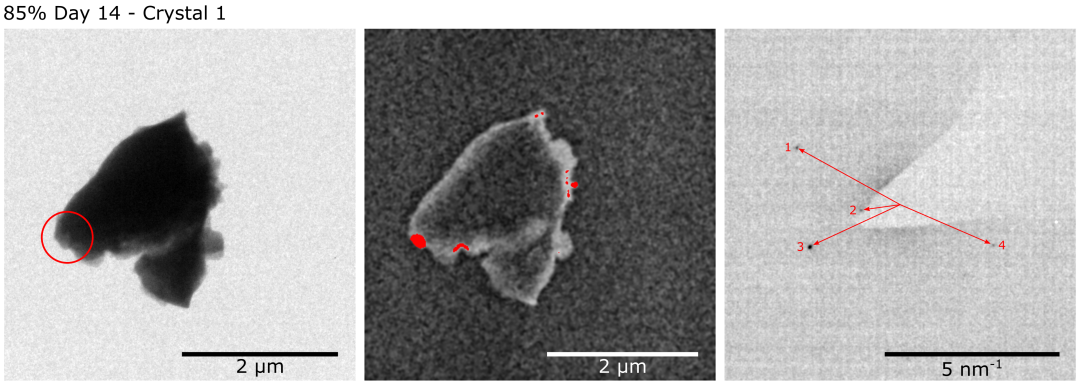

Figure B.4: Crystalline area 1 examined on day 14 of storage at 85% humidity.

Table B.3: Crystalline area 1 examined on day 14 of storage at 85% humidity. Measured d-spacings and angles compared to theoretical values for felodipine polymorphs for the diffraction pattern shown in Figure B.4. Average percentage errors between measured and theoretical values are equal to 6.0 ± 0.4, 2.5 ± 0.5, 1.7 ± 0.4 and 1.2 ± 0.1 for forms I, II, III and IV respectively.

Spot	**Distance** ($\mathbf{nm^{-1}}$)	**d-spacing** ($\mathbf{nm^{-1}}$)	**d-spacing (nm)**				**hkl**			
			I	II	III	IV	I	II	III	IV
1	3.33	0.30	0.28	0.30	0.31	0.30	$41\bar{3}$	260	$12\bar{3}$	$\bar{1}\bar{2}4$
2	1.10	0.91	0.85	0.94	0.92	0.90	011	310	101	011
3	2.83	0.35	0.33	0.36	0.36	0.35	$32\bar{1}$	624	$\bar{3}1\bar{1}$	113
4	2.91	0.34	0.32	0.35	0.35	0.34	230	732	120	310

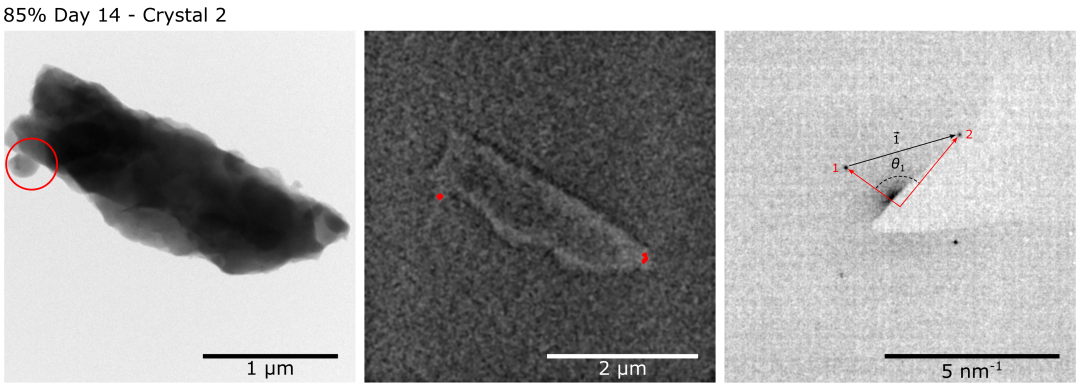

Figure B.5: Crystalline area 2 examined on day 14 of storage at 85% humidity.

Table B.4: Crystalline area 2 examined on day 14 of storage at 85% humidity. Measured d-spacings and angles compared to theoretical values for felodipine polymorphs for the diffraction pattern shown in Figure B.5. Average percentage errors between measured and theoretical values are equal to 1.2 ± 0.7, 0.6 ± 0.4, 7.3 ± 0.2 and 7.0 ± 1.3 for forms I, II, III and IV respectively.

Spot	**Distance** ($\mathbf{nm^{-1}}$)	**d-spacing** ($\mathbf{nm^{-1}}$)	**d-spacing (nm)**				**hkl**			
			I	II	III	IV	I	II	III	IV
1	1.88	0.53	0.53	0.53	0.57	0.57	$1\bar{2}0$	331	111	$11\bar{2}$
2	2.60	0.38	0.38	0.38	0.41	0.41	$\bar{3}\bar{1}2$	$\bar{1}1\bar{6}$	$3\bar{1}\bar{1}$	$2\bar{2}0$
$\vec{1}$	3.38	0.30	0.30	0.30	0.32	0.32	$\bar{4}12$	$\bar{4}\bar{2}\bar{7}$	$2\bar{2}\bar{2}$	$1\bar{3}2$
θ_1	-	96	96	96	97	95	-	-	-	-

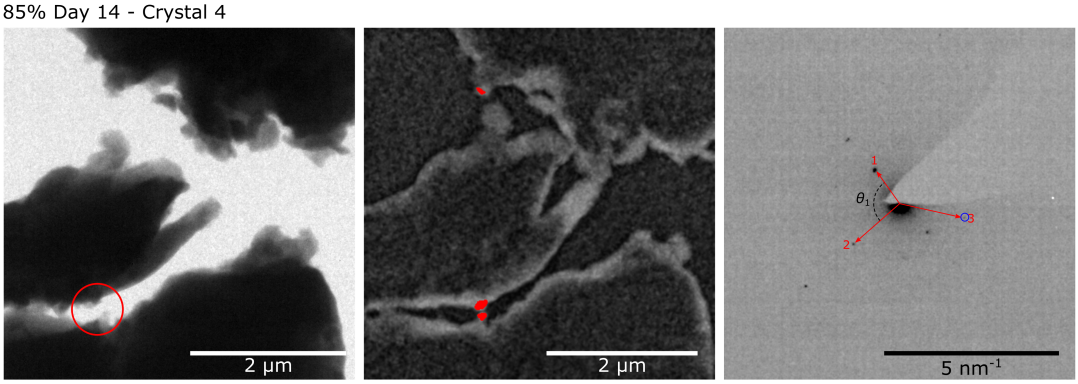

Figure B.6: Crystalline area 4 examined on day 14 of storage at 85% humidity.

Table B.5: Crystalline area 4 examined on day 14 of storage at 85% humidity. Measured d-spacings and angles compared to theoretical values for felodipine polymorphs for the diffraction pattern shown in Figure B.6. Average percentage errors between measured and theoretical values are equal to 5.9 ± 1.9, 0.8 ± 0.9 and 6.0 ± 0.8 for forms I, II and III respectively.

Spot	**Distance** ($\mathbf{nm^{-1}}$)	**d-spacing** (nm)	**d-spacing (nm)**			**hkl**		
			I	II	III	I	II	III
1	1.16	0.86	0.80	0.87	0.81	$11\bar{1}$	021	002
2	1.80	0.56	0.56	0.56	0.52	012	$11\bar{4}$	$21\bar{1}$
3	1.89	0.53	0.53	0.54	0.50	210	330	$30\bar{1}$
θ_1	-	93°	90°	94°	94°	-	-	-

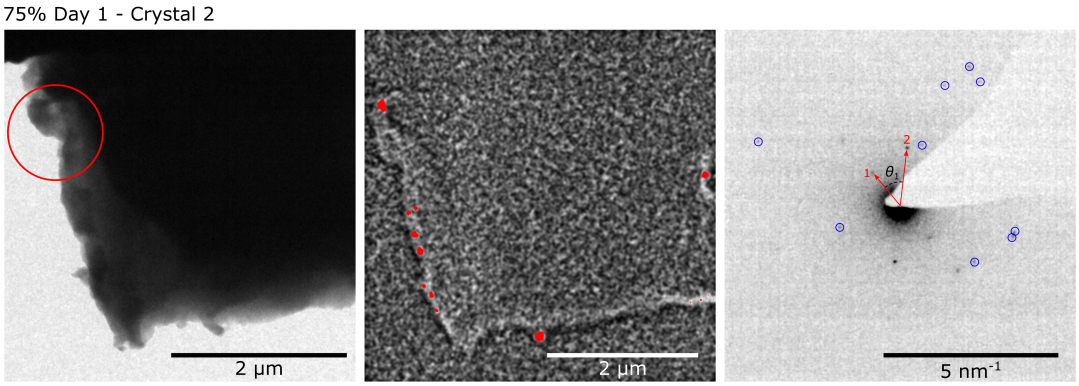

Figure B.7: Crystalline area 2 examined on day 1 of storage at 75% humidity.

Table B.6: Crystalline area 2 examined on day 1 of storage 75% humidity. Measured d-spacings and angles compared to theoretical values for felodipine polymorphs for the diffraction pattern shown in Figure B.7. Average percentage errors between measured and theoretical values are equal to 6.8 ± 1.0, 4.2 ± 0.9 and 1.6 ± 0.5, forms I, II and IV respectively.

Spot	**Distance** ($\mathbf{nm^{-1}}$)	**d-spacing** (nm)	**d-spacing (nm)**			**hkl**		
			I	II	IV	I	II	IV
1	1.25	0.80	0.85	0.77	0.81	$01\bar{1}$	221	110
2	1.62	0.62	0.66	0.60	0.63	$10\bar{2}$	$51\bar{1}$	020
θ_1	-	47°	54°	52°	50°	-	-	-

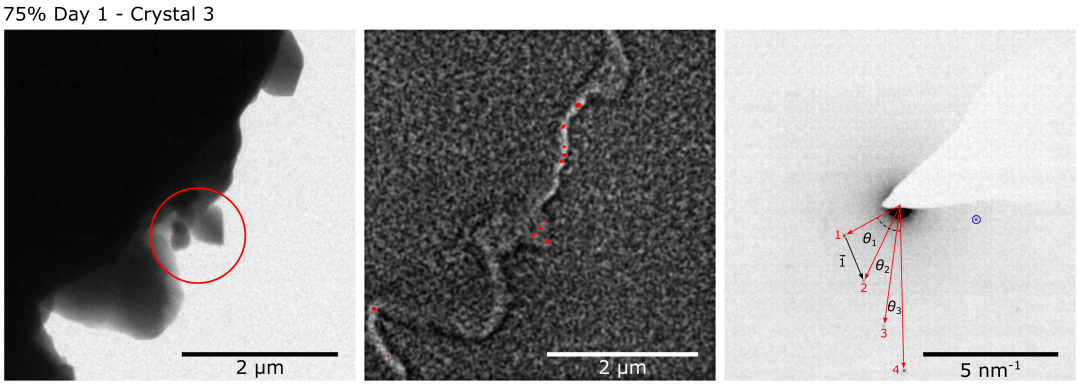

Figure B.8: Crystalline area 3 examined on day 1 of storage 75% humidity.

Table B.7: Crystalline area 3 examined on day 1 of storage 75% humidity. Measured d-spacings and angles compared to theoretical values for felodipine polymorphs for the diffraction pattern shown in Figure B.8. Average percentage errors between measured and theoretical values are equal to 1.7 ± 0.4, 1.4 ± 0.2, 2.7 ± 0.3 and 3.3 ± 1.4, forms I, II, III and IV respectively.

Spot	**Radial Distance** ($\mathbf{nm^{-1}}$)	**d-spacing** ($\mathbf{nm^{-1}}$)	**d-spacing (nm)**				**hkl**			
			I	II	III	IV	I	II	III	IV
1	2.34	0.42	0.42	0.43	0.44	0.41	$11\bar{3}$	622	$30\bar{3}$	013
2	3.07	0.33	0.32	0.33	0.33	0.32	$\bar{1}1\bar{3}$	426	$41\bar{2}$	132
3	4.47	0.22	0.22	0.23	0.23	0.22	$\bar{3}1\bar{3}$	22 10	$52\bar{1}$	351
4	6.11	0.16	0.16	0.17	0.17	0.16	$\bar{5}1\bar{3}$	02 14	630	370
$\vec{1}$	1.81	0.53	0.54	0.56	0.57	0.53	$\bar{2}00$	$\bar{2}04$	111	$12\bar{1}$
θ_1	-	36	36	36	36	37	-	-	-	-
θ_2	-	18	18	18	18	19	-	-	-	-
θ_3	-	9	9	9	9	9	-	-	-	-

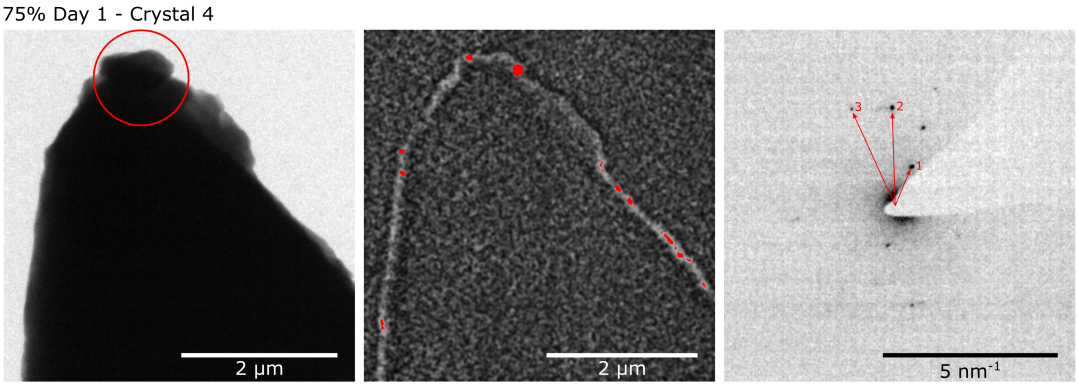

Figure B.9: Crystalline area 4 examined on day 1 of storage 75% humidity.

Table B.8: Crystalline area 4 examined on day 1 of storage 75% humidity. Measured d-spacings and angles compared to theoretical values for felodipine polymorphs for the diffraction pattern shown in Figure B.9. Average percentage errors between measured and theoretical values are equal to 0.3±1.0 and 4.6±0.9, forms I and IV respectively.

Spot	**Distance** ($\mathbf{nm^{-1}}$)	**d-spacing** (nm)	**d-spacing (nm)** I	IV	**hkl** I	IV
1	1.18	0.85	0.85	0.90	011	011
2	2.82	0.36	0.36	0.37	$12\bar{3}$	$30\bar{1}$
3	3.09	0.32	0.32	0.34	$11\bar{4}$	$22\bar{3}$

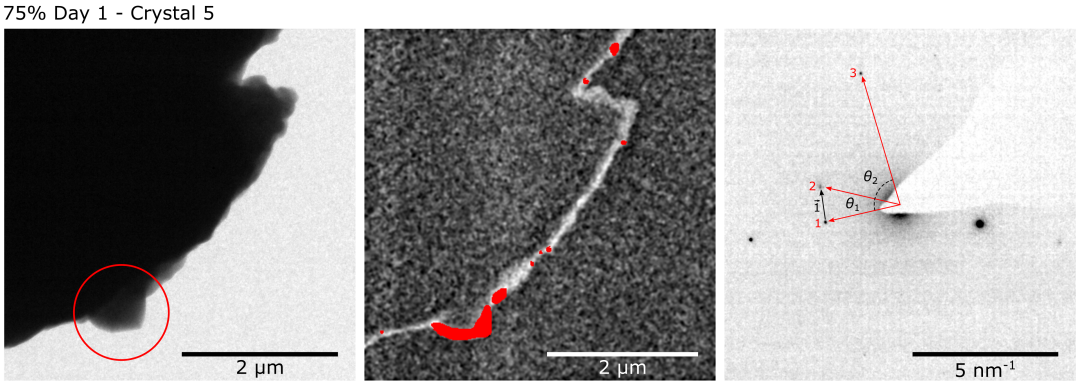

Figure B.10: Crystalline area 5 examined on day 1 of storage 75% humidity.

Table B.9: Crystalline area 5 examined on day 1 of storage 75% humidity. Measured d-spacings and angles compared to theoretical values for felodipine polymorphs for the diffraction pattern shown in Figure B.10. Average percentage errors between measured and theoretical values are equal to 4.1 ± 0.4, 1.6 ± 0.2 and 1.8 ± 0.6, forms I, II and III respectively.

Spot	**Distance** ($\mathbf{nm^{-1}}$)	**d-spacing** (nm)	**d-spacing (nm)**			**hkl**		
			I	II	III	I	II	III
1	2.62	0.38	0.40	0.38	0.38	$30\bar{2}$	$13\bar{5}$	$40\bar{2}$
2	2.77	0.36	0.38	0.36	0.36	$31\bar{1}$	$\bar{3}3\bar{5}$	400
3	4.68	0.21	0.22	0.21	0.21	143	$\bar{1}5\ 1\bar{2}$	117
$\overrightarrow{1}$	1.22	0.82	0.85	0.81	0.81	011	400	002
θ_1	-	26°	26°	26°	26°	-	-	-
θ_1	-	61°	60°	58°	63°	-	-	-

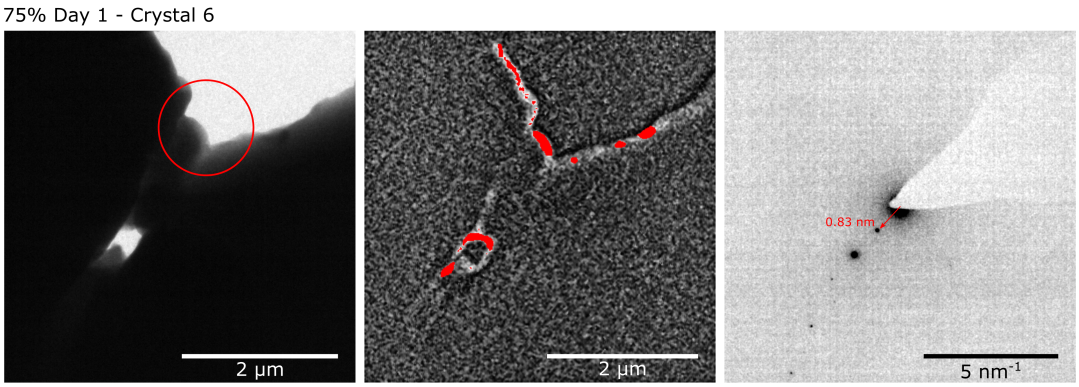

Figure B.11: Crystalline area 6 examined on day 1 of storage 75% humidity. The d-spacing equal to 0.83 nm is similar to the 011, 220, 002 or 110 d-spacings in forms I, II, III and IV felodipine respectively.

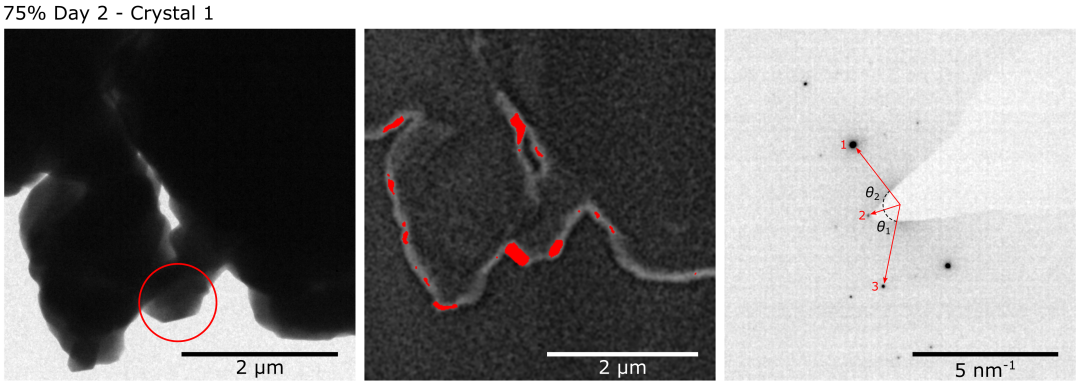

Figure B.12: Crystalline area 1 examined on day 2 of storage 75% humidity.

Table B.10: Crystalline area 1 examined on day 2 of storage 75% humidity. Measured d-spacings and angles compared to theoretical values for felodipine polymorphs for the diffraction pattern shown in Figure B.12. Average percentage errors between measured and theoretical values are equal to 0.9±0.3 and 5.4±0.6, forms II and III respectively.

Spot	**Distance** ($\mathbf{nm^{-1}}$)	**d-spacing** (nm)	**d-spacing (nm)**		**hkl**	
			II	III	II	III
1	2.63	0.38	0.39	0.41	$\bar{1}\bar{1}6$	$31\bar{2}$
2	1.15	0.87	0.88	0.92	$\bar{3}11$	101
3	2.47	0.41	0.41	0.43	$\bar{5}3\bar{4}$	$\bar{1}\bar{1}4$
θ_1	-	60°	60°	60°	-	-
θ_2	-	71°	70°	71°	-	-

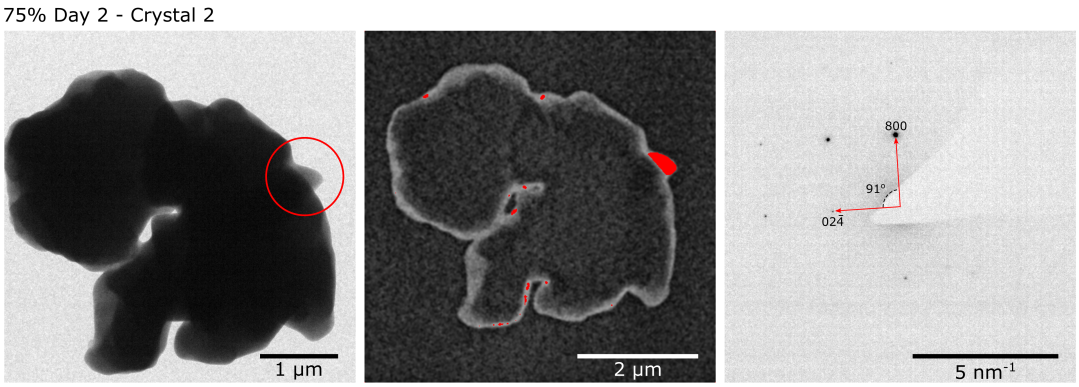

Figure B.13: Crystalline area 2 examined on day 2 of storage 75% humidity. Indexable to form II felodipine, average percentage errors between measured and theoretical values are equal to 0.1 ± 0.5.

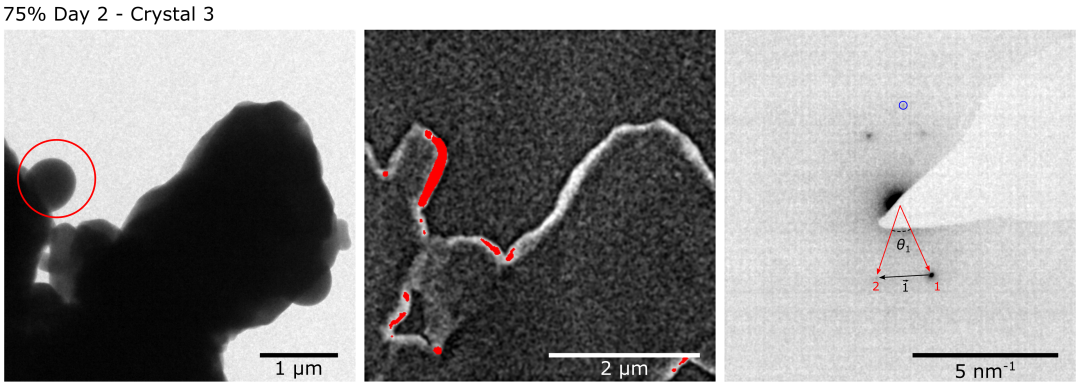

Figure B.14: Crystalline area 3 examined on day 2 of storage 75% humidity.

Table B.11: Crystalline area 3 examined on day 2 of storage 75% humidity. Measured d-spacings and angles compared to theoretical values for felodipine polymorphs for the diffraction pattern shown in Figure B.14. Average percentage errors between measured and theoretical values are equal to 1.7±0.2 and 0.7±2.0, forms I and IV respectively.

Spot	**Distance** ($\mathbf{nm^{-1}}$)	**d-spacing** (nm)	**d-spacing (nm)** I	IV	**hkl** I	IV
1	2.60	0.38	0.38	0.39	$\bar{1}31$	$\bar{1}30$
2	2.61	0.38	0.38	0.39	$13\bar{1}$	130
$\overrightarrow{1}$	1.83	0.55	0.54	0.53	$20\bar{2}$	200
θ_1	-	43°	41°	43°	-	-

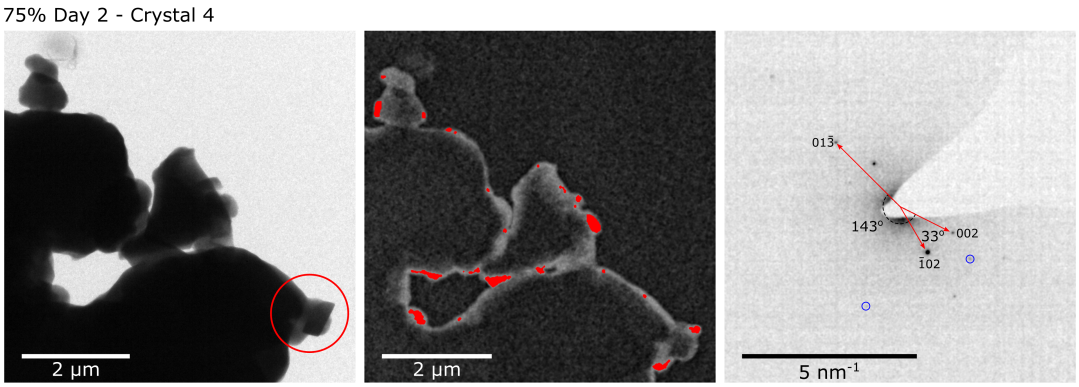

Figure B.15: Crystalline area 4 examined on day 2 of storage 75% humidity. Indexable to form I felodipine, average percentage errors between measured and theoretical values are equal to 1.6 ± 0.9.

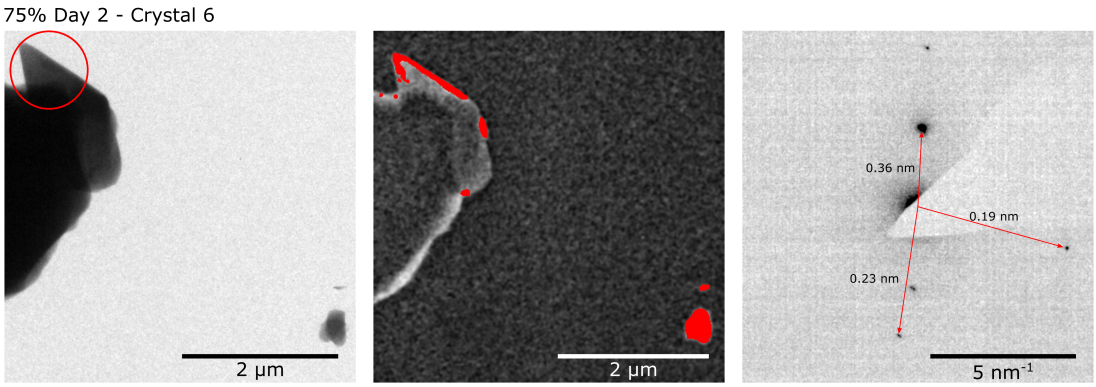

Figure B.16: Crystalline area 6 examined on day 2 of storage 75% humidity. The d-spacings of 0.36 nm, 0.23 nm and 0.19 nm closely match spacings in all forms of felodipine.

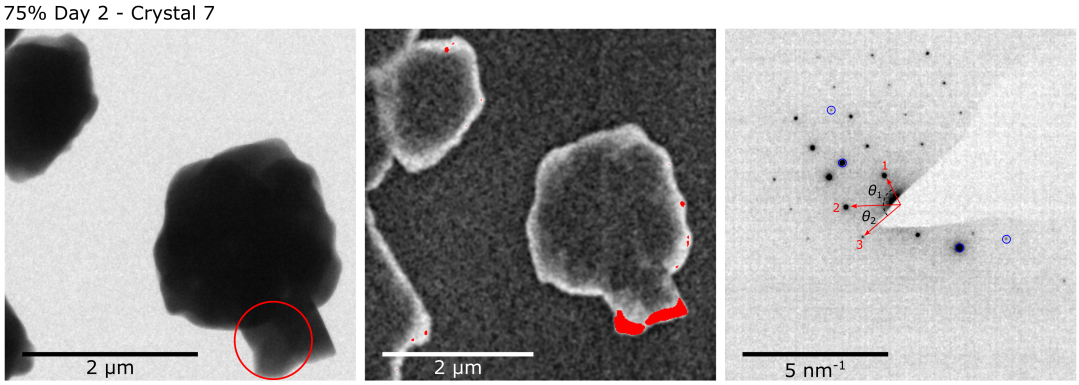

Figure B.17: Crystalline area 7 examined on day 2 of storage 75% humidity.

Table B.12: Crystalline area 7 examined on day 2 of storage 75% humidity. Measured d-spacings and angles compared to theoretical values for felodipine polymorphs for the diffraction pattern shown in Figure B.17. Average percentage errors between measured and theoretical values are equal to 1.2±0.5 and 0.4±0.3, forms I and II respectively.

Spot	**Distance** (nm^{-1})	**d-spacing** (nm)	**d-spacing (nm)**		**hkl**	
			I	II	I	II
1	1.18	0.86	0.85	0.87	011	311
2	1.86	0.54	0.54	0.54	$\bar{1}20$	$4\bar{2}2$
3	1.69	0.59	0.59	0.59	$\bar{1}1\bar{1}$	$1\bar{3}1$
θ_1	-	63	62	64	-	-
θ_2	-	38	38	38	-	-

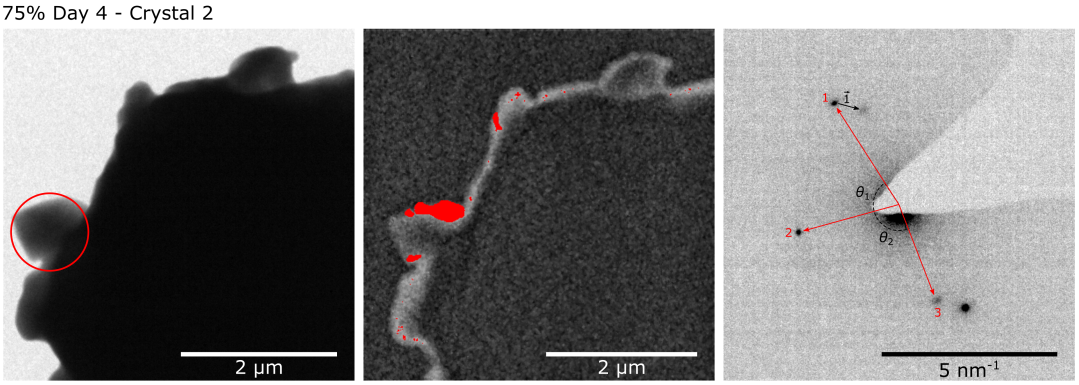

Figure B.18: Crystalline area 2 examined on day 4 of storage 75% humidity.

Table B.13: Crystalline area 2 examined on day 4 of storage 75% humidity. Measured d-spacings and angles compared to theoretical values for felodipine polymorphs for the diffraction pattern shown in Figure B.18. Average percentage errors between measured and theoretical values are equal to 7.5±1.0 and 2.3±0.9, forms I and II respectively.

Spot	**Distance** (nm^{-1})	**d-spacing** (nm)	**d-spacing (nm)** I	II	**hkl** I	II
1	3.45	0.29	0.27	0.30	330	$24\bar{6}$
2	2.98	0.34	0.31	0.34	$3\bar{2}0$	$8\bar{2}\bar{3}$
3	2.86	0.35	0.32	0.36	$\bar{2}\bar{3}0$	$\bar{2}\bar{4}4$
$\overrightarrow{1}$	0.87	1.15	1.09	1.19	100	002
θ_1	-	72	73	76	-	-
θ_2	-	97	97	99	-	-

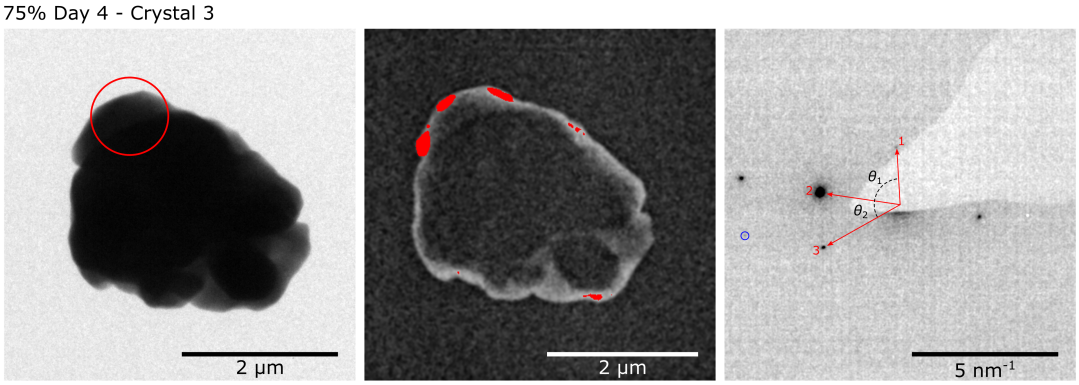

Figure B.19: Crystalline area 3 examined on day 4 of storage 75% humidity.

Table B.14: Crystalline area 3 examined on day 4 of storage 75% humidity. Measured d-spacings and angles compared to theoretical values for felodipine polymorphs for the diffraction pattern shown in Figure B.19. Average percentage errors between measured and theoretical values are equal to 1.3 ± 0.6, 2.3 ± 0.9, 0.7 ± 2.2 and 2.7 ± 2.1, forms I, II, III and IV respectively.

Spot	**Radial Distance** ($\mathbf{nm^{-1}}$)	**d-spacing** ($\mathbf{nm^{-1}}$)	**d-spacing (nm)**				**hkl**			
			I	II	III	IV	I	II	III	IV
1	1.98	0.50	0.49	0.49	0.51	0.50	210	$33\bar{2}$	210	$21\bar{1}$
2	2.75	0.36	0.36	0.36	0.36	0.35	$\bar{1}23$	$8\bar{2}\bar{2}$	$3\bar{1}1$	032
3	3.00	0.33	0.33	0.32	0.35	0.32	$\bar{2}04$	$5\bar{5}\bar{1}$	$1\bar{2}0$	$\bar{2}32$
$\overrightarrow{1}$	1.88	0.53	0.53	0.53	0.54	0.53	$\bar{1}21$	$\bar{3}\bar{3}1$	012	200
θ_1	-	77	73	77	76	74	-	-	-	-
θ_2	-	38	38	37	46	36	-	-	-	-

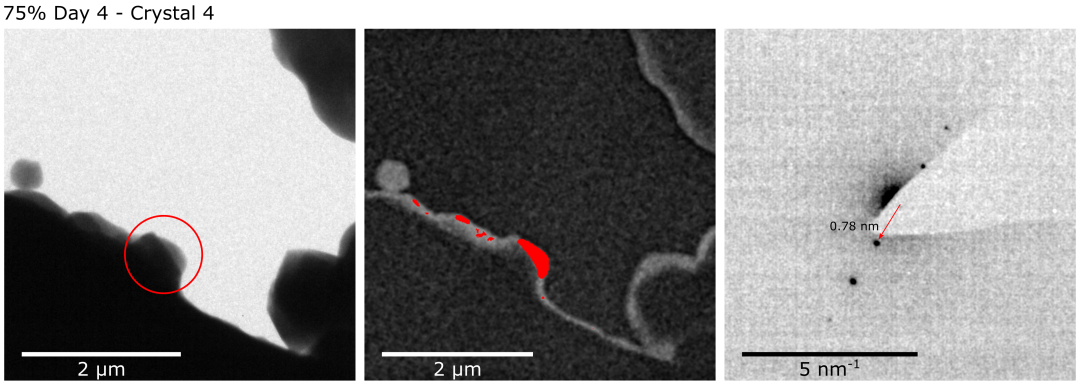

Figure B.20: Crystalline area 4 examined on day 4 of storage 75% humidity. The d-spacing equal to 0.78 nm is similar to the $11\bar{1}$, $22\bar{1}$, 002 or $11\bar{1}$ d-spacings in forms I, II, III and IV felodipine respectively.

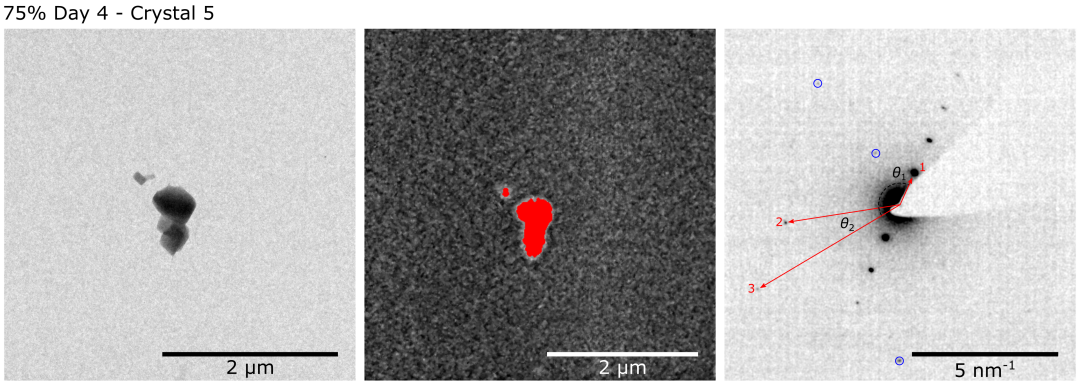

Figure B.21: Crystalline area 5 examined on day 4 of storage 75% humidity.

Table B.15: Crystalline area 5 examined on day 4 of storage 75% humidity. Measured d-spacings and angles compared to theoretical values for felodipine polymorphs for the diffraction pattern shown in Figure B.21. Average percentage errors between measured and theoretical values are equal to 1.7±0.1 and 2.4±0.9, forms II and IV respectively.

Spot	**Distance** ($\mathbf{nm^{-1}}$)	**d-spacing** (nm)	**d-spacing (nm)**		**hkl**	
			II	IV	II	IV
1	1.21	0.82	0.81	0.81	220	110
2	3.96	0.25	0.25	0.25	$\bar{8}\bar{2}\bar{7}$	$\bar{2}0\bar{4}$
3	5.66	0.18	0.17	0.17	$\bar{1}\bar{2}$ $\bar{6}\bar{7}$	$\bar{4}\bar{2}\bar{4}$
θ_1	-	123°	123°	122°	-	-
θ_2	-	22°	21°	21°	-	-

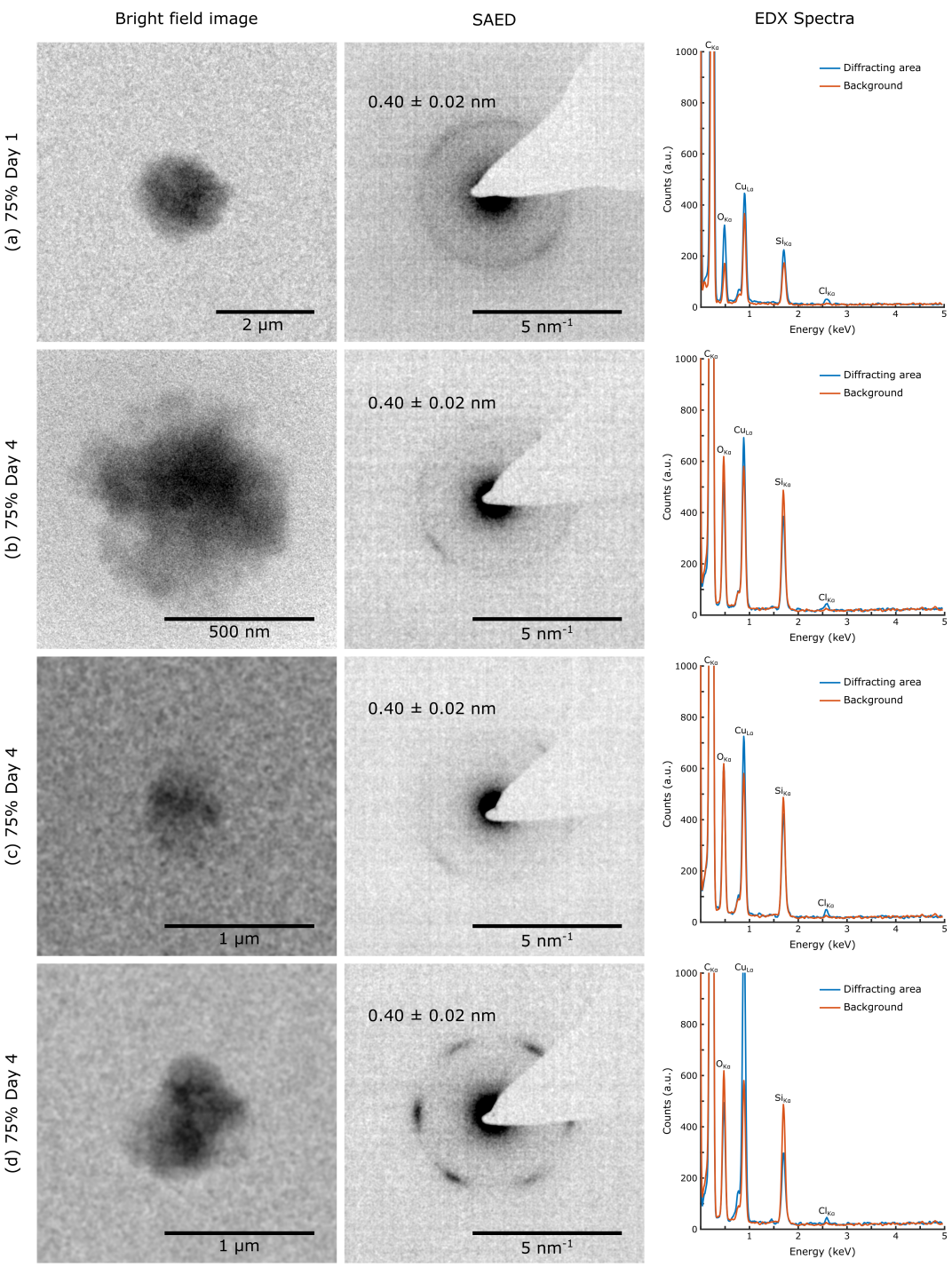

Figure B.22: Bright field image of weakly scattering areas, SAED show textured polycrystalline pattern with a single ring at 0.40 ± 0.02 nm and EDX spectra (a) 75% humidity day 1; (b) 75% humidity day 4; (c) 75% humidity day 4; (d) 75% humidity day 4.

References

Aakeröy, C. B. (1997). Crystal engineering: Strategies and architectures. *Acta Crystallographica Section B*, 53(4):569 – 586. 11

Adibkia, K., Barzegar-Jalali, M., Maheri-Esfanjani, H., Ghanbarzadeh, S., Shokri, J., Sabzevari, A., and Javadzadeh, Y. (2013). Physicochemical characterization of naproxen solid dispersions prepared via spray drying technology. *Powder Technology*, 246:448 – 455. 10

Agrawal, A. M., Dudhedia, M. S., and Zimny, E. (2016). Hot melt extrusion: Development of an amorphous solid dispersion for an insoluble drug from mini-scale to clinical scale. *AAPS PharmSciTech*, 17(1):133 – 147. 12

Akaike, H. (1974). A new look at the statistical model identification. *IEEE T-AC*, 19(6):716–723. 82

Alexander, P. and Charlesby, A. (1954). Energy transfer in macromolecules exposed to ionizing radiations. *Nature*, 173:578–579. 7, 89

Alonzo, D. E., Zhang, G. G. Z., Zhou, D., Gao, Y., and Taylor, L. S. (2010). Understanding the behavior of amorphous pharmaceutical systems during dissolution. *Pharmaceutical Research*, 27(4):608–618. 42

Amidon, G. L., Lennernäs, H., Shah, V. P., and Crison, J. R. (1995). A theoretical basis for a biopharmaceutic drug classification: The correlation of in vitro drug product dissolution and in vivo bioavailability. *Pharmaceutical Research*, 12(3):413 – 420. 2

Anderberg, E., Bisrat, M., and Nystrm, C. (1988). Physicochemical aspects of drug release. VII. the effect of surfactant concentration and drug particle size on solubility and dissolution rate of felodipine, a sparingly soluble drug. *International Journal of Pharmaceutics*, 47(1):67–77. 42

Andronis, V., Yoshioka, M., and Zografi, G. (1999). Effects of sorbed water on the crystallization of indomethacin from the amorphous state. *Journal of Pharmaceutical Sciences*, 86(3):346 – 351. 133, 168

Andronis, V. and Zografi, G. (2000). Crystal nucleation and growth of indomethacin polymorphs from the amorphous state. *Journal of Non-Crystalline Solids*, 271(3):236–248. 135

Arumainayagam, C. R., Lee, H.-L., Nelson, R. B., Haines, D. R., and Gunawardane, R. P. (2010). Low-energy electron-induced reactions in condensed matter. *Surface Science Reports*, 65(1):1 – 44. xii, 27, 28

Baird, J. A. and Taylor, L. S. (2012). Evaluation of amorphous solid dispersion properties using thermal analysis techniques. *Advanced Drug Delivery Reviews*, 64(5):396 – 421. 5, 10, 11, 15

Basavoju, S., Boström, D., and Velaga, S. P. (2008). Indomethacin–saccharin cocrystal: Design, synthesis and preliminary pharmaceutical characterization. *Pharmaceutical Research*, 25(3):530 – 541. 11

Betzig, E. and Trautman, J. K. (1992). Near-field optics: Microscopy, spectroscopy, and surface modification beyond the diffraction limit. *Science*, 257:189–195. 47

Bhardwaj, V., Trasi, N. S., Zemlyanov, D. Y., and Taylor, L. S. (2018). Surface area normalized dissolution to study differences in itraconazole-copovidone solid dispersions prepared by spray-drying and hot melt extrusion. *International Journal of Pharmaceutics*, 540(1):106–119. 20, 38, 136

Bhattacharya, S. and Suryanarayanan, R. (2009). Local mobility in amorphous pharmaceuticals-characterization and implications on stability. *Journal of Pharmaceutical Sciences*, 98(9):2935 – 2953. 18

Bikiaris, D., Papageorgiou, G. Z., Stergiou, A., Pavlidou, E., Karavas, E., Kanaze, F., and Georgarakis, M. (2005). Physicochemical studies on solid dispersions of poorly water-soluble drugs: Evaluation of capabilities and limitations of thermal analysis techniques. *Thermochimica Acta*, 439(1):58 – 67. 106

Bradley, C. R. and Zaluzec, N. J. (1989). Atomic sputtering in the analytical electron microscope. *Ultramicroscopy*, 28(1):335 – 338. 25

Broman, E., Khoo, C., and Taylor, L. S. (2001). A comparison of alternative polymer excipients and processing methods for making solid dispersions of a poorly water soluble drug. *International Journal of Pharmaceutics*, 222(1):139 – 151. 12

Brydson, R. (2011). *AberrationCorrected Analytical Transmission Electron Microscopy*. Wiley. 43

Byard, S. J., Jackson, S. L., Smail, A., Bauer, M., and Apperley, D. C. (2005). Studies on the crystallinity of a pharmaceutical development drug substance. *Journal of Pharmaceutical Sciences*, 94(6):1321 – 1335. 183

Cai, T., Zhu, L., and Yu, L. (2011). Crystallization of organic glasses: Effects of polymer additives on bulk and surface crystal growth in amorphous nifedipine. *Pharmaceutical Research*, 28(10):2458–2466. 175

Chauhan, H., Hui-Gu, C., and Atef, E. (2013). Correlating the behavior of polymers in solution as precipitation inhibitor to its amorphous stabilization ability in solid dispersions. *Journal of Pharmaceutical Sciences*, 102(6):1924 – 1935. 10, 11

Chavda, H., Patel, C., and Anand, I. (2010). Biopharmaceutics classification system. *Systematic Reviews in Pharmacy*, 1(1):62 – 69. 3

Chen, H., Pui, Y., Liu, C., Chen, Z., Su, C.-C., Hageman, M., Hussain, M., Haskell, R., Stefanski, K., Foster, K., Gudmundsson, O., and Qian, F. (2018). Moisture-induced amorphous phase separation of amorphous solid dispersions: Molecular mechanism, microstructure, and its impact on dissolution performance. *Journal of Pharmaceutical Sciences*, 107(1):317 – 326. 175

Chen, Y., Liu, C., Chen, Z., Su, C., Hageman, M., Hussain, M., Haskell, R., Stefanski, K., and Qian, F. (2015). Drugpolymerwater interaction and its implication for the dissolution performance of amorphous solid dispersions. *Molecular Pharmaceutics*, 12(2):576 – 589. 134

Cherns, D., Finnis, M. W., and Matthews, M. D. (1977). Sputtering of gold foils in a high voltage electron microscope a comparison of theory and experiment. *The Philosophical Magazine: A Journal of Theoretical Experimental and Applied Physics*, 35(3):693 – 714. 25

Cherns, D., Minter, F. J., and Nelson, R. S. (1976). Sputtering in the high voltage electron microscope. *Nuclear Instruments and Methods*, 132(1):369 – 376. 25

Chiou, W. L. and Riegelman, S. (1969). Preparation and dissolution characteristics of several fast-release solid dispersions of griseofulvin. *Journal of Pharmaceutical Sciences*, 58(12):1505 – 1510. 9

Chokshi, R. and Zia, H. (2010). Hot-melt extrusion technique: A review. *Iranian Journal of Pharmaceutical Research*, 3(1):3 – 16. 12

Clark, W., Chapman, J., MacLeod, A., and Ferrier, R. (1980). Radiation damage mechanisms in copper phthalocyanine and its chlorinated derivatives. *Ultramicroscopy*, 5(1-3):195–208. 37, 38, 80, 83, 92

Conroy, M., Soltis, J. A., Wittman, R. S., Smith, F. N., Chat-terjee, S., Zhang, X., Ilton, E. S., and Buck, E. C. (2017). Importance of interlayer h bonding structure to the stability of layered minerals. *Scientific Reports*, 7. 91

Cowley, J. (2004). Applications of electron nanodiffraction. *Micron*, 35(5):345 – 360. 197

Crowley, K. J. and Zografi, G. (2002). Water vapor absorption into amorphous hydrophobic drug/poly(vinylpyrrolidone) dispersions. *Journal of Pharmaceutical Sciences*, 91(10):2150 – 2165. 14

Crowley, K. J. and Zografi, G. (2003). The effect of low concentrations of molecularly dispersed poly(vinylpyrrolidone) on indomethacin crystallization from the amorphous state. *Pharmaceutical Research*, 20(9):1417 – 1422. 139

Curtis, G. H. and Ferrier, R. P. (1969). The electric charging of electron-microscope specimens. *Journal of Physics D: Applied Physics*, 2(7):1035. 30

de la Pena, F., Ostasevicius, T., Fauske, V. T., Burdet, P., Prestat, E., Jokubauskas, P., Nord, M., MacArthur, K. E., Sarahan, M., Johnstone, D. N., Taillon, J., Eljarrat, A., Migunov, V., Caron, J., Furnival, T., Mazzucco, S., Aarholt, T., Walls, M., Slater, T., Winkler, F., Martineau, B., Donval, G., McLeod, R., Hoglund, E. R., Alxneit, I., Hjorth, I., Henninen, T., Zagonel, L. F., Garmannslund, A., and 5ht2 (2018). Hyperspy v1.4. 198

Di, L., Fish, P. V., and Mano, T. (2012). Bridging solubility between drug discovery and development. *Drug Discovery Today*, 17(9):486 – 495. 2

Dickson, R. M., Cubitt, A. B., Tsien, R. Y., and Moerner, W. (1997). On/off blinking and switching behaviour of single molecules of green fluorescent protein. *Nature*, 388:355–358. 47

Downing, K. and Li, H. (2001). Accurate recording and measurement of electron diffraction data in structural and difference fourier studies of proteins. *Microscopy and Microanalysis*, 7(5):407 – 417. 37

Duong, T. V., Ludeke, D., Bockstal, P.-J. V., Beer, T. D., Humbeeck, J. V., and den Mooter, G. V. (2018). Polymorphism of indomethacin in semicrystalline dispersions: Formation, transformation, and segregation. *Molecular Pharmaceutics*, 15(3):1037–1051. 173

Duong, T. V., Van Humbeeck, J., and Van den Mooter, G. (2015). Crystallization kinetics of indomethacin/polyethylene glycol dispersions containing high drug loadings. *Molecular Pharmaceutics*, 12(7):2493 – 2504. 133

Eddleston, M. D., Bithell, E. G., and Jones, W. (2010). Transmission electron microscopy of pharmaceutical materials. *Journal of Pharmaceutical Sciences*, 99(9):4072 – 4083. 5, 6, 19, 37, 38, 183

Eerdenbrugh, B. V., Baird, J. A., and Taylor, L. S. (2010). Crystallization tendency of active pharmaceutical ingredients following rapid solvent evaporation-classification and comparison with crystallization tendency from under cooled melts. *Journal of Pharmaceutical Sciences*, 99(9):3826 – 3838. 16

Eerdenbrugh, B. V. and Taylor., L. S. (2011). Application of mid-ir spectroscopy for the characterization of pharmaceutical systems. *International Journal of Pharmaceutics*, 417(1):3 –16. 110

Egerton, R. (2014). Choice of operating voltage for a transmission electron microscope. *Ultramicroscopy*, 145:85–93. 27, 35, 36, 98, 194

Egerton, R. and Rauf, I. (1999). Dose-rate dependence of electron-induced mass loss from organic specimens. *Ultramicroscopy*, 80(4):247–254. 35, 36, 75

Egerton, R. F. (1980). Chemical measurements of radiation damage in organic samples at and below room temperature. *Ultramicroscopy*, 5(1):521–523. 33, 34, 35, 37, 97

Egerton, R. F. (2005). *Physical Principles of Electron Microscopy*. Springer. 43

Egerton, R. F. (2012). Mechanisms of radiation damage in beam-sensitive specimens, for tem accelerating voltages between 10 and 300 kv. *Microscopy Research and Technique*, 75(11):1550 – 1556. 22, 23, 36

Egerton, R. F. (2013). Control of radiation damage in the TEM. *Ultramicroscopy*, 127:100 –108. xii, 6, 25, 26, 28, 31, 35, 36, 97

Egerton, R. F. (2017). Scattering delocalization and radiation damage in STEM-EELS. *Ultramicroscopy*, 180:115 – 124. 35, 194

Egerton, R. F. (2018). Calculation, consequences and measurement of the point spread function for low-loss inelastic scattering. *Microscopy*, 67:i52 – i59. 194

Egerton, R. F., Crozier, P. A., and Rice, P. (1987). Electron energy-loss spectroscopy and chemical change. *Ultramicroscopy*, 23(3):305 – 312. 34

Egerton, R. F., Lazar, S., and Libera, M. (2012). Delocalized radiation damage in polymers. *Micron*, 43(1):2 – 7. 28

Egerton, R. F., Li, P., and Malac, M. (2004). Radiation damage in the TEM and SEM. *Micron*, 35(6):399 –409. xii, 6, 21, 22, 25, 29, 87, 91, 97

Egerton, R. F., McLeod, R., Wang, F., and Malac, M. (2010). Basic questions related to electron-induced sputtering in the tem. *Ultramicroscopy*, 110(8):991 – 997. xii, 23, 24

Eggeman, A., Johnstone, D., Krakow, R., Hu, J., Lozano-Perez, S., Grovenor, C., and Midgley, P. (2015). Decomposing electron diffraction signals in multi-component microstructures. *Microscopy and Microanalysis, 21*, S3:1241 – 1241. 198

Eggeman, A., Leary, R., Johnstone, D., and Midgley, P. (2017). Local layer stacking and structural disorder in graphene oxide studied via scanning electron diffraction. *Microscopy and Microanalysis, 23*, S1:1754 – 1755. 197

Eloy, J. O. and Marchetti, J. M. (2014). Solid dispersions containing ursolic acid in poloxamer 407 and peg 6000: A comparative study of fusion and solvent methods. *Powder Technology*, 253:98 – 106. 10

Flory, P. J. (1942). Thermodynamics of high polymer solutions. *Thermodynamics of High Polymer Solutions*, 10(51). 17, 168

Forster, A., Hempenstall, J., Tucker, I., and Rades, T. (2001). Selection of excipients for melt extrusion with two poorly water-soluble drugs by solubility parameter calculation and thermal analysis. *International Journal of Pharmaceutics*, 226(1):147 – 161. 116

Frank, D. S. and Matzger, A. J. (2017). Influence of chemical functionality on the rate of polymer-induced heteronucleation. *Crystal Growth & Design*, 17(8):4056–4059. 135

Frank, D. S. and Matzger, A. J. (2018). Probing the interplay between amorphous solid dispersion stability and polymer functionality. *Molecular Pharmaceutics*, 15(7):2714 – 2720. 133, 135

Fryer, J. (1987). The effect of dose rate on imaging aromatic organic crystals. *Ultramicroscopy*, 12(3-4):321–327. 7, 37, 89

Fryer, J., McConnell, C., Zemlin, F., and Dorset, D. (1992). Effect of temperature on radiation damage to aromatic organic molecules. *Ultramicroscopy*, 40(2):3389–3398. 7, 37, 89

Fryer, J. R. (1984). Radiation damage in organic crystalline films. *Ultramicroscopy*, 14(3):227–236. 34, 37, 87

Fryer, J. R. and Holland, F. (1983). The reduction of radiation damage in the electron microscope. *Ultramicroscopy*, 11(1):67 – 70. 34

Fryer, J. R. and Holland, F. (1984). High resolution electron microscopy of molecular crystals iii. radiation processes at room temperature. *Journal of Polymer Science Part B: Polymer Physics*, 393(1805):353 – 369. 34

Fu, J., Cui, L., Yang, C., Xiong, H., Ren, G., Ma, X., Jing, Q., and Ren, F. (2018). Screen for inhibitors of crystal growth to identify desirable carriers for amorphous solid dispersions containing felodipine. *AAPS PharmSciTech*, 19(3):1231–1242. 42

Fujiyoshir, Y. (1998). The structural study of membrane proteins by electron crystallography. *Advances in Biophysics*, 35:25 – 80. 35, 37

Girit, Ç. Ö., Meyer, J. C., Erni, R., Rossell, M. D., Kisielowski, C., Yang, L., Park, C.-H., Crommie, M. F., Cohen, M. L., Louie, S. G., and Zettl, A. (2009). Graphene at the edge: Stability and dynamics. *Science*, 323(5922):1705 – 1708. 24

Glaeser, R. M. (1971). Limitations to significant information in biological electron microscopy as a result of radiation damage. *Journal of Ultrastructure Research*, 36(3):466 – 482. 7

Glaeser, R. M., McMullan, G., Faruqi, A. R., and Henderson, R. (2011). Images of paraffin monolayer crystals with perfect contrast: Minimization of beam-induced specimen motion. *Ultramicroscopy*, 111(2):90 – 100. 37

Goldberg, A. H., Gibaldi, M., and Kanig, J. L. (1966). Increasing dissolution rates and gastrointestinal absorption of drugs via solid solutions and eutectic mixtures ii: Experimental evaluation of a eutectic mixture: Urea-acetaminophen system. *Journal of Pharmaceutical Sciences*, 55(5):482 – 487. 9

Goodhew, P. J., Humphreys, J., and Beanland, R. (2001). *Electron Microscopy and Analysis*. Taylor and Francis, third edition. 43

Gordon, M. and Taylor, J. S. (1952). Preparation of glass solutions of three poorly water soluble drugs by spray drying, melt extrusion and ball milling. *Journal of Applied Chemistry*, 2(9):493 – 500. 20, 114, 152

Greenspan, L. (1977). Humidity fixed points of binary saturated aqueous solutions. *Journal of Research of the National Bureau of Standards Section A: Physics and Chemistry*, 81A. 141

Greer, H. F. and Zhou, W. (2011). Electron diffraction and hrtem imaging of beam-sensitive materials. *Crystallography Reviews*, 17(3):163 – 185. 37

Grubb, D. T. (1974). Radiation damage and electron microscopy of organic polymers. *Journal of Materials Science*, 9(10):1715–1736. 33, 37, 83, 85

Gunn, E., Guzei, I. A., Cai, T., and Yu, L. (2012). Polymorphism of nifedipine: Crystal structure and reversible transition of the metastable polymorph. *Crystal Growth & Design*, 12(4):2037–2043. 135

Guns, S., Dereymaker, A., Kayaert, P., Mathot, V., Martens, J. A., and Van den Mooter, G. (2011). Comparison between hot-melt extrusion and spray-drying for manufacturing solid dispersions of the graft copolymer of ethylene glycol and vinylalcohol. *Pharmaceutical Research*, 28(3):673 – 682. 132

Guo, Y., Shalaev, E., and Smith, S. (2013). Physical stability of pharmaceutical formulations: solid-state characterization of amorphous dispersions. *TrAC Trends in Analytical Chemistry*, 49:137 – 144. 10, 11, 15, 18, 134

Hann, M. M. and Oprea, T. I. (2004). Pursuing the leadlikeness concept in pharmaceutical research. *Current Opinion in Chemical Biology*, 8(3):255 – 263. 2

Harmon, P., Galipeau, K., Xu, W., Brown, C., and Wuelfing, W. P. (2016). Mechanism of dissolution-induced nanoparticle formation from a copovidone-based amorphous solid dispersion. *Molecular Pharmaceutics*, 13(5):1467 – 1481. 167

Henderson, R. and Glaeser, R. M. (1985). Quantitative analysis of image contrast in electron micrographs of beam-sensitive crystals. *Ultramicroscopy*, 16(2):139–150. 6, 7, 29, 32, 34, 37

Hickey, M. B., Peterson, M. L., Scoppettuolo, L. A., Morrisette, S. L., Vetter, A., Guzmán, H., Remenar, J. F., Zhang, Z., Tawa, M. D., Haley, S., Zaworotko, M. J., and Almarsson, O. (2007). Performance comparison of a co-crystal of carbamazepine with marketed product. *European Journal of Pharmaceutics and Biopharmaceutics*, 67(1):112 – 119. 11

Hobbs, L. W. (1979). *Radiation Effects in Analysis of Inorganic Specimens by TEM*, pages 437 – 480. Springer US, Boston, MA. 26

Hobbs, L. W. (1990). Murphys law and the uncertainty of electron probes. *Scanning Microscopy Supplement*, 4:171 – 183. 30

Howitt, D. G. and Thomas, G. (1977). Electron damage in organic crystals. *Radiation Effects*, 34(4):209–215. 83

Huang, J., Wigent, R. J., and Schwartz, J. B. (2006). Nifedipine molecular dispersion in microparticles of ammonio methacrylate copolymer and ethylcellulose binary blends for controlled drug delivery: Effect of matrix composition. *Drug Development and Industrial Pharmacy*, 32(10):1185 – 1197. 11

Huang, L.-F. and Tong, W.-Q. T. (2004). Impact of solid state properties on developability assessment of drug candidates. *Advanced Drug Delivery Reviews*, 56(3):321 – 334. 4

Huang, S. and Williams, R. O. (2018). Effects of the preparation process on the properties of amorphous solid dispersions. *AAPS PharmSciTech*, 19(5):1971 – 1984. 132, 135

Ingram-Jones, V. J., Slade, R. C. T., Davies, T. W., Southern, J. C., and Salvador, S. (1996). Dehydroxylation sequences of gibbsite and boehmite: study of differences between soak and flash calcination and of particle-size effects. *Journal of Materials Chemistry*, 6(1):73–79. 92

International Experimental Study Group (1986). Cryoprotection in electron microscopy. *Journal of Microscopy*, 141(3):385–391. 34, 35, 97

Isaacson (1975). *Physical Aspects of Electron Microscopy and Microbeam Analysis*. Wiley, first edition. 33, 36, 80, 89

Isabell, T., Fischione, P., O'Keefe, C., Guruz, M., and Dravid, V. (1999). Plasma cleaning and its applications for electron microscopy. *Microscopy and Microanalysis*, 5(2):126 – 135. 29

Ishida, H., Wu, T., and Yu, L. (2007). Sudden rise of crystal growth rate of nifedipine near tg without and with polyvinylpyrrolidone. *Journal of Pharmaceutical Sciences*, 96(5):1131–1138. 175

Ishizuka, A., Hytch, M., and Ishizuka, K. (2017). STEM moiré analysis for 2D strain measurements. *Microscopy*, 66(3):217–221. 183

Janssens, S., de Armas, H. N., DAutry, W., Schepdael, A. V., and den Mooter, G. V. (2008). Characterization of ternary solid dispersions of itraconazole in polyethylene glycol 6000/polyvidone-vinylacetate 64 blends. *European Journal of Pharmaceutics and Biopharmaceutics*, 69(3):1114 – 1120. 11

Janssens, S. and Van den Mooter, G. (2009a). Review: physical chemistry of solid dispersions. *Journal of Pharmacy and Pharmacology*, 61(12):1571 – 1586. 4, 18

Janssens, S. and Van den Mooter, G. (2009b). The role of polymer concentration on the molecular mobility and physical stability of nifedipine solid dispersions. *Journal of Pharmacy and Pharmacology*, 61(12):1571 – 1586. 132

Jermain, S. V., Brough, C., and Williams, R. O. (2018). Amorphous solid dispersions and nanocrystal technologies for poorly water-soluble drug delivery an update. *International Journal of Pharmaceutics*, 535(1):379–392. 8, 42

Jiang, N. and Spence, J. C. H. (2012). On the dose-rate threshold of beam damage in tem. *Ultramicroscopy*, 112:77 – 82. 31, 35

Johari, G., Ram, S., Astl, G., and Mayer, E. (1990). Characterizing amorphous and microcrystalline solids by calorimetry. *Journal of Non-Crystalline Solids*, 116(2):282 – 285. 106

Johari, G. P. and Goldstein, M. (1970). Molecular mobility in simple glasses. *The Journal of Physical Chemistry*, 74(9):2034 – 2035. 18

Jones, W. and Thomas, J. M. (1979). Application of electron microscopy to organi solid-state chemistry. *Progress in Solid State Chemistry*, 12(2):101–124. 6

Jones, W., Thomas, J. M., Williams, J. O., and Hobbs, L. W. (1975). Electron microscopic studies of extended defects in organic molecular crystals. part 1.p-terphenyl. *J. Chem. Soc., Faraday Trans. 2*, 71:138 – 145. 37

Kanaze, F. I., Kokkalou, E., Niopas, I., Georgarakis, M., Stergiou, A., and Bikiaris, D. (2006). Dissolution enhancement of flavonoids by solid dispersion in pvp and peg matrixes: A comparative study. *Journal of Applied Polymer Science*, 102(1):460 – 471. 19

Kang, S., Johnstone, D., Jinnai, H., Higuchi, T., Murase, H., and Midley, P. (2016). Scanning electron diffraction of polyethylene. *The 16th European Microscopy Congress, Lyon, France.*, http://emc-proceedings.com/abstract/scanning-electron-diffraction-of-polyethylene.(Accessed: August 22, 2017). 197

Karavas, E., Georgarakis, E., Sigalas, M. P., Avgoustakis, K., and Bikiaris, D. (2007). Investigation of the release mechanism of a sparingly water-soluble drug from solid dispersions in hydrophilic carriers based on physical state of drug, particle size distribution and drugpolymer interactions. *European Journal of Pharmaceutics and Biopharmaceutics*, 66(3):334–347. 20, 38, 42

Karavas, E., Ktistis, G., Xenakis, A., and Georgarakis, E. (2005). Miscibility behavior and formation mechanism of stabilized felodipine-polyvinylpyrrolidone amorphous solid dispersions. *Drug Development and Industrial Pharmacy*, 31(6):473 – 489. 113

Karavas, E., Ktistis, G., Xenakis, A., and Georgarakis, E. (2006). Effect of hydrogen bonding interactions on the release mechanism of felodipine from nanodispersions with polyvinylpyrrolidone. *European Journal of Pharmaceutics and Biopharmaceutics*, 63(2):103–114. 42

Karavas, E., Ktistis, G., Xenakis, A., and Georgarakis, E. (2008). Miscibility behavior and formation mechanism of stabilized felodipine-polyvinylpyrrolidone amorphous solid dispersions. *Drug Development and Industrial Pharmacy*, 31(6):473 – 489. 113

Karuppasamy, M., Karimi Nejadasl, F., Vulovic, M., Koster, A. J., and Ravelli, R. B. G. (2011). Radiation damage in single-particle cryo-electron microscopy: effects of dose and dose rate. *Journal of Synchrotron Radiation*, 18(3):398 – 412. 31

Ke, P., Hasegawa, S., Al-Obaidi, H., and Buckton, G. (2012). Investigation of preparation methods on surface/bulk structural relaxation and glass fragility of amorphous solid dispersions. *International journal of pharmaceutics*, 422(1-2):170–178. 135

Kestur, U. S. and Taylor, L. S. (2010). Role of polymer chemistry in influencing crystal growth rates from amorphous felodipine. *CrystEngComm*, 12(8):2390 – 2397. 110, 111, 113, 150

Khadka, P., Ro, J., Kim, H., Kim, I., Kim, J. T., Kim, H., Cho, J. M., Yun, G., and Lee, J. (2014). Pharmaceutical particle technologies: An approach to improve drug solubility, dissolution and bioavailability. *Asian Journal of Pharmaceutical Sciences*, 9(6):304 – 316. 4

Kim, E.-J., Chun, M.-K., Jang, J.-S., Lee, I.-H., Lee, K.-R., and Choi, H.-K. (2006). Preparation of a solid dispersion of felodipine using a solvent wetting method. *European Journal of Pharmaceutics and Biopharmaceutics*, 64(2):200 – 205. 12

Kim, S., Lee, S., Kondo, Y., Lee, K., Byun, G., Lee, S., and Lee, K. (2013a). Strained hetero interfaces in Si/SiGe/SiGe/SiGe multi-layers studied by scanning moiré fringe imaging. *Journal of Applied Physics*, 114(5):053518. 183

Kim, S., Lee, S., Oshima, Y., Kondo, Y., Okunishi, E., Endo, N., Jung, J., Byun, G., Lee, S., and Lee, K. (2013b). Scanning moiré fringe imaging for quantitative strain mapping in semiconductor devices. *Applied Physics Letters*, 102. 183

Klar, T. A., Jakobs, S., Dyba, M., Egner, A., and Hell, S. W. (2000). Fluorescence microscopy with diffraction resolution barrier broken by stimulated emission. *PNAS*, 97:8206–8210. 47

Klein, N. D., Hurley, K. R., Feng, Z. V., and Haynes, C. L. (2015). Dark field transmission electron microscopy as a tool for identifying inorganic nanoparticles in biological matrices. *Analytical Chemistry*, 87(8):4356–4362. 144

Knapek, E. and Dubochet, J. (1980). Beam damage to organic material is considerably reduced in cryo-electron microscopy. *Journal of Molecular Biology*, 141(2):147–161. 32, 34, 37, 97

Knapek, E., Formanek, H., Lefranc, G., and Dietrich, I. (1984). The interpretation of radiation damage measurements with electron diffraction of organic materials at very low temperatures. *Ultramicroscopy*, 14(2):253–263. 37, 83, 85

Koehler, J. S. (1959). Diffusion of lattice defects in a stress field. *Phys. Rev.*, 181(3):1015–1019. 85

Koivisto, M., Heinänen, P., Tanninen, V. P., and Lehto, V.-P. (2006). Depth profiling of compression-induced disorders and polymorphic transition on tablet surfaces with grazing incidence X-ray diffraction. *Pharmaceutical Research*, 23(4):813 – 820. 183

Kolb, U., Gorelik, T. E., Mugnaioli, E., and Stewart, A. (2010). Structural characterization of organics using manual and automated electron diffraction. *Polymer Reviews*, 50(3):385–409. 87, 92

Kondo, Y. and Okunishi, E. (2014). Magnified pseudo-elemental map of atomic column obtained by moir/'e method in scanning transmission electron microscopy. *Microscopy*, 63(5):391 – 395. 183

Kondo, Y., Okunishi, E., Fukunage, K.-i., and Endo, N. (2017). Way to reduce electron dose in pseudo atomic column elemental maps by 2D stem moiré. *Proceedings of Microscopy & Microanalysis 2017*, 23:1790 – 1791. 183

Konno, H., Handa, T., Alonzo, D. E., and Taylor, L. S. (2008). Effect of polymer type on the dissolution profile of amorphous solid dispersions containing felodipine. *European Journal of Pharmaceutics and Biopharmaceutics*, 70(2):493–499. 42, 43

Konno, H. and Taylor, L. S. (2006). Influence of different polymers on the crystallization tendency of molecularly dispersed amorphous felodipine. *Journal of Pharmaceutical Sciences*, 95(12):2692–2705. 14, 42, 109, 110, 111, 116, 132

Konno, H. and Taylor, L. S. (2008). Ability of different polymers to inhibit the crystallization of amorphous felodipine in the presence of moisture. *Pharmaceutical Research*, 25(43):969–978. 133

Kothari, K., Ragoonanan, V., and Suryanarayanan, R. (2015a). The role of drugpolymer hydrogen bonding interactions on the molecular mobility and physical stability of nifedipine solid dispersions. *Molecular Pharmaceutics*, 12(1):162 – 170. 133

Kothari, K., Ragoonanan, V., and Suryanarayanan, R. (2015b). The role of polymer concentration on the molecular mobility and physical stability of nifedipine solid dispersions. *Molecular Pharmaceutics*, 12(5):1477 – 1484. 133

Kumar, S. and Adams, W. (1990). Electron beam damage in high temperature polymers. *Polymer*, 31(1):15–19. 7, 37, 80, 83, 87, 92

Lee, A. Y., Erdemir, D., and Myerson, A. S. (2011). Crystal polymorphism in chemical process development. *Annual Review of Chemical and Biomolecular Engineering*, 2(1):259–280. 173

Leijten, Z. J. W. A., Keizer, A. D. A., de With, G., and Friedrich, H. (2017). Quantitative analysis of electron beam damage in organic thin films. *The Journal of Physical Chemistry C*, 121(19):10552–10561. 83

Leuner, C. and Dressman, J. (2000). Improving drug solubility for oral delivery using solid dispersions. *European Journal of Pharmaceutics and Biopharmaceutics*, 50(1):47 – 60. 5, 11

Li, N., Gilpin, C. J., and Taylor, L. S. (2017). Understanding the impact of water on the miscibility and microstructure of amorphous solid dispersions: An afmlcr and temedx study. *Molecular Pharmaceutics*, 14(5):1691 – 1705. 166

Li, P. and Egerton, R. F. (2004). Radiation damage in coronene, rubrene and p-terphenyl, measured for incident electrons of kinetic energy between 100 and 200 keV. *Ultramicroscopy*, 101(2-4):161–172. 32, 33, 37, 83, 89

Li, Y., Pang, H., Guo, Z., Lin, L., Dong, Y., Li, G., Lu, M., and Wu, C. (2013). Interactions between drugs and polymers influencing hot melt extrusion. *Journal of Pharmacy and Pharmacology*, 66(2):148 – 166. xi, 16

Lin, S.-Y., Liao, C.-M., Hsiue, G.-H., and Liang, R.-C. (1995). Study of a theophylline-eudragit l mixture using a combined system of microscopic fourier-transform infrared spectroscopy and differential scanning calorimetry. *Thermochimica Acta*, 254:153 – 166. 14, 20

Lindfors, L., Skantze, P., Skantze, U., Westergren, J., and Olsson, U. (2007). Amorphous drug nanosuspensions. 3. particle dissolution and crystal growth. *Langmuir*, 23(19):9866–9874. 167

Lipinski, C. A. (2000). Drug-like properties and the causes of poor solubility and poor permeability. *Journal of Pharmacological and Toxicological Methods*, 44(1):235 – 249. 2

Lou, B., Bostrm, D., and Velaga, S. P. (2009). Polymorph control of felodipine form ii in an attempted cocrystallization. *Crystal Growth & Design*, 9(3):1254–1257. 173

Lu, Q. and Zografi, G. (1998). Phase behavior of binary and ternary amorphous mixtures containing indomethacin, citric acid, and pvp. *Pharmaceutical Research*, 15(8):1202–1206. 152

Luebbert, C. and Sadowski, G. (2017). Moisture-induced phase separation and recrystallization in amorphous solid dispersions. *International Journal of Pharmaceutics*, 532(1):635 – 646. 170

Mahamid, J., Schampers, R., Persoon, H., Hyman, A. A., Baumeister, W., and Plitzko, J. M. (2015). A focused ion beam milling and lift-out approach for site-specific preparation of frozen-hydrated lamellas from multicellular organisms. *Journal of Structural Biology*, 192(2):262 – 269. 182

Mahmah, O., Tabbakh, R., Kelly, A., and Paradkar, A. (2013). A comparative study of the effect of spray drying and hotmelt extrusion on the properties of amorphous solid dispersions containing felodipine. *Journal of Pharmacy and Pharmacology*, 66(2):275–284. 42

Marc Adrian, Jacques Dubochet, J. L. and McDowall, A. W. (1984). Cryo-electron microscopy of viruses. *Nature*, 308:32 – 36. 34

Marsac, P. J., Konno, H., Rumondor, A. C. F., and Taylor, L. S. (2008a). Recrystallization of nifedipine and felodipine from amorphous molecular level solid dispersions containing poly(vinylpyrrolidone) and sorbed water. *Pharmaceutical Research*, 25(3):647–656. 42, 43

Marsac, P. J., Konno, H., and Taylor, L. S. (2006). A comparison of the physical stability of amorphous felodipine and nifedipine systems. *Pharmaceutical Research*, 23(10):2306–2316. 16, 18, 42, 43

Marsac, P. J., Li, T., and Taylor, L. S. (2008b). Estimation of drug-polymer miscibility and solubility in amorphous solid dispersions using experimentally determined interaction parameters. *Pharmaceutical Research*, 26(1):139. 11

Marsac, P. J., Rumondor, A. C., Nivens, D. E., Kestur, U. S., Stanciu, L., and Taylor, L. S. (2010). Effect of temperature and moisture on the miscibility of amorphous dispersions of felodipine and poly(vinyl pyrrolidone). *Journal of Pharmaceutical Sciences*, 99(1):169–185. 20, 38, 133, 136

Martin, D. C., Chen, J., Yang, J., Drummy, L. F., and Kübel, C. (2005). High resolution electron microscopy of ordered polymers and organic molecular crystals: Recent developments and future possibilities. *Journal of Polymer Science Part B: Polymer Physics*, 43(14):1749 – 1778. 37, 38

Martineau, B. and Eggeman, A. (2016). Clustering for scanning transmission electron diffraction data. *European Microscopy Congress 2016: Proceedings*, pages 669 – 670. 198

Mellert, W., Deckardt, K., Gembardt, C., Hildebrand, B., and Schulte, S. (2004). Carcinogenicity and chronic toxicity of copovidone (kollidon va 64) in wistar rats and beagle dogs. *Food and Chemical Toxicology*, 42(10):1573 – 1587. 42

Meng, F., Gala, U., and Chauhan, H. (2015). Classification of solid dispersions: correlation to (i) stability and solubility (ii) preparation and characterization techniques. *Drug Development and Industrial Pharmacy*, 41(9):1401 – 1415. xi, 9, 10, 135

Miller, D. A., Ellenberger, D., and Gil, M. (2016). *Spray-Drying Technology*, pages 437–525. Springer International Publishing, Cham. 14

Mistry, P., Mohapatra, S., Gopinath, T., Vogt, F. G., and Suryanarayanan, R. (2015). Role of the strength of drugpolymer interactions on the molecular mobility and crystallization inhibition in ketoconazole solid dispersions. *Molecular Pharmaceutics*, 12(9):3339 – 3350. 132

Mistry, P. and Suryanarayanan, R. (2016). Strength of drugpolymer interactions: Implications for crystallization in dispersions. *Crystal Growth and Design*, 16(9):5141–5149. 132

Moeck, P., Rouvimov, S., Rauch, E. F., Véron, M., Kirmse, H., Husler, I., Neumann, W., Bultreys, D., Maniette, Y., and Nicolopoulos, S. (2011). High spatial resolution semi-automatic crystallite orientation and phase mapping of nanocrystals in transmission electron microscopes. *Crystal Research and Technology*, 46(6):589 – 606. 197, 198

Moneghini, M., Bellich, B., Baxa, P., and Princivalle, F. (2008). Microwave generated solid dispersions containing ibuprofen. *International Journal of Pharmaceutics*, 361(1):125 – 130. 12

Murakami, Y., Sasaki, T., Ohkubo, T., and Hono, K. (2015). Strain measurements from Nd2Fe14B grains in sintered magnets using artificial moiré fringes. *Acta Materialia*, 101:101–106. 183

Naden, A. B., OShea, K. J., and MacLaren, D. A. (2018). Evaluation of crystallographic strain, rotation and defects in functional oxides by the moiré effect in scanning transmission electron microscopy. *Nanotechnology*, 29(16):165704. 183

Nollenberger, K., Gryczke, A., Meier, C., Dressman, J., Schmidt, M., and Brhne, S. (2009). Pair distribution function xray analysis explains dissolution characteristics of felodipine melt extrusion products. *Journal of Pharmaceutical Sciences*, 98(4):1476–1486. 42

Nurzynska, K., Booth, J., Roberts, C. J., McCabe, J., Dryden, I., and Fischer, P. M. (2015). Long-term amorphous drug stability predictions using easily calculated, predicted, and measured parameters. *Molecular Pharmaceutics*, 12(9):3389–3398. 40

Okonogi, S., Oguchi, T., Yonemochi, E., Puttipipatkhachorn, S., and Yamamoto, K. (1997). Improved dissolution of ofloxacin via solid dispersion. *International Journal of Pharmaceutics*, 156(2):175 – 180. 10

Pan, M. and Crozier, P. (1993). Quantitative imaging and diffraction of zeolites using a slow-scan ccd camera. *Ultramicroscopy*, 52(3):487 – 498. 7, 37

Pan, Y.-H., Vaughan, G., Brydson, R., Bleloch, A., Gass, M., Sader, K., and Brown, A. (2010). Electron-beam-induced reduction of fe3+ in iron phosphate dihydrate, ferrihydrite, haemosiderin and ferritin as revealed by electron energy-loss spectroscopy. *Ultramicroscopy*, 110(8):1020 – 1032. 7, 37

Pandey, M. M., Jaipal, A., Charde, S. Y., Goel, P., and Kumar, L. (2016). Application of mid-ir spectroscopy for the characterization of pharmaceutical systems. *Pharmaceutical Development and Technology*, 21(4):463 –474. 109

Panova, O., Chen, X. C., Bustillo, K. C., Ophus, C., Bhatt, M. P., Balsara, N., and Minor, A. M. (2016). Orientation mapping of semicrystalline polymers using scanning electron nanobeam diffraction. *Micron*, 88:30 – 36. 197, 198, 204

Parmenter, C. D., Fay, M. W., Hartfield, C., and Eltaher, H. M. (2016). Making the practically impossible "merely difficult"- cryogenic FIB lift-out for "damage fre'e' soft matter imaging. *Microscopy Research and Technique*, 79(4):298 – 303. 182

Patil, H., Tiwari, R. V., and Repka, M. A. (2016). Hot-melt extrusion: from theory to application in pharmaceutical formulation. *AAPS PharmSciTech*, 17(1):20 – 42. 12

Patterson, J. E., James, M. B., Forster, A. H., Lancaster, R. W., Butler, J. M., and Rades, T. (2007). Preparation of glass solutions of three poorly water soluble drugs by spray drying, melt extrusion and ball milling. *International Journal of Pharmaceutics*, 336(1):22 – 34. 116, 153

Patterson, J. E., James, M. B., Forster, A. H., and Rades, T. (2008). Melt extrusion and spray drying of carbamazepine and dipyridamole with polyvinylpyrrolidone/vinyl acetate copolymers. *Drug Development and Industrial Pharmacy*, 34(1):95 – 106. 114, 116

Prudic, A., Ji, Y., Luebbert, C., and Sadowski, G. (2015). Influence of humidity on the phase behavior of api/polymer formulations. *European Journal of Pharmaceutics and Biopharmaceutics*, 94:352 – 362. 170

Pudipeddi, M. and Serajuddin, A. T. (2005). Trends in solubility of polymorphs. *Journal of Pharmaceutical Sciences*, 94(5):929 – 939. 4

Purohit, H. S. and Taylor, L. S. (2017). Phase behavior of ritonavir amorphous solid dispersions during hydration and dissolution. *Pharmaceutical Research*, 34(12):2842 – 2861. 168

Qi, S., Belton, P., Nollenberger, K., Gryczke, A., and Craig, D. Q. M. (2011). Compositional analysis of low quantities of phase separation in hot-melt-extruded solid dispersions: A combined atomic force microscopy, photothermal fourier-transform infrared microspectroscopy, and localised thermal analysis approach. *Pharmaceutical Research*, 28(9):2311–2326. 13, 20, 136, 175, 180

Reimer, L., Golla, U., Bongeler, R., Kassens, M., Schindler, B., and Senkel, R. (1992). Charging of bulk specimens, insulating layers and free-supporting films in scanning electron microscopy. *Optik*, 92(1):14 – 22. 30

Reimer, L. and Spruth, J. (1982). Interpretation of the fading of diffraction patterns from organic substances irradiated with 100 keV electrons at 10-300 K. *Ultramicroscopy*, 10(3):199–210. 32, 35, 37, 83, 84, 87

Revol, J. F. and Manley, R. S. J. (1986). Lattice imaging in polyethylene single crystals. *Journal of Materials Science Letters*, 5(3):249 – 251. 7

Ricarte, R. G., Lodge, T. P., and Hillmyer, M. A. (2015). Detection of pharmaceutical drug crystallites in solid dispersions by transmission electron microscopy. *Drug Development and Industrial Pharmacy*, 12(3):983 – 990. 19, 20, 38, 135, 136, 143

Ricarte, R. G., Lodge, T. P., and Hillmyer, M. A. (2016). Nanoscale concentration quantification of pharmaceutical actives in amorphous polymer matrices by electron energy-loss spectroscopy. *Langmuir*, 32:7411 – 7419. 38

Robard, A., Patterson, D., and Delmas, G. (1977). The "delta chi effect" and polystyrene-poly(vinyl methyl ether) compatibility in solution. *Macromolecules*, 10(3):706–708. 168

Rodriguez-Aller, M., Guillarme, D., Veuthey, J.-L., and Gurny, R. (2015). Strategies for formulating and delivering poorly water-soluble drugs. *Journal of Drug Delivery Science and Technology*, 30(Part B):342 – 351. 4

Rose, A. (1973). *Vision: Human and Electronic*. Springer US, first edition. 144

Ross, M. W. and DeVore, T. C. (2008). Desorption of nitric acid from boehmite and gibbsite. *The Journal of Physical Chemistry A*, 112(29):6609–6620. 92

Rubino, S., Akhtar, S., Melin, P., Searle, A., Spellward, P., and Leifer, K. (2012). A site-specific focused-ion-beam lift-out method for cryo Transmission Electron Microscopy. *Journal of Structural Biology*, 180(3):572 – 576. 182

Rumondor, A. C. and Taylor, L. S. (2010a). Application of partial least-squares (pls) modeling in quantifying drug crystallinity in amorphous solid dispersions. *International Journal of Pharmaceutics*, 398(1):155–160. 146

Rumondor, A. C. F., Ivanisevic, I., Bates, S., Alonzo, D. E., and Taylor, L. S. (2009a). Evaluation of drug-polymer miscibility in amorphous solid dispersion systems. *Pharmaceutical Research*, 26(11):2523 – 2534. 14, 17, 18

Rumondor, A. C. F., Marsac, P. J., Stanford, L. A., and Taylor, L. S. (2009b). Phase behavior of poly(vinylpyrrolidone) containing amorphous solid dispersions in the presence of moisture. *Molecular Pharmaceutics*, 6(59):1492 – 1505. 170

Rumondor, A. C. F., Stanford, L. A., and Taylor, L. S. (2009c). Effects of polymer type and storage relative humidity on the kinetics of felodipine crystallization from amorphous solid dispersions. *Pharmaceutical Research*, 26(12):2599–2606. 14, 42, 43, 169

Rumondor, A. C. F. and Taylor, L. S. (2010b). Effect of polymer hygroscopicity on the phase behavior of amorphous solid dispersions in the presence of moisture. *Molecular Pharmaceutics*, 7(2):477 – 490. 19, 133

Rumondor, A. C. F., Wikstrm, H., Eerdenbrugh, B. V., and Taylor, L. S. (2011). Understanding the tendency of amorphous solid dispersions to undergo amorphousamorphous phase separation in the presence of absorbed moisture. *AAPS PharmSciTech*, 12(4):1209 – 1219. 133

Salih, S. M. and Cosslett, V. E. (1974). Reduction in electron irradiation damage to organic compounds by conducting coatings. *The Philosophical Magazine: A Journal of Theoretical Experimental and Applied Physics*, 30(1):225 – 228. 34

Salisbury, I. G., Timsit, R. S., Berger, S. D., and Humphreys, C. J. (1984). Nanometer scale electron beam lithography in inorganic materials. *Applied Physics Letters*, 45(12):1289 – 1291. 35

Sareen, S., Mathew, G., and Joseph, L. (2012). Improvement in solubility of poor water-soluble drugs by solid dispersion. *International Journal of Pharmaceutical Investigation*, 2(12):12 – 17. 4

Schwarz, G. (1978). Estimating the dimension of a model. *Ann. Statist.*, 6(2):461–464. 82

Sekiguchi, K. and Obi, N. (1961). Studies on absorption of eutectic mixture. i. a comparison of the behavior of eutectic mixture of sulfathiazole and that of ordinary sulfathiazole in man. *Chemical & Pharmaceutical Bulletin*, 9(11):866 – 872. 9

Serajuddin, A. T. M. (2000). Solid dispersion of poorly water-soluble drugs: Early promises, subsequent problems, and recent breakthroughs. *Journal of Pharmaceutical Sciences*, 88(10):1058 – 1066. 13

Shah, B., Kakumanu, V. K., and Bansa, A. K. (2006). Analytical techniques for quantification of amorphous/crystalline phases in pharmaceutical solids. *Journal of Pharmaceutical Sciences*, 95(8):1641 – 1665. 146

Shamblin, S. L. and Zografi, G. (1999). The effects of absorbed water on the properties of amorphous mixtures containing sucrose. *Pharmaceutical Research*, 16(7):1119 – 1124. 168

Shockley, W. (1961). Problems related top-n junctions in silicon. *Czechoslovak Journal of Physics*, 11(2):81 – 121. 27

Siegel, G. (1972). Influence of very low temperature on radiation damage of organic crystals irradiated by 100 kev electrons. *Z. Naturforsch*, 27a(2):325–332. 34, 35, 37, 84, 85, 97

Sigworth, F. (2013). Readdmfile. *MATLAB Central File Exchange*, Retrieved September 29, 2016. 76

Simha, R. and Boyer, R. F. (1962). On a general relation involving the glass temperature and coefficients of expansion of polymers. *The Journal of Chemical Physics*, 37(5):1003 – 1007. 114

Six, K., Verreck, G., Peeters, J., Brewster, M., and Mooter, G. V. d. (2004). Increased physical stability and improved dissolution properties of itraconazole, a class II drug, by solid dispersions that combine fast- and slow-dissolving polymers. *Journal of Pharmaceutical Sciences*, 93(1):124 – 131. 116

Skrovanek, D. J., Howe, S. E., Painter, P. C., and Coleman, M. M. (1985). Hydrogen bonding in polymers: infrared temperature studies of an amorphous polyamide. *Macromolecules*, 18(9):1676 – 1683. 110

Smith, L. I. (2002). A tutorial on principal component analysis. *Accessed online*, http://www.cs.otago.ac.nz/cosc453/studenttutorials/principalcomponents.pdf. (September 3, 2018). 78

Song, Y., Wang, L., Yang, P., Wenslow, R. M., Tan, B., Zhang, H., and Deng, Z. (2013). Physicochemical characterization of felodipine-kollidon va64 amorphous solid dispersions prepared by hot-melt extrusion. *Journal of Pharmaceutical Sciences*, 102(6):1915 – 1923. 20, 42, 110, 113, 114, 150

Stark, H., Zemlin, F., and Boettcher, C. (1996). Electron radiation damage to protein crystals of bacteriorhodopsin at different temperatures. *Ultramicroscopy*, 63(2):75 – 79. 37

Stenn, K. and Bahr, G. (1970). Specimen damage caused by the beam of the transmission electron microscope, a correlative reconsideration. *Journal of Ultrastructure Research*, 31(5-6):526 –550. 6, 25, 37, 83, 84, 85, 91

Stranski, I. N. and Totomanow, D. (1933). Nucleation rate and ostwald step rule. *Journal of Physical Chemistry*, 162A(1). 173

Su, D. and Zhu, Y. (2010). Scanning moiré fringe imaging by scanning transmission electron microscopy. *Ultramicroscopy*, 110(3):229–233. 182, 183

Surov, A. O., Solanko, K. A., Bond, A. D., Perlovich, G. L., and Bauer-Brandl, A. (2012). Crystallization and polymorphism of felodipine. *Crystal Growth and Design*, 12(8):4022–4030. 41, 42, 117

Takagi, T., Ramachandran, C., Bermejo, M., Yamashita, S., Yu, L. X., and Amidon, G. L. (2006). A provisional biopharmaceutical classification of the top 200 oral drug products in the united states, great britain, spain, and japan. *Molecular Pharmaceutics*, 3(6):631 – 643. 2

Tang, X. C., Pikal, M. J., and Taylor, L. S. (2002). A spectroscopic investigation of hydrogen bond patterns in crystalline and amorphous phases in dihydropyridine calcium channel blockers. *Pharmaceutical Research*, 19(4):477–483. 109, 110, 132

Tao, J. and Yu, L. (2006). Kinetics of cross-nucleation between polymorphs. *The Journal of Physical Chemistry B*, 110(14):7098–7101. 135

Taylor, L. S., Langkilde, F. W., and Zografi, G. (2001). Fourier transform raman spectroscopic study of the interaction of water vapor with amorphous polymers. *Journal of Pharmaceutical Sciences*, 90(7):888 – 901. 113, 150, 170

Taylor, L. S. and Zografi, G. (1998). Sugarpolymer hydrogen bond interactions in lyophilized amorphous mixtures. *Journal of Pharmaceutical Sciences*, 87(12):1615 – 1621. 116, 153

Thomas, L. C. (2015). Interpreting unexpected events and transitions in dsc results. *Accessed online*, http://www.tainstruments.com/pdf/literature/TA039.pdf. (July 27, 2018. 114

Tian, Y., Booth, J., Meehan, E., Jones, D. S., Li, S., and Andrews, G. P. (2013a). Construction of drug-polymer thermodynamic phase diagrams using flory-huggins interaction theory: Identifying the relevance of temperature and drug weight fraction to phase separation within solid dispersions. *Molecular Pharmaceutics*, 10(1):236 – 248. 18

Tian, Y., Caron, V., Jones, D. S., Healy, A.-M., and Andrews, G. P. (2013b). Using floryhuggins phase diagrams as a pre-formulation tool for the production of amorphous solid dispersions: a comparison between hot-melt extrusion and spray drying. *Journal of Pharmacy and Pharmacology*, 66(2):256 – 274. 132

Tres, F., Treacher, K., Booth, J., Hughes, L. P., Wren, S. A. C., Aylott, J. W., and Burley, J. C. (2016). Indomethacin-kollidon va64 extrudates: A mechanistic study of ph-dependent controlled release. *Molecular Pharmaceutics*, 13(3):1166–1175. 43

Tsai, C.-Y., Chang, Y.-C., Lobato, I., Van Dyck, D., and Chen, F.-R. (2016). Hollow cone electron imaging for single particle 3d reconstruction of proteins. *Scientific Reports*, 6. 144

Turnbull, D. (1981). Metastable structures in metallurgy. *Metallurgical Transactions B*, 12(2):217–230. 173

Turnbull, D. and Fisher, J. C. (1949). Rate of nucleation in condensed systems. *The Journal of Chemical Physics*, 17(1):71–73. 173

Ueda, H., Aikawa, S., Kashima, Y., Kikuchi, J., Ida, Y., Tanino, T., Kadota, K., and Tozuka, Y. (2014). Anti-plasticizing effect of amorphous indomethacin induced by specific intermolecular interactions with PVA copolymer. *Journal of Pharmaceutical Sciences*, 103(9):2829 – 2838. 133, 134

Ungár, T., Gubicza, J., Ribárik, G., and Borbély, A. (2001). Crystallite size distribution and dislocation structure determined by diffraction profile analysis: principles and practical application to cubic and hexagonal crystals. *Journal of Applied Crystallography*, 34(3):298–310. 171

van Drooge, D. J., Hinrichs, W. L. J., Visser, M. R., and Frijlink, H. W. (2006). Characterization of the molecular distribution of drugs in glassy solid dispersions at the nano-meter scale, using differential scanning calorimetry and gravimetric water vapour sorption techniques. *International Journal of Pharmaceutics*, 310(1):220 – 229. 10

Van Eerdenbrugh, B. and Taylor, L. S. (2012). Molecular weight effects on the miscibility behavior of dextran and maltodextrin with poly(vinylpyrrolidone). *Pharmaceutical Research*, 29(10):2754 – 2765. 17

Vasanthavada, M., Tong, W.-Q. T., Joshi, Y., and Kislalioglu, M. S. (2005). Phase behavior of amorphous molecular dispersions ii: Role of hydrogen bonding in solid solubility and phase separation kinetics. *Pharmaceutical Research*, 22(3):440 – 448. 14

Vishweshwar, P., McMahon, J. A., Bis, J. A., and Zaworotko, M. J. (2006). Pharmaceutical co-crystals. *Journal of Pharmaceutical Sciences*, 95(3):499 – 516. 11

Vo, C. L.-N., Park, C., and Lee, B.-J. (2013). Current trends and future perspectives of solid dispersions containing poorly water-soluble drugs. *European Journal of Pharmaceutics and Biopharmaceutics*, 85(3, Part B):799 – 813. 9, 10

Vogt, M., Kunath, K., and Dressman, J. B. (2008). Dissolution improvement of four poorly water soluble drugs by cogrinding with commonly used excipients. *European Journal of Pharmaceutics and Biopharmaceutics*, 68(2):330 – 337. 12

Vyazovkin, S. and Dranca, I. (2005). Physical stability and relaxation of amorphous indomethacin. *The Journal of Physical Chemistry B*, 109(39):18637 – 18644. 18, 19

Wade, R. (1984). The temperature dependence of radiation damage in organic and biological materials. *Ultramicroscopy*, 14(3):265–270. 34, 37, 85, 87

Wade, R. and Pelissier, J. (1982). The temperature dependence of the electron irradiation resistance of crystalline paraffin. *Ultramicroscopy*, 10(3):285–290. 34, 37, 84, 85, 87

Wall, J. S. (1980). Contamination in the STEM at ultra high vacuum. *Scanning Electron Micrscopy*, pages 99 – 106. 29

Wang, L., Song, Y., Yang, P., Tan, B., Zhang, H., and Deng, Z. (2015). Preparation and thermodynamic properties of felodipine form IV. *Journal of Thermal Analysis and Calorimetry*, 120(1):947 – 951. 41, 117

Wegiel, L. A., Mauer, L. J., Edgar, K. J., and Taylor, L. S. (2013). Crystallization of amorphous solid dispersions of resveratrol during preparation and storageimpact of different polymers. *Journal of Pharmaceutical Sciences*, 102(1):171 – 184. 133

Wen, H., Zhang, H., Liu, Z., Liu, C., Liu, S., Yang, X., Liu, F., and Xie, H. (2018). Stress mapping of a strain superlattice using scanning moiré fringe imaging. *Applied Physics Letters*, 113(3):031905. 183

Westbrook, M. L., Sindelar, R. L., and Fisher, D. L. (2015). Radiolytic hydrogen generation from aluminum oxyhydroxide solids: theory and experiment. *Journal of Radioanalytical and Nuclear Chemistry*, 303(1):81–86. 91

Wilkens, M. and Rapps, P. (1977). Electron diffraction in crystalline specimens containing a high density of lattice defects. i. development of a statistical theory. *Physica Status Solidi (a)*, 44(1):173–182. 85

Williams, D. B. and Carter, C. B. (2009). *Transmission Electron Microscopy: A Textbook for Materials Science*. Springer, second edition. 22, 30, 43, 45, 51, 182, 183

Wingstrand, K., Abrahamsson, B., and Edgar, B. (1990). Bioavailability from felodipine extended-release tablets with different dissolution properties. *International Journal of Pharmaceutics*, 60(2):151 – 156. 42

Wu, B. and Neureuther, A. R. (2001). Energy deposition and transfer in electron-beam lithography. *Journal of Vacuum Science & Technology B: Microelectronics and Nanometer Structures Processing, Measurement, and Phenomena*, 19(6):2508 – 2511. 27

Wu, G. and Zaefferer, S. (2009). Advances in tem orientation microscopy by combination of dark-field conical scanning and improved image matching. *Ultramicroscopy*, 109(11):1317–1325. 144

Xiang, T.-X. and Anderson, B. D. (2017). Molecular dynamics simulation of amorphous hydroxypropylmethylcellulose and its mixtures with felodipine and water. *Journal of Pharmaceutical Sciences*, 106(3):803 – 816. 133

Yao, B., Sun, T., Warren, A., Heinrich, H., Barmak, K., and Coffey, K. R. (2010). High contrast hollow-cone dark field transmission electron microscopy for nanocrystalline grain size quantification. *Micron*, 41(3):177–182. 144

Yonekura, K., Maki-Yonekura, S., and Namba, K. (2002). Quantitative comparison of zero-loss and conventional electron diffraction from two-dimensional and thin three-dimensional protein crystals. *Biophysical Journal*, 82(5):2784–2797. 99

Yoshioka, M., Hancock, B. C., and Zografi, G. (1995). Inhibition of indomethacin crystallization in poly(vinylpyrrolidone) coprecipitates. *Journal of Pharmaceutical Sciences*, 84(8):983 – 986. 139

Yu, L. (2001). Amorphous pharmaceutical solids: preparation, characterization and stabilization. *Advanced Drug Delivery Reviews*, 48(1):27 – 42. 106

Yu, L. (2016). Surface mobility of molecular glasses and its importance in physical stability. *Advanced Drug Delivery Reviews*, 100:3–9. 175

Zhang, J. and Zografi, G. (2001). Water vapor absorption into amorphous sucrosepoly(vinyl pyrrolidone) and trehalosepoly(vinyl pyrrolidone) mixtures. *Journal of Pharmaceutical Sciences*, 90(9):1375 – 1385. 168

Zhou, W., Apkarian, R., Wang, L. Z., and Joy, D. (2006). *Scanning Microscopy for Nanotechnology. Techniques and Applications*, chapter Fundamentals of Scanning Electron Microscopy (SEM), pages 1–40. Springer. 43